Graphene Nanomaterials

Fabrication, Properties and Applications

Satyendra Mishra
Dharmesh Hansora

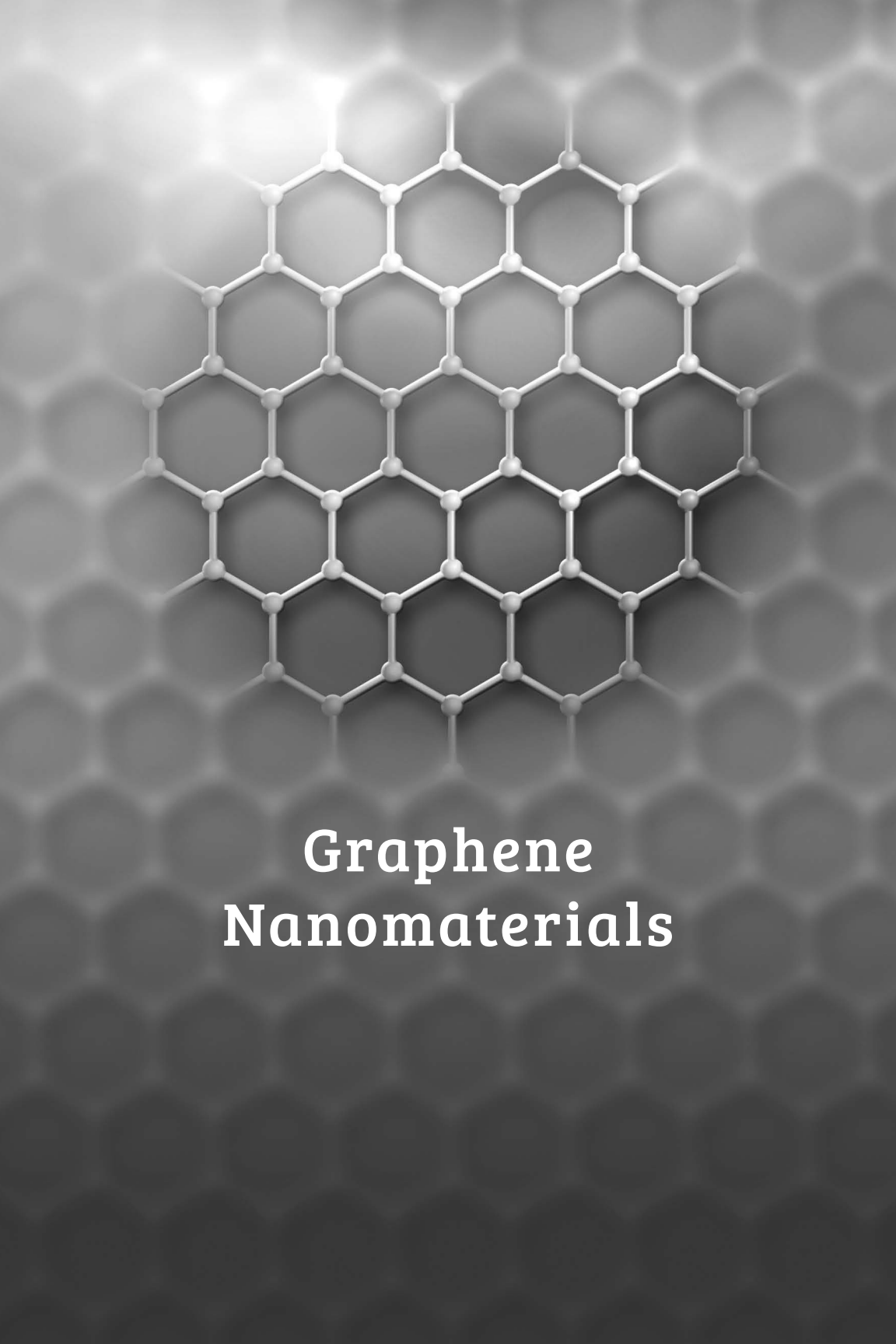

Graphene Nanomaterials

Graphene Nanomaterials

Fabrication, Properties and Applications

Satyendra Mishra
Dharmesh Hansora

Pan Stanford Publishing

Published by

Pan Stanford Publishing Pte. Ltd.
Penthouse Level, Suntec Tower 3
8 Temasek Boulevard
Singapore 038988

Email: editorial@panstanford.com
Web: www.panstanford.com

British Library Cataloguing-in-Publication Data
A catalogue record for this book is available from the British Library.

Graphene Nanomaterials: Fabrication, Properties and Applications

ISBN 978-981-4745-41-3 (Hardcover)
ISBN 978-1-315-36455-1 (eBook)

Printed in the USA

Contents

Preface

The graphene-based nanomaterials have been developed due to their potential and immense interest in areas such as science, engineering and technology. The graphene-based nanomaterials include graphene derivatives, graphene-supported inorganic nanomaterials and thin films, graphene–metal-decorated nanostructures, core–shell structures of nanocarbon-graphene and graphene-doped polymer hybrid nanocomposites, etc. These graphene-based nanomaterials have been prepared by various methods such as exfoliation of graphite, chemical vapour deposition, chemical reduction of graphene oxide, catalysis, sono sol–gel route, in-situ hydroxylation, silver mirror reaction, reduction methods, hydrothermal methods, electrochemical methods and ex-situ methods. The graphene-related nanomaterials are ideal templates due to their attractive properties and also made them and useful as functional materials in biomedical, electronics, optics, energy-based products, gas sensing, ion exchange and molecular adsorption.

This book provides a basic overview of the recent advances in graphene-based nanomaterials including their fabrication, functionalisation, surface modification, properties and their potential applications. The book, deals with novel approaches for preparation of graphene-based nanomaterials which will boost both product- and process-oriented industrial research. It will also be helpful to scientists, research scholars, post-graduate and under graduate students.

Satyendra Mishra

Dharmesh Hansora

Fall 2017

Chapter 1

Introduction

Nanotechnology has blossomed since more than two decades and also it has proved its importance useful in potential areas [1–18]. Nowadays, graphene is a emerging star and also a new paradigm of relativistic condensed-matter physics and material science. The graphene's discovery is an important addition, which has been considered as a world's thinnest material. Graphene's derivatives play a significant key role in modern life [19]. The fundamental breakthroughs towards the physical understanding of graphene and graphite were already discussed in the 1940s and 1950s [20, 21].

1.1 Discovery of Graphene Nanomaterials

The word graphene is originated from the Greek word "Graphein" that means to write. Earlier research, focusing on preparation and fundamental properties of nanocarbons (e.g. epitaxial graphene films, nanoribbons and nanopatches), provides a basic fundamental knowledge. Graphene's research has been successfully capitalised after its first revolution by Novoselov et al. [19, 20, 22, 23] in 2004. Graphenes, being an intriguing or evolution from of 2-dimensional (2D) to 3D topology, have potential properties. These 3D materials can be functionalised by the substituting the carbon atoms with heteroatoms or entire functional groups [19, 21, 24–28].

Graphene Nanomaterials: Fabrication, Properties and Applications
Satyendra Mishra and Dharmesh Hansora

ISBN 978-981-4745-41-3 (Hardcover), 978-1-315-36455-1 (eBook)
www.panstanford.com

Graphene is a layered structure or a one-atom-thick planar nanosheet of sp^2-bonded carbon atoms packed in a honeycomb crystal lattice [29] or multi layers of carbon atoms that are densely packed into benzene rings stripped of their hydrogen atoms. This 2D nanocarbon–based conducting nanomaterials (NMs) have exceptional characteristics like electronic property, physical properties, chemical tunability and high crystal quality. Graphene's research has already shown a profusion of new physics and their potential applications [30]. Graphene is a structural parent of all carbon allotropes including graphite, fullerenes, carbon fibres, nanobuds, nanorings, single walled carbon nanotubes (SWCNTs), double walled CNTs (DWCNTs) and multi-walled CNTs (MWCNTs) [19–21]. Graphene sheets have types which include single-layer, bilayer and few-layer (<10). Kuilla et al. [25] reported about single-layer graphene sheets and 2D carbon crystals. Functional nanocomposites and nanohybrids of graphene sheets have been researched since past decade. The scientists have synthesised graphene-based nanohybrids with various nanostructures that can be engineered by incorporating dissimilar nanoaparticles (NPs) in a composite form. The various forms of carbon (e.g. diamond, graphite, fullerene, CNTs, graphene and their derivatives), chemically stable metal NPs (e.g. gold, copper), metal oxides NPs (e.g. alumina, silica, zirconia, titania), oxide ceramics (e.g. Al_2O_3, CuO), metal nitrides (e.g. AlN, SiN), metal carbides (e.g. SiC), and functionalised NPs. Graphene has already shown an effective support for the nanostructures and defective carbon sheets. Controlled and easily tunable NPs are used for the rational design of new functional materials and also for the development of quite powerful model systems for different applications. The graphene-based hybrid nanostructures are known to be used for improvement in characteristic properties of the composites.

This chapter provides a basic overview of graphene-related NMs. The primarily emphasis is on the different synthetic strategies that have been pursued so far for the preparation of graphene-based inorganic NPs and graphene-doped polymers, as well as the their concerted effect of the properties of the new hybrid functional NMs-based individual components that will present the special features for potential applications. The prospective applications of these graphene-based hybrid NMs will be presented [61–63] in next chapter.

1.2 History of Graphene

Graphene is a thermodynamically stable form of carbon NMs and extremely intriguing composition of two individual sp^2-hybridised carbon sheets. Scientists have focused to develop hybrid systems made of chemically modified graphene and 3D systems based on the graphene sheet assemblies. Germ and his co-workers, in 2004, observed a single-layer graphene made of atomically thin carbon film, which has received increasing attention and becomes a rapidly rising star on the horizon of materials science and condensed-matter physics [31]. Graphene possesses useful properties such as high values of Young's modulus (~1.1 TPa), a large theoretical specific surface area (2630 m^2/g), and excellent thermal conductivity (~5000 W/m·s). In addition, transport phenomena of graphene has been also reported well, indicating mass less Dirac fermions, a bipolar field effect, room-temperature quantum Hall effect, etc. These performances of graphene family members have attracted important concern in recent years increasing impetus in the field of scientific and technological. These peculiar properties have been harnessed among the numerous methods, and one possible route is to incorporate graphene sheets into hybrid nanocomposites. The easy and low cost synthesis, and also non-toxicity of graphene make it as a promising candidate for technological applications [31–63].

1.3 Types of Graphene-Related Advanced Nanomaterials

1.3.1 Graphene-Based Derivatives

Graphene-based carbon NMs [28, 64, 65] mainly include (i) graphene oxide (GO), (ii) doped graphene (iii) derived graphene nanoribbons (GNRs), (iv) graphane, (v) fluorographene, (vi) graphyne (vii) graphdiyne, (viii) graphone and (ix) porous graphene. Graphene is a semimetal with zero band gap, i.e. conduction and valence bands meet at the Dirac point. A zero band gap can be easily tuned by doping and cutting the 2D graphene into form of 1D GNRs [20, 66]. GO is an oxidised and functionalised derivative and it has been reported as hydrophilic material because it has ability of water dispersion. GO

adheres on interfaces due to its lower interfacial energy, so it has been widely used as surfactant for emulsification of organic solvents in water. It has been used for the dispersion of insoluble graphite and CNTs in water. This capability strengthens it for development of graphene and P-conjugated systems–based functional hybrid NMs [66, 67]. Graphane is hydrogenated form of graphene sheet. It is a non-magnetic semiconductor having an energy gap due to hydrogenation. Graphane is a hydrocarbon with a stoichiometry formula unit of CH, i.e. extended 2D polymer form of carbon. It generally adds a wealth to the carbon-based NMs useful for hydrogen storage and nanoelectronic applications. Generally, the hydrogen atoms alternate the directions along with the graphane sheet and transform the carbon lattice from sp^2 to sp^3 hybridisation. Graphane can be easily transformed back into original graphene sheets by annealing process. Fluorographene, with stoichiometric formula of CF, is an another important structure of graphene. Fluorographene has a geometric structure and sp^3 bonding configuration similar to graphane with each carbon attached to one fluorine atom. Fluorographene has been used as a solid lubricant for developing the batteries under extreme conditions. Graphyne and graphdiyne are another non-natural carbon allotropes, which have better potential than graphene due to their unique structures, electronic and intriguing properties. Graphyne is a one-atom-thick planar sheet of sp- and sp^2-bonded carbon atoms arranged in a crystal lattice form. Graphydine has acetylenic linkages connecting the hexagons of graphene. Graphone, is known as a semi-hydrogenated derivative of graphene, having stoichiometric formula of C_2H [65]. In graphone structure, hydrogen atoms are attached on either side of the carbon sheet and graphone is also known as a hybridised mixture of sp^2 and sp^3 carbon atoms. A porous graphene is a another new class of light weight carbonaceous material. It has a distributed structure within the covalent p-electronic framework of graphene sheet.

1.3.2 Graphene-Based Nanocomposites and Nanohybrids

Pristine graphene sheets are hydrophobic material, and it is also insoluble in most of the solvents. The processing of graphene composites is related to foremost with the solubilisation of

graphene. The different functional groups can be attached to the carbon backbone by chemical modification, covalent, or noncovalent functionalisation for improving the solubility of graphene, e.g. graphene–metal-decorated nanostructures, graphene-supported inorganic NMs hybrid nanofluids and films, core–shell structures of nanocarbon-graphene and graphene doped polymer hybrid nanocomposites etc. The graphene nanocomposites developed using metal (e.g. Au, Ag, Pd, Pt, Ni and Cu) NPs possess advanced properties. Graphene and their derivative NMs have been decorated using metal semiconductor NMs such as metal oxides and dioxides and metal sulfides. The different types of graphene-based nanohybrids materials are discussed below, which have been researched and ported till date [31, 34, 41, 56, 61–63, 68–70].

1.3.2.1 Hybrid nanofluids

Sarkar et al. [61] reported various hybrid nanofluids which can be prepared in water, oil and ethylene glycol etc. Graphene-based hybrid NMs (nanohybrids of CuO/f-graphene, Ag/f-graphene/f-MWCNTs and GO/MWCNTs/Ni) are also prepared in water due to their ease of solubility [31, 56].

1.3.2.2 Graphene–metal NP-based hybrid composites

Recently, various metals, metal oxides and semiconducting NPs have been incorporated into the graphene 2D structures for development of bulk graphene–NPs hybrid nanocomposites, which include materials like GO/RGO hybrid 2D nano structures [34, 41, 46, 54, 56].

1.3.2.3 Core–shell hybrid nanostructures

The graphene-based core/shell nanostructures have been used in advanced functional NMs, e.g. hybrids of SnO_2/graphene. The SnO_2 was used as core material and prepared by high temperature reflux using $SnCl_2$, H_2O and PEG, while GO were used as shell NMs prepared by reduction method [51].

1.3.2.4 Next-generation hybrid nanomaterials

A research on graphene, nowadays, is mainly pushed by the very active materials, which has progressed into next generation graphene

base NMs. This can be divided into two main categories [32]. First, a next generation graphene-based NMs are chemically modified graphene (CMG) sheets composed of graphene and carbon atoms that are replaced by other atoms (N, B, S, P) or entire functional groups. Second, 3D graphene architectures (3DG) assembled by graphene or CMG sheets together forming a 3D interconnected networks of complex nano-objects like crumpled papers, hollow spheres and capsules etc.

1.4 Recent Progress in Graphene-Related Advanced Materials

Scientists have focused more on complex systems like modified graphene and 3D assembly of graphene sheets. Graphene has sensation with half-integer quantum Hall effect and ballistic electron transport [19]. This 2D NM consists of a single layer, but the few-layer graphenes has been one of the interest to be investigated. The research has also led for development of next generation graphene-based NMs such as modified graphene (C atoms replaced by N, B, S, P atoms) and architectures of 3D graphenes (e.g. nanospheres, nanocapsules, nanopapers, nanolayers) [24, 29]. Graphene NMs have attracted scientific interests (both academic and industrial) because these can improve the properties of nanocomposites.

1.4.1 Graphene-Based Disruptive Technologies: An Overview

Technologies can be advanced either by scaling the size and number of transistors on a chip or by transition from vacuum tubes to semiconductor technologies. Lots of improvements are needed in order to become disruptive technologies which are usually characterised by universal, potential and versatile applications. The more universal technology enhances the chances for broad base success. So the inherent novelty associated with graphene-based NMs, an initial roadmap can be envisaged, including short-term milestones and medium- to long-term targets. This could direct the possible transition to a technological platform of graphene-related

NMs, which can generate the many opportunities in different fields and benefits to the society [61].

1.4.1.1 Opportunities

The graphene-related NMs have a major impact in several technological fields, because of their potential properties enabled them for new applications, e.g. (i) electronic applications such as high-frequency devices, touchscreens, flexible and wearable devices, ultrasensitive sensors, superdense data storage, nano-electromechanical systems (NEMS) and photonic devices, (ii) energy field applications such as batteries, supercapacitors (SCs), solar cells to store and transport electrical power. Graphene's most appealing potential lies light transmittance ability as well as electricity, which can improve the performance for light emitting diodes (LEDs), flexible touchscreens, photodetectors and ultrafast lasers.

1.4.1.1.1 *New opportunities for electronics*

More functions in integrated electronics can enable their applications for distributed sensors, actuators and controllers, office automation and environmental control to meet the social request for better safety, health and comfort. An increase in automation should be considered by people at work, the aging population and the need of adequate facilities. Sensors and metrological devices based on graphene-related NMs can extend the functionalities of hybrid circuits. An integration of 3D graphene-related NMs-based devices would be the solution for low cost chips with extended functionalities [61].

1.4.1.1.2 *New energy solutions*

The graphene-based NMs have emerged as new solutions for energy storage and generation, nano-engineered products, etc. The graphene NM–based systems for applications of energy production (photovoltaics, fuel cells), energy storage (SCs, batteries and hydrogen storage) have been prepared via proof of concept demonstrators that will progress towards the targeted technology readiness levels (TRLs). These TRLs are used for commercialisation and to assess the maturity of technologies during their development [61].

1.4.1.1.3 *New technologies and materials: Towards a novel technological platform*

The graphene-based NMs enable the emergence of new technologies after improvement in technologies of existing electronics and optoelectronics. The properties of graphene-related NMs enable technological concepts with a qualitatively different physics as compared to the other materials [61].

Graphene is an engineering NM, and ideal candidate for many applications that have also been realised [71–74]. The "all-surface" nature of graphene can tailor its properties by surface treatments, i.e. chemical functionalisation. The graphene can be easily converted into a band-gap semiconductor hydrogenated graphene and "graphane" [71] or into an insulating fluorinated graphene, or "fluorographene" [72]. Graphene flakes can be easily dispersed [73] into solvents and these dispersed graphene flakes possess their outstanding properties, so they can be embedded in a polymeric matrix for the realisation of nanocomposite materials [74, 75] with improved performance [73–75].

At present, an electronic device such as a mobile phone requires the assembly of a various components. The graphene-related NMs, with many characteristic properties, offer a comprehensive technological platform for different device components such as transistors, batteries, optoelectronic components, ultrafast lasers, photodetectors, photovoltaic cells and bio- and physicochemical sensors. This change in the paradigm of device manufacturing create opportunities for the development of new industries.

1.4.1.2 Scientific output

The graphene-related NMs are suitable examples of an emerging nanotechnological materials, which can be discovered in research laboratories and commercialised into products and devices. The rise in patents since 2007 by various corporations around the world is one of the evidence. The translation of nanotechnology is associated with biomedicine sectors [76], where clinical studies and basic research are well linked up. A giant magneto-resistance [77], which has been moved from an academic and research discovery to a dominant information storage technology in very short time [78]. Similarly, graphene-related NMs have shown a potential and effective

impact, e.g. integrating the graphene-related NM–based components with Si-based electronics allow not only substantial performance improvements but, also more importantly, new applications.

Graphene's research has already emerged in area of materials science. However, due to the unique structures of graphene, many of the possibilities need to be explored and well understood, as a result their analysis requires highly sophisticated methods. According to Nobel Laureate Frank Wilczek's quote: graphene is only the probable system from which ideas from quantum field theory can lead into patentable research innovations [76].

1.4.1.2.1 *Intellectual property landscape analysis*

In the graphene's research area, there has been a particularly rapid increase in patent publication activity since around 2007 [79]. This patentable activity is generally driven by major universities and industrial corporations in South Korea and USA [80]. A high level of patent submitting and filing activity in China is also reported [81]. These trends have pushed academians, researchers and scientists towards graphene innovations arising in Europe that are being exploited [82]. An analysis of the Intellectual Property (IP) gave the evidence, i.e. Europe is a significant foothold in the patent landscape in the area of graphene research and also secured it's value. As the underlying space of graphene technology develops the patent of graphene-related NMs landscape matures. The redistribution of the patent is inevitable and Europe is taking benefits from patent-based commercialisation of graphene-related NMs. This is the indication of high levels of the graphene patent landscaping which is now growing rapidly in sub-segments of the semiconductor and biotechnology industries [83]. The active business of patenting in such sub-sectors include 'portfolio of maximisation and optimisation' [83] strategies, and the sub-sectors experience the development of 'patent thickets' [83], or multiple overlapping granted patent rights [83].

The IP analysis, shown in Fig. 1.1, clearly highlights the disparity between graphene-related NMs scientific production (number of publications), graphene-related NMs associated with technical exploitation (patent applications), which provide an evidence indicating requirement to bring leading researchers of academia (for scientific publications) and industrial leaders (patent applications) together.

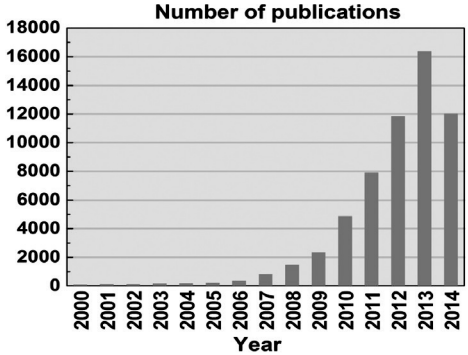

Figure 1.1 Publications on graphene from 2000 to August 2014. Reproduced with permission from Ref. [61] under Creative Commons Attribution.

1.4.1.2.2 *Graphene IP landscape analysis*

Figure 1.2 clearly indicates that the global IP activities on graphene-related NMs have surged since 2007, mimicking the trend in research, which is also an evidence that research investment is fuelling rapidly for growth of graphene technology.

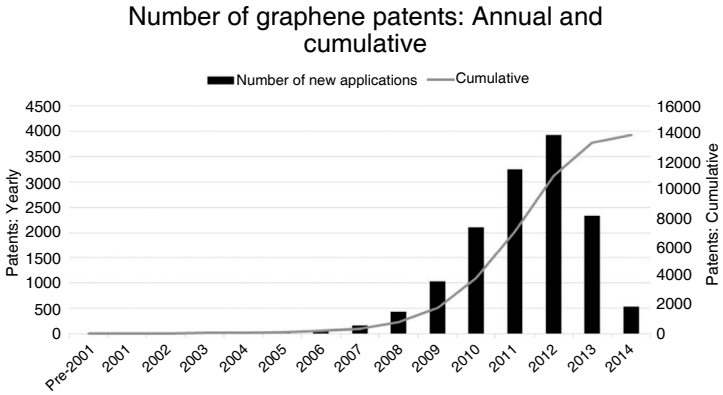

Figure 1.2 Patent applications on graphene-related NMs as a function of application year. Accordingly, 2013 and 2014 are under-represented. Data updated as of July 2014. Reproduced with permission from Ref. [61] under Creative Commons Attribution.

A review on the patent dataset indicates that patents have been filed for different applications including characterisation [84], polymer composites [85], transparent displays [86], transistors [87],

capacitors [88], solar cells [89], biosensors [90], conductive inks [91–93], windows [94], saturable absorbers [95], photodetectors [96] and tennis rackets [97]. Overall, the space on patent of graphene's research comprises of mainly in synthesis (like chemical vapour deposition and exfoliation) area and electronics (like transistors, displays and computer chips) area.

1.5 Scientific and Technological Objectives

Ferrari et al. [61] summarised the objectives towards the development of graphene-related NMs and hybrid systems–based products. These graphene-related NMs are combination of properties required for many applications, generating new products. The creation of disruptive technologies is conditional to reach various objectives and also to overcome several challenges throughout the value chain, from materials to components and systems.

The scientific and technological objectives mainly include:

(A) Technologies for materials:
- Identification and analysis of new layered materials.
- Reproducible, reliable, sustainable, safe, large scale production of graphene-related NMs, that can satisfy the needs for different areas of applications.

(B) Technologies for components:
- Identification of new concepts for device enabled by graphene-related NMs.
- Identification of technologies for component based on graphene-related NMs.
- Electronic technologies comprising of high-frequency electronics, spintronics, optoelectronics and sensors.

(C) Systems integration:
- Routes and protocols to bring graphene-related NMs–based components and structures into systems that can provide new functionalities and application areas.
- New concepts for integration of the graphene-related NMs in platforms of existing technology.
- Integration routes of nanocomposites for flexible electronics and energy applications.

The science and technology roadmap (STR) indicates the principal routes for development of graphene-related NMs and therefore their production for development of new devices. A main key area is advanced methods for production of graphene-related NMs, with structural functions for embedded electronics in an environmentally sustainable manner. The STR of the graphene-related NMs explores beyond mainstream to novel sensor applications and composites that can take advantage with chemical, biological and mechanical properties.

Graphene's large surface area and high electrical conductivity make it a novel material for energy storage applications such as advanced batteries and SCs. These energy-based applications have an impact on portable electronics and electric cars. The prospect of rapidly chargeable light weight batteries will give environment friendly transportation, i.e. the implementation of electric cars in urban and suburban areas. Strong and light weight composites are useful to build new cars, airplanes and other structures utilising less material and energy, and hence these could contribute directly to a more sustainable world (see Fig. 1.3).

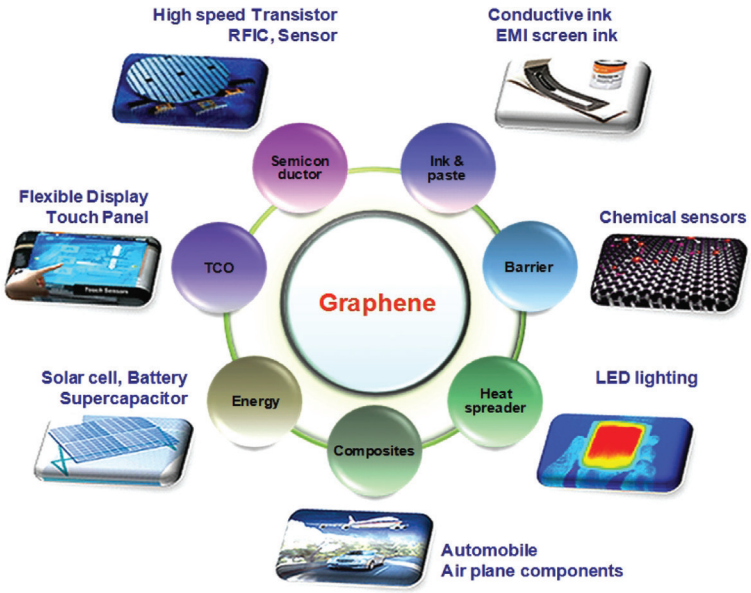

Figure 1.3 Overview of applications of graphene in different sectors. Reproduced with permission from Ref. [61] under Creative Commons Attribution.

1.6 Conclusion and Perspectives

In this chapter, the synthesis, characterisation, and implementation of graphene-related NMs have been discussed for a host of potential applications. While numerous excellent reviews have been already reported which cover synthesis, characteristic properties, and potential applications, of graphene-related NMs and also their implementation into specific applications. We present here complex review of past research work done covering all modes and synthesis methods for graphene-related NMs including hybrids, nanocomposites, nanostructured materials, their characteristic properties, their utilisation for potential applications. This chapter will inspire and initiate the interest from various interdisciplines as well as highlight an upcoming field wherein graphene-related NMs will bring significant advantages to a wide variety of applications.

In this chapter, we also outline and try to summarise research progresses of nano-engineering of the graphene-related NMs. However, there are several key issues to be resolved for the future development on the graphene nano-engineering.

References

1. Sonawane S.S., Mishra S., Shimpi N.G. (2010). *Polym. Plast. Technol. Eng.,* **49(1)**, 38–44.
2. Shimpi N.G., Kakade R.U., Sonawane S.S., Mali A.D., Mishra S. (2011). *Polym. Plast. Technol. Eng.*, **50**, 758–761.
3. Mishra S., Shimpi N.G., Mali A.D. (2011). *J. Polym. Res.,* **18(6)**, 1715–1724.
4. Shimpi N.G., Mishra S. (2012). *Polym. Plast. Technol. Eng.,* **51(2)**, 111–115.
5. Chatterjee A., Mishra S. (2013). *Macromol. Res.,* **21(5)**, 474–483.
6. Shimpi N.G., Mishra S. (2013). *J. Reinf. Plast. Comp.,* **32(13)**, 947–954.
7. Shimpi N.G., Sonawane H.A., Mali A.D., Mishra S. (2014). *Polym. Bull.,* **71**, 515–531.
8. Hazra C., Kundu D., Chatterjee A., Chaudhari A., Mishra S. (2014). *Coll. Surf. A: Physicochem. Eng. Aspects,* **449**, 96–113.
9. Mishra S., Shimpi N.G. (2008). *Polym. Plast. Technol. Eng.,* **47(1)**, 72–81.

10. Mishra S., Sonawane S., Mukherji A., Mruthyunjaya H.C. (2006). *J. Appl. Polym. Sci.,* **100(5)**, 4190–4196.
11. Shimpi N.G., Mali A.D., Hansora D.P., Mishra S. (2015). *Nanosci. Nanoeng.,* **3(1)**, 8–12.
12. Yeole B., Sen T., Hansora D.P., Mishra S. (2015). *J. Appl. Polym. Sci.,* **132**, 42379.
13. Sen T., Shimpi N.G., Mishra S. (2014). *Sens. Actuators B*, **190**, 120–126.
14. Mishra S., Shimpi N.G., Sen T. (2013). *J. Polym. Res.,* **20(49)**, 1–10.
15. Shimpi N.G., Mishra S. (2010). *J. Nanopart. Res.,* **12(6)**, 2093–2099.
16. Mishra S., Chatterjee A. (2011). *Polym. Adv. Technol.*, **22(12)**, 1593–1601.
17. Ratna D., Jagtap S.B., Rathor R., Kushwaha R.K., Shimpi N.G., Mishra S. (2013). *Polym. Comp.,* **34(6)**, 1004–1011.
18. Chatterjee A., Mishra S. (2013). *Particulogy,* **11(6)**, 760–767.
19. Novoselov K.S., Geim A.K., Morozov S.V., Jiang D., Zhang Y., Duobonos S.V., Grigorieva I.V., Firsov A.A. (2004) *Science,* **306 (5696)**, 666–669.
20. Raza H. (2012). *Graphene Nanoelectronics,* Heidelberg, Germany: Springer-Berlin, pp. 586.
21. Geim A.K., Novoselov K.S. (2007). *Nat. Mater.,* **6(3)**, 183–191.
22. Singh V., Joung D., Zhai L., Das S., Khondaker S.I., Seal S. (2011). *Prog. Mater. Sci.,* **56(8)**, 1178–1271.
23. Fuhrer M.S., Lau C.N., MacDonald A.H. (2010). *MRS Bull.,* **35(4)**, 289–295.
24. Agnoli S., Granozzi G. (2013). *Surf. Sci.,* **609**, 1–5.
25. Kuilla T., Bhadra S., Yaoa D., Kim N.H., Bose S., Lee J.H. (2010). *Prog. Polym. Sci.,* **35(11)**, 1350–1375.
26. Geim A.K. (2011). *Angew. Chem., Int. Ed.,* **50(31)**, 6967–6985.
27. Horing N.J.M. (2010). *Philos. Trans. R. Soc., A,* **368(1932)**, 5525–5556.
28. Li N., Wang Z., Shi Z., Mikhailov S. (eds) (2011). *Synthesis of Graphene with Arc-Discharge Method*, Rijeka, Croatia: Intech, pp. 23–36.
29. Rao C.N.R., Sood A.K., Subrahmanyam K.S., Govindaraj A. (2009). *Angew. Chem. Int. Ed.,* **48(42)**, 7752–7777.
30. Zhu Y., Murali S., Cai W., Li X., Suk J.W., Potts J.R., Ruoff R.S. (2010). *Adv. Mat.,* **22(35)**, 3906–3924.
31. Sarkar J., Ghosh P., Adil A. (2015). *Renew. Sust. Ener. Rev.,* **43**, 164–177.
32. Agnoli S., Granozzi G. (2013). *Surf. Sci.,* **609**, 1–5.

33. Gilje S., Han S., Wang M., Wang K.L., Kaner R.B. (2007). *Nano Lett.*, **7(11)**, 3394–3398.
34. Singh V., Joung D., Zhai L., Das S., Khondaker S.I., Seal S. (2011). *Prog. Mater. Sci.*, **56**, 1178–1271.
35. Wang H., Robinson J.T., Diankov G., Dai H. (2010). *J. Am. Chem. Soc.*, **132**, 3270.
36. Williams G., Seger B., Kamat P.V. (2008). *ACS Nano*, **2**, 1487.
37. Wang D., Kou R., Choi D., Yang Z., Nie Z., Li J. (2010). *ACS Nano*, **4**, 1587.
38. Yang S., Feng X., Ivanovici S., Müllen K. (2010). *Angew. Chem. Int. Ed.*, **49**, 8408.
39. Liu C., Yu Z., Neff D., Zhamu A., Jang B.Z. (2010). *Nano Lett.*, **10**, 4863.
40. Wang D.W., Li F., Zhao J.P., Ren W.C., Chen Z.G., Tan J. (2009). *ACS Nano*, **3**, 1745.
41. Huang X., Yin Z., Wu S., Qi X., He Q., Zhang Q., Yan Q., Boey F., Zhang H. (2011). *Small*, **7(14)**, 1876–1902.
42. Yang S., Feng X., Ivanovici S., Müllen K. (2010). *Angew. Chem. Int. Ed.*, **49**, 8408.
43. Huang X., Zhou X.Z., Wu S.X., Wei Y.Y., Qi X.Y., Zhang J., Boey F., H. Zhang. (2010). *Small,* **6**, 513.
44. Zhou X.Z., Huang X., Qi X.Y., Wu S.X., Xue C., Boey F., Yan Q.Y., Chen P., Zhang H. (2009). *J. Phys. Chem. C*, **113**, 10842.
45. Zhou H.Q., Qiu C.Y., Liu Z., Yang H.C., Hu L.J., Liu J., Yang H.F., Gu C.Z., Sun L.F. (2010). *J. Am. Chem. Soc.*, **132**, 944.
46. Mikhailov S. (2011). *Physics and Applications of Graphene: Experiments,* InTech, Available from: http://www.intechopen.com/books/physics-and-applications-of-graphene-experiments
47. Li G.L. (2010). *J. Phys. Chem. C,* **114(29)**, 12742–12747.
48. Chen S., Zhu J., Huang H., Zeng G., Nie F., Wang X. (2010). *J. Solid State Chem.*, **183**, 2552–2557.
49. Xu C., Wang X. (2009). *Small*, **5(19)**, 2212–2217.
50. Xu C., Wang X., Zhu J., Yang X., Lu L. (2008). *J. Mater. Chem.*, **18(46)**, 5625–5629.
51. Chaudhuri R.G., Paria S. (2012). *Chem. Rev.*, **112**, 2373–2433.
52. Zhu B.Y., Murali S., Cai W., Li X., Suk J.W., Potts J.R., Ruoff R.S. (2010). *Adv. Mater.*, **22**, 3906–3924.

53. Rangappa D., Jang J.H., Honma I. (2011). Supercritical fluid processing of graphene and graphene oxide. In *Graphene: Synthesis, Characterization, Properties and Applications,* Jang J.H. (ed.), InTech, pp. 45–58.

54. Rao C.N.R., Subrahmanyam K.S., Ramakrishna Matte H.S.S., Govindaraj A., (2001). Chapter 1: Graphene: synthesis, functionalization and properties, In *Graphene And Its Fascinating Attributes* (Eds, Pati S.K., Enoki T., Rao C.N.R.) World Scientific Publishing Co. Pte. Ltd, pp 1–32.

    http://www.worldscientific.com/doi/suppl/10.1142/7989/suppl_file/7989_chap01.pdf

55. Tang Q., Zhou Z., Chen Z. (2013). *Nanoscale*, **5**, 4541.

56. Georgakilas V., Otyepka M., Bourlinos A.B., Chandra V., Kim N., Christian Kemp K., Hobza P., Zboril R., Kim K.S. (2012). *Chem. Rev.*, **112(11)**, 6156–6214.

57. Hassan H.M.A., Abdelsayed V., Rahman A.E., Khder S., AbouZeid K.M., Terner J., El-Shall M.S., Al-Resayes S.I., El-Azhary A.A. (2009). *J. Mater. Chem.*, **19**, 3832.

58. Chandra V., Kim K.S. (2011). *Chem. Commun.*, **47**, 3942.

59. Terrones M., Méndez A.R.B., Delgado J.C., Urías F.L., Cantú Y.I.V., Macías F.J.R., Elías A.L., Sandoval E.M., Márquez Charlier A.G.C., Terrones J.C. (2010). *Nano Today*, **5(4)**, 351–372.

60. Novoselov K.S., Falko V.I., Colombo L., Gellert P.R., Schwab M.G., Kim K. (2012). *Nature*, **490**, 192–200.

61. Ferrari A.C., Bonaccorso F., Fal'ko V., Novoselov K.S., Roche S., Bøggild P., Borini S., Koppens F.H.L., Palermo V., Pugno N., Garrido J.A., Sordan R., Bianco A., Ballerini L., Prato M., Lidorikis E., Kivioja J., Marinelli C., Ryhänen T., Morpurgo A., Coleman J.N., Nicolosi V., Colombo L., Fert A., Hernandez M.G., Bachtold A., Schneider G.F., Guinea F., Dekker C., Barbone M., Sun Z., Galiotis C., Grigorenko A.N., Konstantatos G., Kis A., Katsnelson M., Vandersypen L., Loiseau A., Morandi V., Neumaier D., Treossi E., Pellegrini V., Polini M., Tredicucci A., Williams G.M., Hong B.H., Ahn J.H., Kim J.M., Zirath H., Wees van B.J., Zant van der H., Occhipinti L., Di Matteo A., Kinloch I.A., Seyller T., Quesnel E., Feng X., Teo K., Rupesinghe N., Hakonen P., Neil S.R.T., Tannock Q., Löfwander T., Kinare J. (2015). *Nanoscale*, **7**, 4598.

62. Rao C.N.R., Sood A.K., Subrahmanyam K.S., Govindaraj A. (2009). *Angew. Chem. Int. Ed.*, **48**, 7752–7777.

63. Awasthi K., Kumar R., Raghubanshi H., Awasthi S., Pandey R., Singh D., Yadav T.P., Srivastava O.N. (2011). *Bull. Mater. Sci.,* **34(4)**, 607–614.

64. Tang Q., Zhou Z., Chen Z. (2013). *Nanoscale,* **2013(5)**, 4541–4583.
65. Peng Q., Dearden A.K., Crean J., Han L., Liu S., Wen X., De S. (2014). *Nanotechnol. Sci. Appl.,* **2014(7)**, 1–29.
66. Huang X., Yin Z., Wu S., Qi X., He Q., Zhang Q., Yan Q., Boey F., Zhang H. (2011). *Small,* **7(14)**, 1876–1902.
67. Cote L.J., Kim J., Tung V.C., Luo J., Kim F., Huang J. (2011). *Pure Appl. Chem.,* **83(1)**, 95–110.
68. Mel A.A. E., Duvail J.L., Gautron E., Xu W., Choi C.H., Angleraud B., Granier A., P.Y. Tessier. (2012). *Beilstein J. Nanotechnol.*, **3**, 846–851.
69. Yang M., Hou Y., Kotov N.A. (2012). *Nanotoday*, **7(5)**, 430–447.
70. Castanié F., Nony L., Gauthier S., Bouju X. (2012). *Beilstein J. Nanotechnol.*, **3**, 301–311.
71. Elias D.C., Nair R.R., Mohiuddin T.M.G., Morozov S.V., Blake P., Halsall M.P., Ferrari A.C., Boukhvalov D.W., Katsnelson M.I., Geim A.K., Novoselov K.S. (2009). *Science,* **323**, 610–613.
72. Nair R.R., Ren W., Jalil R., Riaz I., Kravets V.G., Britnell L., Blake P., Schedin F., Mayorov A.S., Yuan S., Katsnelson M.I., Cheng H.M., Strupinski W., Bulusheva L.G., Okotrub A.V., Grigorieva I.V., Grigorenko A.N., Novoselov K.S., Geim A.K. (2010). *Small,* **6**, 2877–2884.
73. Hernandez Y., Nicolosi V., Lotya M., Blighe F.M., Sun Z., De S., McGovern I.T., Holland B., Byrne M., Gun'ko Y.K., Boland J.J., Niraj P., Duesberg G., Krishnamurthy S., Goodhue R., Hutchison J., Scardaci V., Ferrari A.C., Coleman J.N. (2008). *Nat. Nanotechnol.,* **3**, 563–568.
74. Ramanathan T., Abdala A.A., Stankovich S., Dikin D.A., Herrera-Alonso M., Piner R.D., Adamson D.H., Schniepp H.C., Chen X., Ruoff R.S., Nguyen S.T., Aksay I.A., Prud'Homme R.K., Brinson L.C. (2008). *Nat. Nanotechnol.,* **3**, 327–331.
75. Park S., An J., Piner R.D., Jung I., Yang D., Velamakanni A., Nguyen S.T., Ruoff R.S. (2008). *Chem. Mater.,* **20**, 6592–6594.
76. Kinaret J., Ferrari A.C., Falko V. Kivioja J. (2011). *Procedia Comput. Sci.,* (2011), **7**, 30–33.
77. Grünberg P.A. (2008). *Rev. Mod. Phys.,* **80**, 1531–1540.
78. Fert A. (2008). *Angew. Chem., Int. Ed.,* 2008, **47**, 5956–5967.
79. http://www.cambridgeip.com/industries/nanotechnology/graphene.
80. Brumfiel G. (2012). Graphene goes global: Britain's big bet on graphene, *Nature News*.
81. Tannock Q., Duffy R. (2012). *Patenting Flatland: Graphene—Exploitation Challenges and Opportunities*, Cambridge IP.

82. Stephens P. (2012). Graphene: Invented in the UK, Largely being Developed Elsewhere, *Financial Times*.
83. Harfhof D. (2007). *The Strategic Use of Patents and its Implications for Enterprise and Competition Policies,* 9–12.
84. Colli A., Awan S.A., Lombardo A., Echtermeyer T.J., Kulmala T.S., Ferrari A.C. (2013). US 20130162333.
85. Rozhin O., Ferrari A.C., Milne W.I. (2010). US 20100003528.
86. Woo Y., Seo S.A., Kim D., Chung H. (2011). US 20110089403.
87. Kobayashi T. (2013). EP 2393107.
88. Song L., Zhamu A., Guo J. Jang B.Z. (2009). US 2009762334.
89. Yoon S.M., Choi W.M., Shin H.J., Choi J.Y. (2014). EP 2439779.
90. Owen G. (2011). GB 2471672.
91. Jang B.Z., Zhamu A. (2008). US 20100000441.
92. Murphy R., Rozhin O., Ferrari A.C., Robertson J., Milne W.I. (2007). US 20070275230.
93. Torrisi F., Hasan T., Bonaccorso F., Ferrari A.C. (2014). WO 2014064432 A1.
94. Andersson H. (2011). US 20110311029.
95. Rozhin O., Ferrari A.C., Milne W.I. (2007). US 8323789 B2.
96. Avouris P., Steiner M.B., Engel M., Krupke R., Ferrari A.C., Lombardo A. (2013). US 20130107344 A1.
97. Lammer H. (2010). US 20100125013.

Chapter 2

Fabrication, Functionalisation and Surface Modification

In this chapter, we discuss fabrication, functionalisation and surface modification of graphene and related NMs. We have briefly described the primary methods to synthesise the graphene, GO and RGO followed by an in depth analysis of the various methods for the synthesis of graphene–NP hybrid nanostructures and graphene-encapsulated hybrid NPs, with particular emphasis on the surface morphological properties and characteristics.

2.1 Preparation Methods

A valuable and significant efforts have been carried out for synthesizing the graphene, its derivatives and related NMs due to their many unique and advantageous characteristics properties. Graphene-based hybrid NMs are classified into two categories depending on their structural morphology: (i) graphene–NP composites made of NPs grown or decorated on graphene sheets or their derivatives and (ii) graphene-encapsulated NP composites made of NPs wrapped by graphene and their derivatives. The size ratio or aspect ratio is the main difference between the lateral dimensions of the graphene sheets and the diameter of the NPs. The

Graphene Nanomaterials: Fabrication, Properties and Applications
Satyendra Mishra and Dharmesh Hansora

ISBN 978-981-4745-41-3 (Hardcover), 978-1-315-36455-1 (eBook)
www.panstanford.com

diameter of the NPs ranges from few to hundred nanometers and these NPs can be decorated onto the graphene sheets because they are small in comparison to the sheets and form graphene NP–based hybrid composites. A larger size NPs become more comparable with the graphene sheets, the small 2D graphene sheets can be wrapped around the NPs resulting in graphene-encapsulated hybrid NPs.

2.1.1 Synthesis Methods of Graphene-Related Carbon NMs

2.1.1.1 GO and graphene sheets

A most widely used precursor of graphene is GO [1], which has 150 years of history as single-layer sheet, and it has received scientific interest of chemists as an oxide-functionalised derivative of graphene [2]. GO can be mass-produced by the first-step chemical oxidation of natural graphite and the subsequent exfoliation. Graphite oxide is produced by reacting graphite with strong oxidising agents in aqueous form. Three oxidation methods are in use: Brodie [3], Staudenmaier [4] and Hummers [5] methods. The oxidation reaction generally breaks the long-range π–π conjugation present on the surface of the original graphite and which could form sp^2 graphitic domains surrounded by disordered sp^3-oxidised domains with various oxygen functional groups, including epoxides, quinine, ketone, hydroxyls (–OH), carbonyls (–C=O) and phenol. This is because oxygen-containing functional groups reduce the interlayer forces, impart strongly hydrophilic character and, as a result, facilitates the chemical processing of graphite oxide in the solution to exfoliate into individual GO sheets via ultrasonication and either stirring or rapid heating [6].

GO can also be prepared by the direct oxidation of free-standing or epitaxial graphene by using atomic oxygen in ultra-high vacuum conditions [7, 8] by exposure to molecular oxygen [9–12] or ozone [13] under high temperatures, by the photochemical reaction in the presence of ultraviolet light and ozone [14, 15], and also by electrochemical oxidation in nitric acid under potentiostatic conditions [16, 17]. Theoretical studies on graphene–oxygen interactions are mainly focused on the oxidation process between

the free-standing graphene and reactive O atoms or O_2 molecules [18–20]. The oxygen chemisorption on graphene generally forms the epoxy (1,2-ether) groups, which is predicted to be associated with the unzipping of CNTs or graphene sheets [21, 22]. Under a directional flow, the GO sheets can be reassembled into free-standing large sheets and foil-like material also called GO paper [23]. This GO paper outperforms other traditional clay- and carbon-based materials in strength and stiffness. GO is a soft material, and its mechanical strength is lower as compared with pristine graphene [24], but possesses great strength (prestress of 76.8±19.9 MPa for an assigned 0.7 nm thickness and Young's modulus of 207.6±23.4 GPa), thus proving itself for great potential in fabricating composite materials [25, 26]. GO layers are insulating or semiconducting at a large length, but also depending on the degree of oxidation, so the electronic and optical properties can be controlled by the removal or addition of oxygen-containing groups to produce the semimetal graphene sheets. The tunable optoelectrical properties of GO grant the prospects for using in the field of electric and optical devices [27, 28], spintronic devices [29], catalysts [30–33], SCs [34, 35], electrode materials [36], and chemical or biological sensors [37].

Various synthesis methods for graphene have been reported such as (i) catalytic chemical vapour deposition (CCVD) or microwave CVD [38–52], (ii) arc-discharge method [38, 44, 45], (iii) micromechanical exfoliation [38, 41, 43, 45–47, 53–57], (iv) epitaxial growth on SiC [38–47, 50, 52], (v) chemical reduction [38, 43, 47, 50, 55, 50–58], (vi) thermal reduction [38, 40, 44], (vii) liquid-phase exfoliation [38, 40, 45, 46, 54–57], (viii) unzipping of CNTs [51] and (ix) gas phase microwave plasma reactor [38]. As discussed earlier, the oxidation of graphite for synthesis of GO includes various methods such as Brodie, Staudenmaier and Hummers. The first two methods use combination of oxidants such as $KClO_3$ with HNO_3, while the Hummers method involves combination of $KMnO_4$ and H_2SO_4.

A chemical reduction method using reducing agents such as hydrazine, hydroquinone, sodium borohydride and ascorbic acid was reported for the preparation of GO [46, 58]. Derivatives of graphene, i.e. graphyne, have been synthesised using dehydrobenzo annulene, while graphdiyne (graphyne with acetylene group) was synthesised via cross-coupling reaction using hexaethynyl benzene on copper substrates. Another important derivative of graphene,

graphone, was prepared by applying pressure onto boron, nitrogen and hydrogenated graphene sheets, so that nitrogen could pick hydrogen easily from graphene sheet. On releasing pressure, the dehydrogenated graphene sheet is formed with all hydrogen atoms on the one side. Another derivative graphane was synthesised by the annealing of graphene crystals at 573 K in the presence of an argon atmosphere. These graphene crystals were exposed to cold hydrogen plasma and then allowed to pass from hydrogen-argon mixture at low pressure for 2 h. A scalable method for hydrogenation of graphene to form gram quantity of graphane has also been reported, which includes thermal exfoliation of GO without plasma source and in the presence of hydrogen atmosphere at 6000–15,000 KPa pressure and 493–823 K temperature. Thus, it can be a potential candidate for mass production [59].

Graphene sheets can be obtained using three primary methods: (i) mechanical exfoliation, (ii) CVD onto metal or Si substrates, and (iii) chemical, electrochemical or thermal reduction of GO (Fig. 2.1) [60]. The CVD method is most effective for the mass production of graphene and can be used to fabricate large areas of graphene while limiting the number of defects [61]. Consequently, CVD grown graphene can have a carrier mobility values as high as 2000–4000 $cm^2/V{\cdot}s$ [62].

On the other hand, a high-quality graphene with a carrier mobility of ~10,000 $cm^2/V{\cdot}s$ can be achieved at room temperature by mechanical exfoliation using the Scotch tape method or by rubbing lithographically patterned pillars with “tipless” atomic force microscopy (AFM) cantilevers [63]. The graphene sheets have lateral physical dimensions limit in the order of 10–100 μm. However, the mechanical exfoliation method has poor reproducibility and also not suitable for large-scale fabrication [60]. So the reduction route of GO is economical and a facile technique for the production of graphene; however, it was reported that the quality of these graphene (RGO) sheets, in terms of electrical conductivity, is generally lower than that produced using the other two methods discussed [64]. Overall for the mass production, the CVD method is more efficient for high-quality graphene, while the reduction method is better for small graphene sheets. Hence, the application of graphene must first be considered before the appropriate selection of the synthesis method

(Fig. 2.1). The GO sheets have many distinct characteristics which greatly differentiate them from those of graphene because of the presence of numerous epoxy and oxygen-containing hydroxyl groups on the basal plane, along with traces of phenol, carbonyl, carboxyl, lactone and quinone present at the edges [65], which collectively inhibit the electron transfer (Fig. 2.2A and B). Generally, GO films are hydrophilic and typically insulating with an energy gap in the electron density of states and a sheet resistance of about 10 Ω/sq or higher [66, 67]. However, GO exhibits excellent electronic, thermal, electrochemical and mechanical properties due to its flexibility, transparency and also biocompatibility and hydrophilic nature similar to graphene. In terms of its fabrication, GO is most commonly produced using variation of the Brodie, Staudenmaier and Hummer methods [68, 69].

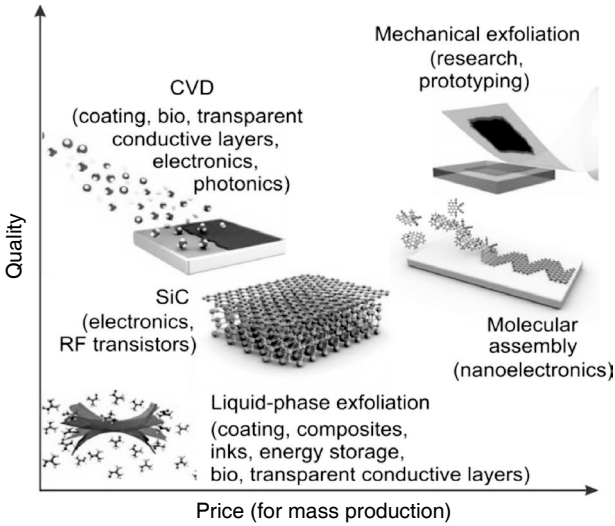

Figure 2.1 Methods for the mass production of graphene depending on the particular application, in terms of size, quality (e.g. presence of defects and impurities) and price. Reprinted by permission from Macmillan Publishers Ltd: *Nature*, Ref. [60], Copyright 2012.

All three methods involve the oxidation of graphite and the formation of hydrophilic groups on the surface [70a, 70b]. After the oxidation process, the resulting graphene is then exfoliated to obtain single- or multilayered GO sheets by common ultrasonication

procedure. Finally, RGO sheets can be obtained from GO through chemical, electrochemical or thermal reduction method, which removes the oxygen-containing branches from the basal planes and edges of the GO sheets (Fig. 2.2C) [69, 71]. The electrical conductivity as well as thermal stability of GO can be restored similar to the levels found in graphite. The electrical conductivity of RGO has been reported in the range of 200–42,000 S/m [64, 72]. Significantly, this depends on parameters such as type of reducing agent, duration, annealing time and annealing temperature used during the reduction method. Moreover, the specific capacitance of RGO is significantly higher than that of GO; the transparency and dispersibility of RGO are significantly reduced when compared to pure GO sheets. Hydrazine, hydroquinone, sodium borohydride and ascorbic acid are used for the removal of the hydroxyl groups from GO sheets to form RGO. Electrochemical tools are also reported to fabricate RGO using either sulphuric acid or nonacidic solutions such as Na-phosphate-buffered saline (PBS), K-PBS, NaOH and KCl in the presence of a constant reduction potential or sweeping potential [73]. Finally, thermal reduction is a well-known method for the removal of oxygen functional groups in the form of water, carbon monoxide and carbon dioxide by placing the GO sample in a preheated furnace at 1000–1100°C in the absence of air [74]. However, chemical and electrochemical methods require mild conditions.

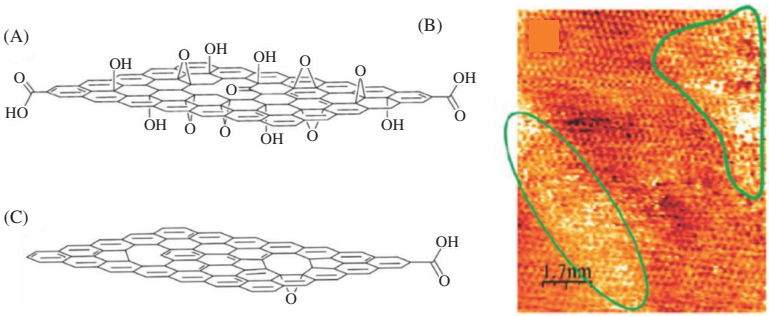

Figure 2.2 Structure of GO and reduced GO. (A) Chemical structure of GO. (B) Scanning tunnelling microscope (STM) image of a GO monolayer on a highly oriented pyrolytic graphite substrate. Oxidised regions are marked by green contours. Panel (B) reprinted with permission from Ref. [70b], Copyright 2007, American Chemical Society. (C) Chemical structure of RGO. Panels (A) and (C) reprinted by permission from Ref. [71], Copyright 2010, John Wiley and Sons.

2.1.1.2 Doped graphene and derived GNRs

Doping is one of the most feasible methods for tuning the band gap of graphene, and cutting of the 2D graphene into 1D GNRs is another remarkable strategy.

2.1.1.2.1 *Substrate and electric field induced doping*

A band gap in graphene is possibly opened through either electrical field gating or the perturbations from underlying substrates, which has attracted a lot of studies and investigations. A small gap (0.26 eV) can be opened owing to the electronic coupling between graphene grown on SiC and the underlying substrate [75–78]. The Fermi level shift with respect to the conical point during absorption of graphene on the metal substrate, which is driven by the work function difference and the chemical interaction between graphene and the metal. Even the weak bonding on the Ag, Al, Au, Cu and Pt surfaces can lead to a Fermi level shift of graphene by 0.5 eV [79]. Generally, bilayer graphene has a gapless band structure, and previous studies predicted that a band gap can be opened by applying an electric field which induces an asymmetry between the two graphene layers [80, 81].

2.1.1.2.2 *Atomic and electrochemical doping*

Atomic and electrochemical doping is an alternative method to interact with the graphene system by internal controls. A top-gated single-layer graphene transistor using an electrochemical dopant such as solid polymer electrolyte is able to reach electron- or hole-doping levels of up to 5×10^{13} cm^{-2} [82]. For surface atomic adsorption [83, 84], a substantial hole doping in the conical band structure of epitaxial graphene can be achieved by absorbing metals with higher electron affinities such as bismuth, antimony and gold [85]. The formation of strong ionic bonding and large charge transfer make alkaline metals as attractive n-type dopant candidates. The surface coating of alkaline metals can produce superconductivity in the chemically doped graphene [86].

2.1.1.2.3 *Substitutional B and N-doping*

Incorporation of foreign atoms or substitutional doping into the carbon lattice is a straightforward way, which can regulate the electronic structure of graphene [87, 88]. Boron and nitrogen serve as natural dopants since they have one fewer or more electron but roughly the same atomic radius as carbon. According to theoretical predictions, substitutionally boron or nitrogen doping can result in the transformation of graphene into p- or n-type semiconductor, respectively, accompanied by the large modifications of electronic transports and charge mobilities [89–92]. Nitrogen doping in graphene (2D CxNy graphene) leads to a metal–semiconductor transition with band gap ranging up to 5 eV, thereby expanding the possible electronic and optoelectronic applications of graphene [93].

The substitutionally doped B-graphene was achieved experimentally and characterised as p-type semiconductors. For instance, Kim et al. [95] prepared single-layer graphene substitutionally doped with boron via the mechanical exfoliation of boron-doped graphite. Tang et al. [96] produced B-doped graphene with tunable electronic band gaps and p-type transport properties via controllable doping through reaction of graphene with the ion atmosphere of trimethylboron decomposed by the low-energy microwave plasma. Panchakarla et al. [97] prepared B-doped bilayer graphene by arc discharge of graphite electrodes in the presence H_2+B_2H_6 and by carrying out arc discharge using a boron-stuffed graphite electrode. The experimental realisation of N-doped graphene is even more inspiring; many methods have been proven successful to introduce nitrogen dopant into the graphene framework. Probably, CVD method is the most important method to produce N-doped graphene. Wei et al. [94] first synthesised the N-doped graphene (Fig. 2.3) by CVD, followed by several other groups using different precursors [98–101], and the experimentally obtained N-doped graphene exhibited an n-type semiconducting behaviour. Zhao et al. [102] grew N-doped graphene films using CVD on copper foil substrate and confirmed that the individual nitrogen atoms are incorporated as graphitic dopants. Arc discharge

is another important method to synthesise doped graphene. Panchakarla et al. [97] prepared nitrogen-doped bilayer graphene by employing the arc-discharge method [103, 104] in the presence of H_2 + pyridine or H_2 + ammonia and by the transformation of nanodiamond in the presence of pyridine. Nitrogen doping can be alternatively achieved by using many other techniques, such as nitrogen plasma treatment of graphene [105, 106], solvothermal synthesis of tetrachloromethane with lithium [107], electrothermal reactions of graphene with ammonia [108], NH_3 annealing after N^+-ion irradiation of graphene [109], denotation process with cyanuric chloride and trinitrophenol as reagents [110], vacuum annealing of embedded nitrogen and carbon sources [111], thermal annealing of graphite oxide in [112] NH_3 or melamine [113], self-assembly of pyridine molecules [114], and hydrothermal reduction of graphite oxide under hydrazine and ammonia [115]. In addition to single B or N dopants, complex BN doping also emerges. Due to their commensurate lattice parameters, graphene and BN sheets are considered good candidates for fabricating hybrid BN/C materials. A recent example is the incorporation of hexagonal BN domains within graphene (Fig. 2.4), which is prepared by a CVD technique on Cu substrate using methane and amineboran as precursors [116].

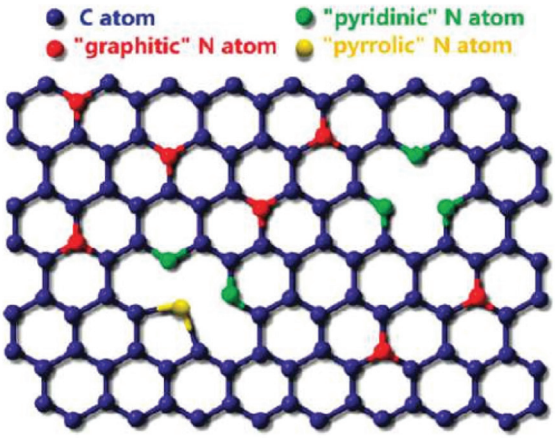

Figure 2.3 Schematic representation of graphitic, pyridinic and pyrrolic types of N atoms in the N-doped graphene. Reprinted by permission from Ref. [94], Copyright 2009, American Chemical Society.

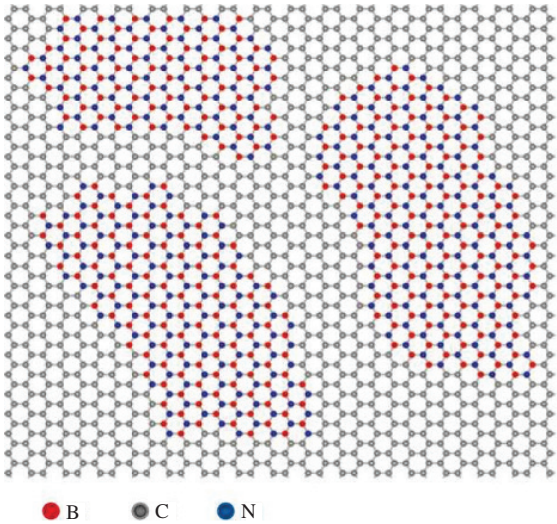

Figure 2.4 Atomic model of the h-BNC film showing hybridised h-BN and graphene domains. Reprinted by permission from Macmillan Publishers Ltd: *Nature*, Ref. [116], Copyright 2010.

2.1.1.2.4 *Alkaline and transition metal (TM) substitutional doping*

Alkaline and transition metal substitutional impurities have also received particular attention due to their abilities to inject charge into the electron system of graphene [116]. This type of doping is formed by replacing the C atoms with metal atoms at the sites of single or multiple vacancies [117, 118]. Aside from the theoretical studies, many transition metals have also been experimentally embedded into graphene framework. The Au- and Pt-embedded graphene have been fabricated recently via electric arc discharge, and the migration of Au and Pt in graphene layers has been monitored in real time by transmission electron microscopy (TEM), which shows a high activation energy of 2.2~2.5 eV [119]. The Ni [120], Pt, Co and In [121] substitution in the in-plane graphitic phase has also been experimentally detected.

2.1.1.2.5 *Molecular doping*

Molecular doping of graphene via charge transfer between graphene and electron-donating or electron-withdrawing molecules also gives

rise to significant changes in the electronic structures of graphene [122–130]. This kind of doping usually involves noncovalent functionalisation of graphene, and the adsorbed molecule, aromatic or non-aromatic, can either release electron to graphene (n-doping) or pull them from graphene (p-doping) depending on its electron-donating or -accepting ability. According to Widenkvist et al.'s experiment, the intercalation of Br_2 into graphite results in significantly weaker interlayer binding between graphite layers and can, therefore, facilitate the sonochemical exfoliation of intercalated graphite into suspended graphene flakes [131]. Br_2 intercalation also offers an effective method to enable the mechanical exfoliation of graphene grown on Ir(111) substrate [132]. Moreover, epitaxial graphene thermally grown on 6H-SiC (0001) can be p-type doped via doping a strong electron acceptor, tetrafluoro-tetracyanoquinodimethane (F4-TCNQ) [133–136]. The n-type doped graphene sheets can be realised by depositing electron-donor molecules such as vanadyl-phthalocyanine (VOPc) [137] and tetrathiafulvalene (TTF) [138]. Graphene with top self-assembled molecule layers such as phosphonic acids [139], 3,4,9,10-perylene tetracarboxylic dianhydride (PTCDA) [140, 141] and fluoroalkyl silane [142] have been successfully synthesised, and these molecules can also induce the carrier changes of graphene to a large extent.

2.1.1.3 Graphane

Graphane is an extended 2D polymer of carbon and hydrogen with a stoichiometric formula unit CH, which adds to the wealth of carbon-based materials which show great potentials for near-future nanoelectronic devices. Graphane can be regarded as a fully hydrogenated derivative of graphene, where all the carbon atoms are in sp^3 configuration and hydrogen atoms are attached to the carbon atoms alternatively on the opposite sides of the carbon network, structurally analogous to the a hydrogenated (111) sheet of diamond. Many theoretical studies have been directed towards the understanding of such novel material [143–146]. The structure and stability of graphane were first predicted in 2007 by Sofo et al. [143]. Graphane prefers the chair-like configuration with a C–C bond length of 1.52 Å and a C–H bond length of 1.11 Å, where the sp^3-hybridised C–C bond is much larger than the characteristic of sp^2-hybridised C–C bond (1.42 Å) in graphene (Fig. 2.5a). Graphane is predicted

to be a stable structure with a binding energy comparable to other hydrocarbons such as benzene, cyclohexane and polyethylene. The alteration of carbon-hybridised state from sp^2 into sp^3 confines the p_z electrons into covalent bonds, making the π bands in pristine graphene disappear, and the σ bands in graphane move to the top of the valence bands and a large band gap is opened (Fig. 2.5) [147]. Due to its inherent gap-opening, the large on-state currents as well as high I_{on}/I_{off} ratios in graphane-based field-effect transistors have been theoretically predicted [148].

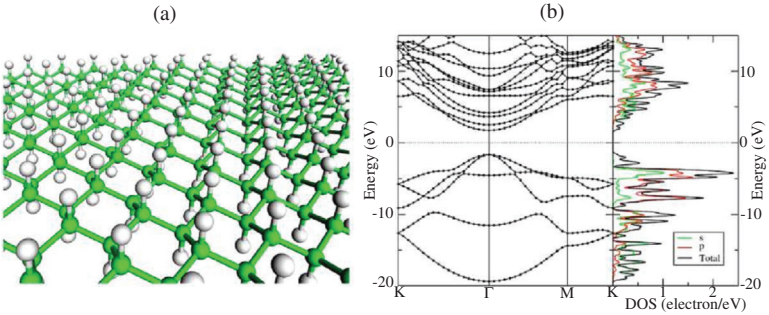

Figure 2.5 (a) Structure of graphane in the chair conformation. The carbon atoms are shown in green and the hydrogen atoms in white. (b) Band structure and density of states for the chair-type graphane. Reprinted by permission from Ref. [143], Copyright 2007, American Physical Society.

2.1.1.3.1 *Graphane and partially hydrogenated graphene*

Hydrogenation is an important strategy to modulate the surface geometries and electronic properties of graphene. Plasma is an important method for hydrogenation. By exposing the as-prepared graphene to the cold hydrogen plasma, Elias et al. [149] first synthesised graphane, the two-sided fully hydrogenated graphene, in 2009. In addition, the one-side hydrogenated graphene was achieved by depositing the graphene sheet on a silica substrate, which allows the availability of only one side of graphene to atomic hydrogen. Besides plasma hydrogenation, graphane and partially hydrogenated graphene can be obtained through many other routes [150, 151]. For instance, hydrogenation of graphene can be realised by dissociating the hydrogen silsesquioxane (HSQ) via e-beam lithography on the mechanically exfoliated graphene [152].

Recently, Jones et al. [153] have synthesised graphane and partially hydrogenated graphene by electron irradiation of graphene having chemisorbed H_2O and NH_3 adsorbates on the surface. Zhou et al. [154, 155] predicted that fully hydrogenated graphene can become half-hydrogenated with the desorption of H atoms from one side of graphane by applying an electric field. The resulting semi-hydrogenated graphene is also called "graphone". The chemical hydrogenation can also take place in bilayer or multilayer graphene [156]. Ab initio computations revealed that in the case of hydrogenated bilayer graphene, the weak van der Walls forces between graphene layers are replaced by strong interlayer C–C chemical bonds, and at maximum coverage (50% hydrogen saturation), a bilayer analogue of graphane (bilayer graphane) is formed [157].

2.1.1.4 Fluorographene

Besides GO and graphane, the fully fluorinated graphene (fluorographene, with a stoichiometric formula unit of CF) is another important structural derivative of graphene. Fluorographene has similar geometric structure and sp^3 bonding configurations to graphane with each carbon covalently bonded to one fluorine atom. In fact, the fluorination of sp^2 carbon can be dated back to decades, and the fluorinated bulk graphite, which has been known ever since 1934 [158], has been studied extensively [159–162] and widely used as a superior solid lubricant [163, 164]. Fluorinated graphene is synthesised mainly by reacting graphene with XeF_2 and F_2 or by mechanical and chemical exfoliation of graphite fluoride. Though sophisticated techniques are used to fully characterise graphene and graphane, the complete structure of fluorographene remains experimentally elusive due to the limitation of Raman spectra in specifying the CnF structure and the different preparation conditions. Experimentally, the fully and partially fluorinated graphene with CnF for $n \leq 4$ have been synthesised by exposing graphene to XeF_2 and F_2.

XeF_2 is an excellent agent for providing reactive fluorine radicals upon heating. In 2010, Robinson et al. [165] synthesised fluorographene when exposing the graphene grown on Cu foils to XeF_2 at 30°C on one or both sides. The single-side fluorination is possible and results in a crystalline F_4C structure with a large band

gap of 2.93 eV. At the nearly same time, Nair et al. [166] achieved perfluorographene material with an optical band gap of 3 eV by starting from the cleaved graphene crystals on gold and nickel grids and exposing the graphene to XeF_2 at 70°C. Structurally, fluorination leads to a slight expansion of the cell parameter of graphene by about 1%, in contrast to the hydrogenated case, which shows a compressed lattice. Similarly, Jeon et al. [167] prepared partially fluorinated graphene by direct chemical reaction of graphene with XeF_2. Compared with the pristine graphene, which is well-dispersed in ethanol, fluorographene precipitates in ethanol since the fluorographene with sp^3-hybridised C atoms does not have free p_z orbitals to form pseudohydrogen bonds with the –OH groups of ethanol (Fig. 2.6b). The near edge X-ray absorption spectroscopy (NEXAFS) also verified that the π^* feature, a characteristic of sp^2 bonding in graphene, is progressively decreased with increasing fluorine content, indicating the formation of sp^3 bonds in the substance (Fig. 2.6c).

The resulting fluorographene shows a wide band gap of at least 3.80 eV based on photoluminescence measurement, exhibiting excitonic absorption in ultraviolet (UV) and visible light regions (Fig. 2.6d). Moreover, gaseous F_2 was also used to fluorinate graphene. Cheng et al. [168] reported the reversible fluorination of multilayer graphene (with an F/C ratio of 0.7) by interacting with high-temperature F_2 gas, showing that the conductivity of graphene can be reversibly modified through fluorination and reduction reactions. The stoichiometric fluorographene can also be prepared by directly exfoliating the layered graphite fluoride, like the method used in isolating graphene from graphite. Withers et al. [169] realised the mechanical exfoliation of fluorinated graphite, and the transistor fabricated using the obtained fluographene has a strongly temperature-dependant resistance. Alternatively, Zbořil et al. [170] achieved the liquid-phase exfoliation of graphite fluoride using sulpholane [170] or dimethylformamide [171] as the solvent. The fluorographene is predicted to have higher thermodynamic stability than other four graphene derivatives, namely graphane, graphene bromide, chloride and iodide [170, 172], using the halide-exchange process (reacting fluorographene and KI), and the fluorographene can be transformed into graphene via graphene iodide, a

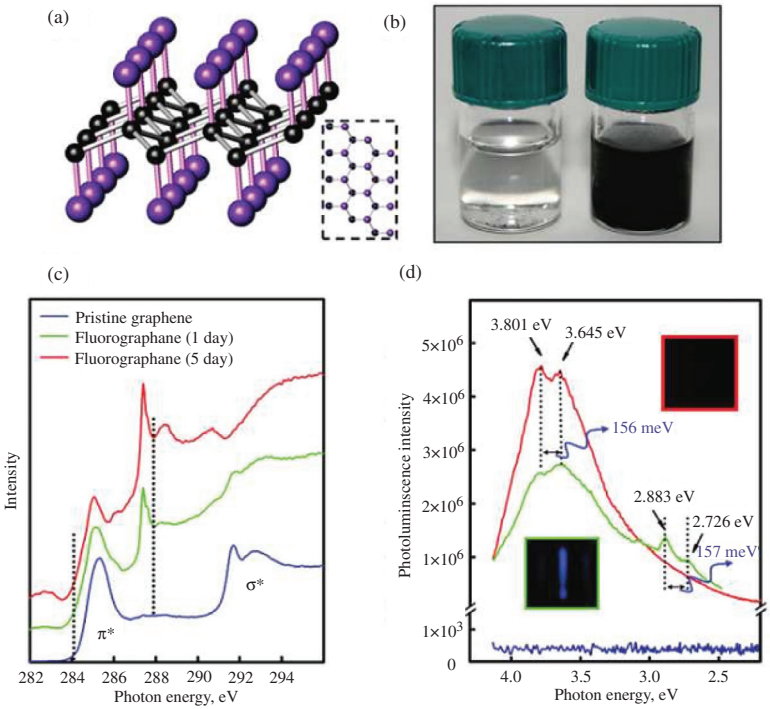

Figure 2.6 (a) Structure of CF; black and purple spheres indicate carbon and fluorine atoms, respectively, which are bonded alternatively on both sides of graphene. The inset, dotted area, is a plan view. (b) Fluorographene (left vial) and pristine graphene (right vial) in ethanol. These samples were sonicated for 30 s in ethanol. (c) NEXAFS spectra of pristine graphene and fluorographene with two different contents of fluorine. The dashed lines at 284.1 and 287.9 eV mark the leading edges of the π^* resonance for the pristine and fluorinated samples, respectively. (d) Room temperature photoluminescence (PL) emission of the pristine graphene/fluorographene dispersed in acetone using 290 nm (4.275 eV) excitation. The dotted lines are used for guiding eyes. The interval of dotted line is ~156 meV. Optical images (top view) of the blue emission observed after the PL emission were recorded with the samples in 3.5 mL quartz cuvettes. Reprinted by permission from Ref. [167], Copyright 2011, American Chemical Society.

spontaneously decomposing intermediate [170]. In addition, the chemical exfoliation of graphite fluoride by ion liquids 1-butyl-3-methylimidazolium bromide ([bmim]Br) under ambient conditions was utilised to generate single- or few-layer fluorographene (Fig. 2.7) [173]. The formation of fluorographene layers may be attributed

to surface-energy matching between the ionic liquids and the carbon sheets in fluoro-graphite. Due to the strong π–π interaction between the hexagonal carbon lattice and their imidazole ring, the intercalation of [bmim]Br molecules into the interlayer space of fluoro-graphite can dramatically weaken the van der Waals force between neighbouring layers. Upon mild ultrasonication, the fluoro-graphite can be readily exfoliated into single- and few-layer fluorographene sheets to yield a highly concentrated quasi-sol (5 mg/mL). [bmim]Br also acts as an electrostatic stabilising agent to facilitate the stable dispersion of the resultant quasi-sol [173].

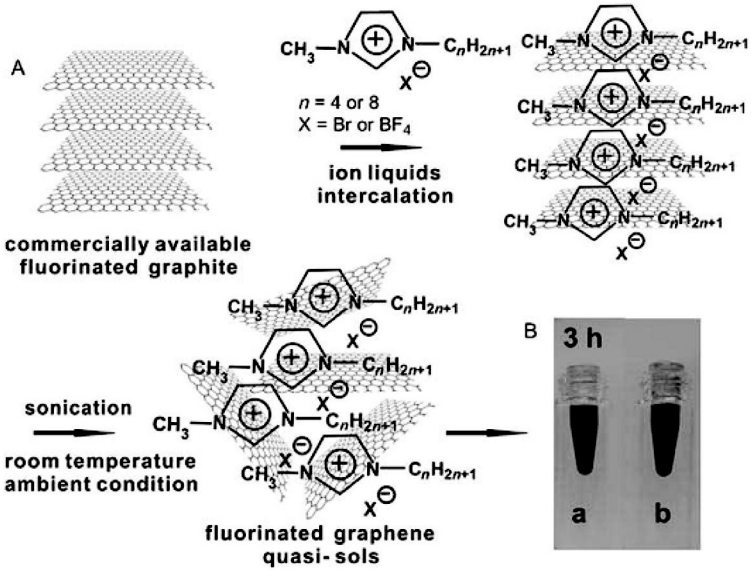

Figure 2.7 (A) Illustration of the one-step synthesis of fluorographene. (B) Digital images of (a) 0.25 (C/F ratio) fluorographene (5 mg/mL) and (b) 0.5 (C/F ratio) fluorographene (5 mg/mL) quasi-sols in [bmim]Br after standing for 3 h. No precipitation was observed. Reprinted by permission from Ref. [173], Copyright 2011, John Wiley and Sons.

2.1.1.5 Graphyne and graphdiyne

Carbon has various hybridised states (sp, sp^2 and sp^3) and can form diverse bonds, yet the well-established crystalline phases contain either all sp^3 or all sp^2 carbon atoms. Synthesising and discovering new carbon phases with novel bonding characteristics will be an

ongoing effort for both theoretical and synthetic scientists [174, 175].

As new forms of non-natural carbon allotropes, graphyne and graphdiyne have been the subjects of interest due to their unique structures and intriguing electronic, optical and mechanical properties. Inspired by the theoretical predictions, many experimental efforts have been dedicated to synthesising graphyne and graphdiyne. Although the large-scale synthesis of graphyne has not been achieved, reasonable synthesis approaches to fabricate its smaller and larger substructures have been developed [176–178]. Amazingly, Li et al. [179, 180] successfully synthesised large-area graphdiyne films with 3.61 cm^2 on the copper surface via a cross-coupling reaction using hexaethynyl benzene as the monomer (Fig. 2.8). In the process of forming graphdiyne, the Cu foil serves as both catalyst and substrate for growing graphdiyne film. The prepared films are composed of graphdiyne multilayers, with thickness of about 1 μm, as indicated from the STM and AFM observations. The high-resolution TEM image exhibits clear fringes of 4.1913 Å without defects or dislocations.

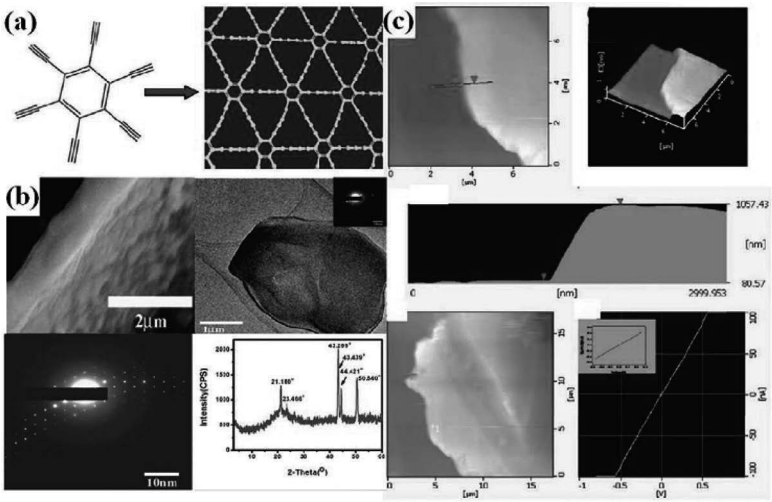

Figure 2.8 (a) Schematic of hexaethynyl benzene monomer and graphdiyne film. Reprinted with permission from Ref. [180]. (b) SEM, TEM, SAED and XRD pattern of a large-area graphdiyne film, and (c) corresponding AFM images and I-V curve. Reprinted by permission from Ref. [180], Copyright 2010, American Chemical Society.

Both selected area electron diffraction (SAED) and X-ray diffraction (XRD) pattern confirm the high crystallinity of the as-grown graphdiyne film. The measured current-voltage (I-V) curve of graphdiyne film exhibits a typical Ohmic behaviour, which shows a linear relationship with a line slope of 2.53×10^{-3}. The conductivity is calculated as 2.516×10^{-4} S/m, which is comparable to silicon, demonstrating excellent semiconducting properties. In addition to 2D graphdiyne sheet, through an anodic aluminium oxide template catalysed by Cu foil, Li et al. [181] fabricated graphdiyne nanotube arrays which display high performance field emission properties. More recently, graphdiyne nanowire semiconductors with a conductivity of 1.9×10^{3} S/m and mobility of 7.1×10^{2} $cm^2/V{\cdot}s$ were successfully constructed by vapour–liquid–solid (VLS) growth process [182].

2.1.1.6 Porous graphene

Porous graphene is a new class of light-weight porous material, featured as well-defined and orderly distributed inherent porous structures within the covalent π-electronic framework of graphene [183]. It resembles the 2D structure of graphene but with periodically missing phenyl rings and possesses drastically distinct properties from graphene. Typically porous graphene can be generated by either top-down or bottom-up methodologies. The first method utilises the electron beam ablation or electron irradiation to drill holes [184, 185] or introduce vacancy defects [186] in graphene sheet, and the dangling bonds can be saturated by H or F atoms under vacuum hydrogen/fluorine atmosphere or by N atoms through doping with ammonium [187]. However, a precise control of the shape, size and the functional groups within the pore as well as the uniformity of the created porous structure using these top-down techniques might be challenging. The second approach is to first synthesise organic building blocks and then assemble the building blocks via chemical bonds into a larger sheet of porous graphene. This method has the clear advantage of being able to design a porous structure with specified pore size, shape and functional groups inside the pore

and allow for an elaborate control over the chemical nature and properties of the resulting networks.

Such bottom-up synthetic strategy has been successfully applied to the fabrication of 2D porous polytriazine via dynamic trimerisation of terephthalonitrile [188] and a polyphenylene-based polymer material PP-CMP by Suzuki cross-coupling polycondensation reaction [189]. Particularly, Bieri et al. [190] successfully fabricated one-atom thick porous graphene, or 2D polyphenylene networks, by the silver-promoted coupling reactions of well-designed molecular building blocks (hexaiodo-substituted macrocycle cyclohexa-m-phenylene, CHP) (Fig. 2.9). The fabrication process starts with the deposition and dehalogenation of CHP molecules on the Ag (111) surface at room temperature. Then, annealing the substrate to temperatures above 570 K initiates the polymerisation reaction and results in the formation of a complete honeycomb network depicted as porous graphene, which is thermally stable up to the roughness of transition temperature of Ag. The produced porous graphene shows a uniform pore spacing of 7.4 Å by a structural analysis of the high-resolution STM image and is the first example of an sp^2-bonded hydrocarbon superhoneycomb framework.

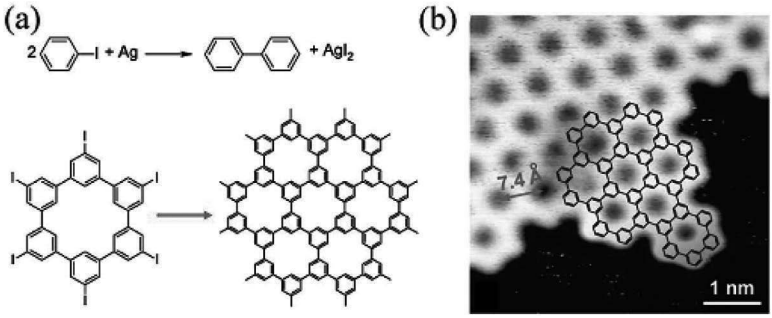

Figure 2.9 (a) Mechanism of Ag-promoted Aryl–Aryl coupling of iodobenzene to biphenyl, the structure of hexaiodo-substituted cyclohexa-m-phenylene (CHP) and a fraction of the polyphenylene superhoney comb network. (b) A high-resolution STM image of an edge of the polyphenylene network after the polymerisation process at 805 K. Reproduced from Ref. [190] with permission of The Royal Society of Chemistry.

2.1.2 Synthesis Methods of Graphene-Related Nanocomposites

Graphene–NP composites, wherein sheets of graphene, GO or RGO, are decorated with NPs which are a few nanometres to a couple hundred nanometres in diameter [191], can be obtained by anchoring various types of NPs to the surface of graphene sheets through both in situ (e.g. growing the NPs on the graphene surface) and ex situ (e.g. attaching premade NPs to the graphene surface) methods. GO and RGO are especially promising templates for this purpose as the presence of defects and oxygen functional groups on their surfaces allows for the nucleation, growth and attachment of various metal (e.g. Au [192], Ag [193], Pt [194], etc.) and metal oxide NPs (e.g. FeO [195], TiO [196], ZnO [197], SnO_2 [198], Cu_2O [199], MnO_2 [200], NiO [201] etc.). The resulting graphene–NP composites are then able to offer numerous unique and advantageous properties for various applications depending on the particular characteristics possessed by the NPs used to form the composites. For example, graphene–NP composites can confer excellent catalytic activity, enhancements in mass transport, and a significantly higher effective surface area [65]. As such, recent efforts in this area have not only focused on methods to form graphene–NP composites while preserving the excellent properties of graphene but also on precisely tuning the physicochemical features that are present. In this section, different methods are discussed, which are available for the preparation of graphene–NP composites including various in situ (e.g. reduction, hydro- thermal and electrochemical) and ex situ methods.

2.1.2.1 Reduction methods

Graphene–metal NP composites are most frequently fabricated via the reduction of metallic salts (e.g. $HAuCl_4$, $AgNO_3$ and K_2PtCl_4) using chemical agents such as ethylene glycol, sodium citrate and sodium borohydride [193, 202].

More specifically, the negatively charged functional groups which exist on the surface of GO allow for the nucleation of positively charged metallic salts, resulting in the growth of metal NPs on the GO surface. By utilising this method to form RGO–metal NP composites, it is possible to preserve the excellent electrical properties of graphene. Moreover, by controlling the density of oxygen-containing groups on the GO and RGO surface, one can easily tune the density

of NPs formed on the resulting graphene–NP composites. In general, to form graphene–metal NP composites in situ via reduction, a one-step method is used wherein the metal precursor and GO sheets are mixed in an aqueous solution and then reduced simultaneously (Fig. 2.10). This reaction is similar to conventional NP synthesis

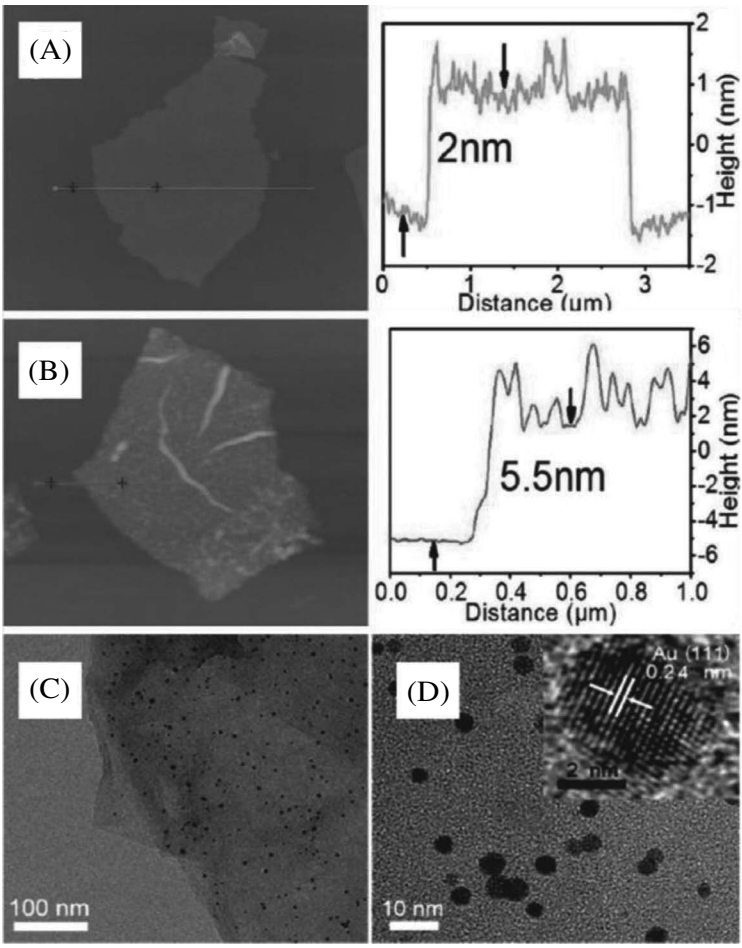

Figure 2.10 Graphene–NP composite composed of GO sheets decorated with AuNPs. (A) AFM image of a single GO sheet and (B) a GO sheet decorated with 3.5 nm AuNPs. The corresponding curves on the right side show the thicknesses of the GO sheet and the GO/AuNP sheet. (C and D) TEM images of the GO/AuNP sheet with different magnifications. Inset of (D) shows a high-resolution TEM image of a single AuNP. Reprinted by permission from Ref. [204], Copyright 2013, American Chemical Society.

methods and follows three steps: (i) reduction, (ii) nucleation and (iii) NP growth. More specifically, the functionalities which exist on the GO and RGO surface, such as alcohols, carbonyl groups and acids, are responsible for the attachment of free metal ions through electrostatic interactions. Subsequently, the addition of a reducing agent promotes the reduction of the attached metal ions, thereby enabling the growth of metal NPs on the GO and RGO surfaces [203]. While this method is highly efficient and easy to perform, the size and morphology of the metal NPs on the resulting composite can be difficult to control, resulting in samples which are decorated with NPs that have a wide size distribution [204].

To date, the reduction technique has been used primarily for the preparation of graphene–noble metal NP composites. Noble metal NPs, especially gold (AuNP) and silver NPs (AgNPs), are among the most extensively studied NMs and have led to the development of numerous biotechniques and applications, including diagnostics, imaging, drug delivery and other therapeutics [205]. Noble metal NPs are of particular interest because of their unique and unusual properties such as high biocompatibility and optical properties (e.g. surface plasmon resonance), which can be easily tuned to the desired wavelength according to their shape (NPs, nanoshells, nanorods, etc.), size and composition [206]. In addition, when combined with graphene as a composite, graphene–noble metal NP hybrids are able to exhibit SERS as well as enhanced catalytic potential [207]. To this end, numerous methods have been used to fabricate graphene–AuNP composites, which are currently the most commonly prepared and utilised graphene–NP composite. Briefly, graphene–AuNP composites can be attained by mixing $HAuCl_4$ precursor with exfoliated GO and sodium citrate, resulting in gold precursors anchoring to the surface of GO via electrostatic interaction. Afterwards, the gold precursors are reduced using $NaBH_4$ to form AuNPs [208]. Similarly, graphene–AgNP composites can be obtained by mixing GO with $AgNO_3$, followed by reduction with $NaBH_4$ [209]. Finally, graphene decorated with platinum or palladium NPs has also been produced by mixing graphene with chloroplatinic acid (H_2PtCl_6) or tetrachlor-opalladic acid (H_2PdCl_4),

followed by reduction with ethylene glycol, respectively [210]. In terms of the characteristics which are imparted by the formation of graphene–noble metal NP composites, Subrahmanyam et al. [210] recently studied the interaction between noble metal NPs and graphene utilising Raman spectroscopy. Specifically, they reported that the decoration of graphene with noble metal NPs results in electronic interactions which give rise to significant changes in the ionisation energies of the metals as well as in their charge-transfer interaction and, subsequently, the Raman spectrum of the graphene sheets. On the other hand, graphene–NP composites containing bimetallic NP hybrids can also be obtained utilising a two-step reduction process.

By fabricating such a structure, not only can synergism be achieved between the different NP species that are present, but also between the bimetallic NPs and graphene [211]. For example, the reduction of H_2PdCl_4 by formic acid, followed by the addition of K_2PtCl_4 and reduction by AA, yielded a graphene–PtPd bimetallic NP composite structure (Fig. 2.11) [212]. The resulting bimetallic hybrid composite showed much higher catalytic activity than conventional graphene–platinum NPs (PtNP) hybrid structures and PtPd bimetallic catalysts. This can be attributed to a combination of the increased surface area of Pt in bimetallic NPs, which is an essential factor in improving catalytic activity, as well as their better dispersion on graphene nanosheets which have high surface area [213]. Similarly, Yang et al. described the preparation of another bimetallic NP hybrid wherein GO was decorated with PtCo bimetallic NPs [211]. In this case, ethylene glycol-functionalised GO sheets were loaded with PtCo bimetallic NPs by the addition of H_2PtCl_6 and $CoCl_2$ at room temperature, followed by reduction with $NaBH_4$. Similar to the graphene–PtPd bimetallic NP composites, the resulting graphene–PtCo bimetallic NP composites also exhibited good stability, resistance to degeneration and an especially high catalytic activity as compared to other PtNPs and graphene–PtNP composites, presumably for the same reasons as mentioned for graphene–PtPd composites.

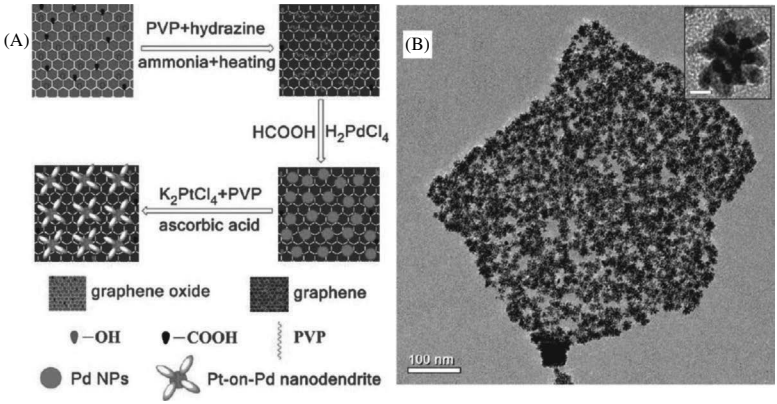

Figure 2.11 Graphene–bimetallic NP composites. (A) Procedure to fabricate graphene nanosheet/Pt-on-Pd bimetallic nanodendrite hybrids. (B) TEM images of the graphene–bimetallic NP composites. Inset of (B) shows the Pt-on-Pd bimetallic nanodendrites at a higher magnification. Reprinted by permission from Ref. [212], Copyright 2010, American Chemical Society.

Finally, as an alternative to the traditional reduction methods used to prepare graphene–NP composites, microwaves can also be used as a source of energy which facilitates the process [214]. For instance, graphene and its derivatives were decorated with metal (e.g. Au [214], Ag [215] and Pt [216]) and metal oxide (e.g. Co_3O_4 and MnO_2) NPs [217], in the presence or absence of reducing agents and stabilising molecules, with the help of rapid microwave irradiation. The main advantage of microwave irradiation is the uniform and rapid heating of the reaction mixture, thereby reducing the barrier to reduction, nucleation and ion incorporation [218]. Hence, NPs with a very small size and narrow size distribution can be obtained.

2.1.2.2 Hydrothermal methods

The hydrothermal method is also commonly used to synthesise inorganic NPs which have high crystallinity and narrow size distribution on graphene sheets. Moreover, this method allows for the formation of NPs on graphene without the need for post-annealing and calcination [219]. In general, the process involves the use of high temperatures and pressures, which induce the growth of nanocrystals and, at the same time, reduce GO to RGO. However, while the high temperature and long reaction times can partially or

completely reduce GO on its own, in most cases, reducing agents are added to ensure the complete reduction of GO [219, 220].

Graphene–metal oxide NP composites (e.g. ZnO [221], TiO_2 [222], Fe_3O_4 [223], SnO_2 [224],) are, by far, the most common hybrids synthesised using the hydrothermal method. Specifically, metal oxide NPs can provide the graphene–metal oxide NP hybrids with a number of advantages such as a higher capacitance, which depends on the NP structure, size and crystallinity, while suppressing agglomeration and the restacking of graphene [225]. Moreover, graphene–metal oxide NP composites result in enhanced electron conductivity, shortened ion paths and a significant increase in the available surface area when compared to graphene alone, which altogether lead to higher electrochemical activity [226]. For example, in 2012, Park et al. reported the one-pot synthesis of RGO–SnO_2 NP composites, wherein the resulting composites exhibited outstanding cycling performance and could be used as an electrode [224]. In their study, a hydrothermal synthesis assisted by hydrazine, which promoted the complete reduction of GO to RGO, was utilised. The resulting composites exhibited a first discharge capacity of 1662 mA·h/g, which rapidly stabilised and remained at 626 mA·h/g even after 50 cycles when cycled at a current density of 100 mA/g, whereas the capacity of pure SnO_2 NPs decreases continuously. This could be attributed to the lack of aggregation in the RGO-supported SnO_2 composites and the uncontrolled aggregation of the pure SnO_2 NPs. On the other hand, Ren et al. [62] reported the synthesis of graphene–magnetic NP (MNP) composites. In particular, these graphene–MNP composites exhibited excellent electrical conductivity and mechanical strength while possessing the magnetic properties of the attached MNPs [227]. In this case, a one-step hydrothermal method was performed, wherein anhydrous $FeCl_3$ provided the source of iron, and ethylene glycol (or a bisolvent of diethylene glycol and ethylene glycol) was used as the reductant and solvent. Consequently, Fe_3O_4 NPs with a diameter of 7 nm were densely and uniformly deposited on the RGO sheets. Moreover, the reduction of GO by this process was comparable to that achieved by conventional methods. For example, the D/G intensity ratio of RGO in the aforementioned hybrids was 2.30:1, which is similar to the ratio typically obtained for pristine graphene (2.45:1), indicating the recovery of the sp^2 domain in the carbon network [227]. In addition,

various chalcogenide QDs such as CdS [228], ZnS [229], Cu_2S [230], MoS_2 [231], Sn_3S_4 [232] and CdTe [233] have been successfully immobilised on graphene utilising hydrothermal methods. These semiconductor nanostructures have attracted intense interest due to their fundamental importance as well as their enormous potential in optoelectronic, magnetic and catalytic applications [234]. Specifically, for biological applications, QDs provide high quantum yield (0.1–0.8 [visible], 0.2–0.7 [NIR] versus 0.5–1.0 [visible], 0.05–0.25 [NIR] for organic dyes) [235], high molecular extinction coefficients (10–100× that of organic dyes) [236], broad absorption with narrow symmetric photoluminescence spectra (full-width at half-maximum 25–40 nm) spanning from ultraviolet (UV) to NIR, high resistance to photobleaching, and exceptional resistance to photo- and chemical degradation [237]. Moreover, because of their size-tunable fluorescence emission and the broad excitation spectra, QDs have a significant advantage over molecular dyes. However, these semiconductor NPs are limited by their tendency to aggregate, resulting in a reduction in the surface area that is available for subsequent applications. In terms of the fabrication of RGO–sulphide nanocomposites, the sulphur sources often act as a reducing agent for GO. Zhang et al. [238] recently reported the synthesis of graphene–CdS NP composites wherein a facile one-step hydrothermal approach was utilised to simultaneously form CdS NPs and reduce GO (Fig. 2.12) [238]. By combining these two excellent materials in a single composite, the graphene–CdS NP composites were able to serve as promising visible light-driven photocatalysts, whose excellent photoactivity could be attributed to the integrative effect of the enhanced light absorption intensity, high electron conductivity of graphene, which significantly prolonged the lifetime of photogenerated electron–hole pairs, and its significant influence on the morphology and structure of the samples.

Finally, there have also been some reports utilising hydrothermal methods for the preparation of RGO–noble metal NP composites (Fig. 2.13) [239]. In the case of graphene–AuNPs, a solution of $HAuC_4{\cdot}3H_2O$ and NaOH was mixed with GO [240]. Subsequently, the solution was sonicated at a frequency of 40 kHz and heated to 180°C. The resulting graphene–AuNP composites had AuNPs with a narrow size distribution in the range of 2 or 18 nm, with and without sonication, respectively. Graphene–Pt or –PdNP composites

can also be prepared by a similar method using $H_2PtCl{\cdot}6H_2O$ and $PdCl_4$, respectively [240]. Moreover, graphene bimetallic NP hybrid composites have been reported using the hydrothermal method. For instance, platinum–ruthenium NPs with a mean size of 2.17 nm were decorated on graphene nanosheets, and it was found that the size and morphology of these NPs could easily be controlled by modifying the synthesis temperature and the initial materials used [241].

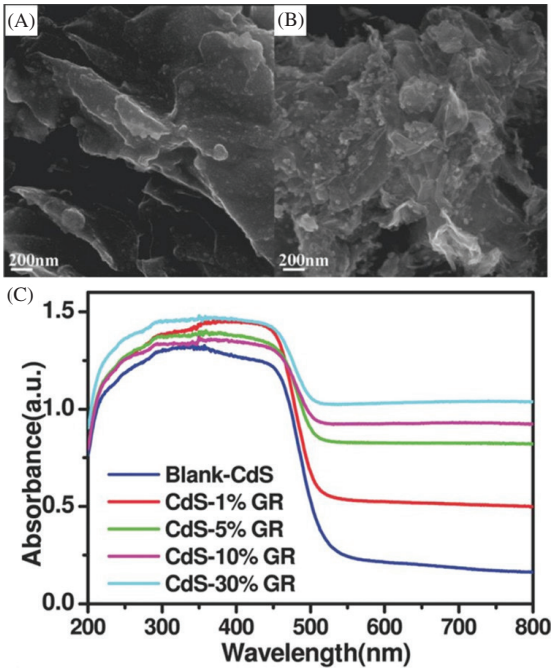

Figure 2.12 Graphene–quantum dot composites. SEM images of the as-prepared samples of (A) CdS–5% graphene, (B) CdS–30% graphene and (C) UV–vis diffuse reflectance spectra of the samples of blank- CdS and Cd-GR nanocomposites with different weight addition ratios. Reprinted by permission from Ref. [238], Copyright 2011, American Chemical Society.

2.1.2.3 Electrochemical methods

Electrochemical deposition is a simple, fast and green technique that can be used to form graphene–NP composites while preventing the contamination of synthesised materials. In addition, it is low cost, easy to miniaturise and automate, and is highly stable and

reproducible [242]. As such, by utilising electrochemical deposition, the size and shape of the NPs which are deposited can be precisely controlled by simply altering the conditions of electrochemical deposition. In particular, electrochemical deposition methods have been developed extensively for the fabrication of graphene–inorganic NP composites with the vast majority of composites formed using this method being noble metals such as Au [243], Ag [244], Pt [245], as well as bimetallic metals.

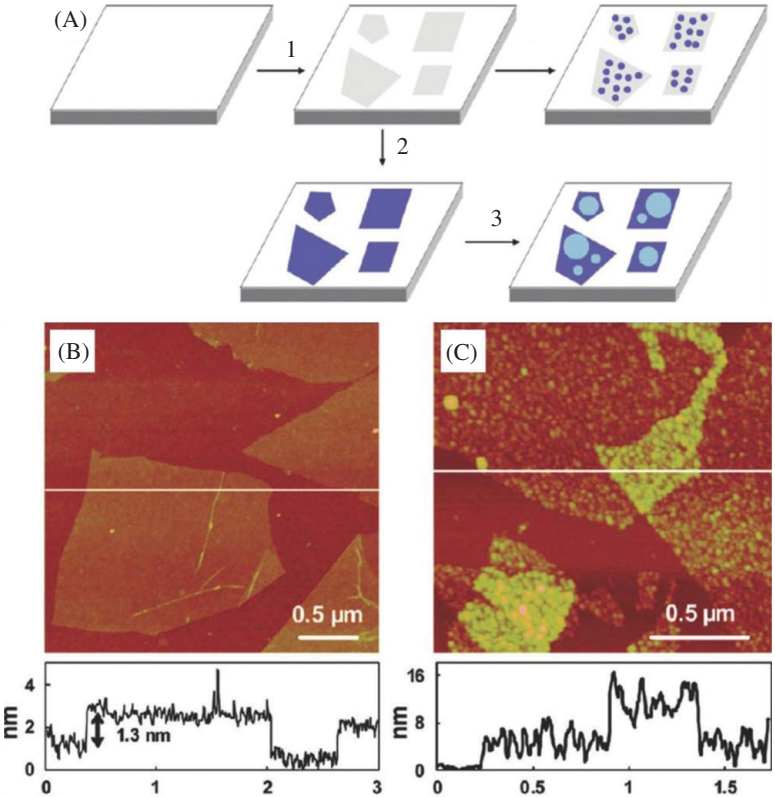

Figure 2.13 Hydrothermal methods to synthesise graphene–AgNP composites. (A) (1) GO is adsorbed on the APTES-modified SiO_x substrate. (2) GO is reduced, and RGO is obtained. (3) Growth of Ag particles by heating the RGO substrate in 0.1 M $AgNO_3$ at 75°C for 30 min. (4) Growth of AgNPs by heating the GO substrate in 0.1 M $AgNO_3$ at 75°C for 30 min. (B) Tapping mode AFM topographic image and height profile of a single layer of GO adsorbed on an APTES-modified SiO_x substrate. (C) SEM image of Ag particles grown on an RGO surface. Reprinted by permission from Ref. [239b], Copyright 2009, American Chemical Society.

In a typical electrochemical deposition experiment, there are three steps wherein (i) the graphene sheets are first assembled onto an electrode, (ii) the graphene-coated electrode is then immersed in an electrolytic solution containing metallic precursors, and (iii) a potential is applied. For the formation of graphene–AgNP composites, Golsheikh et al. recently reported an electrochemical deposition method wherein the resulting NPs fell within a very narrow size distribution with a mean size of 20 nm [244]. In this case, a solution containing silver–ammonia [$Ag(NH_3)_2OH$] and GO was exposed to cyclic voltammetry (CV), which was performed using a three-electrode system which consisted of an indium tin oxide (ITO) working electrode, a platinum foil counter electrode and a saturated calomel electrode (SCE) reference electrode (scanning between −1.5 V and 0 V at the rate of 25 mV/s). Fisher et al. also utilised electrochemical tools to fabricate graphene–PtNP composites wherein PtNPs were decorated on multilayered graphene petal nanosheets (MGPNs) [245]. According to their report, a three-electrode system, wherein the MGPNs acted as the working electrode, Pt gauze as the auxiliary electrode and Ag/AgCl as the reference electrode, was dipped in a solution containing $H_2PtCl_6{\cdot}6H_2O$ and Na_2SO_4. Utilising this method, the density, size and morphology of the PtNPs could be precisely controlled by simply adjusting the intensity of the pulse current. In particular, this allowed for the simultaneous reduction of GO and H_2PtCl_6 to RGO and PtNPs using an electrolyte solution containing $CuSO_4$ in a conventional three-electrode system, wherein the RGO electrode, a Pt mesh and an Ag/AgCl electrode were used as the working, counter and reference electrodes, respectively (Fig. 2.14A) [246]. To fundamentally study the nucleation of Cu on RGO via electrochemical deposition, the authors used CV, Tafel plots and chronoamperometry. From CV, it was inferred that Cu deposition on RGO electrodes initiated at a more positive potential of 0.105 V (versus Ag/AgCl) as compared to that found for glassy carbon and pencil graphite.

On the other hand, the Tafel plot confirmed that the rate-determining step for Cu deposition on RGO was mass transport and, finally, that nucleation on RGO occurred either instantaneously or progressively depending on the initial concentration of the elec-

trolyte (e.g. instantaneously at higher concentrations [50 mM] and progressively at lower concentrations [10 mM]). Last, although the vast majority of research efforts have concentrated on the electrochemical deposition of metal NPs on the graphene sheets, there have also been several reports of the electrochemical deposition of metal oxide NPs onto graphene. For instance, Wu et al. [247] deposited Cl-doped n-type Cu_2O NPs, which are abundant and nontoxic NPs which have a direct band gap of ca. 2.0 eV [247], on RGO electrodes, resulting in a carrier concentration of up to 1×10^{20} cm^{-3} [248]. Specifically, to deposit Cl–Cu_2O NPs on RGO, a solution of $CuSO_4$, $CuCl_2$ and lactic acid was added to a three-electrode system where the RGO electrode, a Pt mesh, and an SCE were used as the working, counter and reference electrodes, respectively. The deposition used a potentiostatic process (potential of −0.4 V, charge density of 2 C/cm^2) at a temperature of 60°C. Similarly, ZnO nanorods could also be deposited on RGO films using a solution containing $ZnCl_2$ and KCl as the supporting electrolyte in a conventional three-electrode system, where RGO-polyethylene terephthalate electrode, a Pt mesh, and an SCE were used as the working, counter and reference electrodes, respectively [249].

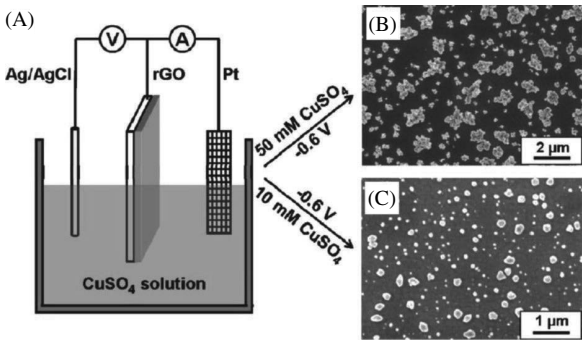

Figure 2.14 Electrochemical deposition of Cu NPs on RGO. Electrochemical experiments were performed by an electrochemical workstation (CHI600C, CH Instrument Inc., U.S.) in a conventional three-electrode electrochemical cell. The RGO electrode, a Pt mesh and an Ag/AgCl (3 M NaCl) electrode were used as the working, counter and reference electrodes, respectively. (B) SEM image of Cu electrodeposited on an RGO electrode in 50 mM $CuSO_4$ solution at −0.6 V. (C) SEM image of Cu electrodeposited on an RGO electrode in 10 mM $CuSO_4$ solution at −0.6 V. Reprinted by permission from Ref. [246], Copyright 2011, American Chemical Society.

2.1.2.4 Ex situ methods

Graphene–NP composites can also be produced by the ex situ assembly of NPs onto the graphene surface. In this method, the NPs are synthesised in advance and then later attached to the surface of the graphene sheets via linking agents which can utilise either covalent or noncovalent interactions, including van der Waals interactions, hydrogen bonding, π–π stacking, or electrostatic interactions. Although this method requires more time and steps to complete, it can offer a number of advantages when compared to in situ growth. For instance, ex situ methods result in a significantly narrower size distribution as well as better control over the size, shape and density of the NPs which decorate the graphene sheets while utilising self-assembly [250]. For the covalent attachment of NPs, GO rather than RGO is preferred due to the large amount of oxygen-containing groups on its surface, which can facilitate linkage with other functional groups. A variety of NPs have been attached to graphene using this method. Fan et al. [251] covalently attached MNPs to GO by first modifying the Fe_3O_4 NPs with tetraethyl orthosilicate and (3-aminopropyl) triethoxysilane (APTES), thereby introducing amino groups on its surface [251]. Next, these amino groups were reacted with the carboxylic groups on the surface of GO with the aid of 1-ethyl-3-(3- (dimethylamino)propyl)carbodiimide (EDC) and *N*-hydroxy succinimide (NHS), resulting in the formation of GO-Fe_3O_4 NP composites. Moreover, they demonstrated that the GO could subsequently be reduced to RGO using $NaBH_4$ as the reducing agent. Similarly, cadmium sulphide (CdS) QDs have been immobilised covalently on GO nanosheets [252]. In this case, amino-functionalised CdS QDs were first prepared by the modification of the kinetic trapping method [253]. Next, GO nanosheets were aceylated with thionyl chloride to introduce acyl chloride groups on its surface. To covalently bond the QDs to the GO nanosheets, an amidation reaction between the amino groups on the QDs and the acyl chloride groups on the GO surface was performed. Finally, noble metal NPs such as AuNPs have also been covalently attached to graphene. Specifically, Ismaili et al. [254] demonstrated the light-activated covalent formation of AuNPs on RGO. In this study, 4 nm AuNPs were modified with a 3-aryl-3-(trifluoromethyl)-diazirine functionality. Correspondingly, upon irradiation with wavelengths

above 300 nm and in the presence of RGO, the terminal diazirine group lost nitrogen to generate a reactive carbene which could then undergo addition or insertion reactions with the functional groups on graphene leading to covalent linkage.

Alternatively, NPs can be attached to graphene sheets via noncovalent bonds, including van der Waals interactions, hydrogen bonding, π–π stacking, and electrostatic interactions. Among these noncovalent bonds, π–π stacking and electrostatic interactions have been the most widely used. For π–π stacking, generally, aromatic compounds are attached to the NP surface, which enables their attachment to graphene via π–π stacking. For example, derivatives of the pyrene molecule as well as pyrene-functionalised block copolymers have provided an effective way for the noncovalent functionalisation of carbon NMs, including graphene [255]. In particular, pyrene groups have the ability to interact strongly with the basal plane of graphene via π–π stacking. For example, 1-pyrenebutyric acid (PBA) is one of the simplest pyrene-containing molecules attached to a carboxyl group. Resultantly, graphene sheets functionalised with PBA become negatively charged allowing for the attachment of positively charged NPs via electrostatic interaction [256]. The use of pyrene-containing molecules has been reported for various NPs. Examples include PBA, which was used to form graphene–AuNP hybrids [192], and pyrene-grafted poly(acrylic acid), which was used to form graphene–CdSe NP hybrids [257]. Pyridine is another aromatic structure which has also seen significant use in anchoring NPs such as Au [207, 258] and CdSe [259] NPs to the basal planes of GO/RGO sheets via π–π stacking. Importantly, pyrene- or pyridine-modified graphene sheets have a high loading capacity for NPs, and the amount of NP assembling on the graphene sheets can be easily modulated by controlling the feeding weight ratio of both components [192, 260].

DNA molecules, which contain both purine and pyrimidine bases, have also been used to mediate the fabrication of graphene–NP composites. In particular, DNA is able to interact with graphene via π–π stacking interactions as well as the surface binding model wherein DNA electrostatically interacts with graphene basal planes, which is similar to what is observed between single-stranded DNA (ssDNA) and CNTs [260]. For instance, Liu et al. developed a strategy wherein thiolated DNA oligos ($d(GT)_{29}SH$) were first adsorbed onto

GO sheets (DNA–GO) and then reduced by hydrazine to obtain DNA–RGO sheets [261]. Consequently, the addition of a large excess of 6 nm AuNPs to a solution containing either DNA–GO or DNA–RGO resulted in the formation of GO–AuNP and RGO–AuNP composites, respectively. Similarly, Wang et al. [262] fabricated GO–AuNP and GO–AgNP composites by first functionalising AuNPs or AgNPs with DNA via didentate capping ligands and then assembling them onto GO via π–π stacking interactions [262].

As mentioned previously, electrostatic interactions are also commonly used to modify graphene with various NPs as these provide a facile and scalable method to form composite structures in a controlled manner while avoiding conglomeration. GO and RGO have an inherent negative charge as a result of the ionisation of the oxygen functional groups on their surface. As such, they can be decorated with positively charged inorganic NPs through electrostatic interactions. For instance, graphene–metal oxide NP composites (e.g. RGO–Fe_3O_4 NP composites [263] and GO–MnO_2 NP composites [264]) have been formed by mixing positively charged metal oxide NPs with negatively charged graphene nanosheets [263]. Similarly, graphene–noble metal and other inorganic NPs have also been prepared in this way. To this end, Lu et al. noncovalently decorated GO sheets with positively charged aerosol Ag nanocrystals which were synthesised from an arc plasma source using an electrostatic force-directed assembly technique [265]. Moreover, reports have decorated graphene with APTES-modified SiNPs [266]. Specifically, while the amine functional groups of APTES can function to reduce GO and form covalent bonds with RGO, APTES can also help disperse RGO and SiNPs due to polar–polar interactions.

Finally, Deng et al. utilised a novel nontoxic synthetic method wherein bovine serum albumin (BSA) was utilised for the fabrication of graphene–NP composites, which could be composed of various types of NPs (Au, Pt, Pd, Ag and polystyrene beads) [267]. In this study, the use of BSA not only effectively reduced GO to RGO, but also acted as a stabiliser to induce the attachment of NPs onto the graphene surface (Fig. 2.15A). Specifically, BSA–GO/RGO conjugates were first obtained via the adsorption of BSA onto the basal planes of GO/RGO. Afterwards, the NPs were mixed in a solution containing the BSA–GO/RGO conjugates overnight to form the final graphene–

NP composites. Moreover, the density of NPs on the graphene–NP composites could be controlled by simply changing the concentration of BSA and NaCl during assembly (Fig. 2.15B–D). Similarly, Wang et al. recently reported an inexpensive and unique green, synthetic method for the production of Ag–GO nanocomposites which utilised glucose as both the reducing and the stabilising agent, eliminating the need for toxic reduction agents [268]. In particular, Wang et al. demonstrated that AgNPs could be directly reduced from silver ions on GO in a glucose solution.

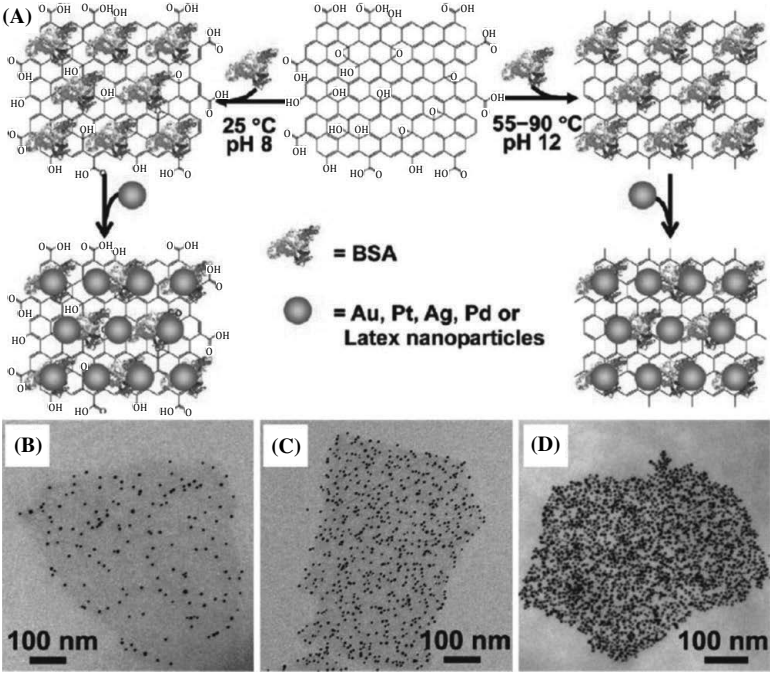

Figure 2.15 Protein-induced reduction and decoration of GO for the assembly of multiple NPs. (A) General scheme depicting the BSA protein-based decoration and reduction of GO, leading to a general nanoplatform for NP assembly. (B) TEM images of AuNP decorated BSA–GO with well-controlled densities of AuNPs. (B, C) AuNP densities were varied by increasing the concentrations of BSA from 0.5 mg/mL (B) to 20 mg/mL (C), during the preparation of BSA–GO. NaCl was omitted for the samples in (B, C). (D) AuNP density was further increased (in comparison with (C)) by adding 0.1 M NaCl to the assembly system as in (C). Reprinted by permission from Ref. [267], Copyright 2010, American Chemical Society.

2.1.3 Synthesis Methods of Graphene-Related Nanohybrids

Graphene-based CMG and 3DG materials have been prepared by various methods such as CVD of hydrocarbon on metal surface, liquid-phase exfoliation of graphite, chemical reduction of GO, silver mirror reaction, catalysis, in situ hydroxylation and sono sol–gel route [269–290].

2.1.3.1 Vapour deposition and liquid-phase exfoliation method

Nanohybrids of Ag/f-graphene/f-MWCNT and CuO/f-graphene can be easily prepared by CVD of hydrocarbon on metal surface. Hydrogen-functionalised graphene (HEG) was prepared from GO during exfoliation. As a result, most of the functional groups were removed from graphene. Then the HEG and MWCNT were functionalised in H_2SO_4 and HNO_3 acid medium, which were used for Ag decoration. A specified quantity of silver nitrate solution is generally added to the above solution under stirring. After some time, a mixture of $NaBH_4$ and NaOH was added drop wise to the above solution. Nanofluids were synthesised by dispersing a specific amount of Ag(HEG/MWCNT) in base fluids under ultrasound environment. Similarly, they dispersed to other combinations of Ag/HEG/MWNT to form hybrid nanofluids [269]. CMG materials are generally prepared by the CVD method, e.g. platinum-based graphene-supported electro catalyst for oxygen reduction reaction [291]. In order to extend the advantage of CNT spacers, a 3D CNT/graphene sandwiched (CGS) structure with CNT pillars grown between the graphene layers was developed via the CVD process [271].

2.1.3.2 Catalysis

GO/MWCNT/Ni hybrid nanocomposites can be easily prepared by solution-free green catalysis method [269] using focused solar electromagnetic radiation. A fine powder of GO–f-MWCNT composite was made by refluxing a 1:1 ratio of GO and f-MWCNT in HNO_3 for 2 h followed by washing to neutral pH and drying. Then stable nanofluids were prepared by dispersing the NMs in polar base fluids [269].

2.1.3.3 Polymerisation

Graphene-based hybrid polymer nanocomposites have been prepared by various methods such as solution blending (e.g. PVA/GO, PAA/GO, PAN/GO), melt mixing (e.g. PMMA/graphene, PP/graphene, PC/graphene), and in situ polymerisation (e.g. PMMA/GO, PP/GO, PE/graphene) [270]. The atom transfer radical polymerisation (ATRP) method has also been employed to graft poly(tert-butyl acrylate) (PtBA) from GO. The GO was reacted with trichloro(4-chloromethylphenyl) silane to prepare the ATRP initiator-coupled GO nanosheets. The modified GO particles were then used as the initiator in the polymerisation of PtBA to give GO nanosheets with covalently grafted PtBA. The grafted hydrophobic polymer brushes produced a substantial enhancement of GO solubility in organic solvents, and the GO-g-PtBA nanosheets formed a stable dispersion in toluene. The functionalised GO nanosheets were successfully integrated into an electroactive polymer matrix and subsequently a composite material based on a thin film of poly(3-hexylthiophene) (P3HT) containing 5 wt% GO-g-PtBA in an Al/GO-g-PtBA+P3HT/indium tin oxide (ITO) sandwich structure, where bi-stable electrical conductivity switching behaviour and a nonvolatile electronic memory effect were observed. Finally, water-dispersible GO-g-poly(acrylic acid) (PAA) nanosheets were prepared by hydrolysis, allowing gold NP-decorated GO-g-PAA nanofilms to be prepared from aqueous dispersions (Fig. 2.16)[274–290, 292, 293].

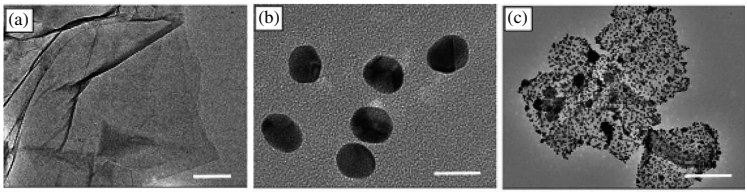

Figure 2.16 TEM images of (a) GO-g-PAA nanosheets, (b) AuNPs of 18 nm in diameter and (c) GO-g-PAA nanosheets decorated with 18 nm AuNPs processed from aqueous dispersions. The respective scale bars for (a), (b) and (c) are 200, 20 and 500 nm. Reprinted by permission from Ref. [292], Copyright 2010, American Chemical Society.

2.1.3.4 Graphenisation

Many different types of synthesis methods have been developed for preparing graphene–NPs composites, including three main

strategies: pre-graphenisation, post-graphenisation and syn-graphenisation. In the pre-graphenisation method, pre-synthesised RGO is mixed with the NPs for hybrid composite manufacturing. The incorporation of second-phase NPs and solubility of RGO in various solvents are important considerations for the composite preparation. The post-graphenisation method consists of thorough mixing of separately prepared NPs and/or salt water soluble metal precursors with GO suspension followed by the reduction to form RGO/NPs composite. This synthesis technique has been used to deposit metal NPs (e.g. Au, Pd, Pt, Ag), metal oxide NPs (Fe_2O_3, Fe_3O_4, Al_2O_3, SnO_2, NiO, MnO_2, TiO_2, ZnO, Cu_2O and Co_3O_4) and semiconducting NPs (CdSe, CdS, ZnS) on GO. The procedure consists of mixing of respective metal salts ($HAuCl_4$, K_2PtCl_4, K_2PdCl_4 and $AgNO_3$) to GO suspension followed by reduction using hydrazine monohydrate or sodium borohydride. Syn-graphenisation is often called the one-pot approach in which the second components of the composite act as a stabiliser for improving composite properties [270]. Various composites based on functionalised graphene with metals, semiconductors and metal oxides are summarised in Table 2.1.

Table 2.1 A summary of NP-decorated RGO composites and their proposed applications

Graphenisation	Synthesis step	Application
Pre	N-doped RGO + DMF + NaOH + ethylene glycol + H_2PtCl_6 + $6H_2O$ (stirring at 160°C)	Electrocatalytic activity (methanol fuel cell)
	High-temperature reaction of ferric triacetylacetonate with GO in 1-methyl-2-pyrrolidone	Magnetised RGO
	Nafion + glucose oxidase + chloroplatinic acid (H_2PtCl_6, $6H_2O$) phosphate buffer (K_2HPO_4 + KH_2PO_4) + RGO	Biosensor (amperometric biosensor)

(*Continued*)

Table 2.1 (*Continued*)

Graphenisation	Synthesis step	Application
	GO + H_2SO_4 + HNO_3 + $KClO_3$ reacted with ODA thionyl chloride	Showed potential for utilisation in plasmonics and optoelectronic devices
	H_2 electrochemical plasma RGO + Na_2PdCl_4 + $LiClO_4$	Gas sensing
	RGO + SnO_2 (obtained from hydrolysis of Sn Cl_4 + NaOH)	Lithium energy storage
	$Cd(SA)_2$/HDA/TOPO (in situ growing)	Optoelectronic device
	RGO + ultrasonic spray pyrolysis ZnO (LBL) assembly	Supercapacitor
	AuNPs deposited on top of RGO (micro-patterning method)	Memory devices
Post	GO + CdSe + TOPO ligands	Transparent film, photo switching
	AuNPs formation by reduction of Au ions in a gold salt solution on the RGO films	—
	GO + Fe_3O_4 + doxorubicin hydrochloride	Magnetic hybrid graphene (drug delivery)
	APS-modified NPs + GO > encapsulating GO/NPs	Lithium storage electrode (capacitor)
	GO + HCl + $SnCl_2$ + 60°C for 6 h	Capacity behaviour
	Ethylene glycol + metal precursor (K_2PtCl_4, K_2PdCl_4, $HAuCl_4$ + H_2O) 100°C heat in oil bath	Metal nanocomposite prevents restacking graphene
	$Ni(CH_3COO)_2$ + DMF + GO > crystal growth on graphene $Ni(OH)_2$	—

Graphenisation	Synthesis step	Application
	GO + Fe_3O_4 functionalising with TEOS, APTES, EDC, NHS and magnetic separation	Magnetic hybrid graphene (heterogenous catalysts and drug delivery)
	Direct growing, two-step method (TiO_2 + GO) + antanase hydrothermal treatment	Photocatalytic activity (solar cell and lithium ion battery)
	Mn_3O_4 on GO, two-step method ($Ni(OH)_2$ + GO, TiO_2 + GO) + $KMnO_4$ = $Mn(CH_3COO)_2$ + DMF/H_2O]	Lithium ion battery
	GO + $TiCl_3$ + Na_2SO_4 + H_2O_2 (self-assembly)	Photocatalytic activity, p/n heterojunction
	In situ growth, hydrothermal treatment, 200–300°C, 2 h in furnace with N_2	Photoeletrochemical cells, blue luminescence (PL) (optoelectronics and biological labelling)
	GO + $Ti(OBu)_4$ + DEA + NH_4OH + H_2O_2 (sol–gel process)	Photoconductor for ink print methods
	TiO_2 colloidal solution + GO (UV light reaction)	Dye-sensitised solar cell
	TS CuPc + GO (hydrate heat 1 h at 90°C with stirring)	Optoelectronics devices
	ZnO nanowire grown on RGO/PDMS substrate using hydrothermal method	Transparent and flexible optoelectronics
	TiO_2 + UV> + GO (became RGO)> + Ag ion (photocatalytic methods)	Chem/biological sensor
	TiO_2 + GO sheets (photocatalytic reduction) 100 mW/cm^2 mercury lamp at 275, 350, 660 nm	Photoinactivation of bacteria in solar light irradiation

(*Continued*)

Table 2.1 (*Continued*)

Graphenisation	Synthesis step	Application
	GO + Co_3O_4 Di water + H_2O_2 centrifugation, HCl wash and vacuum oven 60°C for 3 days	Catalytic effect for Al perchlorate decomposition
	GO + $RuCl_3$ + NaOH (reduced at 150°C)	Electrochemical capacitor and supercapacitor (energy storage)
	CdTe + GO + molecular beacon + abtamer	Biomolecular sensor
	TiO_2 colloidal solution + GO (UV light reduction)	Photoactive devices
	TMOS + GO (sol–gel)	Transparent conductors
Syn	Heating 75°C GO on 3-aminopropyltriethoxysilane + AgNPs	—
	GO + $TiCl_3$ + H_2O_2 in SDS solution > self-assembly TiO_2	Investigation Li ion insertion properties
	DMSO reduction of GO an deposing CdS occur simultaneously (solvothermal)	Optoelectronic device
	$Cd(CH_3COO)_2 \cdot 2H_2O$ + GO $Zn(CH_3COO)_2 \cdot 2H_2O$ + GO (solvothermal)	Photovoltaics

Source: Reprinted with permission from Ref. [270].

Schematic illustrations of two-step $Ni(OH)_2$ nanocrystal growth on graphene sheets and GO are shown in Fig. 2.17A and Fig. 2.17B, respectively. After the first step of the growth process (Ni precursor coating), the same coating of $Ni(OH)_2 \cdot 0.75H_2O$ was obtained both on GS and GO. After the second step (hydrothermal transformation), however, the coating on GS diffused and recrystallised into large single-crystalline hexagonal $Ni(OH)_2$ nanoplates (Fig. 2.17C), while the coating on GO remained as densely packed NPs pinned by the functional groups and defects on the GO surface (Fig. 2.17D) [294].

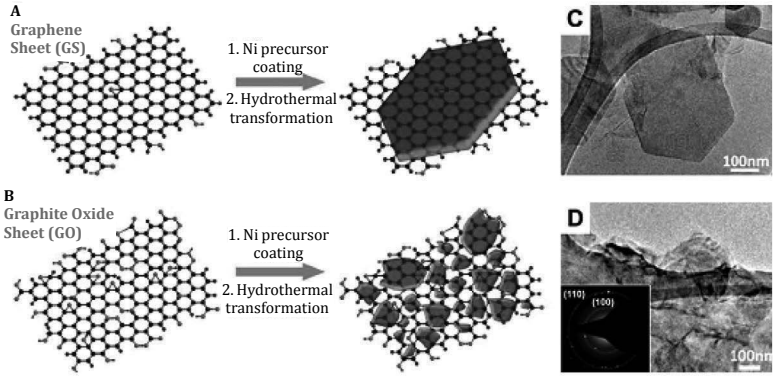

Figure 2.17 Schematic illustration of two-step $Ni(OH)_2$ nanocrystal growth on (A) graphene sheets and (B) GO; (C) coating on GS diffused and recrystallised into large single-crystalline hexagonal $Ni(OH)_2$ nanoplates; (D) coating on GO remained as densely packed NPs pinned by the functional groups and defects on the GO surface. Reprinted by permission from Ref. [294], Copyright 2010, American Chemical Society.

2.1.3.5 Sol–gel method

The sol–gel method has also been employed to fabricate graphene/silica composite thin films for transparent conductors, consisting of hydrolysis of tetramethyl orthosilicate in the presence of GO suspension in water. This film was subsequently reduced in the presence of hydrazine vapours for RGO/SiO_2 conductive composite film. Recently, a modified sol–gel method was adopted for TiO_2/GO composite using blending of GO sheets with a titanium hydroxide-based ionic salt, which was further reduced photo-catalytically [270, 294].

2.1.3.6 Reduction routes

Following are the reduction routes employed to prepare graphene-based nanohybrids [270, 271, 293].

2.1.3.6.1 *Chemical reduction*

One of the most straightforward approaches to prepare graphene–metal NP composites is the direct chemical reduction of the metal precursors in the presence of GO or RGO suspensions. The first graphene–AuNP composite was prepared by the reduction of $AuCl_4$

with $NaBH_4$ in an RGO-octadecylamine (ODA) solution. In addition to AuNPs, PdNPs supported on GO were prepared by bubbling hydrogen through a suspension of Pd^{2+}–GO in ethanol, and the obtained composites were used as catalysts in the Suzuki–Miyaura coupling reaction [271, 272].

2.1.3.6.2 *Ultraviolet light–assisted reduction*

UV-assisted photocatalytic reduction of GO was also observed and employed for composites of GO under UV in the presence of TiO_2 NPs. This strategy avoids chemical reduction and maintains well-dispersed TiO_2-RGO in suspension. Under UV radiation, TiO_2 NPs generate long lifetime electron–hole pairs. The generated holes are scavenged, leaving electrons on TiO_2 surface and reduce the oxidised groups on the GO surface (Fig. 2.18).

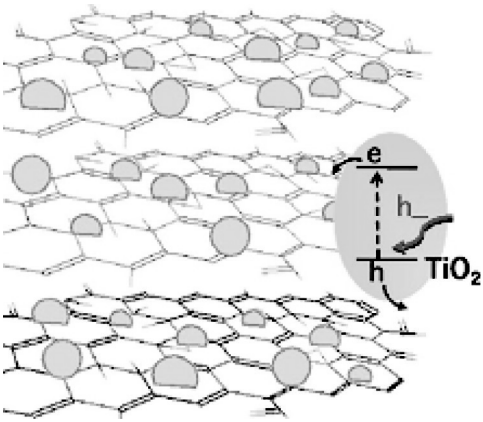

Figure 2.18 Schematic of TiO_2–graphene composite and its response under UV-excitons. Reprinted by permission from Ref. [295], Copyright 2008, American Chemical Society.

The UV-assisted reduction is fast and straightforward but only applicable to those NP systems which are sensitive to external light irradiation, such as TiO_2 and ZnO [270, 295].

2.1.3.6.3 *Photochemical reduction*

As a green, facile and efficient synthetic route, photochemical reduction can be applied as a supplement or alternative to the chemical reagent–based reduction for the synthesis of graphene–

metal NP composites. Fluorescent Au nanodots (NDs) on octadecyl thiol (ODT)-coated RGO sheets were synthesised by the photochemical reduction of $HAuCl_4$ in ethanol. These AuNDs self-assemble into short ND-chains on RGO surfaces, along the <100> direction of the RGO lattice. It is demonstrated that the organic molecules with self-assembled patterns on graphene surface can further direct the orientation and arrangement of the in situ synthesised NPs [271].

2.1.3.6.4 *Microwave-assisted reduction*

In the microwave irradiation method, the formation of metal NPs and the reduction of GO take place simultaneously, which allows for large-scale and highly efficient production. Additionally, this method can be applied to a number of metal precursors, such as those for Cu, Pd, Au and Ag. For example, after a water suspension of RGO is mixed with potassium permanganate powder by ultrasonication, the mixture is heated in a household microwave oven for only 5 min to obtain the graphene–MnO_2 NP composites [271].

2.1.3.7 Electroless metallisation

For the electroless deposition method, AgNPs are synthesised on GO and RGO surfaces, by heating the GO or RGO films adsorbed on 3-aminopropyltriethoxysilane-modified Si/SiO_x substrates in an $AgNO_3$ aqueous solution, without the use of any reduction agent and surfactants [271].

2.1.3.8 In situ crystallisation

The in situ crystallisation approach has been considered one of the most commonly used methods to synthesise composites of GO or RGO and semiconductor NMs [271]. Graphene–CdS nanocomposites were prepared by mixing GO and $Cd(CH_3COO)_2$ in DMSO, which was then heated in an autoclave at 180°C for 12 h. During the synthetic process, the hydrothermal process results in the simultaneous formation of CdS NPs and the reduction of GO to RGO in DMSO, which acts as both the solvent and the sulphur source. Time-resolved fluorescence spectroscopy data showed a picosecond ultrafast electron transfer process from CdS NPs to the graphene sheet, which demonstrates the potential optoelectronic application of this

graphene–CdS hybrid material. In another work, graphene–Co_3O_4 hybrid material was synthesised by reacting $Co(NO_3)_2{\cdot}6H_2O$ and ammonia solution in the presence of GO sheets, followed by drying and heating at 450°C to result in the graphene–Co_3O_4 nanocomposite used for the Li ion battery application. The in situ crystallisation approach is also applicable to the synthesis of many other types of semiconductor nanostructures on graphene-based templates such as MnO_2 nanoneedles, TiO_2 rods and SnO_2 NPs [271].

Generally, GO is insulated owing to the introduction of large amounts of functional groups. The oxygen-containing functional groups of GO are eliminated to restore the aromatic graphene networks, which is necessary for obtaining graphene sheets. In Fig. 2.19a, a two-step solvothermal procedure was developed to synthesise graphene–MnOOH nanocomposites through reducing GO–MnO_2 using ethylene glycol. Initially, GO sheets were decorated randomly by the rod-like MnO_2 (the left image in Fig. 2.19b), where a significant morphological transformation is observed after solvothermal treatment with ethylene glycol [297].

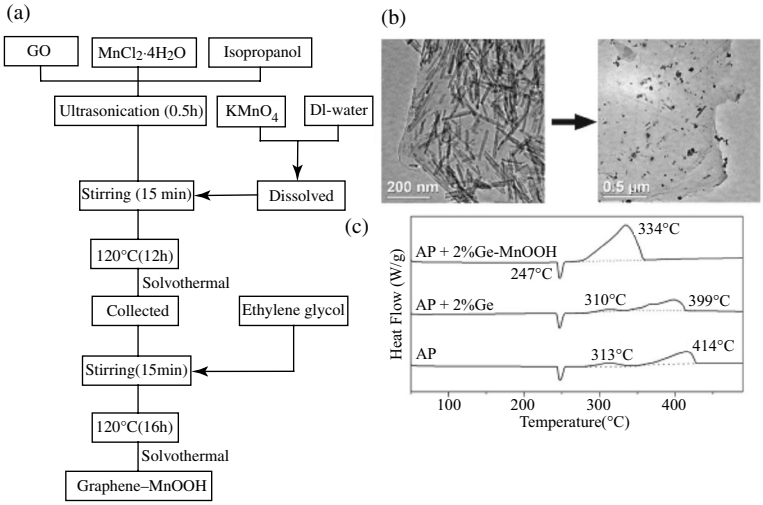

Figure 2.19 (a) Preparation procedure of graphene–MnOOH nanocomposites; (b) TEM images of GO–MnO_2 and graphene–MnOOH nanocomposites; (c) DSC curves for the thermal decomposition of AP, AP with 2% graphene, and AP with 2% graphene–MnOOH nanocomposites. Reprinted from Ref. [296], Copyright 2010, with permission from Elsevier.

The rod-like MnO_2 transfers to particulate MnOOH with diameters ranging from 20 to 80 nm. The dissolution-crystallisation mechanism is speculated to be responsible for this process. Additionally, the catalysis of as-obtained graphene–MnOOH nanocomposite on the decomposition of ammonium perchlorate (AP) was displayed in Fig. 2.19. With the addition of 2% graphene into the system, the low hand high decomposition temperature decreased to 310 and 399°C, respectively, probably due to the catalytic action of graphene. However, when graphene–MnOOH nanocomposites were added, the two steps (LTD and HTD) blended into one process at 334°C with the exothermic heat (1392 J/g) much larger than that of net AP and AP–graphene composites (590 and 540 J/g), revealing a good catalytic effect [293, 296].

2.1.3.9 Solution mixing

Graphene–NP-based semiconductor nanocomposites are prepared by the solution mixing approach. For example, commercialised TiO_2 NPs were mixed with Nafion-coated graphene to fabricate graphene–TiO_2 composites for dye-sensitised solar cell application, where the Nafion served as a "glue" to tightly bind graphene sheets and NPs. A solution of oleic acid-capped TiO_2 nanorods was prepared in toluene, which was mixed with GO water suspension and stirred for 24 h. The TiO_2 nanorods were able to assemble on the GO surface at the water/toluene interface [271].

2.1.3.10 Electrochemical deposition

A novel strategy used to prepare graphene-encapsulated metal oxide hybrids has been developed. Negatively charged GO sheets wrapped around the positively charged Co_3O_4 NPs (modified by aminopropyltrimethoxysilane, APS) were prepared through the electrostatic interaction, where GO was chemically reduced to RGO. The obtained composites were successfully used for the Li ion battery application as shown in Fig. 2.20(A–C). Consequently, the anode made from the graphene–Co_3O_4 NP composites showed a very high reversible capacity of 1100 mA·h/g in the first 10 cycles, and over 1000 mA·h/g after 130 cycles. Thin film–based applications require post-synthetic deposition of the composite materials on substrates by techniques such as spin-coating, drop casting and transfer printing.

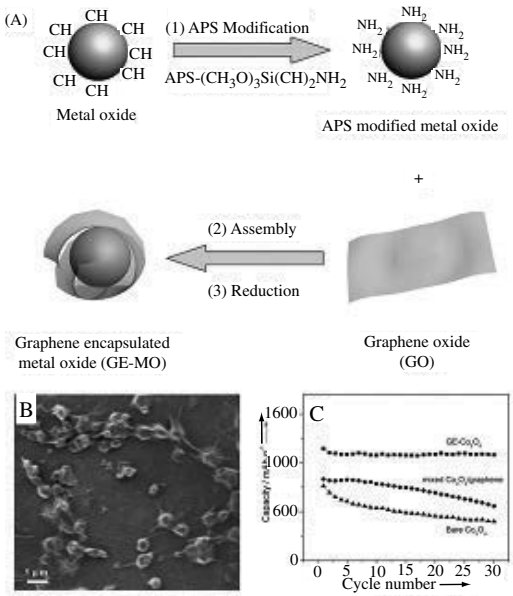

Figure 2.20 (A) Schematic illustration of fabrication of graphene-encapsulated metal oxide NPs. (B) Typical SEM image of graphene-encapsulated Co_3O_4. (C) Cycle performance of graphene-encapsulated Co_3O_4. Reprinted by permission from Ref. [297], Copyright 2010, John Wiley and Sons.

Therefore, the direct electrochemical deposition of NPs on graphene-based substrates is an attractive approach to prepare certain types of graphene–semiconductor NM hybrid films, such as ZnO, Cu_2O and CdSe [271, 297].

2.1.4 Synthesis Methods of Graphene-Encapsulated NPs

Because of the flexible and 2D sheet-like nature of graphene and its derivatives, these sheets can be easily used to wrap or encapsulate NPs that range in diameter from 100 nm to several hundreds of nanometres and even micrometres (Fig. 2.21). RGO sheets are the most frequently utilised carbon material for the encapsulation of NPs due to their slightly hydrophilic nature and the ease with which small fractions of RGO can be fabricated. In particular, methods used to fabricate graphene-encapsulated NPs typically utilise noncovalent bonds. For instance, the most frequently used method to encapsulate NPs with RGO consists of endowing the surface of the

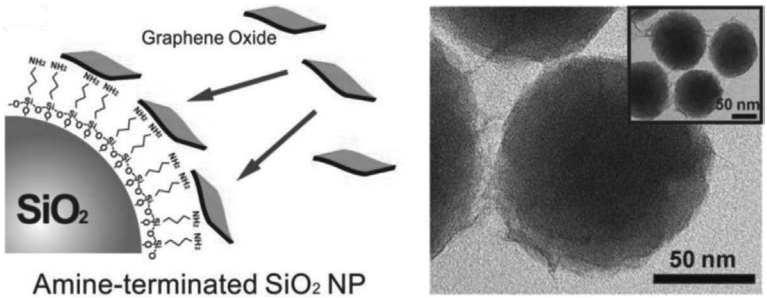

Figure 2.21 Fabrication process for graphene-coated NPs. Schematic diagram of GO assembly on amine-functionalised NPs and TEM image of NPs coated with GO (inset: zoomed-out TEM image of NPs coated with GO). Reprinted by permission from Ref. [266b], Copyright 2011, John Wiley and Sons.

NP with a positive charge (e.g. by coating with APTES), resulting in the strong attachment of RGO via electrostatic interaction [266b, 298]. By controlling the size of cracked RGO, a variety of NMs such as polymer as well as inorganic, metal and metal oxide NPs can be encapsulated by graphene/RGO to enhance their properties as well as to obtain additional advantages. In terms of its benefits, the encapsulation of NPs with graphene endows similar enhancements in electrical, electrochemical and optical properties that were observed for graphene–NP composites. However, due to the characteristically strong negative charge of RGO, the encapsulation of small NPs with RGO also results in the suppression of aggregation, which is a major issue in many NP-based bioapplications [261, 299]. Moreover, because of the high degree of contact between graphene and the encapsulated NP, which is significantly greater than that seen in graphene–NP composites, graphene-encapsulated NPs are very stable, thereby limiting the degree of exfoliation of the NPs from graphene or vice versa [226].

Numerous reports have demonstrated the encapsulation of metal oxide NPs with graphene. For example, Yang et al. reported RGO-encapsulated cobalt oxide NPs (Co_3O_4). These RGO-encapsulated Co_3O_4 NPs exhibited a very high reversible capacity (1000 mA·h/g) over 130 cycles, which was superior to normal cobalt oxide NPs used for capacitors [298]. In particular, using alternating current impedance measurements (30 cycles), Nyquist plots were obtained wherein the diameter of the semicircle for

RGO-encapsulated Co_3O_4 electrodes in the high–medium frequency region was much smaller than that of bare Co_3O_4 electrodes. This suggested that the RGO-encapsulated Co_3O_4 electrodes possessed lower contact and charge-transfer impedances. Feng et al. [300] also reported graphene-encapsulated TiO_2 nanospheres for efficient photocatalysis due to their high specific surface area (133 m^2/g). Specifically, the resulting hybrid material was much more efficient at decomposing rhodamine B (91%) than normal TiO_2 (65%) due to the presence of graphene, which was beneficial for the separation of photogenerated electrons and holes [300]. Similarly, the performance of tin oxide (SnO_2) NPs was also improved by the encapsulation of individual aggregates with graphene, resulting in excellent performance, including a charge capacity of 700 mA·h/g at the current density of 0.1 A/g and 423 mA·h/g after a 10-fold increase in the current density to 1 A/g in the 0.005–2 V voltage window [301]. Finally, Lin et al. [302] recently created RGO-encapsulated amine-functionalised Fe_3O_4 MNPs to support Pt catalysts. Specifically, after the Fe_3O_4 NPs were functionalised with APTES and coated with RGO, PtNPs were uniformly anchored by a polyol reduction reaction and the GO was simultaneously reduced to RGO. Resultantly, the electrochemical activity of the catalyst for methanol oxidation was significantly improved. The authors claimed that this was due to the accessibility of the PtNPs on the graphene surface and the greatly enhanced electronic conductivity of the underlying RGO-encapsulated Fe_3O_4 NPs. Others have focused on encapsulating metal NPs with graphene. For instance, Zhang et al. recently reported an interesting material, a "graphene-veiled gold nanostructure". In this study, they used graphene as a passivation nanosheet to prevent metal–molecule chemical interactions and to control the spatial resolution of molecules to achieve sensitive SERS signals from analytes of interest [61]. Kawasaki et al. have also reported graphene-encapsulated cobalt nanomagnets, wherein the cobalt NPs were first functionalised with benzylamine groups [303]. These 30 nm graphene-encapsulated NPs had a high specific surface area of 15 m^2/g and a high strength saturation magnetisation of 158 emu/g, which led to efficient extraction of analytes by magnetic separation for surface-assisted laser desorption/ionisation mass spectrometry (affinity SALDI-MS) analysis. In addition to the above examples, our group recently reported a method to convert nonconducting silicon oxide NPs into conducting RGO-encapsulated

NPs, which could then be used as the "bridging-material" in a field-effect transistor (FET)-based biosensor [266, 304]. Specifically, SiO_2 NPs were functionalised with APTES, thereby imparting them with a positive surface charge, which allowed for encapsulation with RGO via electrostatic interaction (Fig. 2.22). In doing so, we were able to prevent aggregation while maintaining a high electrical conductivity and enhanced surface area for the detection of cancer markers. Similarly, Zhou et al. [305] also encapsulated SiNPs with RGO via electrostatic interaction, again using APTES [305].

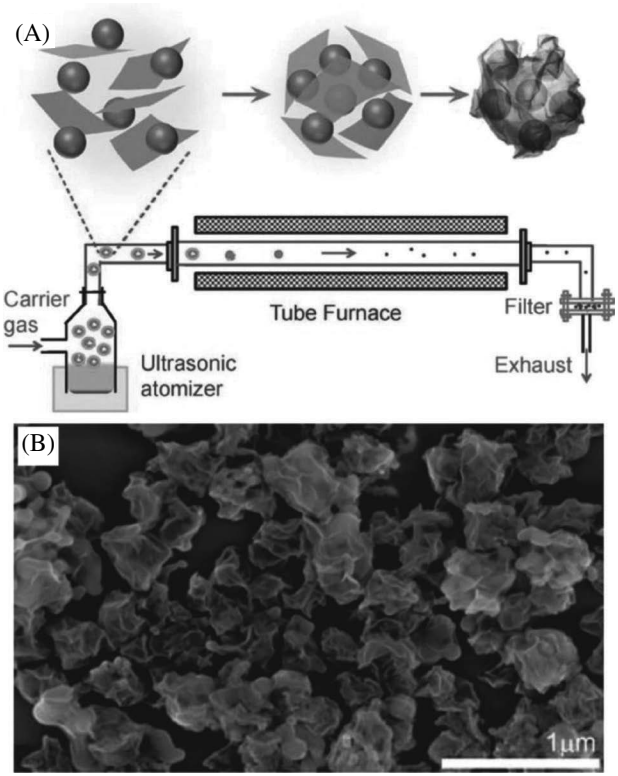

Figure 2.22 Crumpled graphene-encapsulated SiNPs. (A) Schematic drawing illustrating aerosol-assisted capillary assembly of crumpled graphene–wrapped SiNPs. Aqueous dispersion of GO and SiNPs was nebulised to create a mist of aerosol droplets, which were passed through a preheated tube furnace. During evaporation, GO sheets first migrated to the surface of the droplets and then tightly wrapped the Si particles upon complete evaporation. (B) SEM image showing the crumpled capsules of graphene-wrapped Si. Reprinted by permission from Ref. [306], Copyright 2012, American Chemical Society.

As a consequence of encapsulation, the SiNPs exhibited less aggregation and destruction than pristine SiNPs and acted as an outstanding electrode, exhibiting high reversible capacity (902 mA·h/g after 100 cycles at 300 mA/g). On the other hand, pristine SiNPs exhibited an initial discharge capacity of 3220 mA·h/g, which dropped to 13 mA·h/g after only 50 cycles. Finally, while electrostatic interaction has been the most commonly used method to form graphene-encapsulated NPs, Luo et al. reported an innovative method to fabricate graphene-encapsulated NPs via a facile and scalable, capillary-driven aerosol droplet method. Specifically, in a typical experiment, SiNPs in an aqueous suspension were directly added to a dispersion of micrometre-sized GO sheets. Nebulisation of the colloidal mixture resulted in the formation of aerosol droplets, which were blown through a preheated tube furnace at 600°C with an N_2 carrier gas (Fig. 2.22A). As a result, during the process of evaporation, the amphiphilic GO sheets migrated to the surface of the droplets to form a shell, and as the droplets evaporated further, the GO shell collapsed forming a "crumpled" shell around the SiNPs (Fig. 2.22B) [306].

2.2 Functionalisation Steps

2.2.1 External Electric Field, Edge Functionalisations and Doping of GNRs

Owing to the novel edge states and the resulting edge reactivity, zigzag GNRs can exhibit a variety of electronic properties with possibilities of finely tuning the electronic structures by external electric field, edge functionalisation and doping.

2.2.1.1 External field

DFT studies [307–309] revealed that the semiconducting zigzag GNRs can be turned into half-metals when exposed to an external field, which is caused by the opposite responses of the band gaps to the electric field for the up and down spins. With applied transverse electric field, the degeneracy between the occupied and unoccupied edge state bands at E_F for the two spin orientations is destroyed, and the band gap for one spin orientation is narrowed, while the

gap for another spin orientation is widened, resulting in conducting behaviour for one spin and insulating behaviour for the other spin under an appropriate critical electric field. The critical electric field for achieving half-metallicity in zigzag GNRs decreases as the width increases because the electrostatic potential difference between the two edges is proportional to the system size. In the case of an 8-chain zigzag GNR, the required critical field is 2 V/nm. Similar to single-layer zigzag GNRs, the band gap of bilayer zigzag GNRs is also sensitive to the external field, and a semiconducting half-metallic transition can be induced [310].

2.2.1.2 Edge functionalisation

Recent theoretical studies have suggested that half-metallicity of zigzag GNRs can be realised by functionalising with a donor and an acceptor on either edge to create an effective potential gradient or by introducing a spin-polarised impurity state at the Fermi level through hybrid modification at one edge. The edge-modified zigzag GNRs with CH_3 group at one edge and NO_2 group at the other edge are half-metals [311]. For 8-zigzag GNRs with decorated CH_3NO_2 pair, the band gap near the Fermi level experiences a metallic spin-down channel and a semiconducting spin-up channel, and the spin density mainly distributes on the edge carbon atoms (Fig. 2.23). The observed half-metallicity is still preserved even at lower CH_3 and NO_2 concentration on the wider zigzag edges. Wu et al. [312] suggested that half-metallicity in zigzag GNRs can also be achieved by modifying one edge with hybrid X groups (X = SO_2, NO_2 or CN) and hydrogen (H) atoms.

GNRs edge terminated with O, S, F, NH_2 and OH groups have also been theoretically studied [313–319]. These edge functionalisations offer effective routes to control the electronic and spin transports of zigzag GNRs.

2.2.1.3 Substitutional doping at the edge

The two free edges of GNRs serve as effective and active sites for substitutional doping. By simply replacing the C atoms at the edges with different types of dopants at different sections, one can selectively control the electronic and transport properties of GNRs [320–323]. The dangling bonds at the edge C atom of GNRs are

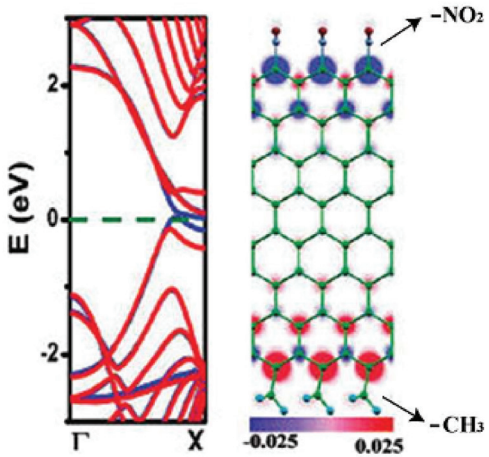

Figure 2.23 Band structure (left) and spin density (right) of 8-zigzag GNR with modified CH_3–NO_2 pair. Red and blue represent spin-up and spin-down channel, respectively. Reprinted by permission from Ref. [308], Copyright 2011, American Chemical Society.

typically saturated by H atoms, yet an alternative way is to substitute the edge C atoms with B or N dopants [324]. The substitutional B atoms at the nanoribbon edges play a role of scattering centres and can suppress the metallic bands near the Fermi level, giving rise to a semiconducting system [325]. The zigzag GNRs with B doping on both edges are stabilised as a ferromagnetic ground state and show half-metallic behaviour irrespective of the ribbon width. However, doping N atoms at both zigzag edges stabilises the system as an antiferromagnetic ground state and shows metallic behaviours [308].

Based on spin-unrestricted DFT computations, Li et al. [326] investigated the effects of N-doping defects on the electronic and magnetic properties of zigzag GNRs. One substitutional N atom shows the maximum stability when located at the C site of the ribbon edge, as compared with those interior sites. Such single N atom doping can remove the spin polarisation on the doped edge, while the spin polarisation on the undoped edge is less influenced (Fig. 2.24a), and the doped 10-zigzag GNR is converted to be a spin gapless semiconductor with vanished density of states around the

Fermi level, where the conduction band minimum (CBM) of the spin-up channel and the valence band maximum (VBM) of the spin-down channel touch each other at the Fermi level, and the gap is, therefore, closed.

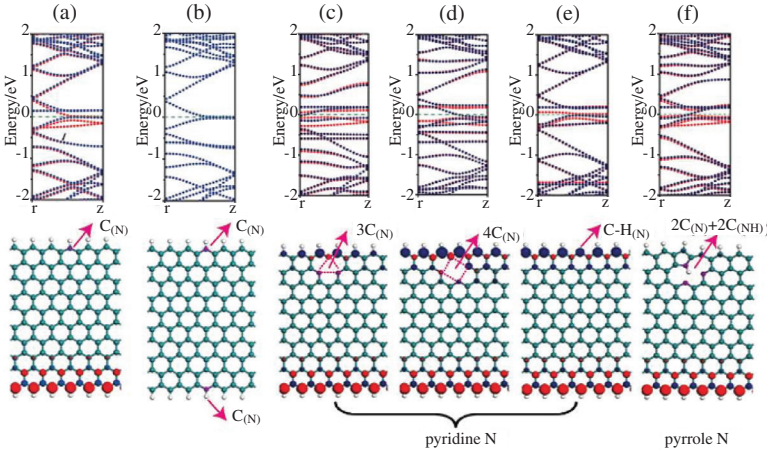

Figure 2.24 Band structure (upper) and spin density distribution (lower) for different kinds of N-doping in 10-zigzag GNR: (a) single and (b) double N-doping on the edge C atoms; (c, d, e) pyridine-like and (f) pyrrole-like N-doping. Reprinted by permission from Ref. [326], Copyright 2009, American Chemical Society.

Spin gapless semiconductors are quiet promising candidates for spin devices, since no energy is required to excite the electrons from valence band to the conduction band, and the excited electrons can achieve 100% spin polarisation, like half-metals. When the second N atom is substituted for C atom, the two doped N atoms are preferably localised at two opposite edges, and the spin polarisations on both edges are fully suppressed, making the 10-zigzag GNR become a nonmagnetic metal (Fig. 2.24b). Two special N-doping defects, namely the pyridine-like N-doping (constructed by creating C or C–C vacancy and substituting the nearest C atoms with N atoms, or directly substituting the edge C-H bond with an N atom) and pyrrole-like N-doping (constructed by creating C–C vacancy and substituting the two nearest C atoms with N atoms, and the remaining two nearest C atoms are substituted by one N–H bond), also prefer to form near the ribbon edges. These two kinds of N-doping also break the

degeneracy of the two edge states due to the presence of defects, and the resulting doped zigzag GNRs are spin gapless semiconductors or half-metals.

2.2.1.4 Isoelectronic BN9 pair doping

The structural hybridisation by substituting the graphene C–C chains with isoelectronic BN chains at the edge or inner sites of GNRs also achieves significant tuning on the electronic transmission of GNRs [327–332]. For BN-embedded zigzag GNRs, a gradual replacement of the zigzag C–C chains in the middle part of the ribbon by zigzag B–N chains transforms the system finally to the zigzag BN nanoribbons, and the electronic structures vary accordingly with the doping concentration [327]. At a high doping concentration, the hybrid nanoribbons with terminated polyacene C chains at the edge and all the substituted B–N chains in the internal part act as half-metallic antiferromagnets for all the widths. The Lewis acid character of boron is identified to be responsible for the charge transfer from the adjacent C atoms to the B atoms, resulting in an interface potential gradient analogous to the effect of external electric field and invoking the half-metallicity in the hybrid systems.

2.2.1.5 Atomic and molecular adsorption

Metal adatoms adsorbed on the surface of GNRs can induce spontaneous magnetism and novel electronic behaviours [333–335]. When Ni lies along the edge of zigzag GNRs, many resonant peaks, relating to the change of magnetisation, appear within an energy interval of ±2 eV with respect to the Fermi level [333]. Fe and Ti adsorption on the edge of armchair GNRs can convert the ribbons into half-metals with 100% spin polarisations at the Fermi level [334]. After adsorbing the main-group adatoms (C, B or N), the antiferromagnetism of pristine zigzag GNRs is transformed into ferrimagnetism [336]. At the experimental side, the trapping of Au atoms at the graphene edges has been observed by aberration-corrected TEM techniques [337].

Similar to graphene, the hole and electron doping in GNRs can also be successfully done by molecular charge transfer using strong donor or acceptor molecules adsorbed on their surface [338–340]. Without the aid of large external electric fields, the zigzag GNRs can be driven into half-metals by surface deposition with a critical cover-

age of ferroelectric polymer, poly(vinylidenefluoride) (PVDF), which arises from the electrostatic potential on the zigzag GNR induced by the strong dipole moments of PVDFs [341]. Therefore, as in the case of graphene, doping offers a large amount of appreciable and effective ways to manipulate the electronic and magnetic properties of GNRs with myriads of possible nanodevice applications.

2.2.2 Functionalisation of GO

GO-related materials possess plentiful and reactive oxygen-containing functional groups. These oxygen species are the reactive sites and susceptible to various chemical reactions and surface modifications, via either covalent or noncovalent functionalisation or surface transition metal adsorption.

2.2.2.1 Covalent functionalisation

Different functional groups have their unique selectivity in specific chemical reactions [342], which offers site selectivity for covalent functionalisations. The carboxylic acid groups located at the GO edge are mainly utilised in chemical reactions such as amidation and esterification. Taken as examples, the porphyrin and fullerene units have been covalently grafted through robust amide bonds at the periphery carboxylic sites of GO (Fig. 2.25a) [343], and the assembled hybrid materials offer superior performances than any of the separated components in enhancing the nonlinear optical properties in the nanosecond regime. Few-layer graphene nanosheets could be covalently functionalised via ester linkages between carboxylic acid moieties on the nanosheets and hydroxyl groups on poly(vinyl alcohol) (PVA) (Fig. 2.25b) [344], and the resulting products were demonstrated to increase the solubility and dispersibility in organic solvents to form a stable solution, which enabled characterisations in terms of solution-phase techniques. The epoxy groups on the basal planes of GO can be modified by nucleophilic ring-opening reactions. Yang et al. [345] reported the covalent attachment of NH_2-terminated ionic liquid (1-(3-aminopropyl)-3-methylimidazolium bromide; IL-NH2) onto the basal plane of GO platelet by ring-opening at the epoxy site (Fig. 2.25c). The chemically converted graphene sheets were stably dispersed in solvents such as water, DMF and DMSO. Likewise, the solid-phase dispersibility of chemically converted

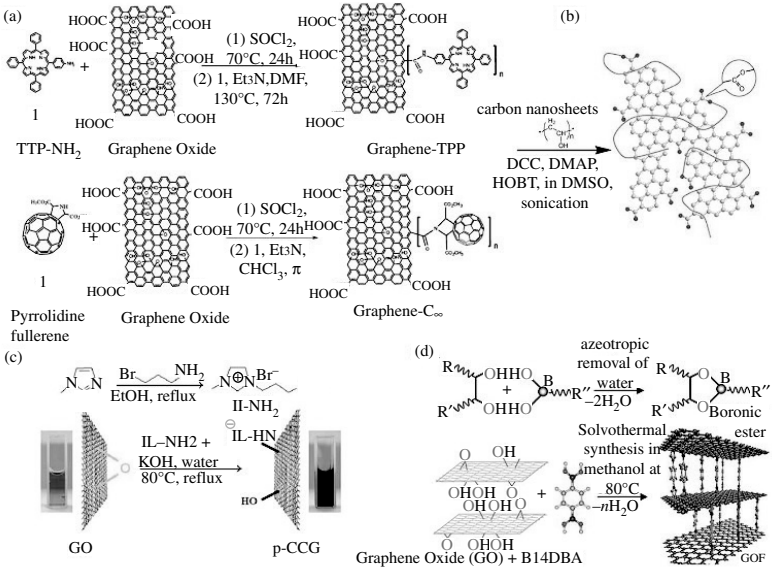

Figure 2.25 (a) Synthesis schemes of covalently functionalised GO by porphyrin and fullerene units. Reprinted by permission from Ref. [343], Copyright 2009, American Chemical Society. (b) Functionalisation via esterification between the carboxylic acid moieties in oxidised carbon nanosheets and hydroxyl groups in poly (vinyl alcohol). Reproduced from Ref. [344] with permission of The Royal Society of Chemistry. (c) Illustration of the preparation of covalently functionalised GO by ionic liquid 1-(3-aminopropyl)-3-methylimidazolium bromide. Reproduced from Ref. [345] with permission of The Royal Society of Chemistry. (d) Representations of boronic ester and GOF formation. Idealised GO framework (GOF) materials proposed are formed of layers of GO connected by benzenedi-boric acid pillars. Reprinted by permission from Ref. [347], Copyright 2010, John Wiley and Sons.

graphene nanosheets was stabilised via covalent grafting by 3-amino-propyltriethoxysilane (APTS). The resulting functionalised composite can enhance the mechanical properties of silica monoliths as reinforcing component after its incorporation into the silica matrix [346]. The surface hydroxyl groups of GO sheets can also engage in reactions. For example, the interlayer boron ester bonds formed by the surface hydroxyl groups of GO and diboronic acids can lead to the formation of a new layered 3D GO framework (GOF) (Fig. 2.25d) [347]. Such GO framework can have tunable pore widths, volumes and binding sites depending on the chosen linkers, and exhibits hydrogen uptake properties. The covalently functionalised

GO demonstrates great potentials in biological applications. Lots of efforts have been made towards constructing hybrids of biological and carbon nanocomposites due to their paramount importance in both biosensing and drug delivery [348]. Polyethylene glycol (PEG) can be covalently grafted onto the carboxyl groups of GO sheets.

The branched PEG-grafted nanoscale GO (NGO) sheets (PEG-NGO) demonstrate intrinsic photoluminescence in the near-infrared range and have a unique ability of loading various types of insoluble, aromatic drug molecules, thus may perform as useful nanocarriers for cancer-drug delivery [349]. The straight-chain PEG-modified GO sheets with fluorescein functionalisation serve as a fluorescence probe for intracellular imaging [350]. Wang et al. [351] developed an intracellular protease sensor for living-cell caspase-3 detection based on the covalent conjugation of GO and peptide substrate with fluorophore labels. The antibodies immobilised on the GO array via an amidation reaction are demonstrated to be useful in rotavirus detection [352].

2.2.2.2 Noncovalent functionalisation

GO can be noncovalently functionalised by organic and biological molecules via π–π bonds and hydrogen bond interactions [353–355]. A GO-doxorubicin hydrochloride (DXR) hybrid material was prepared via a simple noncovalent method [356]. The pH-dependent loading and releasing behaviour of DXR on GO may be due to the hydrogen bonding between –OH and $-CO_2H$ groups of GO and –OH and $-NH_2$ groups in DXR. At the same time, the fluorescence spectrum and electrochemical characterisation suggested that strong π–π stacking interactions also existed between them. Lu et al. [357] reported the noncovalent binding between GO and dye-labelled single-stranded DNA (ssDNA) and showed that this hybrid complex holds a robust platform for fast, selective and sensitive detection for DNA or thrombin (Fig. 2.26). The strong adsorption of dye-labelled ssDNA on GO can result in up to 97% fluorescence quenching due to electron transfer from fluorophore excited states to the π system of GO. With the addition of target (DNA or protein molecule), the configuration of ssDNA can be altered due to the ssDNA–target binding and consequently disturb the interaction between ssDNA and GO, resulting in the release of dye-labelled DNA from the GO and restoration of dye fluorescence.

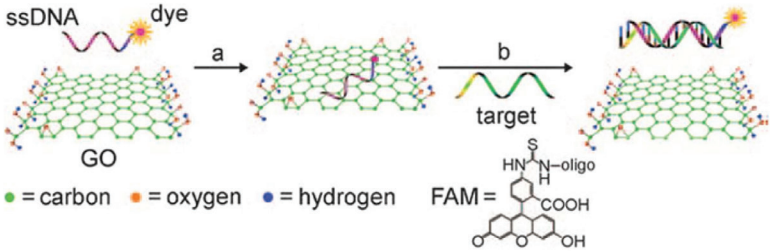

Figure 2.26 Schematic representation of the target-induced fluorescence change of the ssDNA-FAM-GO complex. FAM is the fluorescein-based fluorescent dye. Reprinted by permission from Ref. [357], Copyright 2009, John Wiley and Sons.

Wang et al. [358] constructed an intracellular biosensor by employing GO nanosheets as the efficient cargo and protector of DNA (oligonucleotides), and using the designed DNA-adsorbed GO nanocomplex for cellular delivery of genes and in situ molecular probing of adenosine triphosphate (ATP).

2.2.2.3 Transition metal adsorption

The surface –OH and epoxy groups are active sites for anchoring the under-coordinated transition metals. Wang et al. [359] suggested that Ti atoms could bind strongly to the oxygen sites of the experimentally accessible GO with binding energy as high as 450 kJ/mol. The Ti-anchored GO not only forms a stable motif but also acts as an excellent substrate for hydrogen storage. Besides Ti, Fe atom can also be anchored onto the epoxy sites of GO [360]. The high-diffusion barrier of Fe atom on the GO precludes the issue of metal clustering, and the strong binding strength between them assures the structural stability of the Fe–GO system. Similar to the case of Fe-embedded graphene, the Fe-anchored GO also demonstrated a good catalytic performance for the CO oxidation with O_2 to form CO_2 [360].

2.2.2.4 Through diazonium salt reaction

The patterned graphane/graphene hybrid superlattices can be functionalised by controllably exchanging the surface C–H bonds with C–C bonds through diazonium salt reaction [361].

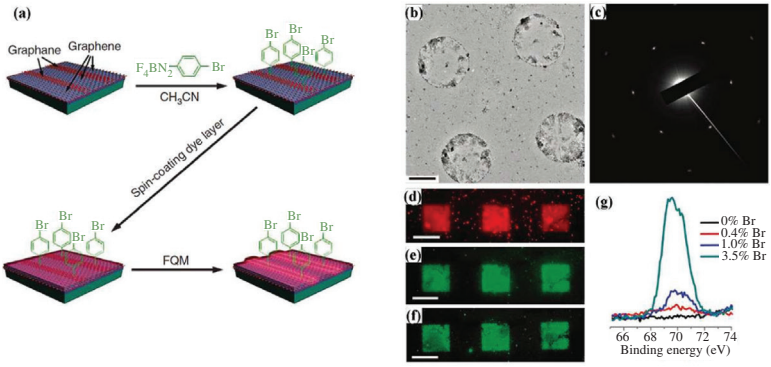

Figure 2.27 Controllable exchange of sp^3 C–H bonds with sp^3 C–C bonds using 4-bromo phenyldiazonium tetrafluoroborate. (a) Schematic illustration of the fabrication of sp^3 C–C exchanged superlattices and subsequent fluorescence quenching microscopy (FQM) imaging. (b) TEM image of diazonium-functionalised graphene film covering a TEM grid with four suspended areas shown. The scale bar in (b) is 0.5 µm. (c) SAED pattern of diazonium-functionalised graphene. (d–f) FQM images of diazonium-functionalised graphene superlattices. The dye molecules used in FQM are rhodamine B in (d), fluorescein isothiocyanate (FITC) in (e) and fluorescein sodium in (f). The scale bars in (d) to (f) are 50 µm. (g) XPS of samples containing different percentages of 4-bromophenylene functionality by tuning the hydrogenation process. The bromine content could be controlled from 0 to 3.5%. Reprinted by permission from Macmillan Publishers Ltd: *Nature Communications*, Ref. [361], Copyright 2011.

The selectively hydrogenated graphane/graphene domains were fabricated by first defining a pattern on the graphene films via conventional photolithography and then hydrogenating the exposed area of graphene. Hydrogenation activates the basal plane of graphene, and the subsequent reaction towards diazonium functionalisation (4-bromophenyldiazonium tetrafluoroborate) is most likely to go through a free radical mechanism. The TEM image (Fig. 2.27) and selected area electron diffraction pattern prove that the graphene sample is maintained after the chemical treatment of hydrogenation and diazonium reaction. Fluorescence quenching microscopy (FQM) revealed the same diazonium-functionalised graphene superlattices with different dye molecules. Typically, the dark areas are pristine graphene, which more efficiently quenches

the fluorescence of the thin top dye layer, and the bright areas are graphane or diazonium-functionalised domains since its fluorescence quenching ability is much weaker than in graphene due to its loss of conjugation. By tuning the extent of hydrogenation, the grafted Br-containing functional groups with density ranging between 0.4% and 3.5% can be achieved. This two-step route with controlled covalent functionalisation on the basal plane holds potential for engineering the electronic and chemical properties of graphene and might be promising for specifically patterned optoelectronic and sensor devices.

2.3 Surface Modification Methods

Forefront research on graphene is mainly pushed by active materials, which has progressed to next-generation graphene-related NMs. These materials are divided into two main categories [42, 46]: (i) chemically modified graphene (CMG) and (ii) 3D graphene architectures (3DG). In CMG materials, carbon atoms of graphene sheets are replaced by other atoms of N, B, S, P or entire functional groups. In 3DG materials, graphene or CMG sheets are assembled together to form 3D interconnected networks or highly complex nano-objects. Graphene sheets can be functionalised by chemical and electrochemical surface modification [43, 45], which give CMG and 3DG NMs.

2.3.1 Chemical Modification of Surface

Pristine graphene materials are unsuitable for intercalation with polymer chains because bulk graphene has a pronounced tendency to agglomerate in a polymer matrix. Chemical functionalisation of graphene-related NM is an attractive target because it can tune its stability, electronic and magnetic properties and improve the solubility, processability and interactions with organic polymers. Doping of graphene-related NM is done for tuning their different properties. Doping can be done by various techniques. Graphene can be organochemically modified by different approaches [43–45, 59] such as reduction of GO, covalent modification of

graphene, noncovalent functionalisation of graphene, nucleophilic substitution, diazonium salt coupling and adsorption of metal. Reduction of GO is carried in a stabilised medium; e.g. KOH-treated GO can be modified with hydroxyl, epoxy or carboxylic acid groups. Covalent modification of graphene is done by using lithium reagents, isocynates and di-isocynates to reduce the hydrophilic character of GO, e.g. chitosan functionalised GO and CNT [47, 362–363] for biological and medical applications. GO nanoplatelets can be also functionalised by polysodium styrene sulphonate, which is an example of noncovalent functionalisation [47, 59]. Amine-modified GO is an example of nucleophilic substitution. GO can be reduced by hydrazine and treated by aryl diazonium salts, which is an example of diazonium salt coupling. Atoms of transition metals such as Ti and Fe can be anchored to adsorb on the surface of GO. Derivatives of graphane can be fabricated by changing the substrate atoms (C, Si, Ge, P) and the surface atoms (H, –OH, $-NH_2$, He, Li, Fe, Mn, all VII A group elements) [59].

2.3.2 Electrochemical Modification of Surface

A colloidal suspension of graphene can be prepared from electrochemically modified graphite [43]. In this electrochemical reaction of 30 min, a commercial graphite electrode was used as a cathode and immersed in a phase-separated mixture of water and imidazolium-based ionic liquids. A constant potential of 10–20 V was applied across the electrodes, so that ionic liquid functionalised graphene sheets can be precipitated from the anode. A homogeneous dispersion of 1 mg/ml was prepared by ultrasonication process using functionalised and dried graphene sheets in DMF. These types of graphene dispersions show a Tyndall effect [55].

2.3.3 π–π Interaction

It is reported that graphene can be modified by considering the π–π interaction between the π orbitals of graphene and poly(isopropylacrylamide) in the presence of water [43]. Water-dispersible graphene can be produced by ultrasonication in an ice bath. Another example of π–π interaction is graphene with pyrene

derivative soluble in DMF [45]. Graphene can be incorporated with metal NPs. This may keep graphene sheets in de-aggregated form during the reduction of GO [45].

2.4 Conclusion and Perspectives

Due to distinct characteristics of graphene, its applications focus mainly on electronics, molecular gas sensors and energy storage. As a result, the massive production of high quality graphene is required. The production of graphene in decagram scale with high purity can be achieved by the arc-discharge method. Deposition of graphene on catalysts has been also demonstrated using thermal CVD process. Monolayer graphene can be formed on catalyst through the surface catalytic pyrolysis of carbon-containing precursors. It can be transferred to arbitrary substrates via a transfer process with or without support media. A color contrast using optical microscope and Raman spectroscopy is useful for distinguishing the number of graphene layers. So, the graphene morphology is closely dependent on the catalyst material, for selection of right catalyst. A CVD plays an important role in graphene fabrication for supply of high-quality large-size graphene sheets with massive production. The versatility of CVD grown graphene polymer nanocomposites suggests their potential application in automotive, electronics, aerospace and packaging. However, a lack of effective methods for scalable graphene production, which translates as higher costs, results in difficult manipulation of graphene sheets in processing due to its extremely low bulk density. The lack of local sites or tensioned bonds on the graphene sheets to anchor functional moieties make it more processable and compatible with other materials. The main drawback of GO is the disruption of the sp^2 network that can transform it into a completely insulating material. Irreversible sp^3 defects are created under strongly oxidizing conditions, worsening the final properties of graphene. Considerable efforts have been made in the functionalisation of pristine graphene and expanded graphite for polymer nanocomposites in order to obtain materials with higher performance.

References

1. Brodie B. (1855). *Ann. Chim. Phys.,* **45**, 351.
2. Chen D., Feng H., Li J. (2012). *Chem. Rev.,* **112**, 6027–6053.
3. Philos Brodie B.C. (1859). *Trans. R. Soc. London,* **149**, 249–259.
4. Staudenmaier L. (1898). *Ber. Dtsch. Chem. Ges.*, **31**, 1481–1487.
5. Hummers W.S., Offeman R.E. (1958). *J. Am. Chem. Soc.,* **80**, 1339.
6. Paredes I., Villar-Rodil S., Martínez-Alonso A., Tascón J. M. D. (2008). *Langmuir,* **24**, 10560–10564.
7. Hossain M.Z., Johns J.E., Bevan K.H., Karmel H.J., Liang Y.T., Yoshimoto S., Mukai K., Koitaya T., Yoshinobu J., Kawai M., M.Lear A., Kesmodel L.L., Tait S.L., Hersam M.C. (2012). *Nat. Chem.,* **4**, 305–309.
8. Vinogradov N.A., Schulte K., Ng M.L., Mikkelsen A., Lundgren E., Martensson N., Preobrajenski A.B., (2011) *J. Phys. Chem. C*, **115,** 9568–9577.
9. Liu L., Ryu S., Tomasik M.R., Stolyarova E., Jung N., Hybertsen M.S., Steigerwald M.L., Brus L.E., Flynn G.W. (2008). *Nano Lett.,* **8**, 1965–1970.
10. Starodub E., Bartelt N.C., McCarty K.F. (2010). *J. Phys. Chem. C*, **114**, 5134–5140.
11. Yamamoto M., Einstein T.L., Fuhrer M.S., Cullen W.G. (2012). *ACS Nano,* **6**, 8335–8341.
12. Surwade S.P., Li Z., Liu H. (2012). *J. Phys. Chem. C*, **116**, 20600–20606.
13. Lee G., Lee B., Kim J., Cho K. (2009). *J. Phys. Chem. C,* **113**, 14225–14229.
14. Zhao S., Surwade S.P., Li Z., Liu H. (2012). *Nanotechnology,* **23**, 355703.
15. Cheng Y.C., Kaloni T.P., Zhu Z.Y., Schwingenschlogl U. (2012). *Appl. Phys. Lett.,* **101**, 073110.
16. Ramesh P., Itkis M.E., Bekyarova E., Wang F., Niyogi S., Chi X., Berger, de Heer W., Haddon R.C. (2010). *J. Am. Chem. Soc.,* **132**, 14429–14436.
17. Itkis M.E., Wang F., Ramesh P., Bekyarova E., Niyogi S., Chi X., Berger C., de Heer W.A., Haddon R.C. (2011). *Appl. Phys. Lett.,* **98**, 093115.
18. Li J., Kudin K.N., McAllister M.J., Prud'homme R.K., Aksay I.A., Car R. (2006). *Phys. Rev. Lett.,* **96**, 176101.
19. Boukhvalov D.W., Son Y.W. (2012). *Chem. Phys. Chem,* **13**, 1463–1469.
20. Xu Z., Xue K. (2010). *Nanotechnology,* **21**, 045704.

21. Li Z., Zhang W., Luo Y., Yang J., Hou J.G. (2009). *J. Am. Chem. Soc.,* **131**, 6320–6321.
22. Sun T., Fabris S. (2012). *Nano Lett.,* **12**, 17–21.
23. Dikin D.A., Stankovich S., Zimney E.J., Piner R.D., Dommett G.H.B., Evmenenko G., Nguyen S.T., Ruoff R.S. (2007). *Nature,* **448**, 457–460.
24. Paci J.T., Belytschko T., Schatz G.C. (2007). *J. Phys. Chem. C,* **111**, 18099–18111.
25. Suk J.W., Piner R.D., An J., Ruoff R.S. (2010). *ACS Nano*, **4**, 6557–6564.
26. Kim J.E., Han T.H., Lee S.H., Kim J.Y., Ahn C.W., Yun J.M., Kim S.O. (2011). *Angew. Chem. Int. Ed.,* **50**, 3043–3047.
27. Loh K.P., Bao Q., Eda G., Chhowalla M. (2010). *Nat. Chem.,* **2**, 1015–1024.
28. Zhao J., Pei S., Ren W., Gao L., Cheng H.M. (2010). *ACS Nano,* **4**, 5245–5252.
29. Gao X., Wang L., Ohtsuka Y., Jiang D.E., Zhao Y., Nagase S., Chen Z. (2009). *J. Am. Chem. Soc.,* **131**, 9663–9669.
30. Yeh T.F., Syu J.M., Cheng C., Chang T.H., Teng H. (2010). *Adv. Funct. Mater.,* **20**, 2255–2262.
31. Krishnamoorthy K., Mohan R., Kim S.J. (2011). *Appl. Phys. Lett.,* **98**, 244101.
32. Dreyer D.R., Jia H.P., Bielawski C.W. (2010). *Angew. Chem. Int. Ed.,* **49**, 6813–6816.
33. Pyun J. (2011). *Angew. Chem. Int. Ed.,* **50**, 46–48.
34. Zhang L.L., Zhao S., Tian X.N., Zhao X.S. (2010). *Langmuir,* **26**, 17624–17628.
35. Chen S., Zhu J., Wu X., Han Q., Wang X. (2010). *ACS Nano,* **4**, 2822–2830.
36. Eda G., Fanchini G., Chhowalla M. (2008). *Nat. Nanotech.,* **3**, 270–274.
37. Robinson J.T., Perkins F.K., Snow E.S., Wei Z.Q., Sheehan P.E. (2008). *Nano Lett.,* **8**, 3137–3140.
38. Raza H. (2012). *Graphene Nanoelectronics*, Heidelberg, Germany: Springer-Berlin, pp. 15–586.
39. Geim A.K., Novoselov K.S. (2007). *Nat. Mater.*, **6(3)**, 183–191.
40. Singh V., Joung D., Zhai L., Das S., Khondaker S.I., Seal S. (2011). *Prog. Mater. Sci.,* **56(8)**, 1178–1271.
41. Fuhrer M.S., Lau C.N., MacDonald A.H. (2010). *MRS Bull.,* **35(4)**, 289–295.

42. Agnoli S., Granozzi G. (2013). *Surf. Sci.,* **609**, 1–5.
43. Kuilla T., Bhadra S., Yaoa D., Kim N.H., Bose S., Lee J.H. (2010). *Prog. Polym. Sci.,* **35(11)**, 1350–1375.
44. Li N., Wang Z., Shi Z. (2011). *Synthesis of Graphene with Arc-Discharge Method,* Mikhailov S. (ed.), Rijeka, Croatia: Intech, pp. 23–36.
45. Rao C.N.R., Sood A.K., Subrahmanyam K.S., Govindaraj A. (2009). *Angew. Chem., Int. Ed.,* **48(42)**, 7752–7777.
46. Zhu Y., Murali S., Cai W., Li X., Suk J.W., Potts J.R., Ruoff R.S. (2010). *Adv. Mat.,* **22(35)**, 3906–3924.
47. Huang X., Yin Z., Wu S., Qi X., He Q., Zhang Q., Yan Q., Boey F., Zhang H. (2011). *Small,* **7(14)**, 1876–1902.
48. Li K., Eres G., Howe J., Chuang Y.J., Li X., Gu Z., Zhang L., Xie S., Pan Z. (2013). *Sci. Rep.,* **3(2353)**, 1–4.
49. Sivudu K.S., Mahajan Y. (2012). *Mass production of high quality graphene: An analysis of worldwide patents,* Nanotech Insights, Accessed 24 April 2012.
50. Park S., Ruoff R.S. (2009). *Nat. Nanotechnol.,* **4(4)**, 217–224.
51. Bae S., Kim H., Lee Y., Xu X., Park J.S., Zhang Y., Balakrishnan J., Lei T., Kim H.R., Song Y.I., Kim Y.J., Kim K.S., Ozyilmaz B., Ahn J.H., Hong B.H., Iijima S. (2010). *Nat. Nanotechnol.,* **5(8)**, 574–578.
52. Li Y., Chopra N. (2015). *JOM,* **67(1)**, 44–52.
53. Novoselov K.S., Geim A.K., Morozov S.V., Jiang D., Zhang Y., Duobonos S.V., Grigorieva I.V., Firsov A.A. (2004). *Science,* **306 (5696**), 666–669.
54. Khan U., O'neill A., Porwal H., May P., Nawaz K., Coleman J.N. (2012). *Carbon,* **50(2)**, 470–475.
55. Nuvoli D., Alzari V., Sanna R., Scognamillo S., Piccinini M., Peponi L., Kenny J.M., Mariani A. (2012). *Nanoscale Res. Lett.,* **7(1)**, 674–680.
56. Bourlinos A.B., Geogakilas V., Zboril R., Steriotis T.A., Stubos A.K. (2009). *Small,* **5(16)**, 1841–1845.
57. Li Y., Chopra N. (2015). *JOM,* **67(1)**, 34–43.
58. Cote L.J., Kim J., Tung V.C., Luo J., Kim F., Huang J. (2011). *Pure Appl. Chem.,* **83(1)**, 95–110.
59. Zhou C., Chen S., Lou J., Wang J., Yang Q., Liu C., Huang D., Zhu T. (2014). *Nanoscale Res. Lett.,* **9(1)**, 26–34.
60. Novoselov K.S., Fal'ko V.I., Colombo L., Gellert P.R., Schwab M.G., Kim, K. (2012). *Nature*, **490**, 192.

61. Xu W.G., Xiao J.Q., Chen Y.F., Chen Y.B., Ling X., Zhang J. (2013). *Adv. Mater.*, **25**, 928.

62. Emtsev K.V., Bostwick A., Horn K., Jobst J., Kellogg G.L., Ley L., McChesney J.L., Ohta T., Reshanov S.A., Rohrl J., Rotenberg E., Schmid A.K., Waldmann D., Weber H.B., Seyller T. (2009). *Nat. Mater.*, **8**, 203.

63. (a) Zhang Y.B., Small J.P., Pontius W.V., Kim P. (2005). *Appl. Phys. Lett.*, **86**, 073104. (b) Novoselov K.S., Geim A.K., Morozov S.V., Jiang D., Zhang Y., Dubonos S.V., Grigorieva I.V., Firsov A.A. (2004). *Sci.* **306**, 666. (c) Hernandez Y., Nicolosi V., Lotya M., Blighe F.M., Sun Z.Y., De S., McGovern I.T., Holland B., Byrne M., Gun'ko Y.K., Boland J.J., Niraj P., Duesberg G., Krishnamurthy S., Goodhue R., Hutchison J., Scardaci V., Ferrari A.C., Coleman J.N. (2008). *Nat. Nanotechnol.*, **3**, 563.

64. Pei S.F., Zhao J.P., Du J.H., Ren W.C., Cheng H.M. (2010). *Carbon* **48**, 4466.

65. Chen D., Feng H., Li J. (2012). *Chem. Rev.*, **112**, 6027.

66. Zhu Y.W., Murali S., Cai W.W., Li X.S., Suk J.W., Potts J.R., Ruoff R.S. (2010). *Adv. Mater.*, **22**, 3906.

67. (a) Lee W.C., Lim C.H.Y.X., Shi H., Tang L.A.L., Wang Y., Lim C.T., Loh K.P. (2011). *ACS Nano*, **5**, 7334. (b) Sun X.M., Liu Z., Welsher K., Robinson J.T., Goodwin A., Zaric S., Dai H.J. (2008). *Nano Res.*, **1**, 203.

68. Chua C.K., Pumera M. (2014). *Chem. Soc. Rev.*, **43**, 291.

69. Dreyer D.R., Park S., Bielawski C.W., Ruoff R.S. (2010). *Chem. Soc. Rev.*, **39**, 228.

70. (a) Park S., Ruoff R.S. (2009). *Nat. Nanotechnol.*, **4**, 217 (b) Gomez-Navarro C., Weitz R.T., Bittner A.M., Scolari M., Mews A., Burghard M., Kern K. (2007). *Nano Lett.*, **7**, 3499.

71. Compton O.C., Nguyen S.T. (2010). *Small*, **6**, 711.

72. Pei S.F., Cheng H.M. (2012). *Carbon*, **50**, 3210.

73. Zhou M., Wang Y.L., Zhai Y.M., Zhai J. F., Ren W., Wang F.A., Dong S.J. (2009). *Chem. Eur. J.*, **15**, 6116.

74. (a) Schniepp H.C., Li J.L., McAllister M.J., Sai H., Herrera-Alonso M., Adamson D.H., Prud'homme R. K., Car R. , Saville D.A., Aksay I.A.J. (2006). *Phys. Chem. B*, **110**, 8535. (b) Kuila T., Mishra A.K., Khanra P., Kim N.H., Lee J.H. (2013). *Nanoscale*, **5**, 52.

75. Zhou S.Y., Gweon G.-H., Fedorov A.V., First P.N., de Heer W. A., Lee D.-H., Guinea F., Castro Neto A.H., Lanzara A. (2007). *Nat. Mater.,* **6**, 770–775.

76. Kopylov S., Tzalenchuk A., Kubatkin S., Fal'ko V.I. (2010). *Appl. Phys. Lett.,* **97**, 112109.

77. Varchon F., Feng R., Hass J., Li X., Ngoc Nguyen B., Naud C., Mallet P., Veuillen J.Y., Berger C., Conrad E.H., Magaud L. (2007). *Phys. Rev. Lett.,* **99**, 126805.
78. Mattausch A., Pankratov O. (2007). *Phys. Rev. Lett.,* **99**, 076802.
79. Giovannetti G., Khomyakov P.A., Brocks G., Karpan V.M., Brink van den J., Kelly P.J. (2008). *Phys. Rev. Lett.,* **101**, 026803.
80. Castro E.V., Novoselov K.S., Morozov S.V., Peres N.M.R., Lopes dos Santos J.M.B., Nilsson J., Guinea F., Geim A.K., Castro Neto A.H. (2007). *Phys. Rev. Lett.,* **99**, 216802.
81. Gava P., Lazzeri M., Saitta A.M., Mauri F. (2009). *Phys. Rev. B,* **79**, 165431.
82. Das A., Pisana S., Chakraborty B., Piscanec S., Saha S.K., Waghmare U.V., Novoselov K.S., Krishnamurthy H.R., Geim A.K., Ferrari A.C., Sood A.K. (2008). *Nat. Nanotech.,* **3**, 210–215.
83. Chan K.T., Neaton J.B., Cohen M.L. (2008). *Phys. Rev. B,* **77**, 235430.
84. Uchoa B., Lin C.Y., Castro Neto A.H. (2008). *Phys. Rev. B,* **77**, 035420.
85. Gierz I., Riedl C., Starke U., Ast C.R., Kern K. (2008). *Nano Lett.,* **8**, 4603–4607.
86. Loh K.P., Bao Q., Ang P.K., Yang J. (2010). *J. Mater. Chem*., **20**, 2277–2289.
87. Sun Z., Yan Z., Yao J., Beitler E., Zhu Y., Tour J.M. (2010). *Nature,* **468**, 549–552.
88. Attaccalite C., Wirtz L., Lazzeri M., Mauri F., Rubio A. (2010). *Nano Lett.,* **10**, 1172–1176.
89. Yu S., Zheng W., Wang C., Jiang Q. (2010). *ACS Nano*, **4**, 7619–7629.
90. Lherbier A., Blase X., Niquet Y.M., Triozonand F., Roche S. (2008). *Phys. Rev. Lett.,* **101**, 036808.
91. Zheng B., Hermet P., Henrard L. (2010). *ACS Nano,* **4**, 4165–4173.
92. Pontes R.B., Fazzio A., Dalpian G.M. (2009). *Phys. Rev. B,* **79**, 033412.
93. Deifallah M., McMillan P.F., Corà F. (2008). *J. Phys. Chem. C*, **112**, 5447–5453.
94. Wei D., Liu Y., Wang Y., Zhang H., Huang L., Yu G. (2009). *Nano Lett.,* **9**, 1752–1758.
95. Kim Y.A., Fujisawa K., Muramatsu H., Hayashi T., Endo M., Fujimori T., Kaneko K., Terrones M., Behrends J., Eckmann A., Casiraghi C., Novoselov K.S., Saito R., Dresselhaus M.S. (2012). *ACS Nano,* **6**, 6293–6300.
96. Tang Y.B., Yin L.C., Yang Y., Bo X.H., Cao Y.L., Wang H.E., Zhang W.J., Bello I., Lee S.T., Cheng H.M., Lee C.S. (2012). *ACS Nano,* **6**, 1970–1978.

97. Panchakarla L.S., Subrahmanyam K.S., Saha S.K., Govindaraj A., Krishnamurthy H.R., Waghmare U.V., Rao C.N.R. (2009). *Adv. Mater.,* **21**, 4726–4730.
98. Imamura G., Saiki K. (2011). *J. Phys. Chem. C*, **115**, 10000–10005.
99. Usachov D., Vilkov O., Grüneis A., Haberer D., Fedorov A., Adamchuk V.K., Preobrajenski A.B., Dudin P., Barinov A., Oehzelt M., Laubschat C., Vyalikh D.V. (2011). *Nano Lett.,* **11**, 5401–5407.
100. Jin Z., Yao J., Kittrell C., Tour J.M. (2011). *ACS Nano,* **5**, 4112–4117.
101. Luo Z., Lim S., Tian Z., Shang J., Lai L., MacDonald B., Fu C., Shen Z., Yu T., Lin J. (2011). *J. Mater. Chem.,* **21**, 8038–8044.
102. Zhao L., He R., Rim K.T., Schiros T., Kim K.S., Zhou H., Gutierrez C., Chockalingam S.P., Arguello C.J., Palova L., Nordlund D., Hybertsen M.S., Reichman., D.R., Heinz T.F., Kim P., Pinczuk A., Flynn G.W., Pasupathy A.N. (2011). *Sci.,* **333**, 999–1003.
103. Li N., Wang Z., Zhao K., Shi Z., Gu Z., Xu S. (2010). *Carbon,* **48**, 255–259.
104. Palnitkar U.A., Kashid R.V., More M.A., Joag D.S., Panchakarla L.S., Rao C.N.R. (2010). *Appl. Phys. Lett.,* **97**, 063102.
105. Wang Y., Shao Y., Matson D.W., Li J., Lin Y. (2010). *ACS Nano,* **4**, 1790–1798.
106. Soin N., Roy S.S., Roy S., Hazra K.S., Misra D.S., Lim T.H., Hetherington C.J., McLaughlin J.A. (2011). *J. Phys. Chem. C,* **115**, 5366–5372.
107. Deng D., Pan X., Yu L., Cui Y., Jiang Y., Qi J., Li W.X., Fu Q., Ma X., Xue Q., Sun G., Bao X. (2011). *Chem. Mater.,* **23**, 1188–1193.
108. Wang X., Li X., Zhang L., Yoon Y., Weber P.K., Wang H., Guo J., Dai H. (2009). **324**, 768–771.
109. Guo B., Liu Q., Chen E., Zhu H., Fang L., Gong J.R. (2010). *Nano Lett.,* **10**, 4975–4980.
110. Feng L., Chen Y., Chen L. (2011). *ACS Nano*, **5**, 9611–9618.
111. Zhang C., Fu L., Liu, N. Liu M., Wang Y., Liu Z. (2011). *Adv. Mater.,* **23**, 1020–1024.
112. Li X., Wang H., Robinson J.T., Sanchez H., Diankov G., Dai H. (2009). *J. Am. Chem. Soc.,* **131**, 15939–15944.
113. Sheng Z.H., Shao L., Chen J.J., Bao W.J., Wang F.B., Xia X.H. (2011). *ACS Nano,* **5**, 4350–4358.
114. Xue Y., Wu B., Jiang L., Guo Y., Huang L., Chen J., Tan J., Geng D., Luo B., Hu W., Yu G., Liu Y. (2012). *J. Am. Chem. Soc.,* **134**, 11060–11063.
115. Long D., Li W., Ling L., Miyawaki J., Mochida I., Yoon S. -H. (2010). *Langmuir,* **26**, 16096–16102.

116. Ci L., Song L., Jin C., Jariwala D., Wu D., Li Y., Srivastava A., Wang Z.F., Storr K., Balicas L., Liu F., Ajayan P.M. (2010). *Nat. Mater.,* **9**, 430–435.
117. Rodríguez-Manzo J.A, Cretu O., Banhart F. (2010). *ACS Nano,* **4**, 3422–3428.
118. Ugeda M.M., Brihuega I., Guinea F., Gómez-Rodríguez J.M. (2010). *Phys. Rev. Lett.,* **104**, 096804.
119. Gan Y., Sun L., Banhart F. (2008). *Small,* **4**, 587–591.
120. Banhart F., Charlier J.C., Ajayan P.M. (2000). *Phys. Rev. Lett.,* **84**, 686–689.
121. Wang H., Wang Q., Cheng Y., Li K., Yao Y., Zhang Q., Dong C., Wang P., Schwingenschlögl U., Yang W., Zhang X.X. (2012). *Nano Lett.,* **12**, 141–144.
122. Das B., Voggu R., Rout C.S., Rao C.N.R. (2008). *Chem. Commun.,* 5155–5157.
123. Voggu R., Das B., Rout C.S., Rao C.N.R. (2008). *J. Phys. Condens. Matter,* **20**, 472204.
124. Varghese N., Ghosh A., Voggu R., Ghosh S., Rao C.N.R. (2009). *J. Phys. Chem. C,* **113**, 16855–16859.
125. Lu Y.H., Chen W., Feng Y.P., He P.M. (2009). *J. Phys. Chem. B,* **113**, 2–5.
126. Sun J.T., Lu Y.H., Chen W., Feng Y.P., Wee A.T.S. (2010). *Phys. Rev. B,* **81**, 155403.
127. Chang C.H., Fan X., Li L.J., Kuo J.L. (2012). *J. Phys. Chem. C,* **116**, 13788–13794.
128. Kozlov S.M., Viñes F., Görling A. (2011). *Adv. Mater.,* **23**, 2638–2643.
129. Wehling T.O., Novoselov K.S., Morozov, S.V. Vdovin E.E., Katsnelson M.I., Geim A.K., Lichtenstein A.I. (2008). *Nano Lett.,* **8**, 173–177.
130. Manna A.K., Pati S.K. (2009). *Chem. Asian J.,* **4**, 855–860.
131. Widenkvist E., Boukhvalov D.W., Rubino S., Akhtar S., Lu J., Quinlan R.A., Katsnelson M.I., Leifer K., Grennberg H., Jansson U. (2009). *J. Phys. D: Appl. Phys.,* **42**, 112003.
132. Herbig C., Kaiser M., Bendiab N., Schumacher S., Forster D.F., Coraux J., Meerholz K., Michely T., Busse C. (2012). *J. Phys. Condens. Matter*, **24**, 314208.
133. Chen W., Chen S., Qi D.C., Gao X.Y., Wee A.T.S. (2007). *J. Am. Chem. Soc.,* **129**, 10418–10422.
134. Coletti C., Riedl C., Lee D. S., Krauss B., Patthey L., Klitzing von K., Smet J.H., Starke U. (2010). *Phys. Rev. B,* **81**, 235401.

135. Tian X., Xu J., Wang X. (2010). *J. Phys. Chem. B,* **114**, 11377–11381.
136. Pinto H., Jones R., Goss J.P., Briddon P.R. (2009). *J. Phys. Condens. Matter,* **21**, 402001.
137. Wang X., Xu J.B., Xie W., Du J. (2011). *J. Phys. Chem. C,* **115**, 7596–7602.
138. Choudhury D., Das B., Sarma D.D., Rao C.N.R. (2010). *Chem. Phys. Lett.,* **497**, 66–69.
139. Prado M.C., Nascimento R., Moura L.G., Matos M.J.S., Mazzoni M.S.C., Cancado L.G., Chacham H., Neves B.R.A. (2011). *ACS Nano,* **5**, 394–398.
140. Huang H., Chen S., Gao X., Chen W., Wee A.T.S. (2009). *ACS Nano,* **3**, 3431–3436.
141. Wang Q.H., Hersam M.C. (2009). *Nat. Chem.,* **1**, 206–211.
142. Lee B., Chen Y., Duerr F., Mastrogiovanni D., Garfunkel E., Andrei E.Y., Podzorov V. (2010). *Nano Lett.,* **10**, 2427–2432.
143. Sofo J.O., Chaudhari A.S., Barber G.D. (2007). *Phys. Rev. B,* **75**, 153401.
144. Bhattacharya A., Bhattacharya S., Majumder C., Das G.P. (2011). *Phys. Rev. B,* **83**, 033404.
145. Samarakoon D.K., Wang X.Q. (2009). *ACS Nano,* **3**, 4017–4022.
146. Dzhurakhalov A.A., Peeters F.M. (2011). *Carbon,* **49**, 3258–3266.
147. Lebègue S., Klintenberg M., Eriksson O., Katsnelson M.I. (2009). *Phys. Rev. B,* **79**, 245117.
148. Fiori G., Lebègue S., Betti A., Michetti P., Klintenberg M., Eriksson O., Lannaccone G. (2010). *Phys. Rev. B,* **82**, 153404.
149. Elias D.C., Nair R.R., Mohiuddin T.M.G., Morozov S.V., Blake P., Halsall M.P., Ferrari A.C., Boukhvalov D.W., Katsnelson M.I., Geim A.K., Novoselov K.S. (2009). *Sci.,* **323**, 610–613.
150. Balog R., Jørgensen B., Wells J., Lægsgaard E., Hofmann P., Besenbacher F., Hornekær L. (2009). *J. Am. Chem. Soc.,* **131**, 8744–8745.
151. Guisinger N.P., Rutter G.M., Crain J.N., First P.N., Stroscio J.A. (2009). *Nano Lett.*, **9**, 1462–1466.
152. Ryu S., Han M.Y., Maultzsch J., Heinz T.F., Kim P., Steigerwald M.L., Brus L.E. (2008). *Nano Lett.,* **8**, 4597–4602.
153. Jones J.D., Mahajan K.K., Williams W.H., Ecton P.A., Mo Y., Perez J.M. (2010). *Carbon,* **48**, 2335–2340.
154. Zhou J., Wang Q., Sun Q., Chen X.S., Kawazoe Y., Jena P. (2009). *Nano Lett.,* **9(11)**, 3867–3870
155. Zhou J., Wu M.M., Zhou X., Sun Q. (2009). *Appl. Phys. Lett.,* **95**, 103–108.

156. Luo Z., Yu T., Kim K., Ni Z., You Y., Lim S., Shen Z., Wang S., Lin J. (2009). *ACS Nano,* **3**, 1781–1788.

157. Leenaerts O., Partoens B., Peeters F.M. (2009). *Phys. Rev. B,* **80**, 245422.

158. Ruff O., Bretschneider O. (1934). *Z. Anorg. Allg. Chem.,* **217**, 1–18.

159. Kita Y., Watanabe N., Fujii Y. (1979). *J. Am. Chem. Soc.,* **101**, 3832–3841.

160. Charlier J.C., Gonze X., Michenaud J.P. (1993). *Phys. Rev. B,* **47**, 16162.

161. Takagi Y., Kusakabe K. (2002). *Phys. Rev. B,* **65**, 121103.

162. Zajac A., Pelikán P., Minár J., Noga J., Straka M., Banacký P, Biskupic S. (2000). *J. Solid State Chem.,* **150**, 286–293.

163. Fusaro R.L., Sliney H.E. (1970). *ASLE Trans.,* **13**, 56–65.

164. Kamarchik Jr. P., Margrave J. L. (1978). *Acc. Chem. Res.,* **11**, 296–300.

165. Robinson J.T., Burgess J.S., Junkermeier C.E., Badescu S.C., Reinecke T.L., Perkins F.K., Zalalutdniov M.K., Baldwin J.W., Culbertson J.C., Sheehan P.E., Snow E.S. (2010). *Nano Lett.,* **10**, 3001–3005.

166. Nair R.R., Ren W.C., Jalil R., Riaz I., Kravets V.G., Britnell L., Blake P., Schedin F., Mayorov A.S., Yuan S.J., Katsnelson M.I., Cheng H.M., Strupinski W., Bulusheva L.G., Okotrub A.V., Grigorieva I.V., Grigorenko A.N., Novoselov K.S., Geim A.K. (2010). *Small,* **6**, 2877–2884.

167. Jeon K., Lee Z., Pollak E., Moreschini L., Bostwick A., Park C., Mendelsberg R., Radmilovic V., Kostecki R., Richardson T.J., Rotenberg E. (2011). *ACS Nano,* **5**, 1042–1046.

168. Cheng S.H., Zou K., Okino F., Gutierrez H.R., Gupta A., Shen N., Eklund P.C., Sofo J.O., Zhu J. (2010). *Phys. Rev. B,* **81**, 205435.

169. Withers F., Dubois M., Savchenko A.K. (2010). *Phys. Rev. B,* **82**, 073403.

170. Zbořil R., Karlický F., Bourlinos A.B., Steriotis T.A., Stubos A.K., Georgakilas V., Šafářová K., Jančík D., Trapalis C., Otyepka M. (2010). *Small*, **6**, 2885–2891.

171. Bourlinos A.B., Safarova K., Siskova K., Zbořil R. (2012). *Carbon,* **50**, 1425–1428.

172. Karlický F., Zbořiland R., Otyepka M. (2012). *J. Chem. Phys.,* **137**, 034709.

173. Chang H., Cheng J., Liu X., Gao J., Li M., Li J., Tao X., Ding F., Zheng Z . (2011). *Chem. Eur. J.,* **17**, 8896–8903.

174. Hirsch A. (2010). *Nat. Mater.,* **9**, 868–871.

175. Enyashin A.N., Ivanovskii A.L. (2011). *Phys. Status Solidi B,* **248**, 1879–1883.

176. Haley M.M. (2008). *Pure Appl. Chem.,* **80**, 519–532.

177. Kehoe J.M., Kiley J.H., English J.J., Johnson C.A., Petersen R.C., Haley M.M. (2000). *Org. Lett.,* **2**, 969–972.

178. Yoshimura T., Inaba A., Sonoda M., Tahara K., Tobe Y., Williams R.V. (2006). *Org. Lett.,* **8**, 2933–2936.

179. Li G., Li Y., Liu H., Guo Y., Li Y., Zhu D. (2010). *Chem. Commun.,* **46**, 3256–3258.

180. Liu H., Xu J., Li Y., Li Y. (2010). *Acc. Chem. Res.,* **43**, 1496–1508.

181. Li G., Li Y., Qian X., Liu H., Lin H., Chen N., Li Y. (2011). *J. Phys. Chem. C,* **115**, 2611–2615.

182. Qian X., Ning Z., Li Y., Liu H., Ouyang C., Chen Q., Li Y. (2012). *Dalton Trans.,* **41**, 730–733.

183. Xu P.T., Yang J.X., Wang K.S., Zhou Z., Shen P. W. (2012). *Chin. Sci. Bull.,* **57**, 2948–2955.

184. Fischbein, M.D., Drndić, M. (2008). *Appl. Phys. Lett.*, **93**, 113107.

185. Merchant C.A., Healy K., Wanunu M., Ray V., Peterman N., Bartel J., Fischbein M.D., Venta K., Luo Z., Charlie Johnson A.T., Drndić M. (2010). *Nano Lett.,* **10**, 2915–2921.

186. Hashimoto A., Suenaga K., Gloter A., Urita K., Iijima S. (2004). *Nature*, **430**, 870–873.

187. Wang X., Li X., Zhang L., Yoon Y., Weber P.K., Wang H., Guo J., Dai H. (2009). *Science,* **324**, 768–771.

188. Kuhn P., Forget A., Su D., Thomas A., Antonietti M. (2008). *J. Am. Chem. Soc.,* **130**, 13333–13337.

189. Chen L., Honsho Y., Seki S., Jiang D. (2010). *J. Am. Chem. Soc.,* **132**, 6742–6748.

190. Bieri M., Treier M., Cai J., Aït-Mansour K., Ruffieux P., Gröning O., Gröning P., Kastler M., Rieger R., Feng X., Müllen K., Fasel R. (2009). *Chem. Commun.,* 6919–6921.

191. Kong B.S., Geng J.X., Jung H.T. (2009). *Chem. Commun.,* **16**, 2174.

192. (a) Muszynski R., Seger B., Kamat, P.V. (2008). *J. Phys. Chem. C*, **112**, 5263. (b) Goncalves G., Marques P.A.A.P., Granadeiro C.M., Nogueira H.I.S., Singh M.K. (2009). *J. Chem. Mater.*, **21**, 4796. (c) Hong W.J., Bai H., Xu Y.X., Yao Z.Y., Gu Z.Z., Shi G.Q. (2010). *J. Phys. Chem. C*, **114**, 1822.

193. Tien H.W., Huang Y.L., Yang S.Y., Wang J.Y., Ma C.C.M. (2011). *Carbon*, **49**, 1550.

194. (a) Qiu J.D., Wang G.C., Liang R.P., Xia X.H., Yu H.W. (2011). *J. Phys. Chem. C*, **115**, 15639. (b) Li Y.J., Gao W., Ci L.J., Wang C.M., Ajayan P.M. (2010). *Carbon*, **48**, 1124.

195. (a) Lin J., Raji A.R.O., Nan K.W., Peng Z.W., Yan Z., Samuel E.L.G., Natelson D., Tour J.M. (2014). *Adv. Funct. Mater.*, **24**, 2044. (b) Yang X., Chen C.L., Li J.X., Zhao G.X., Ren X.M., Wang X.K. (2012). *RSC Adv.*, **2**, 8821.

196. Liang Y.Y., Wang H.L., Casalongue H.S., Chen Z., Dai H.J. (2010). *Nano. Res.*, **3**, 701.

197. (a) Kim Y.J., Lee J.H., Yi G.C. (2009). *Appl. Phys. Lett.*, **95**, 73701. (b) Son D.I., Kwon B.W., Park D.H., Seo W.S., Yi Y., Angadi B., Lee C.L., Choi W.K. (2012). *Nat. Nanotechnol.*, **7**, 465.

198. (a) Lin J., Peng Z., Xiang C., Ruan G., Yan Z., Natelson D., Tour J.M. (2013). *ACS Nano*, **7**, 6001. (b) Su D.W., Ahn H.J., Wang G.X. (2013). *Chem. Commun.*, **49**, 3131.

199. (a) Deng S., Tjoa V., Fan H.M., Tan H.R., Sayle D.C., Olivo M., Mhaisalkar S., Wei J., Sow C.H. (2012). *J. Am. Chem. Soc.*, **134**, 4905. (b) Li B.J., Cao H.Q., Yin G., Lu Y.X., Yin, J.F. (2011). *J. Mater. Chem.*, **21**, 10645.

200. (a) Peng L.L., Peng X., Liu B.R., Wu C.Z., Xie Y., Yu G.H. (2013). *Nano Lett.*, **13**, 2151. (b) He Y., Chen W., Li X., Zhang Z., Fu J., Zhao C., Xie E. (2013). *ACS Nano*, **7**, 174.

201. (a) Zhou G.M., Wang D.W., Yin L.C., Li N., Li F., Cheng H.M. (2012). *ACS Nano*, **6**, 3214. (b) Yang H.B., Guai G.H., Guo C.X., Song Q.L., Jiang S.P., Wang Y.L., Zhang W., Li C.M. (2011). *J. Phys. Chem. C*, **115**, 12209.

202. (a) Xu C., Wang X., Zhu J.W. (2008). *J. Phys. Chem. C*, 112, 19841. (b) Chen Y., Li Y., Sun D., Tian D.B., Zhang J.R., Zhu J.J. (2011). *J. Mater. Chem.*, **21**, 7604.

203. Gao W., Alemany L.B., Ci L.J., Ajayan P.M. (2009). *Nat. Chem.*, **1**, 403.

204. Zhuo Q.Q., Ma Y.Y., Gao J., Zhang P.P., Xia Y.J., Tian Y.M., Sun X.X., Zhong J., Sun X.H. (2013). *Inorg. Chem.*, **52**, 3141.

205. Jain P.K., Huang X.H., El-Sayed I.H., El-Sayed M.A. (2008). *Acc. Chem. Res.*, **41**, 1578.

206. (a) Eustis S., El-Sayed M.A. (2006). *Chem. Soc. Rev.*, **35**, 209. (b) Liao H.W., Nehl C.L., Hafner J.H. (2006). *Nanomedicine*, **1**, 201.

207. (a) Duch M.C., Budinger G.R.S., Liang Y.T., Soberanes S., Urich D., Chiarella S.E., Campochiaro L.A., Gonzalez A., Chandel N.S., Hersam M.C., Mutlu G.M. (2011). *Nano Lett.*, **11**, 5201. (b) Huang J., Zhang L.M., Chen B.A., Ji N., Chen F.H., Zhang Y., Zhang Z.J. (2010). *Nanoscale*, **2**, 2733.

208. Zhang H., Hines D., Akins D.L. (2014). *Dalton Trans.*, **43**, 2670.
209. (a) Lim E.J., Choi S.M., Seo M.H., Kim Y., Lee S., Kim W.B. (2013). *Electrochem. Commun.*, **28**, 100. (b) Wang Y., Li S.S., Yeh Y.C., Yu C.C., Chen H.L., Li F.C., Chang Y.M., Chen C.W. (2013). *Nanoscale*, **5**, 1687.
210. (a) Subrahmanyam K.S., Manna A. K., Pati S.K., Rao C.N.R. (2010). *Chem. Phys. Lett.*, **497**, 70. (b) Li Y.M., Tang L.H., Li J.H. (2009). *Electrochem. Commun.*, **11**, 846. (c) Seger B., Kamat P.V. (2009). *J. Phys. Chem. C*, **113**, 7990.
211. (a) Zhang S., Shao Y.Y., Liao H.G., Liu J., Aksay I.A., Yin G.P., Lin Y.H. (2011). *Chem. Mater.*, **23**, 1079. (b) Yang P., Jin S.Y., Xu Q.Z., Yu S.H. (2013). *Small*, **9**, 199. (c) Wang R., Wu Z., Chen C., Qin Z., Zhu H., Wang G., Wang H., Wu C., Dong W., Fan W., Wang J. (2013). *Chem. Commun.*, **49**, 8250. (d) Gao L.N., Yue W.B., Tao S.S., Fan L.Z. (2013). *Langmuir*, **29**, 957.
212. Guo S.J., Dong S.J., Wang E.K. (2010). *ACS Nano*, **4**, 547.
213. (a) Guo S.J., Dong S.J., Wang E.K. (2009). *J. Phys. Chem. C*, **113**, 5485. (b) Guo S.J., Wang L., Dong S.J., Wang E.K. (2008). *J. Phys. Chem. C*, **112**, 13510.
214. Jasuja K., Linn J., Melton S., Berry V. (2010). *J. Phys. Chem. Lett. C*, **1**, 1853.
215. Han Y.J., Luo Z.M., Yuwen L.H., Tian J., Zhu X.R., Wang L.H. (2013). *Appl. Surf. Sci.*, **266**, 188.
216. Kundu P., Nethravathi C., Deshpande P.A., Rajamathi M., Madras G., Ravishankar N. (2011). *Chem. Mater.*, **23**, 2772.
217. Chen S.Q., Wang Y.J. (2010). *Mater. Chem.*, **20**, 9735.
218. Tsuji M., Hashimoto M., Nishizawa Y., Tsuji T. (2004). *Mater. Lett.*, **58**, 2326.
219. Bai S., Shen X. (2012). *RSC Adv.*, **2**, 64.
220. Zhou Y., Bao Q.L., Tang L.A.L., Zhong Y.L., Loh K.P. (2009). *Chem. Mater.*, **21**, 2950.
221. (a) Zou W.B., Zhu J.W., Sun Y.X., Wang X. (2011). *Mater. Chem. Phys.*, **125**, 617. (b) Wu J.L., Shen X.P., Jiang L., Wang K., Chen K.M. (2010). *Appl. Surf. Sci.*, **256**, 2826. (c) Saravanakumar B., Mohan R., Kim S.J. (2013). *Mater. Res. Bull.*, **48**, 878.
222. (a) Shen J.F., Shi M., Yan B., Ma H.W., Li N., Ye M.X. (2011). *Nano Res.*, **4**, 795. (b) Shen J.F., Yan B., Shi M., Ma H.W., Li N., Ye M.X. (2011). *J. Mater. Chem.*, **21**, 3415. (c) Perera S.D., Mariano R.G., Vu K., Nour N., Seitz O., Chabal Y., Balkus K.J. (2012). *ACS Catal.*, **2**, 949.

223. (a) Zhou K.F., Zhu Y.H., Yang X.L., Li C.Z. (2011). *Electroanalysis,* **23**, 862. (b) Castrillon M., Mayoral A., Urtizberea A., Marquina C., Irusta S., Meier J.G., Santamaria J. (2013). *Nanotechnology,* **24**, 505702.

224. (a) Huang X.D., Zhou X.F., Zhou L., Qian K., Wang Y.H., Liu Z.P., Yu C.Z. (2011). *Chem. Phys. Chem.*, **12**, 278. (b) Park S.K., Yu R.H., Pinna N., Woo S., Jang B., Chung Y.H., Cho Y.H., Sung Y.E., Piao Y.J. (2012). *Mater. Chem.*, **22**, 2520.

225. (a) Wu Z.S., Wang D.W., Ren W., Zhao J., Zhou G., Li F., Cheng H.M. (2010). *Adv. Funct. Mater.*, **20**, 3595. (b) Wu Z.S., Ren W.C., Wen L., Gao L.B., Zhao J.P., Chen Z.P., Zhou G.M., Li F., Cheng H.M. (2010). *ACS Nano*, **4**, 3187.

226. Wu Z.S., Zhou G.M., Yin L.C., Ren W., Li F., Cheng H.M. (2012). *Nano Energy*, **1**, 107.

227. Ren L.L., Huang S., Fan W., Liu T.X. (2011). *Appl. Surf. Sci.*, **258**, 1132.

228. Yan S.C., Shi Y., Zhao B., Lu T., Hu D., Xu X., Wu J.S., Chen J.S. (2013). *J. Alloys Compd.*, **570**, 65.

229. Xue L.P., Shen C.F., Zheng M.B., Lu H.L., Li N.W., Ji G.B., Pan L.J., Cao J.M. (2011). *Mater. Lett.*, **65**, 198.

230. Su Y.J., Lu X.N., Xie M.M., Geng H.J., Wei H., Yang Z., Zhang Y.F. (2013). *Nanoscale*, **5**, 8889.

231. (a) Chang K., Chen W.X. (2011). *J. Mater. Chem.*, **21**, 17175. (b) Huang G.C., Chen T., Chen W.X., Wang Z., Chang K., Ma L., Huang F.H., Chen D.Y., Lee J.Y. (2013). *Small*, **9**, 3693.

232. Yuan C.Z., Hou L.R., Yang L., Fan C.G., Li D.K., Li J.M., Shen L.F., Zhang F., Zhang X.G. (2011). *Mater. Lett.*, **65**, 374.

233. Lu Z.S., Guo C.X., Yang H.B., Qiao Y., Guo J., Li C.M. (2011). *J. Colloid Interface Sci.*, **353**, 588.

234. Medintz I.L., Uyeda H.T., Goldman E.R., Mattoussi H. (2005). *Nat. Mater.*, **4**, 435.

235. Resch-Genger U., Grabolle M., Cavaliere-Jaricot S., Nitschke R., Nann T. (2008). *Nat. Methods*, **5**, 763.

236. (a) Jasieniak J., Smith L., Embden van J., Mulvaney P., Califano M. (2009). *J. Phys. Chem. C*, **113**, 19468. (b) Yu W.W., Qu L.H., Guo W.Z., Peng X.G. (2003). *Chem. Mater.*, **15**, 2854.

237. (a) Alivisatos P. (2004). *Nat. Biotechnol.*, **22**, 47. (b) Niemeyer C.M. (2001). *Angew. Chem. Int. Ed.*, **40**, 4128. (c) Kim J.Y., Voznyy O., Zhitomirsky D., Sargent E.H. (2013). *Adv. Mater.*, **25**, 4986.

238. Zhang N., Zhang Y. H., Pan X.Y., Fu X.Z., Liu S.Q., Xu Y.J. (2011). *J. Phys. Chem. C*, **115**, 23501.

239. (a) Shen J.F., Shi M., Yan B., Ma H.W., Li N., Ye M.X. (2011). *J. Mater. Chem.*, **21**, 7795. (b) Zhou X.Z., Huang X., Qi X.Y., Wu S.X., Xue C., Boey F.Y.C., Yan Q.Y., Chen P., Zhang H. (2009). *J. Phys. Chem. C*, **113**, 10842.

240. Zhang H., Chen S., Quan X., Yu H.T., Zhao H.M. (2011). *J. Mater. Chem.*, **21**, 12986.

241. Lee S.H., Kakati N., Jee S.H., Maiti J., Yoon Y.S. (2011). *Mater. Lett.*, **65**, 3281.

242. (a) Bijani S., Martinez L., Gabas M., Dalchiele E.A., Ramos-Barrado J.R. (2009). *J. Phys. Chem. C*, **113**, 19482. (b) Therese G.H.A., Kamath P.V. (2000). *Chem. Mater.*, **12**, 1195.

243. (a) Ding L., Liu Y.P., Zhai J.P., Bond A.M., Zhang J. (2014). *Electroanalysis,* **26**, 121. (b) Hu Y.J., Jin J.A., Wu P., Zhang H., Cai C.X. (2010). *Electrochim. Acta*, **56**, 491.

244. Golsheikh A.M., Huang N.M., Lim H.N., Zakaria R., Yin C.Y. (2013). *Carbon*, **62**, 405.

245. (a) Zhou Y.G., Chen J.J., Wang F.B., Sheng Z.H., Xia X.H. (2010). **46**, 5951. (b) Claussen J.C., Kumar A., Jaroch D.B., Khawaja M.H., Hibbard A.B., Porterfield D.M., Fisher T.S. (2012). *Adv. Funct. Mater.*, **22**, 3399.

246. Wu S.X., Yin Z.Y., He Q.Y., Lu G., Yan Q.Y., Zhang H. (2011). *J. Phys. Chem. C*, **115**, 15973.

247. Han K.H., Tao M. (2009). *Sol. Energy Mater. Sol. Cells*, **93**, 153.

248. Wu S.X., Yin Z.Y., He Q.Y., Lu G., Zhou X.Z., Zhang H.J. (2011). *Mater. Chem.*, **21**, 3467.

249. Wu S.X., Yin Z.Y., He Q.Y., Huang X.A., Zhou X.Z., Zhang H. (2010). *J. Phys. Chem. C*, **114**, 11816.

250. (a) He F.A., Fan J.T., Song F., Zhang L.M., Chan H.L.W. (2011). *Nanoscale*, **3**, 1182. (b) Yang X., Xu M.S., Qiu W.M., Chen X.Q., Deng M., Zhang J.L., Iwai H., Watanabe E., Chen H.Z. (2011). *J. Mater. Chem.*, **21**, 8096.

251. He F.A., Fan J.T., Ma D., Zhang L.M., Leung C., Chan H.L. (2010). *Carbon*, **48**, 3139.

252. Pham T.A., Choi B.C., Jeong Y.T. (2010). *Nanotechnology,* **21**, 465603.

253. Herron N., Wang Y., Eckert H. (1990). *J. Am. Chem. Soc.*, **112**, 1322.

254. Ismaili H., Geng D., Sun A. X., Kantzas T.T., Workentin M. S. (2011). *Langmuir*, **27**, 13261.

255. Bjork J., Hanke F., Palma C.A., Samori P., Cecchini M., Persson M.J. (2010). *Phys. Chem. Lett.*, **1**, 3407.

256. Wang W., Guo S.R., Penchev M., Zhong J.B., Lin J., Bao D.D., Vullev V., Ozkan M., Ozkan C.S. (2012). *J. Nanosci. Nanotechnol.*, **12**, 6913.

257. Zhang X.R., Li S.G., Jin X., Zhang S.S. (2011). *Chem. Commun.*, **47**, 4929.

258. Bourlinos A.B., Georgakilas V., Zboril R., Steriotis T.A., Stubos A.K. (2009). *Small*, **5**, 1841.

259. (a) Lin Y., Zhang K., Chen W.F., Liu Y.D., Geng Z.G., Zeng J., Pan N., Yan L.F., Wang X.P., Hou J.G. (2010). *ACS Nano*, **4**, 3033. (b) Geng X.M., Niu L., Xing Z.Y., Song R.S., Liu G.T., Sun M.T., Cheng G.S., Zhong H.J., Liu Z.H., Zhang Z.J., Sun L.F., Xu H.X., Lu L., Liu L.W. (2010). *Adv. Mater.*, **22**, 638.

260. Geng X.M., Niu L., Xing Z.Y., Song R.S., Liu G.T., Sun M.T., Cheng G.S., Zhong H.J., Liu Z.H., Zhang Z.J., Sun L.F., Xu H.X., Lu L., Liu L.W. (2010). *Adv. Mater*., **22**, 638.

261. Liu J., Li Y., Li Y., Li J., Deng Z. (2010). *J. Mater. Chem.*, **20**, 900.

262. Wang Y., Zhen S.J., Zhang Y., Li Y.F., Huang C.Z. (2011). *J. Phys. Chem. C*, **115**, 12815.

263. Zhu G.X., Liu Y.J., Xu Z., Jiang T.A., Zhang C., Li X., Qi G. (2010). *Chem. Phys. Chem.*, **11**, 2432.

264. Zhai D., Li B., Gao G., Gan L., He Y. (2012). *Carbon*, **50(14)**, 5034.

265. Lu G.H., Mao S., Park S., Ruoff R.S., Chen J.H. (2009). *Nano Res.*, **2**, 192.

266. (a) Jiang T., Kuila T., Kim, N.H., Ku B.C., Lee J.H. (2013). *Compos. Sci. Technol.*, **79**, 115. (b) Myung S., Solanki A., Kim C., Park J., Kim K.S., Lee K.B. (2011). *Adv. Mater.*, **23**, 2221. (c) Howarter J.A., Youngblood J.P. (2006). *Langmuir*, **22**, 11142.

267. Liu J.B., Fu S.H., Yuan B., Li Y.L., Deng Z.X. (2010). *J. Am. Chem. Soc.*, **132**, 7279.

268. Li J.H., Kuang D.Z., Feng Y.L., Zhang F.X., Xu Z.F., Liu M.Q., Wang D.P. (2013). *Biosens. Bioelectron.,* **42**, 198.

269. Sarkar J., Ghosh P., Adil A. (2015). *Renew. Sust. Ener. Rev.*, **43**, 164–177.

270. Singh V., Joung D., Zhai L., Das S., Khondaker S.I., Seal S. (2011). *Prog. Mater. Sci.*, **56**, 1178–1271.

271. Huang X., Yin Z., Wu S., Qi X., He Q., Zhang Q., Yan Q., Boey F., Zhang H. (2011). *Small*, **7(14)**, 1876–1902.

272. Rao C.N.R., Subrahmanyam K.S., Ramakrishna Matte H.S.S., Govindaraj A., *Graphene: Synthesis, functionalization and properties.* Available at http://www.worldscibooks.com/physics/7989.html

273. Ferrari A.C., Bonaccorso F., Fal'ko V., Novoselov K.S., Roche S., Bøggild P., Borini S., Koppens F.H.L., Palermo V., Pugno N., Garrido J.A., Sordan R., Bianco A., Ballerini L., Prato M., Lidorikis E., Kivioja J., Marinelli C., Ryhänen T., Morpurgo A., Coleman J.N., Nicolosi V., Colombo L., Fert A., Hernandez M.G., Bachtold A., Schneider G.F., Guinea F., Dekker C., Barbone M., Sun Z., Galiotis C., Grigorenko A.N., Konstantatos G., Kis A., Katsnelson M., Vandersypen L., Loiseau A., Morandi V., Neumaier D., Treossi E., Pellegrini V., Polini M., Tredicucci A., Williams G.M., Hong B.H., Ahn J.H., Kim J.M., Zirath H., Wees van B.J., Zant van der H., Occhipinti L., Di Matteo A., Kinloch I.A., Seyller T., Quesnel E., Feng X., Teo K., Rupesinghe N., Hakonen P., Neil S.R.T., Tannock Q., Löfwander T., Kinare J. (2015). *Nanoscale*, **7**, 4598.
274. El Mel A.A., Duvail J.L., Gautron E., Xu W., Choi C.H., Angleraud B., Granier A., Tessier P.Y. (2012). *Beilstein J. Nanotechnol.*, **3**, 846–851.
275. Cong H.P., Chen J.F., Yu S.H. (2014). *Chem. Soc. Rev.*, **43**, 7295–7325.
276. Kim H., Abdala A.A., Macosko C.W. (2010). *Macromolecules*, **43**, 6515–6530.
277. Kuilla T., Bhadra S., Yaoa D., Kim N.H., Bose S., Leea J.H. (2010). *Prog. Polym. Sci.*, **35**, 1350–1375.
278. Information available at http://www.nanowerk.com/news2/newsid=32603.php
279. Galpaya D., Wang M., Liu M., Motta N., Waclawik E., Yan C. (2012). *Graphene*, **1**, 30–49.
280. Das S., Wajid A.S., Shelburne J.L., Liao Y.C., Green M.J. (2011). *ACS Appl. Mater. Interf.,* **3(6)**, 1844–1851.
281. Paul D.R., Robeson L.M. (2008). *Polymer*, **49**, 3187–3204.
282. Chao Z., Xi L.T. (2012). *Chin. Sci. Bull.*, **57(23)**, 3010–3021.
283. Das T.K., Prusty S. (2013). *Polym. Plast. Technol. Eng.*, **52**, 319–331.
284. Potts J.R., Dreyer D.R., Bielawski C.W., Ruoff R.S. (2011). *Polymer*, **52**, 5–25.
285. Feng L., Guan G., Li C., Zhang D., Xiao Y., Zheng L., Zhu W. (2013). *J. Macromol. Sci. A*, **50**, 720–727.
286. Ha H.W., Choudhury A., Kamal T., Kim D.H., Park S.Y. (2012). *ACS App. Mater. Interf.*, **4**, 4623–4630.
287. Yoonessi M., Shi Y., Scheiman D.A., Colon M.L., Tigelaar D.M. (2012). *ACS Nano*, **6(9)**, 7644–7655.
288. Vickery J.L., Patil A.J., Mann S. (2009). *Adv. Mater.*, **21**, 2180–2184.

289. Bernard C., Nguyen T., Pellegrin B., Holbrook R.D., Zhao M., Chin J. (2011). *J. Phys. Conference Series*, **304**, 012063.
290. Denga C., Wua J., Cheng R., Menga F., Klok H.A., Zhong Z. (2014). *Prog. Polym. Sci.*, **39**, 330–364.
291. Agnoli S., Granozzi G. (2013). *Surf. Sci.*, **609**, 1–5.
292. Li G.L. (2010). *J. Phys. Chem. C,* **114(29)**, 12742–12747.
293. Mikhailov S., *Physics and Applications of Graphene - Experiments* ISBN: 978-953-307-217-3, InTech, Available from: http://dx.doi.org/10.5772/14422
294. Wang H., Robinson J.T., Diankov G., Dai H. (2010). *J. Am. Chem. Soc.*, **132**, 3270.
295. Williams G., Seger B., Kamat P.V. (2008). *ACS Nano*, **2**, 1487.
296. Chen S., Zhu J., Huang H., Zeng G., Nie F., Wang X. (2010). *J. Solid State Chem.*, **183**, 2552–2557.
297. Yang S., Feng X., Ivanovici S., Müllen K. (2010). *Angew. Chem. Int. Ed.*, **49**, 8408.
298. Yang S., Feng X., Ivanovici S., Müllen K. (2010). *Angew. Chem. Int. Ed.*, **49**, 8408.
299. Lee J.K., Smith K.B., Hayner C.M., Kung H.H. (2010). *Chem. Commun.*, **46**, 2025.
300. Zhang J., Zhu Z.P., Tang Y.P., Feng X.L. (2013). *J. Mater. Chem. A*, **1**, 3752.
301. Ji G., Ding B., Sha Z., Wu J.S., Ma Y., Lee J.Y. (2013). *Nanoscale*, **5**, 5965.
302. Lin S.X., Shen C.M., Lu D.B., Wang C.M., Gao H.J. (2013). *Carbon*, **53**, 112.
303. Kawasaki H., Nakai K., Arakawa R., Athanassiou E.K., Grass R.N., Stark W. (2012). *J. Anal. Chem.*, **84**, 9268.
304. Myung S., Yin P.T., Kim C., Park J., Solanki A., Reyes P.I., Lu Y.C., Kim K.S., Lee K. B. (2012). *Adv. Mater.*, **24**, 6081.
305. Zhou M., Cai T.W., Pu F., Chen H., Wang Z., Zhang H.Y., Guan S.Y. (2013). *ACS Appl. Mater. Interf.,* **5**, 3449.
306. Luo J.Y., Zhao X., Wu J.S., Jang H.D., Kung H.H., Huang J.X. (2012). *J. Phys. Chem. Lett.*, **3**, 1824.
307. Son Y., Cohen M.L., Louie S.G. (2006). *Nature,* **444**, 347–349.
308. Dutta S., Pati S.K. (2008). *J. Phys. Chem. B,* **112**, 1333–1335.
309. Kan E.J., Li Z., Yang J., Hou J. G. (2007). *Appl. Phys. Lett.,* **91**, 243116.
310. Guo Y., Guo W., Chen C. (2010). *J. Phys. Chem. C,* **114**, 13098–13105.
311. Kan E., Li Z., Yang J., Hou J. G. (2008). *J. Am. Chem. Soc.,* **130**, 4224–4225.

312. Wu M., Wu X., Zeng X.C. (2010). *J. Phys. Chem. C,* **114**, 3937–3944.
313. Wu M., Wu X., Gao Y., Zeng X.C. (2009). *Appl. Phys. Lett.,* **94**, 223111.
314. Cantele G., Lee Y.S., Ninno D., Marzari N. (2009). *Nano Lett.,* **9**, 3425–3429.
315. Ramasubramaniam A. (2010). *Phys. Rev. B,* **81**, 245413.
316. Gunlycke D., Li J., Mintmire J.W., White C.T. (2007). *Appl. Phys. Lett.,* **91**, 112108.
317. Hod O., Barone V., Peralta J.E., Scuseria G.E. (2007). *Nano Lett.*, **7**, 2295–2299.
318. Lee G., Cho K. (2009). *Phys. Rev. B,* **79**, 165440.
319. Cervantes-Sodi F., Csányi G., Piscanec S., Ferrari A.C. (2008). *Phys. Rev. B,* **77**, 165427.
320. Yan Q., Huang B., Yu J., Zheng F., Zang J., Wu, J. Gu B.L., Liu F., Duan W. (2007). *Nano Lett.,* **7**, 1469–1473.
321. Wang Z., Hu H., Zeng H. (2010). *Appl. Phys. Lett.,* **96**, 243110.
322. Jaiswal N.K., Srivastava P. (2012). *Solid State Commun.,* **152**, 1489–1492.
323. Lisenkov S., Andriotis A.N., Menon M. (2012). *Phys. Rev. Lett.,* **108**, 187208.
324. Biel B., Blase X., Triozonand F., Roche S. (2009). *Phys. Rev. Lett.,* **102**, 096803.
325. Martins T.B., Miwa R.H., Silva da A.J.R., Fazzio A. (2007). *Phys. Rev. Lett.,* **98**, 196803.
326. Li Y., Zhou Z., Shen P., Chen Z. (2009). *ACS Nano,* **3**, 1952–1958.
327. Dutta S., Manna A. K., Pati S. K. (2009). *Phys. Rev. Lett.,* **102**, 096601.
328. Kan E., Wu X., Li Z., Zeng X. C., Yang J., Hou J. G. (2008). *J. Chem. Phys.,* **129**, 084712.
329. Liu Y., Wu X., Zhao Y., Zeng X. C., Yang J. (2011). *J. Phys. Chem. C,* **115**, 9442–9450.
330. Yu Z., Hu M.L., Zhang C.X., He C.Y., Sun L.Z., Zhong J. (2011). *J. Phys. Chem. C,* **115**, 10836–10841.
331. Ding Y., Wang Y., Ni J. (2009). *Appl. Phys. Lett.,* **95**, 123105.
332. Dong J.C., Li H. (2012). *J. Phys. Chem. C,* **116**, 17259–17267.
333. Rigo V.A., Martins T.B., Silva da A.J.R., Fazzio A., Miwa R.H. (2009). *Phys. Rev. B,* **79**, 075435.

334. Sevinçli H., Topsakal M., Durgun E., Ciraci S. (2008). *Phys. Rev. B,* **77**, 195434.
335. Brito W.H., Miwa R.H. (2010). *Phys. Rev. B,* **82**, 045417.
336. Kan E., Xiang H., Wu F., Lee C., Yang J., Whangbo M.H. (2010). *Appl. Phys. Lett.,* **96**, 102503.
337. Wang H., Li K., Cheng Y., Wang Q., Yao Y., Schwingenschlogl U., Zhang X., Yang W. (2012). *Nanoscale,* **4**, 2920–2925.
338. Huang B., Li Z., Liu Z., Zhou G., Hao S., Wu, J. Gu B., Duan W. (2008). *J. Phys. Chem. C,* **112**, 13442–13446.
339. Nduwimana A., Wang X.Q. (2009). *ACS Nano,* **3**, 1995–1999.
340. Dalosto S.D., Levine Z. H. (2008). *J. Phys. Chem. C,* **112**, 8196–8199.
341. Lee Y.L., Kim S., Park C., Ihm J., Son Y.W. (2010). *ACS Nano*, **4**, 1345–1350.
342. Shim S.H., Kim K.T., Lee J.U., Jo W.H. (2012). *ACS Appl. Mater. Interf.,* **4**, 4184–4191.
343. Liu Z., Xu Y., Zhang X., Zhang X., Chen Y., Tian J. (2009). *J. Phys. Chem. B,* **113**, 9681–9686.
344. Veca L.M., Lu F., Meziani M.J., Cao L., Zhang P., Qi G., Qu L., Shrestha M., Sun Y. (2009). *Chem. Commun.,* 2565–2567.
345. Yang H., Shan C., Li F., Han D., Zhang Q., Niu L. (2009). *Chem. Commun*., **26**, 3880.
346. Yang H., Li F., Shan C., Han D., Zhang Q., Niu L., Ivaska A. (2009). *J. Mater. Chem.,* **19**, 4632–4638.
347. Burress J.W., Gadipelli S., Ford J., Simmons J.M., Zhou W., Yildirim T. (2010). *Angew. Chem*., **49(47)**, 8902–8904.
348. Zhang L., Xia J., Zhao Q., Liu L., Zhang Z. (2010). *Small,* **6**, 537–544.
349. Liu Z., Robinson J.T., Sun X., Dai H. (2008). *J. Am. Chem. Soc.,* **130**, 10876–10877.
350. Peng C., Hu W., Zhou Y., Fan C., Huang Q. (2010). *Small,* **6**, 1686–1692.
351. Wang H.B., Zhang Q., Chu X., Chen T.T., Geand J., Yu R.Q. (2011). *Angew. Chem. Int. Ed.,* **50**, 7065–7069.
352. Jung J.H., Cheon D.S., Liu F., Lee K.B., Seo T.S. (2010). *Angew. Chem. Int. Ed.,* **49**, 5708–5711.
353. He S., Song B., Li D., Zhu C., Qi W., Wen Y., Wang L., Song S., Fang H., Fan C. (2010). *Adv. Funct. Mater.,* **20**, 453–459.
354. Bi S., Zhao T., Luo B. (2012). *Chem. Commun.,* **48**, 106–108.
355. Morales-Narváez E., Merkoçi A. (2012). *Adv. Mater.,* **24**, 3298–3308.

356. Yang X., Zhang X., Liu Z., Ma Y., Huang Y., Chen Y. (2008). *J. Phys. Chem. C*, **112**, 17554–17558.

357. Lu C.-H., Yang H.-H., Zhu C.-L., Chen X., Chen G.-N. (2009). *Angew. Chem. Int. Ed.,* **48**, 4785–4787.

358. Wang Y., Li Z., Hu D., Lin C.-T., Li J., Lin Y. (2010). *J. Am. Chem. Soc.,* **132**, 9274–9276.

359. Wang L., Lee K., Sun Y., Lucking M., Chen Z., Zhao J.J., Zhang S. B. (2009). *ACS Nano,* **3**, 2995–3000.

360. Li F., Zhao J., Chen, Z. (2012). *J. Phys. Chem. C,* **116**, 2507–2514.

361. Sun Z.Z., Pint C.L., Marcano D.C., Zhang C.G., Yao J., Ruan G.D., Yan Z., Zhu Y., Hauge R.H., Tour J.M. (2011). *Nat. Commun.,* **2**, 559.

362. Rana V.K., Choi M.C., Kong J.Y., Kim G.Y., Kim M.J., Kim S.H., Mishra S., Singh R.P., Ha C.S. (2011). *Macromol. Mater. Eng.,* **296(2)**, 131–140.

363. Rana V.K., Akhtar S., Chatterjee S., Mishra S., Singh R.P., Ha C.S. (2014). *J. Nanosci. Nanotechnol.,* **14(3)**, 2425–2435.

Chapter 3

Characteristic Properties

Graphene is known as conductive nanofiller due to remarkable and excellent characteristic properties such as high surface area, aspect ratio, electrical conductivity, thermal conductivity, low coefficient of thermal expansion, tensile strength, flexibility, EMI shielding ability and transparency. These intrinsic properties have generated enormous interest for development of "graphenium" devices with high speed and radio frequency logic devices, thermally and electrically conducting nanocomposite materials, electronic circuits, ultra-thin carbon films, sensors, transparent and flexible electrodes for displays and solar cells. Graphene sheets have shown various characteristic properties which are mainly dependent on fabrication methods, surface modification and functionalisation [1–11].

3.1 Size, Shape, Surface Morphology and Structure

The graphene honeycomb lattice consists of two equivalent sub-lattices made of carbon atoms bonded together with σ-bonds. Each carbon atom has π orbital that contributes to a delocalized network of electrons. This 3D graphene can have 'defects' like topological shapes (pentagons, heptagons or their combination), edges, vacancies, adatoms, cracks and adsorbed impurities [12]. Graphone

Graphene Nanomaterials: Fabrication, Properties and Applications
Satyendra Mishra and Dharmesh Hansora

ISBN 978-981-4745-41-3 (Hardcover), 978-1-315-36455-1 (eBook)
www.panstanford.com

formation can be observed when half of the carbon atoms are hydrogenated, when strong σ bonds are formed between the carbon and hydrogen atoms. These σ bonds are due to the usual π bonding network of metallic and nonmagnetic 2D graphene sheets which can causes the electrons on the unbonded carbon-hydrogen atoms that make them localized and unpaired [13].

The well controlled and ordered metal oxide (SnO_2, SiO_2, NiO, MnO_2)/graphene nanocomposites were prepared by ternary self-assembly approach. Self-assembly of metal oxides, surfactants and graphene for LIB electrodes were used to prepare graphene nanocomposites. The high concentration of RGO (30–60 wt%) with anionic surfactant was used to develop layered metal oxide–graphene composite film electrolyte, as shown in Fig. 3.1 [2, 14].

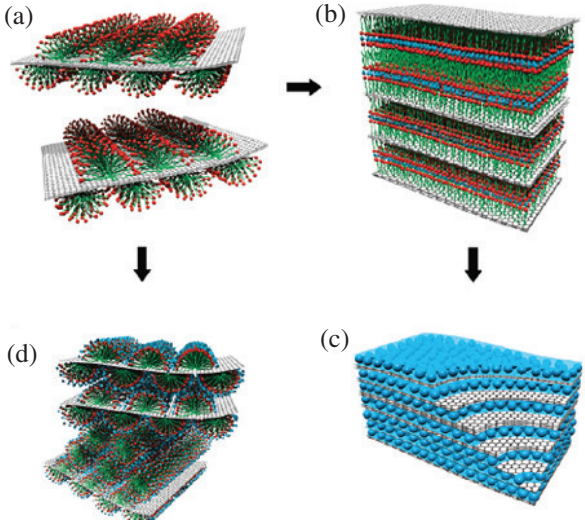

Figure 3.1 Schematic illustrations of metal oxide–graphene nanocomposites. (a) Adsorption of surfactant hemimicelles on the surfaces of the graphene stacks. (b) The self-assembly of anionic sulphonate surfactant on the graphene surface with oppositely charged metal cation (e.g. Sn^{2+}) species and the transition into the lamella mesophase towards the formation of SnO_2 graphene nanocomposites. (c) Metal oxide–graphene layered nanocomposites composed of alternating layers of metal oxide nanocrystals and graphene/graphene stacks. (d) Self-assembled hexagonal nanostructure of metal oxide precursor (e.g. silicate) with nonionic surfactants on graphene stacks. Reprinted by permission from Ref. [14], Copyright 2010, American Chemical Society.

Aggregation of NPs during the charge–discharge cycle can be avoided by a new strategy consisting encapsulated metal oxide particles by graphene sheets (Fig. 3.2). Encapsulation was carried out through the co-assembly of negatively charged GO with positively charged oxide NPs using electrostatic attraction [2, 15].

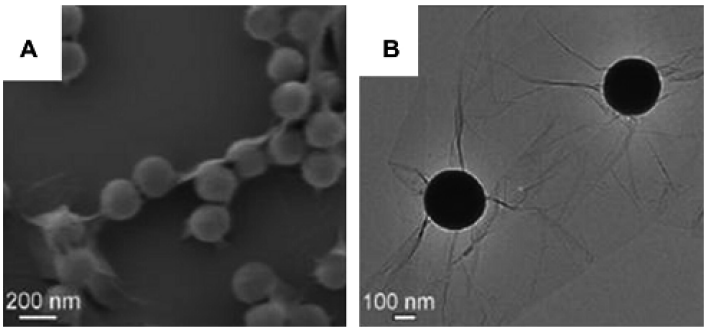

Figure 3.2 (A) SEM and (B) TEM micrographs of graphene-encapsulated silica spheres. Reprinted by permission from Ref. [15], Copyright 2010, John Wiley and Sons.

Figure 3.3(A) clearly shows Au-NDs self-assemble into short ND-chains on RGO surfaces, along the < 1 0 0 > direction of the RGO lattice. Ag NPs were synthesised on surfaces of GO and RGO, by heating their films adsorbed on 3-aminopropyltriethoxysilane (APTES)-modified Si/SiOx substrates in $AgNO_3$ aqueous solution. The number of pristine graphene layers were observed which showed a direct impact on the particle size and density of thermally evaporated Au NPs, i.e. the particle size was observed to be decreased and density was observed to be increased with increasing layer numbers of the graphene film as shown in Figs. 3.3(C,D) [3, 17, 18]. Figure 3.4(a) shows that transparent 2D carbon sheets were decorated thickly by the silver particles. The monolayer carbon nanosheets were observed to be thin because it was difficult to distinguish them with the carbon-supported films on the copper grid. However, the edges and crumpled silk waves of these carbon sheets indicated that these NPs were indeed deposited on supports. Figures 3.4(c,d) show that that these as-synthesised silver NP films can be able to restack and large amounts of silver NPs assembled on the 2D substrates.

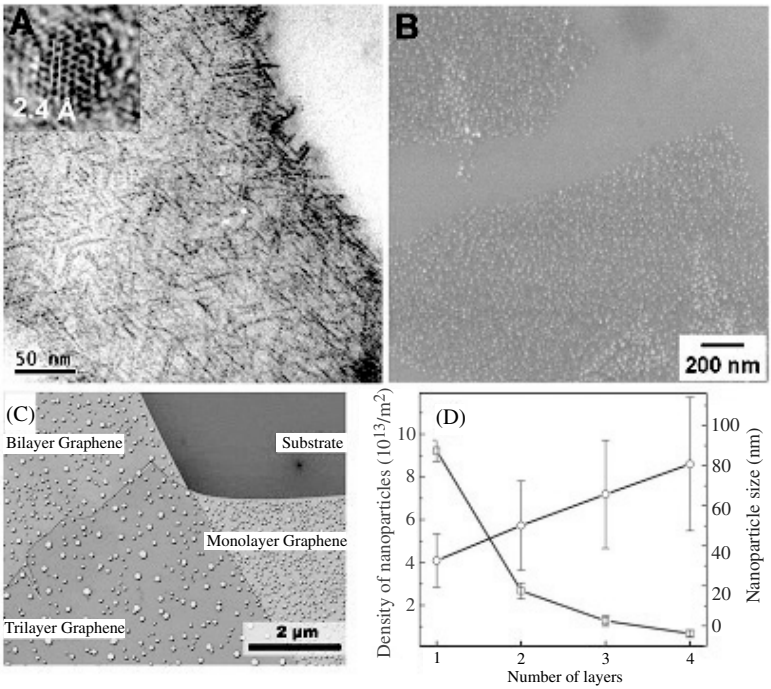

Figure 3.3 (A) Transmission electron microscopy (TEM) micrograph of ODT-capped AuNPs synthesised in situ and assembled on RGO surface. Inset of (A) is a high-resolution TEM image of an AuNP. Reprinted by permission from Ref. [16], Copyright 2010, John Wiley and Sons. (B) Scanning electron microscopy (SEM) micrographs of AgNPs densely grown on GO sheets. Reprinted by permission from Ref. [17], Copyright 2009, American Chemical Society. (C) AuNPs on monolayer, bilayer and trilayer graphene, respectively. (D) Statistics of the size and density of AuNPs on n-layer graphenes. Figs. (C) and (D) reprinted by permission from Ref. [18], Copyright 2010, American Chemical Society.

The negative charged functional groups have been used as anchors for adsorbing the polar materials as well as inorganic NPs. $Ag(NH_3)^{2+}$ as a positive ion interact easily with the negative graphene sheets through electrostatic forces. The in situ reduction of these ions by glucose allows anchoring of these silver NPs onto the surface, and some anchored onto the edges of the GO sheets [4, 19].

Figures 3.5(a–d) show the analysis of TEM, FESEM and DSC results of GO-Co_3O_4 nanocomposites. Exfoliated GO sheets have been

decorated randomly by uniform spherical in situ formed particles of about 100 nm in size. Figure 3.5(a) shows the dark field TEM micrographs of GO-Co_3O_4 nanocomposites, amongst them some of the nano-Co_3O_4 was observed brighter than the ones enveloped by a thin film. This was due to the fact, i.e. the functional groups, especially hydroxyl and epoxy groups appear on both sides of the GO sheet, and thereby in situ formed Co_3O_4 could anchor on both sides. Figure 3.5(d) shows that when individual GO was added then two exothermic peaks of AP were appeared, along with a new exothermic peak at 360 ^oC. The exothermic heat of the two steps was also observed to be larger than that of AP due to the catalytic effect of GO. The Co_3O_4 and GO-Co_3O_4 composites reduced temperature of both LTD and HTD and hence made the two step blend into one process. The decomposition temperature of AP with 2wt% Co_3O_4 (296 ^oC) was observed to be close to that of AP with 2wt% GO-Co_3O_4 (303 ^oC). However, the former exothermic quantity (1127 J/gm) was observed to be much lower than that of the latter (504 J/gm). Therefore, the concerted effect of the individual components for the catalysis of decomposition of AP, the addition of GO-Co_3O_4 brought down the decomposition temperature and also increased the exothermic heat of AP, indicating good catalytic properties [10, 19, 20].

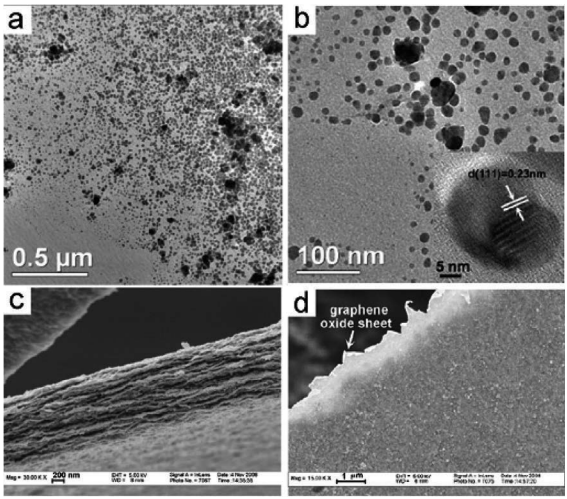

Figure 3.4 TEM (a,b) and FESEM (c,d) micrographs of silver NPs on GO sheets. Reprinted by permission from Ref. [19], Copyright 2009, John Wiley and Sons.

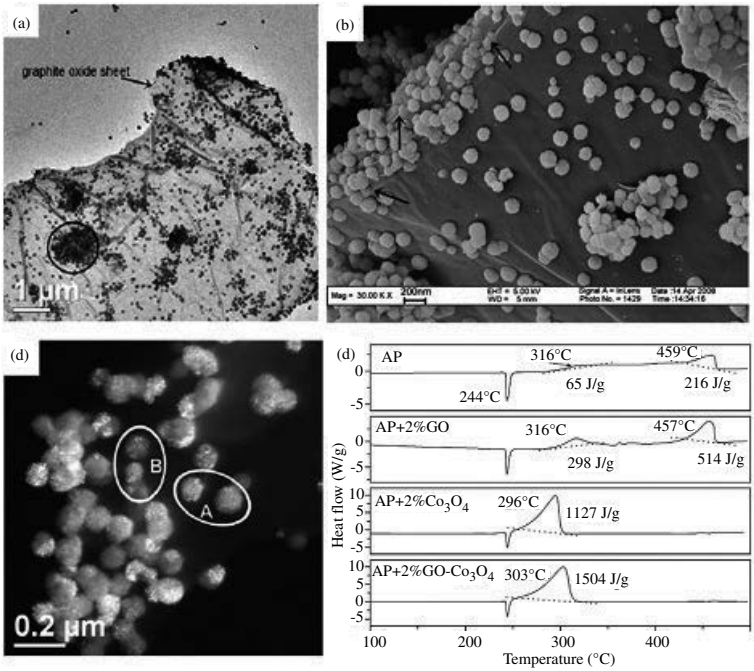

Figure 3.5 TEM (a,c), FESEM (b) images of GO-Co_3O_4 nanocomposites; (d) DSC curves for the decomposition of AP, AP with 2% GO, AP with 2% Co_3O_4 and AP with 2% Co_3O_4-GO nanocomposites. Reproduced from Ref. [20] with permission of The Royal Society of Chemistry.

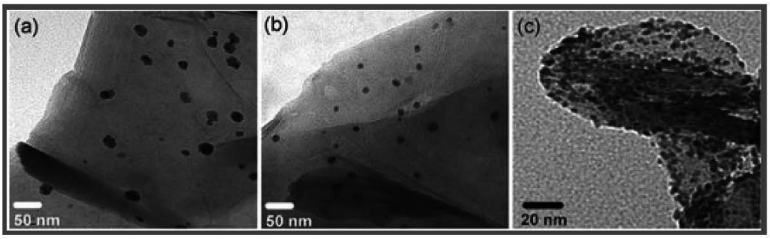

Figure 3.6 TEM images of RGO nanoplatelets decorated with (a) Pd, (b) Cu and (c) CuPd NPs. Reproduced from Ref. [21] with permission of The Royal Society of Chemistry.

The high affinity of palladium to graphene was observed due to the partial covalent nature of binding between Pd and graphene. In the case that a metal salt such as palladium nitrate, copper nitrate,

or a mixture was present in the aquatic phase together with GO. The analogous metal NPs were observed to be deposited on the RGO nanoplatelets (Fig. 3.6) [10, 21]. The in situ prepared composites showed a good exfoliation of GO and homogeneous dispersion in PP matrix (Fig. 3.7) [22], with high electrical conductivity.

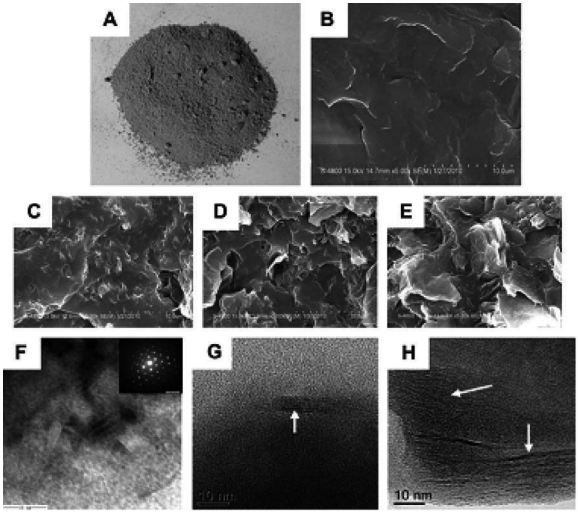

Figure 3.7 (A) PP/GO nanocomposite powder as obtained after coagulation in ethanol (containing 0.1 M HCl). (B) SEM images obtained from fracture surface of neat PP without GO. (C–E) SEM images obtained from fracture surface of composite samples of 0.42, 1.52 and 4.90 wt%, respectively, GO loadings. (F) TEM image of sample PP1 with 0.96 wt% of GO (the inset showing the measured electron diffraction pattern). (G) TEM image of sample PP3 with 1.52 wt% of GO. (H) TEM image of sample PP4 with 4.90 wt% of GO. Reprinted by permission from Ref. [22], Copyright 2010, American Chemical Society.

The in situ polymerisation has also been widely used for proper dispersion of graphite-based layered structures, such as expanded graphite and graphite oxide, in a polymer matrix [23–25]. The in situ polymerisation generally increases interlayer spacing and exfoliates the layered structures of graphite into graphite nanoplates by the intercalation of monomers. These can't generate polymers after polymerisation, producing well-dispersed graphene in a polymer matrix. A variety of composites, such as PANI–GO/PANI–graphene [26], graphene nanosheets/CNT/polyaniline [27] and PANI–GO [28] have been prepared by this approach.

3.2 Mechanical Properties

Unnecessary strain of devices can affect on their performance and life. Generally, applying external stress on crystalline material could alter inter atomic distances, which can result in the redistribution, in local electronic charge. This could also introduce a band gap in electronic structure and modify the electron transport property. Graphene has the highest elastic modulus and strength. A single defect free graphene layer possesses the highest intrinsic tensile strength with stiffness similar to graphite [29–31]. Compressive and tensile strain in graphene layer can be estimated using Raman spectroscopy by monitoring change in the G and 2D peaks with applied stress. The splitting of the G peak and red shift was observed with increasing in strain, while the 2D peak with red shift was observed without splitting for small strains 0.8% [32]. Ni et al. [30] observed the opposite behavior for epitaxial graphene on SiC substrate and found the blue shift in all the Raman bands for the epitaxial graphene as compared to that of the micromechanically cleaved graphene because of the compressive stress in grown graphene. The strain on graphene may change electronic band structure, which is the indication that the energy band gap can be tuned by introducing the controlled strain. The band gap tuning was well reported under uniaxial strain [33].

Mechanical property such as Young's modulus of the defect free graphene was reported to be 1 TPa, while fractural strength was reported to be 130 GPa. Elastic modulus of chemically modified graphene was reported of 0.25 TPa. While, maximum elastic modulus and fracture strength of "GO platelets paper" were reported as ~32 GPa and 120 GPa, respectively. Graphdiyne has been reported as softer material than graphyne or graphene. It has a plane stiffness of 120 N/m and Young's modulus of 375 GPa [12, 13, 34–37].

A single/three-layer graphene deposited on flexible polyethylene terephthalate (PET) showed uniaxial tensile strain (up to 0.8%) after stretching the PET in one direction. The band gap of 0.25 eV was reported under the highest strain (0.78%) for the single-layer graphene. This uniaxial strain affected the electronic properties of graphene because it breaks the bonds of CAC lattice. Enhanced mechanical properties such as elastic modulus and tensile strength of graphene sheets have also given the attention of researchers,

scientists and academia. The graphene reinforced polymer nanocomposites have been employed to explore the intrinsic strength (125 GPa) and elastic modulus (1.1 TPa). This indicates that the mechanical properties are dependent on the reinforcement phase concentration and distribution in the host matrix, interface bonding, reinforcement phase aspect ratio, etc., e.g. an increase in tensile strength of the graphene–PS composite is illustrated in Fig. 3.8, which represents an enhancement in the mechanical properties of the composite due to effective load transfer between graphene and polymer [38].

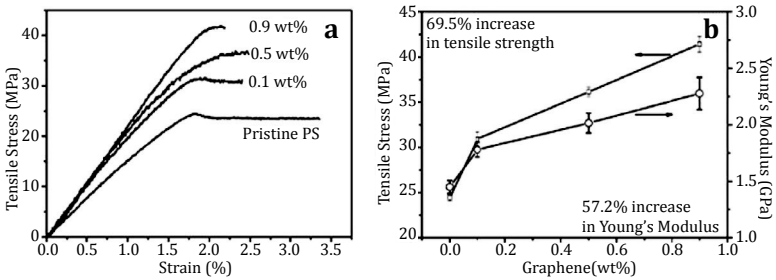

Figure 3.8 Stress–strain curves of the pristine PS and their nanocomposite films with different contents of graphene sheets. (b) Change in Young's modulus and tensile strength with increasing graphene content. Reproduced from Ref. [38] with permission of The Royal Society of Chemistry.

Although the pristine graphene has the highest theoretical strength, the presence of functional groups on the GO surfaces has high level of dispersion in polar solvents and water. The improved GO/polymer interaction provides high molecular level dispersion and enhanced interfacial interaction, which can lead to high mechanical properties to graphene polymer nanocomposites. GO–PVA composite showed an enhancement of 76% and 62% in elastic modulus and strength, respectively, with polymer containing 0.7 wt% GO sheets [39]. Xu et al. [40] observed a similar trend for GO–PVA composite films with layered structures prepared by vacuum filtration [40]. The chemically reduced GO (CRG) and thermally reduced GO (TRG) are different with each other, the presence of defects in the carbon lattice arise due to the reduction process, which has an adverse effect on the mechanical properties [39, 41, 42]. High surface defects and wrinkles in TRG reinforced in poly (ethylene-2,6-

naphthalate) (PEN) were observed, which indicated a small increase in tensile properties as compared to that of the graphite reinforced PEN.

Graphene-based composites have already shown an improvement in the stiffness and the mechanical strength using graphene as filler [39, 43–46]. Other mechanical properties, fracture toughness, fatigue and impact strength of the graphene reinforced composites were also investigated and studied [47–50]. Graphene reinforced Nayon-12 composites have shown the significant improvement in tensile strength (by 35%) and elongation at break (by 200%) with 0.6 wt% addition of graphene filler. An improvement in KIc and impact failure energy was reported as 72% and 175%, respectively. It was reported that the graphene filler suppressed the crack propagation in the epoxy polymer matrix. The improvement in fracture and fatigue resistance was observed after reinforcing the CNT and NPs, but two orders of magnitude lower weight fraction of graphene nanofiller was achieved with the same degree of reinforcement [47]. The superior mechanical properties of composite made of graphene platelets over CNTs was related to their high specific surface area, enhanced nanofiller matrix adhesion/interlocking arising from their wrinkled (rough) surface and 2D flat geometry [50].

3.3 Electrical and Electrochemical Properties

Few-layer graphene and carbon NPs can show semiconducting or insulating behaviour with little change in their resistance in the temperature range of 100 to 373 K. The resistivity was found to be increasing sharply below temperature of 50 K. But, if the graphene is heated to high temperatures then this might decrease, e.g. GNRs and palladium sheets sandwiched between graphene sheets, which possess superconducting nature and it can be used as an electrode material for SCs [13, 37].

Pristine graphene is a two-dimensional honeycomb carbon lattice with zero gap semiconducting material. The sp^2-hybridised carbon atoms are arranged in hexagonal fashion in 2D layer and a single hexagonal ring comprises of three strong in-plane sigma bonds P_z orbitals perpendicular to the planes. Generally, graphene layers are bonded by weak P_z interaction and strong in-plane bonds

keep hexagonal structures stable and facilitate de-lamination of 3D structure of graphite into individual graphene sheet just by applying mechanical stress only. A scotch tape method for investigation of many fundamental properties of this 2D crystal, micromechanically, creates a defect free single layer of graphene sheet and provides a 2D platform. A highly unusual nature of charge carriers, is one of the most interesting aspects of the graphene, which behaves as mass less relativistic particles (Dirac fermions). Dirac fermions behaviour is very abnormal as compared to electrons when subjected to magnetic fields such as the anomalous integer quantum Hall effect (QHE). This effect was also observed at room temperature [51–53]. Graphene possesses distinctive nature of its charge carriers, which mimic relativistic particles. It has been considered as electrons those have lost their rest mass, it is better described with (2 + 1) dimensional Dirac equation [54].

The electrical characterisation of the as-synthesised GO and RGO, both in chemical and thermal route were conducted using two-probe current (I)–voltage (V) measurement and also by three terminal field-effect transistor (FET) devices. As-fabricated GO was found to be insulating because of the presence of the oxidised functional group. The controlled reduction (i.e. thermal or chemical) process resulted in removal of oxidised group providing electrically conductivity to GO. Although, many oxidised groups were removed during reduction process, and remaining oxidised groups limited for electron transport properties of the RGO sheets. The transport properties were characterised by comparing the conductivity values and field-effect mobility values. The conductivity values can be calculated using the following Eq. (3.1), where R indicates the total resistance and t indicates the sheet's thickness.

$$\sigma = (R \cdot t)^{-1} \tag{3.1}$$

The conductivity of RGO was reported to be varied from 0.05 to 500 S/cm depending on the degree of reduction, which is the ratio of the graphitic regions (sp^2) to oxidised regions (sp^3). Few layered RGO sheets (<5 nm) were studied by Jung et al., who compared the conductivity with different reduction processes such as chemical, thermal and a combination of chemical/thermal approach [55].

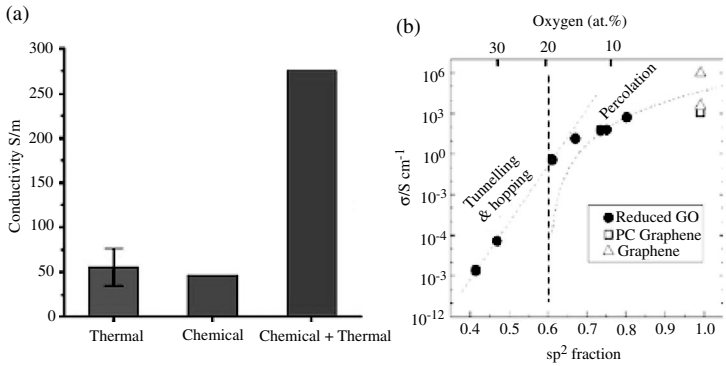

Figure 3.9 (a) Conductivity of single sheets of GO reduced thermal reduction, chemical reduction and combined chemical/thermal reduction. Reprinted by permission from Ref. [55], Copyright 2008, American Chemical Society. (b) Conductivity of TRG as a function of the sp^2 carbon fraction. The vertical dashed line indicates the percolation threshold of 0.6 at sp^2. Fitting of the experimental data reveals two different regimes for electrical transport with sp^2 fraction. Tunnelling and/or hopping (straight dashed line) mechanisms dominates at sp^2 fractions below 0.6, while percolation amongst the sp^2 clusters dominates above the percolation threshold. The 100% sp^2 materials are polycrystalline (PC) graphite and graphene. The two conductivity values are indicating for doped by gating (upper triangle) and intrinsic graphene (lower triangle). Reprinted by permission from Ref. [56], Copyright 2009, John Wiley and Sons.

The graphene samples were treated by a combined chemical/thermal reduction which displayed five times higher conductivity (300 S/m) as compared to the samples prepared by chemical or thermal reduction (Fig. 3.9a). Mattevi et al. investigated the role of graphitic domain (sp^2) fraction on the conductivity of RGO sheets using thermal reduction process (as shown in Fig. 3.9b) [56]. It was reported that the conductivity can be tuned over 12 orders of magnitude by tuning the sp^2 fraction through oxidation and reduction processes. It can also be seen from here that the conductivity of RGO sheets can be brought to that of pristine graphene if sp^2 fraction is increased to more than 0.9 [56]. The thermal reduction is effective for RGO thin film (>5 nm), but only on the top few layers of GO film [57]. This is the indication of that chemical reduction process which could be more effective to achieve high electrical conductivity of the RGO thin film followed by thermal treatments. The conductivity and mobility values of RGO were reported to be low compared as

compared to that of pristine graphene (200,000 $cm^2/V{\cdot}s$). The several reasons were considered for poor performance in RGO sheets, such as (i) the charge percolation was limited by disconnected network of delocalized tracks in the sheets due to remaining oxidised functional groups and (ii) defects in the graphene sheets produced during the reduction process. The trapped state retards charge carrier dissociation on defect sites. Therefore, it controls the initial stages of reduction and oxidation of RGO sheets required for developing the high quality RGO devices.

A high electrical conductivity is the most fascinating property of graphene. When graphene is used as fillers with insulating polymer, it may greatly enhance the electrical conductivity of the polymer composites. Various factors (the aggregation of filler, the presence of functional groups on graphene sheets, concentration of filers, aspect ratio of the graphene sheets, inter-sheet junction, distribution in the matrix, wrinkles and folds, processing methods), were corroborated, that influenced the electrical conductivity and the percolation threshold of the graphene composite. The pristine graphene has been reported with the highest conductivity; however, difficulty was reported in producing a large amount by mechanical exfoliation which limits its use and compels to rely on CRG and TRG. Although, GO is electrically insulating, the thermal reduction eliminates the oxygen functional groups and partially restores the electrical conductivity, which make the reduced GO as suitable conductive filler for composite. Reduced GO sheets provide a conductive path for the electron even when the concentration of the conductive filler is above the percolation threshold. The lowest electrical percolation threshold (of 0.1 vol%) of graphene has been reported for the hydrazine reduced PS-isocyanate treated GO mixture [58]. A TRG has higher electrical conductivity than CRG due to absence of oxygenated functional groups. Thus, polymer composites with TRG may show a better electrical conductivity than that with CRG one. Various polymer matrices such as polyurethane, epoxy [59], polyaniline, polyamide [60], PVDF, PVA [61] and polycarbonate [62] reinforced with CRG, TRG and GO reinforcement have been studied in the past few years. These graphene-based composite materials can be used for electromagnetic shielding [63], sensors, photovoltaic devices and as a conducting paint. The pristine graphene offers a great electrical and transport properties, but the application is

limited due to its poor dispersion into individual sheet in the polymer matrix. Therefore, functionalisation of graphene sheets may provide better improvement in dispersion in a polymer matrix, which can be helpful for improving the mechanical properties. Attaching the foreign molecules may change the charge transport properties.

An electrical percolation reinforcement of TRG in polycarbonate was reported to be required only 0.66 vol% in the composite prepared by melt extrusion, and the TRG remained highly exfoliated throughout the polymer matrix as compared to graphite in polymer matrix [64]. An alignment of the TRG sheets has noticeable effect on electrical conductivity of the polymer composites. The squeezed films were injection moulded using polycarbonate/TRG samples, which have shown lower conductivity than the annealed disks. A similar composite system (polycarbonate/graphene) was studied by emulsion mixing and solution blending followed by compression moulding [62], which exhibited lower electrical percolation threshold of 0.14 and 0.38 vol% respectively, as compared to composites prepared by injection moulded composites [64]. The low percolation threshold and high electrical conductivity were observed due to single and few layer graphene sheets the wrapped around the polycarbonate microsphere, which generated a high conductive path for electrons.

The electrical conductivity of the TRG-based PVDF nanocomposites was affected by temperature [65]. TRG–PVDF nanocomposites showed a decrease in electrical resistance with temperature (negative temperature coefficient) as compared to the increased resistance (positive temperature coefficient, PTC) of the expanded graphite–PVDF composite. This behavior of the TRG-based composite was due to the high aspect ratio of graphene which leads to contact resistance predominating over tunnelling resistance. Tunable PTC of resistance was observed in graphene nanosheets/polyethylene composites during isothermally treatment at 180 ^{o}C for different time interval, which was due to the low viscosity of the polymer matrix that helped in graphene sheets migration and weakened the overlapping conductive joints of graphene sheets [66].

The electrocatalytic activity of methanol oxidation on carbon black- and graphene-supported Pt and Pt–Ru-based catalysts NPs was characterised by cyclic voltammetry in an electrolyte of 1 M

CH_3OH and 0.5 M H_2SO_4 at 50 mV/s. Graphene-supported Pt-based catalysts NPs had a higher activity for methanol oxidation and also a better tolerance to CO in comparison to carbon black-supported Pt-based catalysts NPs (Fig. 3.10).

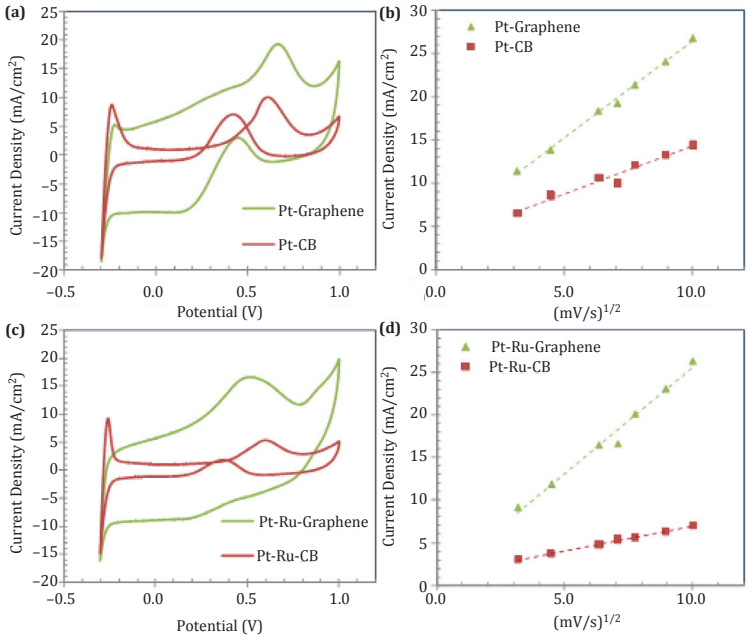

Figure 3.10 Electrocatalytic activity of graphene/carbon black–supported Pt and Pt–Ru-based catalysts NPs for methanol oxidation: cyclic voltammograms of Pt-based catalysts NPs (a) and Pt–Ru-based catalysts NPs (c) in 1 M CH_3OH/0.5 M H_2SO_4 at 50 mV/s between –0.3 V and +1.0 V vs. Ag/AgCl; and the relationship of peak current density vs. scan rate for Pt-based catalysts NPs (b) and Pt–Ru-based catalysts NPs (d). Reproduced from Ref. [4], Copyright 2011, INTECH.

The results suggested that graphene plays a critical role in promoting methanol oxidation of Pt-based catalysts NPs. The ratio of the forward anodic peak current density (IF) to the reverse anodic peak current density (IR) can be used to describe the tolerance of Pt-based catalysts NPs to CO and other carbonaceous species. Graphene-supported Pt-based catalysts NPs had have a ratio of 6.52, which was much higher than carbon black-supported Pt NPs (1.39), and results suggested that graphene-supported Pt-based catalysts NPs generate a more complete oxidation of methanol to carbon

dioxide. As shown in Fig. 3.10(c), the addition of Ru-based catalysts NPs resulted in a negative shift of oxidation potential of methanol at both electrodes with the decreasing of I_R and the increase of the I_F to I_R ratio. The oxidation peak potential of methanol was observed at 0.50 V as compared to an oxidation of 0.65 V for graphene–Pt-based catalysts NPs. This observation suggested that the presence of Ru-based catalysts NPs can significantly decrease the barrier to methanol oxidation and hence Pt–Ru-based catalysts NPs perform in a better way than Pt-based catalysts NPs. Conversely, the results indicated that graphene-supported Pt–Ru-based catalysts NPs may be an ideal candidate for direct methanol fuel cell electrodes. For graphene electrodes especially, there is no obvious reverse peak was observed, as shown in Fig. 3.10(b). As shown in Figs. 3.10(b,d), for all graphene- and carbon black–supported Pt and Pt–Ru-based catalysts NPs, the forward oxidation current density (IF) is proportional to the square root of the scan rate, which suggested that the oxidation behavior of methanol at all electrodes can be controlled by diffusion processes. The slopes for graphene supports are larger than those for carbon black, which indicated of a faster diffusion process of methanol on the surfaces of graphene sheets than that for methanol on the carbon black substrate [4].

3.4 Thermal Properties

Thermal conductivity (κ) of graphene is generally dominated by phonon transport, which is also known diffusive conduction at high temperature and ballistic conduction at low temperature. A thermal conductivity of monolayer graphene was reported to be ~ 6000 W/m·K, which is considered higher than that of graphitic carbon. Thermal conductivity of CVD growth graphene was reported to be ~ 2500 W/m·K at 900 K and 1400 W/m·K at 1046 K. The heat capacity of graphane was reported to be 29.32 ± 0.23 J /mol·K, which is 14.8% higher than the graphene [12, 34, 36, 67, 68].

The enhancement in thermal conductivity was observed with increasing volume fractions of graphene hybrid NPs and also with increasing the temperature, which is due to the high thermal conductivity of graphene and copper oxide NPs. The hybrid nanostructures of MWCNT/f-HEG dispersed in water-based hybrid

nanofluid showed an enhancement of 20% in thermal conductivity for 0.05% vol of f-HEG. An enhancement in thermal conductivity of f-MWCNT/f-HEG (2% for 0.08% volume fraction) and of f-HEG (1% for 0.08% volume fraction) was observed. The Ag/MWCNT–HEG dispersed in ethylene glycol–based hybrid nanofluid also showed an improvement in the thermal conductivity due to the high thermal conductivity of Ag NPs as well as the low stacking effect of graphene layers. The high thermal transport characteristics of graphene–MWCNT-based hybrid nanofluids were ascribed to the high aspect ratio of MWCNT and graphene, which can turn and form tightly bonded clusters, suppressing the interface resistance, that are excellent additives to attain high thermal conductivity. High thermally conductive MWCNTs act as connecting network between the graphene sheets to avoid the stacking of graphene sheets and high thermal conductivity of Ag NPs increases the overall surface area of the resulting nanofluid [1].

Graphene has been envisioned for applications in electronic devices. A thermal management is one of the key factors for better performance and reliability of the electronic components. A considerable amount of heat generates during the device operation which needs to be dissipated. Carbon allotropes such as graphite, diamond and CNTs have already shown higher thermal conductivity due to strong CAC covalent bonds and phonon scattering. CNTs are also known for having the highest thermal conductivity of 3000 W/mK (for MWCNT) at room temperature [69] and 3500 W/mK (for SWCNT) [70]. But, a large thermal contact resistance was the main issue with CNTs-based semiconductor. Recently, the highest thermal conductivity was reported up to 5000 W/mK at room temperature for the single-layer pure defect free graphene, whereas for supported graphene conductivity was reported to be 600 W/mK. Conductivity of the graphene on various supports is needed to be studied much, but their effect was predicted by Klemens [71]. Thermal conductivity was reported within the range of 3000–5000 W/mK at room temperature.

A new approach was used to determine the thermal conductivity of a thin atomic layer of graphene, which is shown in Fig. 3.11 [73]. A suspended graphene layer was heated by laser light (488 nm), the heat propagated laterally towards the sinks on corner side of the flakes. The temperature change was determined by

measuring the shift in the graphene G peak using confocal micro-Raman spectroscopy, which acted as a thermometer. The thermal conductivity was affected by various factors such as defects edge scattering [73] and isotopic doping [74]. These factors are detrimental to the conductivity which is due to phonon scattering at defect and phonons modes localisation due to the doping.

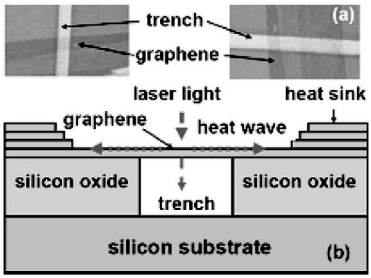

Figure 3.11 (a) High-resolution SEM image of the suspended graphene flakes. (b) Schematic of the experimental setup for measuring the thermal conductivity of graphene. Reprinted from Ref. [72], with permission from AIP Publishing.

Thermal conductivity (j) of the material is generally governed by the lattice vibrations (phonon). The 2D structure of graphene has already shown highest thermal conductivity (3000 W/m·K) [75], which make them an excellent candidate for various polymer matrices to enhance the heat transport. The polymer composites with good thermal conductivity have shown potential applications in heat sink, electronic circuit boards and light weight high performance thermal management systems. An enhancement in thermal conductivity of nanocomposites was not like electrical conductivity similar to the highest thermal conductivity of the graphene sheets. This is due to the contrast of thermal conductivity which is of the order of 4 in comparison to the electrical conductivity having the order of 15–19.

An improvement in thermal conductivity was demonstrated for various polymer matrices reinforced with expanded graphite and multilayer graphene sheets, e.g. epoxy [76–80], PVC [81], polypropylene (PP) [82] and polyethylene (PE) nanocomposites. Most of the studies are focused on the epoxy matrix and graphite nanoplatelets (GNPs) for thermal conductivity of the polymer composites. Haddon and co-workers [76] prepared GNPs from

natural graphite by the acid intercalation followed with the exfoliation by means of rapid thermal shock. The GNPs were dispersed in epoxy matrix which showed thermal conductivity up to 6.44 W/mK at 25 vol% of GNP loading, which is considered higher than the neat epoxy. The effect of orientation of GNPs on thermal properties was studied by Drzal and co-workers [82]. The coefficient of thermal expansion (CTE) was measured along the longitudinal and the transverse direction of the flow of the melt during injection molding for GNP–PP composite. They found that 3 vol% of GNPs loading reduced the CTE of PP by 20–25% in both transverse and longitudinal directions. The thermal conductivity of 25 vol% GNP in PP was reported to be 1.2–1.5 W/mK, which is six times higher than that of virgin PP. In an effort of keeping high aspect ratio and good dispersion of GNPs in polymer matrix during processing, Veca et al. [83] used reinforced graphite in epoxy matrix, in which the expanded graphite was exfoliated into graphene sheets using alcohol and oxidative acid treatment by simultaneous stir and vigorous sonication. This treatment was facilitated with well dispersion of the graphene sheets with a thickness of less than 10 nm in epoxy matrix. The thermal conductivity properties of the resulting epoxy composites were reported highly anisotropic with a large ratio between the in-plane and cross-plane thermal conductivities. The 33 vol% loading of graphene nanosheets showed thermal conductivity of 80 W/m·K. The conductivity was observed to be increased linearly with addition of nanosheets due to the reduced interfacial thermal resistance. Yu et al. proposed a hybrid of CNT and GNPs in polymer matrix to reduce interfacial phonon scattering [84]. He used SWCNT and GNPS filler and combined in epoxy to achieve a synergistic effect in the thermal conductivity enhancement of the composite. An enhancement was originated from the bridging of planar nanoplatelets by the SWCNT, which decreased the thermal interface resistance due to the extended area of the SWCNT–GNP junctions. The composites were optimised by adding SWCNT–GNP hybrid filler loading in the range of 10–20 wt% and the ratio of filler SWCNT/GNP was kept around 1:3, which had shown the highest thermal conductivity (1.75 W/mK). Yang et al. [77] demonstrated the synergistic effect of graphene platelets and MWCNT in improving thermal conductivity of the epoxy nanocomposites. The stacking of GNP was inhibited by the MWCNTs and their long tortuous feature bridge adjacent to GNPs,

which resulted in high contact area between hybrid and polymer matrix. Thermal conductivity was observed to be increased by 147% after addition of 1 wt% (MWCNT:GNP ratio of 1:9).

3.5 Electronic, Optical and Magnetic Properties

Graphene is a 2D semiconductor material with a zero band gap. The first Brillouin zone has two equivalent points, known as Dirac points, where a band crossing occurs. A tight-binding interaction with first neighbour graphene sheet provides the dispersion relation to the electrons near to the Dirac points [10–12, 36, 85, 86]. Graphyne nanoribbons possess the band gaps in the semiconductor range of 0.59–1.25 eV and widths of 1 repeat unit to 8 repeat units. Graphdyne has strain free value of 0.47 eV, which can act as semiconductive material [13].

The electronic properties of GO depend on the oxidation level and chemical composition, and tuning the relative fraction of sp^2 and sp^3 carbon regions by removal or addition of the oxidation groups offers great possibilities for tailoring the electronic structures of GO. GOs are electrically insulating in nature due to the disruption of the delocalized π-electron conjugated networks and also due to direct optical band gap of ~3eV [87]. Eda et al. [88] revealed that the electric transport properties of GO undergoes the insulator–semiconductor–semimetal evolution as a function of reduction treatment, where the transport gap ranges from 10 to 50 meV and approaches to zero with extensive reduction. The theoretical computations of GO structures, with ordered oxidation groups, reveal that the band gap increases with enhancing the O-containing ratios. Yan et al. [89] obtained variable band gaps ranging from 0.2 to 4.2 eV by varying the oxidation coverage and the amount of epoxy and hydroxyl functional groups on the GO surface.

The electronic properties of GNRs depend on their widths and edge topologies. GNRs, with bare edges and the zigzag edges due to the presence of strong dangling bonds, were observed to be less stable than GNRs with armchair edges and a planar reconstruction into pentagon–heptagon configurations occurs under ambient conditions [90]. Hydrogen saturation was used to stabilise both zigzag and armchair edges [91]. It has been reported that armchair

GNRs are non-magnetic semiconductors, while zigzag GNRs are metallic or semiconducting in nature depending on the edge spin orientation. Density functional theory (DFT) computations of graphene revealed that the zigzag GNRs with anti-ferromagnetic configuration is energetically favoured as the ground-state over the ferromagnetic (FM) configuration with same spin orientation between the two edges [92]. The FM zigzag GNRs are metallic by contrast. Armchair and antiferromagnetic zigzag GNRs, with their band gaps, have an inverse dependence with increasing ribbon widths [93]. Hybrid GNRs, can be formed by joining the armchair or zigzag segments via rotating the cutting direction [94, 95]. These hybrid GNRs have irregular edge morphologies with a mixture of armchair and zigzag heterojunctions, e.g. wedge-like zigzag/zigzag (zigzag/armchair) junctions [96, 97] and chevron-like armchair/armchair junctions. FG was studied since 1993, due to the large experimental availability of graphite monofluoride. The formation energy of FG (−0.808 eV) was reported to be much larger than that of graphane (−0.097 eV), which indicates the higher stability of FG.

The sp^3-hybridised C-C and C-F bond length was reported to be 1.58 and 1.37 Å for FG. Similar to graphane and other fluorocarbons (e.g. perfluorohexane), FG was reported to have a wide-band-gap semiconductor with a direct gap of 3.0–4.2 eV predicted by LDA or GGA [98–102]. GW predicted value was much larger than the obtained experimental band gap (3–4 eV). The experimental value of the Young's modulus (~100 N/m) was reported to be half lower than that predicted from first-principles computations (i.e. ~228 N/m) [103]. These inconsistencies were attributed due to the incomplete fluorination of graphene in the presence of structure defects e.g. missing F atoms. Both 1D zigzag and armchair fluoroGNRs (fully fluorinated GNRs), similar to GNRs, are all non-magnetic semiconductors with width-dependant band gaps, but the band gaps of fluoroGNRs were observed to be smaller than that of the corresponding GNRs with the same width [104].

Partially fluorinated GNRs, i.e. the hybrid armchair FG-GNRs are non-magnetic semiconductors, while the hybrid zigzag FG-GNRs with F-terminated graphene edges are half-semiconductors. In these partially fluorinated GNRs where the two zigzag graphene edges adopt an antiferromagnetic coupling state, and the two spin channels have different band gaps. The electronic properties of hybrid zigzag

FG-GNRs can be easily tuned by edge chemical modification or by controlling the width of fluorinated graphene. Theoretical studies suggested that the electronic properties of FG can be tuned in a large scale to explore its technological applications. Surface adsorption of K or Li atoms can lead to charge transfer and electron doping of FG, while adsorption with Au introduces deep levels within the band gap without charge transfer [105]. Li et al. [106] found the presence of weak interactions for tuning the electronic structures of graphane and FG (Fig. 3.12).

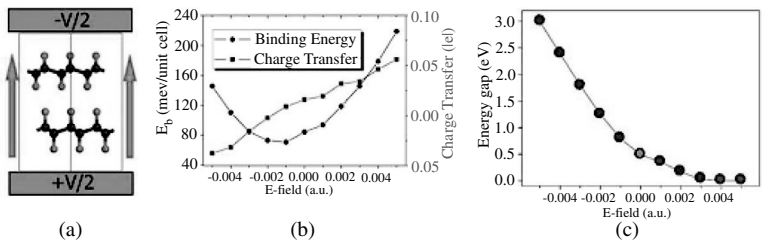

Figure 3.12 (a) Diagram of G/FG bilayer with the E-field. The positive direction of E-field is denoted by two arrows and the infinitely extended direction of G/FG bilayer is perpendicular to that of E-field. (b) Binding energy of G/FG bilayer and charge transfer from FG to graphane as a function of E-field. The negative charge transfer denotes that charges are transferred from graphane to FG. (c) Energy gap of G/FG bilayer as a function of E-field. Reprinted by permission from Ref. [106], Copyright 2012, American Chemical Society.

The graphane/FG bilayer composites can form C-H⋯F-C hydrogen bonding, and hence the binding strength which can be enhanced by applying an external electric field. The graphane/FG bilayer exhibits a band gap (0.5 eV) lower than those of individual graphane and FG. The band gap of graphane/FG bilayer can be modulated by changing the direction and strength of electric field, correspondingly causing a semiconductor–metal transition. The -C≡C- groups present in graphyne or graphdiyne make the π-electron more localized, which can lead to a non-zero gap [107]. Both 2D graphyne and graphdiyne sheets are known as semiconductors with band gaps of 0.52~0.53 eV, while accurate hybrid exchange-correlation functional has a larger band gap of 0.96 eV for graphyne and 1.22 eV for graphdiyne [108]. The band gap of graphyne/graphdiyne can be tuned easily by cutting into 1D nanoribbons. In contrast to GNRs, all the graphene/graphdiyne nanoribbons with an armchair or zigzag edges are

referred to as semiconductors [109–111]. Based on the deformation potential (DP) theory and effective mass approach, the mobilities of charge carriers for graphdiyne nanoribbons were reported to be in the range of 10^2–10^6 cm^2/V and the electrons were demonstrated to have larger mobilities than the holes.

The optical microscope was primarily used to image various layers because it is the cheapest, non-destructive and readily available methodology in laboratories. However, this method requires mounting of graphene layers on silicon dioxide substrate for good contrast imaging. The substrate designing has been given a considerable attention to enhance the visibility of thin graphene sheets [112–114]. The mechanism behind such contrast was well explained in terms of Fabry–Perot interference in the dielectric surface layer which can govern the fluorescence intensity contrasting between graphene layers and substrate.

$$C = \left(\frac{R_{\text{material}} - R_{\text{dielectric}}}{R_{\text{material}} + R_{\text{dielectric}}} \right) \tag{3.2}$$

The visibility of sheets is defined by the Michelson contrast (C) relation as shown in Eq. (3.2) [115], in which, $R_{material}$ is the reflected intensity from the material and $R_{dielectric}$ is the intensity without the material. The material was not detectable if C = 0, while material was brighter than the substrate when C = 0 to +1, and sample would be darker than the substrate C = 0 to 1 the. SiO_2 and Si_3N_4 were the most common overlay materials for enhancing the contrast of graphene layers that are dielectric in nature [116]. Another governing factor that modulates contrast was the wavelength of the incident light. Blake et al. [116] demonstrated the contacts variation using different narrow band filters for detection of thick sheets for SiO_2 support. It was found that sheets were invisible on 200 nm SiO_2 under normal white light illumination, while thick and thin sheets were visible on 300 nm SiO_2 when green light was used, whereas sheets were visible on 200 nm SiO_2 by blue light. Fig. 3.13 shows the optical image of different layers of the graphene micromechanically exfoliated on silicon substrate with 300 nm SiO_2 over-layer. The number of layers was identified by colour contrast and AFM [117]. The demonstrated detection technique was dependent on both the substrate thickness and incident light wavelength. Graphene-based sheets should be

researched more for visualisation independent of support material without any modification of the graphene.

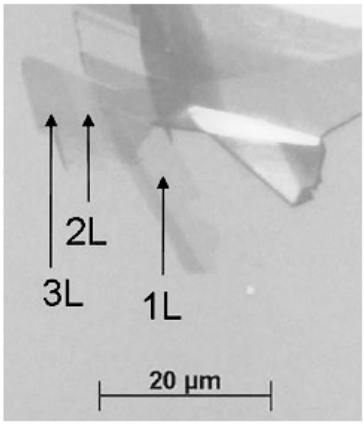

Figure 3.13 Optical microscopy image of single-, double- and triple-layer graphene on Si with a 300 nm SiO_2 over-layer, labelled in the paper as 1L, 2L and 3L, respectively. Reprinted from Ref. [117], Copyright 2009, with permission from Elsevier.

Many researches confirmed that single-layer graphene absorbs the 2.3% of incident light over a broad wavelength range but for a monolayer (Fig. 3.14) [118,119]. Graphene transmittance can be described in terms of fine structure constants [119, 120]. The absorption of light was observed to be increasing with increasing number of layers linearly, for each layer absorption is given by $A = 1 - T = \pi\alpha = 2.3\%$, where $\alpha = 1/37$ is the fine structure constant. The graphene can be imaged by optical image contrast on Si/SiO_2 substrate due to interference, and the contrast increases with the number of layers. The absorption for monolayer graphene was observed to be flat from 300 to 2500 nm. The peak at 250 nm in UV region (Fig. 3.14) attributes to the inter band electronic transition from the unoccupied states [120].

Fluorescent organic compounds are widely used for the development of low cost optoelectronic devices [121]. Blue fluorescence from aromatic or olefinic molecules and their derivatives were reported to be important for display and lighting applications [122]. The blue PL was observed for GO thin films deposited from thoroughly exfoliated suspensions [123]. The PL

characteristic and its dependence on the reduction of GO basically originate from the recombination of electron–hole pairs, localized within small sp^2 carbon clusters embedded in GO matrix [123].

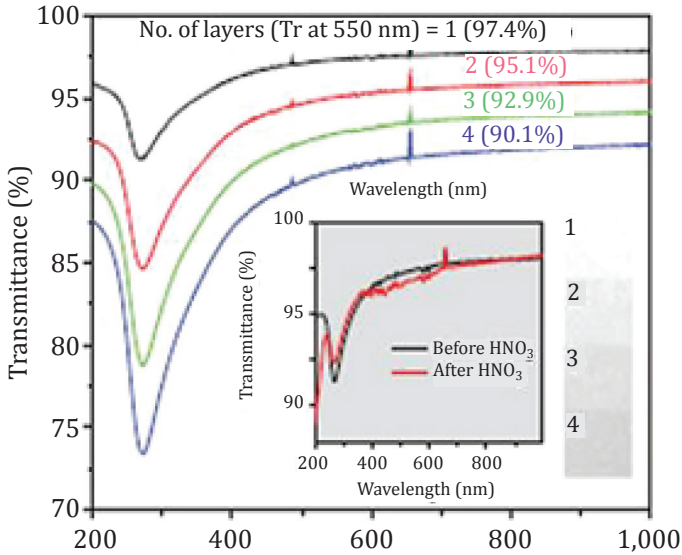

Figure 3.14 Representative of transmittance of different graphene layers. UV–vis spectra roll-to-roll, layer-by-layer transferred graphene films on quartz substrates. The inset shows the UV spectra of graphene films with and without HNO_3 doping. The right inset shows optical images for the corresponding number of transferred layers (1 × 1 cm^2). Reprinted by permission from Macmillan Publishers Ltd: *Nature Nanotechnology*, Ref. [118], Copyright 2010.

The high-frequency conductivity for Dirac fermions in graphene has been stated to be a constant. The expression of (T) and reflectance in terms of fundamental constants does not directly involve material parameters for determination of structure and electronic properties of graphene. A dielectric property of graphyne is a function of energy adsorbed for an electric field parallel and perpendicular to the graphyne sheet [12–14, 34]. Optical properties of GNRs are independent of their edge shapes and widths which make GNR as a suitable candidate for applications in optical and optoelectronic devices [124]. Paramagnetism and certain other magnetic features including spin–glass behaviour and magnetic switching phenomena were also observed in nanographite particles [37]. This observation indicates that graphene exhibits room-temperature

ferromagnetism that led to the investigation of the layer dependent magnetism in transition-metal dichalcogenides. Ferromagnetic and antiferromagnetic domains appear coexisting in graphene.

3.6 Energy Storage Capacity

Various electrode materials based on transition metal oxides such as SnO_2, Co_3O_4, Fe_3O_4, TiO_2 and Mn_3O_4, are proposed for LIBs to achieve higher specific capacities than currently being used graphite. These transition metal oxides possess very high theoretical capacities but extremely low electrical conductivity which restricts their direct application in LIBs. For example Mn_3O_4 has electrical conductivity about 10^{-7}–10^{-8} S/cm which limits its specific capacity lower than 400 mA·h/g. A superior specific capacity of an anode material SnO_2 (with theoretical specific capacitance of 780 mA·h/g) in LIBs was observed to be affected by phase transformation and pulverisation due to Li ion insertion and extraction during the charge–discharge cycles [125]. Electrochemical stability of active materials at various current densities and decrease in cyclic performance are challenges with LIBs. Various conductive additives such as CNTs [126–128] and carbon particles [129] are added to increase specific capacity. Graphitised carbon anode materials possessed low capacity (372 mA·h/g) because of limited Li ion storage sites within sp^2 carbon hexahedrons. The Li intercalation can be increased in the charge/discharge process using the layered structure of graphene nanosheets. Yoo et al. [130] reported the enhanced specific capacity of the carbon-based electrodes made of the interaction of graphene nanosheets with C_{60} and CNT, which facilitates the nanospace size for lithium ion (0.06 nm) intercalation. Higher reversible capacity (794–1054 mA·h/g) and cyclic stability were observed in disordered graphene nanosheets, as the presence of edge and vacancies defects in graphene sheets generally provides an additional reversible storage sites for Li ions (Fig. 3.15) [131].

According to the studies, the addition of the graphene-based material to transition metal oxide enhances the specific capacity of the electrodes at high discharge rate and also improves the electrochemical stability for longer period of cycles. An improvement was due to an excellent thermal and chemical stability, electronic

conductivity, high surface area and mechanical flexibility of monolayer graphene sheets.

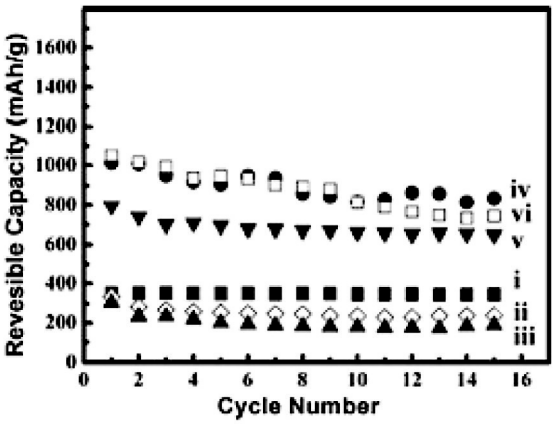

Figure 3.15 Reversible (charge) capacity v/s cycle numbers at a current density of 0.05 A/g, for (i) natural graphite, (ii) pristine GO, (iii) hydrazine reduced GO, (iv) 300°C pyrolytic GO, (v) 600°C pyrolytic GO and (vi) electron beam–reduced GO. Reprinted by permission from Ref. [131], Copyright 2009, American Chemical Society.

The flexible graphene sheets accommodate a large volume expansion of metal oxide during the charge–discharge process and this prevents the pulverisation of the electrodes leading to higher electrical conductivity of the electrode. Wang et al. [132] demonstrated a simple two-step solution–based method for developing the Mn_3O_4–graphene hybrids using slow hydrolysis of their salts (manganese acetate) in DMF and hydrothermal reduction of GO in to RGO. The slow hydrolysis showed the uniform distribution of the RGO nanosheets, which result in enhanced capacity at various current density (Fig. 3.16).

3.7 Gas-Sensing Ability

Single-layer graphene sheet possesses a large surface area ~ 2600 m^2/g, while for surface areas of different few layer graphene sheets were reported in the range of 270–1550 m^2/g. Due to this nature, GNRs are also useful for adsorption of different gas molecules such as CO, CO_2, NO, NO_2, O_2, N_2 and NH_3 [37, 67, 133].

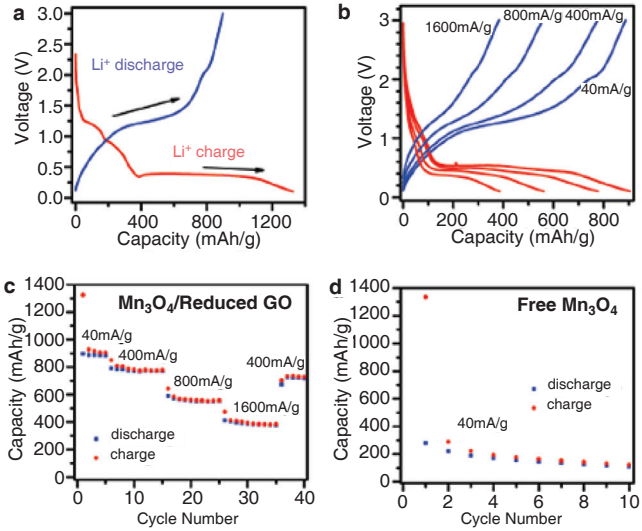

Figure 3.16 Electrochemical characterisations of a half-cell composed of Mn_3O_4/RGO and Li. The specific capacities are based on the mass of Mn_3O_4 in the Mn_3O_4/RGO hybrid. (a) Charge (red) and discharge (blue) curves of Mn_3O_4/RGO for the first cycle at a current density of 40 mA/g. (b) Representative charge (red) and discharge (blue) curves of Mn_3O_4/RGO at various current densities. (c) Capacity retention of Mn_3O_4/RGO at various current densities. (d) Capacity retention of free Mn_3O_4 NPs without graphene at a current density of 40 mA/g. Reprinted by permission from Ref. [132], Copyright 2010, American Chemical Society.

The sensitivity of the gas (or vapour phase) sensor generally depends on the charge carrier transfer on GO/RGO surfaces caused by the adsorption of gases and sensing vapours such as NO_2, NH_3, H_2O, CO, dinitrotoluene (DNT), iodine and ethanol and hydrazine hydrate [134–139]. For example the as synthesised GO transistor showed little response towards detection of chemical gases such as NO_2 [136]. The RGO was observed to be responsive to NO_2 and hence it showed a typical p-type transistor behavior due to the recovery of many graphitic carbon atoms as active sites for NO_2 adsorption. This leads to enhancing charge concentration and a decrease in resistance as a function of time (Fig. 3.17a).

The NH_3 showed n-type RGO transistor behaviors [140, 141] since oxygen groups in RGO were main responsible ions for reactions with NH_3 and C bond [142]. This reaction decreased the device conductivity (Fig. 3.17b) as a function of time [136]. Very high temperature

(1000 °C) reduced GO showed a faster chemoresistive (or resistance changes in time) response than the hydrazine reduced GO and it also showed a low temperature reduction upon exposure to water vapour. This was due to the presence of a larger number of defects during the reduction process [143]. These results also indicated that the gaseous vapour generally respond with both structural defects, such as vacancies, small holes generated during reduction treatments, and functionalised groups. The sensitivity of RGO-based sensors can be modified by reduction treatment process [134, 143]. Reduction by chemical (by hydrazine) and thermal means, the ascorbic acid (vitamin C) has also been used as a mild and green reduction agent for RGO-based chemical sensors [144]. The flexible RGO chemical sensor, using inkjet-printed films of poly-(ethylene terephthalate) (PET) decorated RGO sheets were reported to be reversibly detect NO_2 and Cl_2 vapours at ppb level. This demonstrated that the use of ascorbic acid is as an effective alternative for hydrazine to reduce GO into RGO. Graphene-based composite materials Pt/RGO/SiC-based devices have been studied for hydrogen gas sensing [145]. The electrical characteristics and hydrogen gas sensing mechanism of the device were studied by analyzing the effect of hydrogen interaction at the graphene/SiC and Pt/graphene interfaces. High work function of Pt led to weak interaction energy at the interface and preserved the electronic structure of RGO and electrons transfer from RGO to Pt for equilibration of the Fermi level. The carrier concentration was observed to be increased on exposure of hydrogen gas, which was due to dissociation of hydrogen molecules occured on the Pt surface.

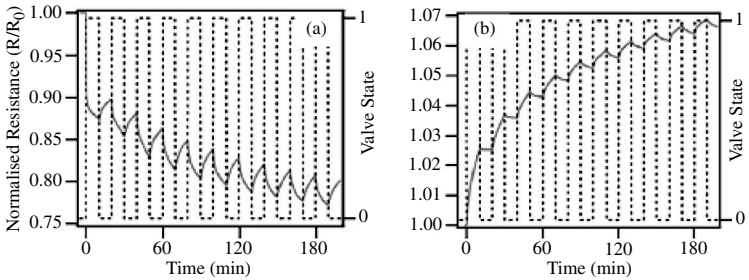

Figure 3.17 (a) NO_2 and (b) NH_3 detection using a graphene film. The sensor was attached with gold electrodes and measurement was done by four wire method with 500 lA driving current. The NO_2 concentration is 5 ppm in dry nitrogen. Reprinted by permission from Ref. [136], Copyright 2009, American Chemical Society.

References

1. Sarkar J., Ghosh P., Adil A. (2015). *Renew. Sust. Ener. Rev.*, **43**, 164–177.
2. Singh V., Joung D., Zhai L., Das S., Khondaker S.I., Seal S. (2011). *Prog. Mater. Sci.*, **56**, 1178–1271.
3. Huang X., Yin Z., Wu S., Qi X., He Q., Zhang Q., Yan Q., Boey F., Zhang H. (2011). *Small*, **7(14)**, 1876–1902.
4. Mikhailov S. *Physics and Applications of Graphene–Experiments,* ISBN: 978-953-307-217-3, InTech, Available from: http://dx.doi.org/10.5772/14422
5. Chaudhuri R.G., Paria S. (2012). *Chem. Rev*., **112**, 2373–2433.
6. Zhu B.Y., Murali S., Cai W., Li X., Suk J.W., Potts J.R., Ruoff R.S. (2010). *Adv. Mater.*, **22**, 3906–3924.
7. Rangappa D., Jang J.H., Honma I. (2011). Supercritical fluid processing of graphene and GO. In *Graphene*: *Synthesis, Characterization, Properties and Applications,* InTech, pp. 45–58.
8. Rao C.N.R., Subrahmanyam K.S., Ramakrishna Matte H.S.S., Govindaraj A., *Graphene: Synthesis, Functionalization and Properties.* Available at http://www.worldscibooks.com/physics/7989.html
9. Tang Q., Zhou Z., Chen Z. (2013). *Nanoscale*, **5**, 4541.
10. Georgakilas V., Otyepka M., Bourlinos A.B., Chandra V., Kim N., Christian Kemp K., Hobza P., Zboril R., Kim K.S. (2012). *Chem. Rev.*, **112 (11)**, 6156–6214.
11. Terrones M., Méndez A.R.B., Delgado J.C., Urías F.L., Cantú Y.I.V., Macías F.J.R., Elías A.L., Sandoval E.M., Márquez A.G.C., Charlier J.C., Terrones H. (2010). *Nano Today*, **5(4)**, 351–372.
12. Zhu Y., Murali S., Cai W., Li X., Suk J.W., Potts J.R., Ruoff R.S. (2010). *Adv. Mat.,* **22 (35)**, 3906–3924.
13. Peng Q., Dearden A.K., Crean J., Han L., Liu S., Wen X., De S. (2014). *Nanotechnol. Sci. Appl.,* **(7)**, 1–29.
14. Wang D., Kou R., Choi D., Yang Z., Nie Z., Li J., et. al. (2010). *ACS Nano*, **4**, 1587.
15. Yang S., Feng X., Ivanovici S., Müllen K. (2010). *Angew. Chem. Int. Ed.*, **49**, 8408.
16. Huang X., Zhou X.Z., Wu S.X., Wei Y.Y., Qi X.Y., Zhang J., Boey F., Zhang H. (2010). *Small*, **6**, 513.
17. Zhou X.Z., Huang X., Qi X.Y., Wu S.X., Xue C., Boey F., Yan Q. Y., Chen P., Zhang H. (2009). *J. Phys. Chem. C*, **113**, 10842.

18. Zhou H.Q., Qiu C.Y., Liu Z., Yang H.C., Hu L.J., Liu J., Yang H.F., Gu C.Z., Sun L.F. (2010). *J. Am. Chem. Soc.*, **132**, 944.
19. Xu C., Wang X. (2009). *Small,* **5(19)**, 2212–2217.
20. Xu C., Wang X., Zhu J., Yang X., Lu L. (2008). *J. Mater. Chem.*, **18(46)**, 5625–5629.
21. Hassan H.M.A., Abdelsayed V., Rahman A.E., Khder S., AbouZeid K.M., Terner J., El-Shall M.S., Al-Resayes S.I., El-Azhary A.A. (2009). *J. Mater. Chem.*, **19**, 3832.
22. Huang Y., Qin Y., Zhou Y., Niu H., Yu Z.Z., Dong J.Y. (2010). *Chem. Mater.*, **22**, 4096.
23. Fim F.C., Guterres J.M., Basso N.R.S., Galland G.B. (2010). *J. Polym. Sci. Part A – Polym. Chem.*, **48**, 692.
24. Chen G., Weng W., Wu D., Wu C. (2003). *Eur. Polym. J.*, **39**, 2329.
25. Chen G., Wu C., Weng W., Wu D., Yan W. (2003). *Polymer*, **44**, 1781.
26. Yan X.B., Chen J.T., Yang J., Xue Q.J., Miele P. (2010). *ACS Appl. Mater. Interf.*, **2**, 2521.
27. Yan J., Wei T., Fan Z.J., Qian W.Z., Zhang M.L., Shen X.D. (2010). *J. Power. Sour.,* **195**, 3041.
28. Wang H.L., Hao Q.L., Yang X.J., Lu L.D., Wang X. (2009). *Electrochem. Commun.,* **11**, 1158.
29. Yu T., Ni Z., Du C., You Y., Wang Y., Shen J. (2008). *Phys. Chem. C*, **112**, 12602.
30. Ni Z.H., Chen W., Fan X.F., Kuo J.L., Yu T., Wee A.T.S. (2008). *Phys. Rev. B*, **77**, 6.
31. Ni Z.H., Wang H.M., Ma Y., Kasim J., Wu Y.H., Shen Z.X. (2008). *ACS Nano,* **2**, 1033.
32. Mohiuddin T.M.G., Lombardo A., Nair R.R., Bonetti A., Savini G., Jalil R. (2009). *Phys. Rev. B,* **79**.
33. Ni Z.H., Yu T., Lu Y.H., Wang Y.Y., Feng Y.P., Shen Z.X. (2008). *ACS Nano*, **2**, 2301.
34. Singh V., Joung D., Zhai L., Das S., Khondaker S.I., Seal S. (2011). *Prog. Mater. Sci.,* **56(8)**, 1271.
35. Tang, Q. Zhou Z., Chen Z. (2013). *Nanoscale,* **5**, 4541–4583.
36. Huang X., Yin Z., Wu S., Qi X., He Q., Zhang Q., Yan Q., Boey F., Zhang H. (2011). *Small,* **7(14)**, 1876–1902.
37. Rao C.N.R., Sood A.K., Subrahmanyam K.S., Govindaraj A. (2009). *Angew. Chem., Int. Ed.,* **48 (42)**, 7752–7777.

38. Fang M., Wang K., Lu H., Yang Y., Nutt S. (2009). *J. Mater. Chem.,* **19**, 7098.

39. Liang J.J., Huang Y., Zhang L., Wang Y., Ma Y.F., Guo T.Y. (2009). *Adv. Funct. Mater.,* **19**, 2297.

40. Xu Y., Hong W., Bai H., Li C., Shi G. (2009). *Carbon,* **47**, 3538

41. Goȉmez-Navarro C., Meyer J.C., Sundaram R.S., Chuvilin A, Kurasch S., Burghard M. (2010). *Nano Lett.,* **10**, 1144.

42. Kim H., Macosko C.W. (2008). *Macromolecules,* **41**, 3317.

43. Xu Z., Gao C. (2010). *Macromolecules,* **43**, 6716.

44. Dongyu C. (2009). *Nanotechnology,* **20**, 085712.

45. Nguyen D.A., Lee Y.R., Raghu A.V., Jeong H.M., Shin C.M., Kim B.K. (2009). *Polym. Int.,* **58**, 412.

46. Raghu A.V., Lee Y.R., Jeong H.M., Shin C.M. (2008). *Macromol. Chem. Phys.,* **209**, 2487.

47. Rafiee M.A., Rafiee J., Srivastava I., Wang Z., Song H., Yu Z.Z. (2010). *Small*, **6**, 179.

48. Yavari F., Rafiee M.A., Rafiee J., Yu Z.Z., Koratkar N. (2010). *ACS Appl. Mater. Interf.,* **2**, 2738.

49. Fang M., Zhang Z., Li J., Zhang H., Lu H., Yang Y. (2010). *J. Mater. Chem.*, **20**, 9635.

50. Rafiee M.A., Rafiee J., Wang Z., Song H., Yu Z.Z., Koratkar N. (2009). *ACS Nano*, **3**, 3884.

51. Zhang Y.B., Tan Y.W., Stormer H.L., Kim P. (2005). *Nature*, **438**, 201.

52. Novoselov K.S., Jiang Z., Zhang Y., Morozov S.V., Stormer H.L., Zeitler U. (2007). *Science,* **315**, 1379.

53. Novoselov K.S., Jiang D., Schedin F., Booth T.J., Khotkevich V.V., Morozov S.V. (2005). *Proc. Natl. Acad. Sci. USA*, **102**, 10451.

54. Geim A.K., Novoselov K.S. (2007). *Nat. Mater.,* **6**, 183.

55. Jung I., Dikin D., Park S., Cai W., Mielke S.L., Ruoff R.S. (2008). *J. Phys. Chem. C*, **112**, 20264.

56. Mattevi C., Eda G., Agnoli S., Miller S., Mkhoyan K.A., Celik O. (2009). *Adv. Funct. Mater.,* **19**, 2577.

57. Erickson K., Erni R., Lee Z., Alem N., Gannett W., Zettl A. (2010). *Adv. Mater.,* **22**, 4467.

58. Stankovich S., Dikin D.A., Dommett G.H.B., Kohlhaas K.M., Zimney E.J., Stach E.A. (2006). *Nature,* **442**, 282.

59. Miller S.G., Bauer J.L., Maryanski M.J., Heimann P.J., Barlow J.P., Gosau J.M. (2010). *Compos. Sci. Technol.,* **70**, 1120.
60. Domingues S.H., Salvatierra R.V., Oliveira M.M., Zarbin A.J.G. (2010). *Chem Commun*, **47**, 2592–2594.
61. Salavagione H.J., Martinez G., Gomez M.A. (2009). *J. Mater. Chem.,* **19**, 5027.
62. Yoonessi M., Gaier J.R. (2010). *ACS Nano,* **4**, 7211.
63. Liang J., Wang Y., Huang Y., Ma Y., Liu Z., Cai J. (2009). *Carbon*, **47**, 922.
64. Kim H., Macosko C.W. (2009). *Polymer*, **50**, 3797.
65. Ansari S., Giannelis E.P. (2009). *J. Polym. Sci. Part B: Polym. Phys.*, **47**, 888.
66. Pang H., Zhang Y.C., Chen T., Zeng B.Q., Li Z.M. (2010). *Appl. Phys. Lett.*, **96**, 251907.
67. Zhou C., Chen S., Lou J., Wang J., Yang Q., Liu C., Huang D., Zhu T. (2014). *Nanoscale Res. Lett.,* **9(1)**, 26–34.
68. Balandin A.A. (2011). *Nat. Mater.,* **10(8)**, 569–581.
69. Kim P., Shi L., Majumdar A., McEuen P.L. (2001). *Phys. Rev. Lett.*, **87**, 215502.
70. Pop E., Mann D., Wang Q., Goodson K., Dai H. (2005). *Nano Lett.,* **6**, 96.
71. Klemens P.G. (2001). *Int. J. Thermophys.*, **22**, 265.
72. Ghosh S., Calizo I., Teweldebrhan D., Pokatilov E.P., Nika D.L., Balandin A.A. (2008). *Appl. Phys. Lett.,* **92**, 151911.
73. Nika D.L., Pokatilov E.P., Askerov A.S., Balandin A.A. (2009). *Phys. Rev. B,* **79**, 155413.
74. Jiang J.W., Lan J., Wang J-S, Li B. (2010). *J. Appl. Phys.,* **107**, 054314.
75. Balandin A.A., Ghosh S., Bao W., Calizo I., Teweldebrhan D., Miao F. (2008). *Nano Lett.,* **8**, 902.
76. Yu A.P., Ramesh P., Itkis M.E., Bekyarova E., Haddon R.C. (2007). *J. Phys. Chem. C,* **111**, 7565.
77. Yang S.Y., Lin W.N., Huang Y.L., Tien H.W., Wang J.Y., Ma C.C.M. (2011). *Carbon,* **49**, 793.
78. Ganguli S., Roy A.K., Anderson D.P. (2008). *Carbon,* **46**, 806.
79. Hu Y., Shen J., Li N., Ma H., Shi M., Yan B. (2010). *Compos. Sci. Technol.,* **70**, 2176.
80. Sun X.B., Ramesh P., Itkis M.E., Bekyarova E., Haddon R.C. (2010). *J. Phys. Condens. Matter.,* **22**, 334216.

81. Vadukumpully S., Paul J., Mahanta N., Valiyaveettil S. (2011). *Carbon,* **49**, 198.
82. Kalaitzidou K., Fukushima H., Drzal L.T. (2007). *Carbon,* **45**, 1446.
83. Veca L.M., Meziani M.J., Wang W., Wang X., Lu F., Zhang P. (2009). *Adv. Mater.,* **21**, 2088.
84. Yu A., Ramesh P., Sun X., Bekyarova E., Itkis M.E., Haddon R.C. (2008). *Adv. Mater.,* **20**, 4740.
85. Li N., Wang Z., Shi Z., Mikhailov S. (ed.) (2011). *Synthesis of Graphene with Arc-Discharge Method,* Rijeka, Croatia: Intech, pp. 23–36.
86. Avouris P. (2010). *Nano Lett.,* **10(11)**, 4285–4294.
87. Luo Z., Vora P.M., Mele E.J., Charlie Johnson A.T., Kikkawa J.M. (2009). *Appl. Phys. Lett.,* **94**, 111909.
88. Eda G., Mattevi C., Yamaguchi H., Kim H., Chhowalla M. (2009). *J. Phys. Chem. C,* **113**, 15768–15771.
89. Yan J.A., Xian L., Chou M.Y. (2009). *Phys. Rev. Lett.,* **103**, 086802.
90. Koskinen P., Malola S., Häkkinen H. (2008). *Phys. Rev. Lett.,* **101**, 115502.
91. Barone V., Hod O., Scuseria G.E. (2006). *Nano Lett.,* **6**, 2748–2754.
92. Duan H., Xie E., Han L., Xu Z. (2008). *Adv. Mater.,* **20**, 3284–3288.
93. Han M.Y., Özyilmaz B., Zhang Y., Kim P. (2007). *Phys. Rev. Lett.,* **98**, 206805.
94. Yoon Y., Guo J. (2007). *Appl. Phys. Lett.,* **91**, 073103.
95. Li Y., Zhou Z., Shen P., Chen Z. (2012). *J. Phys. Chem. C,* **116**, 208–213.
96. Jia X., Hofmann M., Meunier V., Sumpter B.G., Campos-Delgado J., Romo-Herrera J.M., Son H., Hsieh Y.P., Reina A., Kong J., Terrones M., Dresselhaus M.S. (2009). *Science*, **323**, 1701–1705.
97. Li X., Wang X., Zhang L., Lee S., Dai H. (2008). *Science,* **319**, 1229–1232.
98. Karlický F., Zbořiland R., Otyepka M. (2012). *J. Chem. Phys.,* **137**, 034709.
99. Leenaerts O., Peelaers H., Hernández-Nieves A.D., Partoens B., Peeters F.M. (2010). *Phys. Rev. B,* **82**, 195436.
100. Zhou Q., Liang, Dong J. (2010). *Carbon,* **48**, 1405–1409.
101. Samarakoon D.K., Chen Z., Nicolas C., Wang X.Q. (2011). *Small,* **7**, 965–969.
102. Klintenberg M., Lebègue S., Katsnelson M.I., Eriksson O. (2010). *Phys. Rev. B,* **81**, 085433.

103. Muñoz E., Singh A.K., Ribas M.A., Penevand E.S., Yakobson B.I. (2010). *Diamond Relat. Mater.,* **19**, 368–373.
104. Tang S., Zhang S. (2011). *J. Phys. Chem. C*, **115**, 16644–16651.
105. Markevich A., Jones R., Briddon P.R. (2011). *Phys. Rev. B,* **84**, 115439.
106. Li Y., Li F., Chen Z. (2012). *J. Am. Chem. Soc.,* **134**, 11269–11275.
107. Kondo M., Nozaki D., Tachibana M., Yumura T., Yoshizawa K. (2005). *Chem. Phys.,* **312**, 289–297.
108. Jiao Y., Du A.J., Hankel M., Zhu Z.H., Rudolph V., Smith S.C. (2011). *Chem. Commun.,* **47**, 11843–11845.
109. Pan L.D., Zhang L.Z., Song B.Q., Du S.X., Gao H.J. (2011). *Appl. Phys. Lett.*, **98**, 173102.
110. Long M., Tang L., Wang D., Li Y., Shuai Z. (2011). *ACS Nano,* **5**, 2593–2600.
111. Bai H., Zhu Y., Qiao W., Huang Y. (2011). *RSC Adv.,* **1**, 768–775.
112. Jung I., Pelton M., Piner R., Dikin D.A., Stankovich S., Watcharotone S. (2007). *Nano Lett.*, **7**, 3569.
113. Lambacher A., Fromherz P. (1996). *Appl. Phys. A Mater. Sci. Proc.,* **63**, 207.
114. Ni Z.H., Wang H.M., Kasim J., Fan H.M., Yu T., Wu Y.H. (2007). *Nano Lett.,* **7**, 2758.
115. Ward L. (1994). *The Optical Constants of Bulk Materials and Films*, IOP Publishing Ltd, London, UK.
116. Blake P., Hill E.W., Neto A.H.C., Novoselov K.S., Jiang D., Yang R. (2007). *Appl. Phys. Lett.*, **91**, 063124.
117. Park J.S., Reina A., Saito R., Kong J., Dresselhaus G., Dresselhaus M.S. (2009). *Carbon*, **47**, 1303.
118. Bae S., Kim H., Lee Y., Xu X., Park J.S., Zheng Y. (2010). *Nat. Nanotechnol.*, **5**, 574.
119. Nair R.R., Blake P., Grigorenko A.N., Novoselov K.S., Booth T.J., Stauber T. (2008). *Science,* **320**, 1308.
120. Kravets V.G., Grigorenko A.N., Nair R.R., Blake P., Anissimova S., Novoselov K.S. (2010). *Phys. Rev. B,* **81**, 155413.
121. Sheats J.R., Antoniadis H., Hueschen M., Leonard W., Miller J., Moon R. (1996). *Science,* **273**, 884.
122. Rothberg L.J., Lovinger A.J. (1996). *J. Mater. Res.,* **11**, 3174.
123. Eda G., Lin Y.Y., Mattevi C., Yamaguchi H., Chen H.A., Chen I.S. (2010). *Adv. Mater.*, **22**, 505.

124. Cote L.J., Kim J., Tung V.C., Luo J., Kim F., Huang J. (2011). *Pure Appl. Chem.,* **83(1)**, 95–110.

125. Paek S.M., Yoo E., Honma I. (2008). *Nano Lett.*, **9**, 72.

126. Lahiri I., Oh S.W., Hwang J.Y., Cho S., Sun Y.K., Banerjee R. (2010). *ACS Nano*, **4**, 3440.

127. Guo Z.P., Zhao Z.W., Liu H.K., Dou S.X. (2005). *Carbon*, **43**, 1392.

128. Fu Y., Ma R., Shu Y., Cao Z., Ma X. (2009). *Mater. Lett.,* **63**, 1946.

129. Dimov N., Kugino S., Yoshio M. (2004). *J. Power. Sour.*, **136**, 108.

130. Yoo E., Kim J., Hosono E., Zhou H.S., Kudo T., Honma I. (2008). *Nano Lett.,* **8**, 2277.

131. Pan D., Wang S., Zhao B., Wu M., Zhang H., Wang Y. (2009). *Chem. Mater.,* **21**, 3136.

132. Wang H., Cui L.F., Yang Y., Sanchez Casalongue H., Robinson J.T., Liang Y. (2010). *J. Am. Chem. Soc.,* **132**, 13978.

133. Rana V.K., Akhtar S., Chatterjee S., Mishra S., Singh R.P., Ha C.S. (2014). *J. Nanosci. Nanotechnol.,* **14(3)**, 2425–2435.

134. Robinson J.T., Perkins F.K., Snow E.S., Wei Z., Sheehan P.E. (2008). *Nano Lett.,* **8**, 3137.

135. Jung I., Dikin D., Park S., Cai W., Mielke S.L., Ruoff R.S. (2008). *J. Phys. Chem. C,* **112**, 20264.

136. Fowler J.D., Allen M.J., Tung V.C., Yang Y., Kaner R.B., Weiller B.H. (2009). *ACS Nano*, **3**, 301.

137. Lu G., Ocola L.E., Chen J. (2009). *Appl. Phys. Lett.,* **94**, 083111.

138. Arsat R., Breedon M., Shafiei M., Spizziri P.G., Gilje S., Kaner R.B. (2009). *Chem. Phys. Lett.,* **467**, 344.

139. Joshi R.K., Gomez H., Alvi F., Kumar A. (2010). *J. Phys. Chem. C,* **114**, 6610.

140. Ganhua L., Ocola L.E., Chen J. (2009). *Nanotechnol.,* **20**, 445502.

141. Ganhua L., Leonidas E.O., Junhong C. (2009). *Appl. Phys. Lett.,* **94**, 083111.

142. Li X., Wang H., Robinson J.T., Sanchez H., Diankov G., Dai H. (2009). *J. Am. Chem. Soc.,* **131**, 15939.

143. Jung I., Dikin D., Park S., Cai W., Mielke S.L., Ruoff R.S. (2008). *J. Phys. Chem. C,* **112**, 20264.

144. Dua V., Surwade S.P., Ammu S., Agnihotra S.R., Jain S., Roberts K.E. (2010). *Angew. Chem. Int. Ed.,* **49**, 2154.

145. Shafiei M., Spizzirri P.G., Arsat R., Yu J., du Plessis J., Dubin S. (2010). *J. Phys. Chem. C,* **114**, 13796.

Chapter 4

Potential Applications

Graphene-related materials (GRMs) possess the fascinating properties which enable their use in potential applications such as biomedical, optics, electronics, sensing and energy and metal adsorption.

Major applications of GRMs are in development of solar cells, fuel cells, Li-ion batteries and SCs, ion exchange, molecular adsorption, etc. Following categories briefly represent the important applications [1–80].

4.1 Biomedical Applications

A nanotechnology usesful for treatment, monitoring, diagnosis and control of biological systems is called "nanomedicine" [81]. NPs have offered unique properties for their applications as drug delivery systems and image agents [82]. NPs enable to combine the diagnostic process with therapy (theranostics). Most of NPs are available from polymeric and metallic ones, dendrimers, to liposomes, microcapsules, etc. [83]. Recently, GRMs have attracted considerable attention for their potential use in nanomedicine and biology [84]. A graphene can be covalent functionalised by common approach, which offers a new class of solution-dispersible polyaromatic platform for performing polymer chemistry. The presence of the functional groups with graphene makes GO more hydrophilic [85],

Graphene Nanomaterials: Fabrication, Properties and Applications
Satyendra Mishra and Dharmesh Hansora

ISBN 978-981-4745-41-3 (Hardcover), 978-1-315-36455-1 (eBook)
www.panstanford.com

which also allows its easy dispersion in water [86]. The functional groups allow GO to interact with a wide range of inorganic and organic species in non-covalent, covalent and ionic matrices, and hence functional hybrids can be synthesised in this manner [87]. GO is fluorescent over a broad range of wavelengths in contrast to pure graphene [88, 89]. This tunable fluorescence was used in biological applications particularly for sensing [90, 91] and drug delivery [92]. Research on graphene for biomedical applications is progressing rapidly due to the previous know-how gained using CNTs [93], since the surface chemistry is also adaptable. Both materials CNTs and graphene show similar behaviour, i.e. graphene provides additional functionalities with respect to CNTs, e.g. an enhanced loading of biomolecules, due to its 2D shape [94]. Latest challenges confirm the controlled chemical functionalisation of graphene to achieve good processability as well as the fine tuning of various physicochemical properties. Main aim of the controlled surface oxidation is to develop the anchoring points for additional surface groups such as (i) an attachment of biomolecules, e.g. peptides, DNA, growth factors via carboxyl groups and KOH/NaOH activation to induce carboxylic acid functional groups; (ii) PEG coatings for prolonged blood circulation half-life and avoiding the agglomeration; (iii) sulfonation and (iv) halogenation for changing the surface hydrophobicity, starting point for conversion into other functional groups, e.g. amines, anilines, alcohols or thiols [95]. GO provides a robust framework in such a way that two or more components can be incorporated for multifunctional capabilities [96]. A conjugation of multiple components such as tumour-targeting moieties, fluorescent molecules, anticancer drugs or small interfering ribonucleic acid (RNA) to GO represents a viable strategy to target human cancer and also for imaging from inside the body by magnetic resonance or fluorescent imaging. A capability to simultaneously image and treat tumours with nanocarriers generally provide advantages over conventional chemotherapies having added value of reducing secondary effects. Nanocarriers, as molecular transporters, are considered to shuttle various types of drugs, including biological molecules, proteins, RNA, DNA, into cells by endocytosis. All these materials are intended to be used in nanomedicine that must be carefully tested for their potential effects on animals, cells and environment. The nanosize and the tunable surface chemistry of

graphene flakes allow them to interact efficiently with cells, which can be diffused further into tissues and through individual cells. Thus, particle size and shape are key parameter to control particle flow and cell internalisation [97]. Graphene sheets may flow along capillaries, lymphatics or tumour vessels without any obstructions. Flow is dependent on surface functionalisation; because aggregation of flakes must be avoided at any time. All imaging agents must have a rapid clearance from blood to obtain low background signals and high quality images [98]. Surface charge of NPs and hydrodynamic diameter in presence of plasma proteins are more important for their bio-distribution, excretion and rapid clearance from blood [98]. Size control and/or size separation are also necessary to interface with *in vitro* or *in vivo* biological systems. Proper ways such as ultra-centrifugation and filteration are used to control size [99–101]. Graphene sheets have been used in applications related to biosensing and bioelectronics, particularly low electronic noise with chemical stability[102], that offer an excellent platform for the developing the FET-based biosensors [103]. A low noise observed in GFETs (down to 10 μV rms) [102] may enable the detection of small electrical and chemical signals. The modification of the transistor's active area with functional groups and biomolecules (DNA, enzymes, antibodies) allow for the development of sensors specific to particular analytes, which are useful in applications related to proteomics, drug screening and genomics.

Numerous studies have been reported indicating the graphene's bioapplications in chemotherapeutics for the cancer treatment [104],biosensing applications for a host of medical conditions [105] and for the differentiation and imaging of stem cells [106]. Reports have demonstrated that the combination of graphene with NMs such as graphene–NP hybrid structures, offers an additional unique physicochemical properties and functions that are desirable and advantageous for bioapplications (Fig. 4.1) [107]. The graphene–NP hybrid structures display the individual properties of the NPs, such as optical, magnetic, electronic and structural properties that are unavailable in bulk materials, they also exhibit additional advantageous and often synergism of the multi-properties that greatly augment their potential for bioapplications. In general, graphene–NP hybrid materials can be categorised into two classes (Fig. 4.2): (i) graphene–NP composites, i.e. NPs decorated or grown

on graphene sheets (Figs. 4.2A,B) or (ii) graphene-encapsulated NPs, i.e. NPs wrapped or coated with graphene (Figs. 4.2C,D).

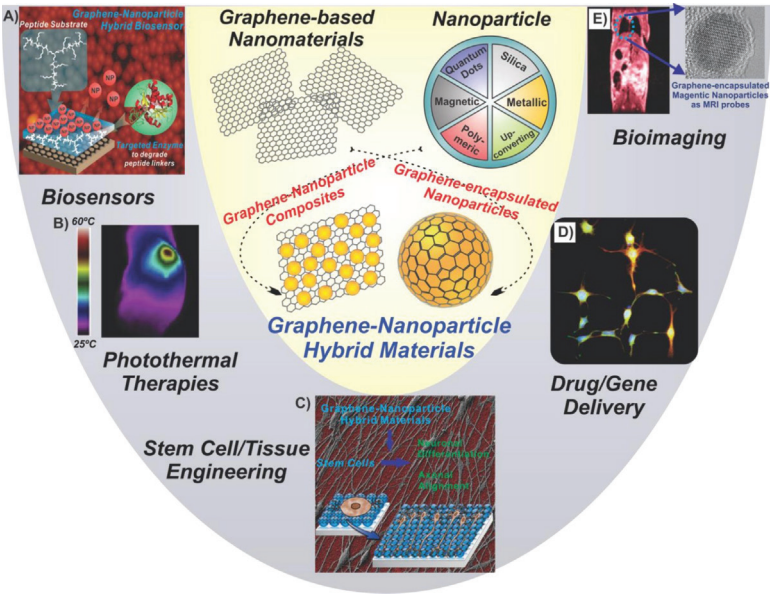

Figure 4.1 Graphene-NP hybrids exist in two forms, as graphene–NP composites and graphene-encapsulated NPs, and can be used for various bioapplications, including biosensors, photothermal therapies, stem cell/tissue engineering, drug/gene delivery, and bioimaging. Panel (A) reprinted by permission from Ref. [108], Copyright 2012, John Wiley and Sons. Panel (B) reprinted from Ref. [109], Copyright 2013, with permission from Elsevier. Panel (C) reprinted by permission from Ref. [110], Copyright 2013, John Wiley and Sons.

Graphene–NP hybrid structures are synthesised by combining the graphene or its derivatives, GO and RGO, with various types of NPs such as quantum dots (QDs), metal (e.g. noble metal and magnetic), metal oxide or silica NPs (Si NPs), depending on the final desired functional properties. Combining these unique and robust materials, striking synergistic properties can often be achieved. Decorating the metal or metal oxide NPs on graphene surfaces has shown some implications on the charge transfer behaviour through the surface modification of the local electronic structure of graphene [111]. Hence these type of composite materials show improved performance as catalysts. As sensing applications perspectives, the

combination of NPs should have excellent conductivity and catalytic properties with graphene materials that enhance the sensitivity and selectivity over the surface of graphene or NP-based sensors alone [107, 114]. By combining the graphene with NPs, resulting composites can be used to deliver RGO (e.g. small molecule drugs, nucleic acids, etc.) to target cells (e.g. cancer cells or stem cells) by enabling complementary multifunctionalities such as imaging (e.g. surface-enhanced Raman spectroscopy (SERS) or magnetic resonance imaging (MRI)) and hyper-thermia (e.g. using near-infrared [NIR] radiation) [115].

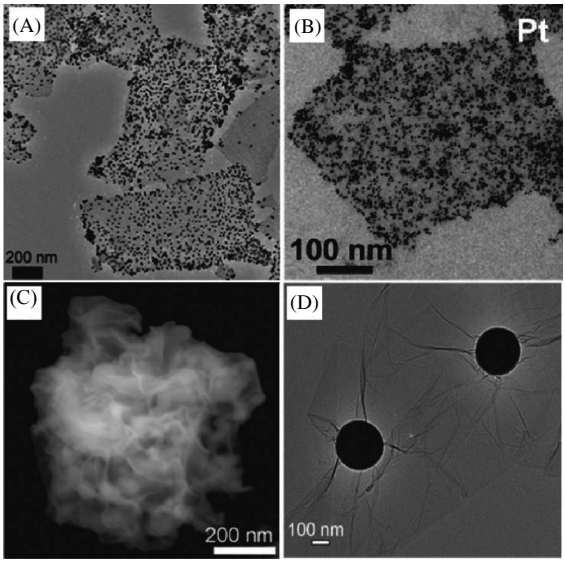

Figure 4.2 Graphene–NP hybrid structures. Panels (A) and (B) show graphene-NP composites wherein NPs are decorated on the surface of graphene sheets. Panel (A) reprinted from Ref. [114c], Copyright 2011, with permission from Elsevier. Panel (B) reprinted with permission from Ref. [112], Copyright 2010, American Chemical Society. Panels (C) and (D) show graphene-encapsulated NPs wherein NPs are wrapped by graphene. Panel (C) reprinted with permission from Ref. [113], Copyright 2012, American Chemical Society. Panel (D) reprinted with permission from Ref. [114a], Copyright 2010, John Wiley and Sons.

Graphene hybrid nanocomposites have been used in numerous biomedical applications like graphene paper, drug delivery, biodevices and bioimaging. Fig. 4.3 shows the molecular coating of a gold NPs that was imaged by masking the crystalline reflections of the

graphene support and the gold NPs. The result suggested atomically thin graphene-supported films that can be used to directly image a diverse range of molecular coatings on NPs such as proteins, DNA and antibody–antigen pairs [24–26, 37–39, 72, 73].

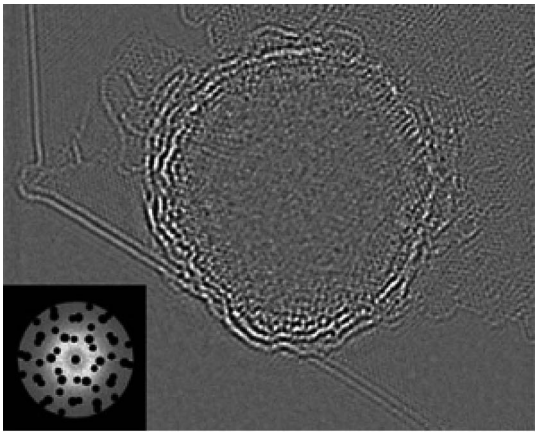

Figure 4.3 Atomic-resolution direct TEM image of the citrate molecules coating a gold NP supported by a graphene sheet. Reprinted with permission from Ref. [40], Copyright 2009, American Chemical Society.

4.1.1 Biosensors

The integration of biological components with electronics is growing field and one of the current challenges for the field of bioelectronics. This holds a great promise for developing the prostheses for injured organs. Biology and electronics may interface at three levels namely molecular, cellular and skeletal. The initial interactions at the bio-molecular level will determine long-term performance for any implanted bioelectronic material. Bioelectronics is associated with skeletal level enhancements (e.g. artificial muscles), and electronic communication with living cells is of interest for tissue engineering or for implantation such as bionic eyes [116] and or ears [117]. For development of bioelectronics, different materials were proposed and investigated. Special material properties [118] such as electrochemical stability, biocompatibility and electronic and chemical functionality are in demand for bioelectronics. Metals,

Si and GaAs and carbon-based materials provide considerable advantages. On other hand, graphene provides a unique combination of physical, electronic and chemical properties, which allow to surpass the state-of-the-art for bioelectronics and biosensor applications [118–121]. Indeed, a graphene is impervious to the harsh ionic solutions found in the human body [122]. Graphene can conduct electrical signals to interface with neurons and other cells that communicate by nerve impulse, or action potential [122]. These features make the graphene as promising candidates for next-generation bionic technology [118, 122]. Current research in nano-biosensors shows a fast growth due to the wide range of novel applications for human healthcare. A biosensor combines a biological component with a physicochemical detector component and hence it is designed for the detection of a certain analyte. Biosensors are used for sensitive and selective detection of biologically-relevant molecules, such as applications in diagnosis (e.g. for detection of the cancer biomarkers), biomedical research, food quality control and environmental monitoring [123]. As Si stability [124, 125] is low, i.e. Si generally oxidises by interacting with atmospheric oxygen and organic solutions, or by hydrolysing with aqueous solutions, to give a SiO_2 surface. The possible use of Si transistors in the human body requires a coating with iron oxide [126] to boost their stability [122]. Other semiconductor technologies such as GaN [127], SiC [128] and diamond [129–131] are also explored, which also increase our interest in flexible biosensors [132]. The use of graphene in biosensors may allow the development of flexible sensors, as well as an improvement of impedance and biocompatibility with a high added value. Graphene are used to implement grids of switches to control multi-array biosensors or to integrate computing/decision power for applications such as impedance sensors, health, medical, pharmaceutical, DNA chips, bio-monitoring, bio-lab–on-a-chip and biomedical calibration.

Biosensors are analytical devices which utilise biological sensing elements to detect and/or quantify a particular target analyte or family of analytes. As such, biosensors are applicable to and are important for virtually every conceivable analytical task in the biomedical field, which can range from applications in

medical diagnostics to drug discovery, food safety, environmental monitoring and defence. In general, biosensors are composed of two fundamental elements: a receptor and a transducer. The receptor consists of any material, either organic or inorganic, which can interact with a target analyte or family of analytes. On the other hand, the transducer converts the recognition event which occurs between the analyte and the receptor (e.g. the binding of an enzyme to its substrate, binding between an antibody and its target protein or reduction/oxidation of an electroactive biomolecule by the sensing electrode) into a measurable signal which can come in many forms, including, but not limited to, electronic, electrochemical and optical signals. In terms of its performance, biosensors are evaluated on the basis of sensitivity to the target(s), limit of detection (LOD), linear and dynamic ranges, reproducibility or precision of its response and selectivity [133]. Other parameters often compared and useful include the sensor's response time (e.g. the amount of time needed for the sensor response to reach 95% of its final value after introduction of the analyte(s)), operational and storage stability, ease of use and portability. Moreover, the ideal biosensor should be reusable, thereby allowing for several consecutive measurements to be made.

Graphene–NP hybrids are particularly well suited for biosensing applications. As mentioned previously, graphene possesses numerous unique and advantageous physicochemical properties, including an extremely high surface area, excellent electrical properties, high mechanical strength, advantageous optical properties (e.g. transparent and can quench fluorescence), and is relatively easy to functionalise and mass produce. As such, there has been significant effort invested in utilising this material for the development of biosensors [134, 135]. Moreover, NPs have also been widely investigated in the field of biosensing due to the exquisite sensitivity that NMs can offer for this type of application [136]. Specifically, because of the diameter of NPs (e.g. 1–100 nm scale), these NMs can display unique physical and chemical features (e.g. quantum size effect, surface effect and macro-quantum tunnel effect). As such, NPs can be used to enhance achievable sensitivities by amplifying the obtained signal as well as increasing the available

surface area for analyte binding. By combining these two excellent and unique modalities as graphene–NP hybrids, a number of advantageous properties are attained for biosensing applications. In particular, it has been observed that graphene acts as an excellent material with which to immobilise NPs and enhance their stability (e.g. preventing aggregation). Moreover, the combination of graphene with NPs can increase the available surface area for analyte binding as well as improve their electrical conductivity and electron mobility, thereby enhancing the achievable sensitivity and selectivity [107]. In particular, the field of graphene–NP hybrid materials for biosensing applications can be generally divided into three classes based on the underlying mechanism of detection. These classes include electronic, electrochemical and optical sensors, with each class having its own advantages and disadvantages.

Several studies have demonstrated RGO-based biosensors as well. Mohanty and Berry [137] reported on the fabrication and functioning of a novel RGO-based (i) single-bacterium device, (ii) label-free DNA sensor and (iii) bacterial DNA/protein and polyelectrolyte transistor. The bacteria/RGO biodevice was highly sensitive with a single bacterium with a p-type FET property.

The presence of DNA on RGO increased both the conductivity and the mobility (Figs. 4.4(a,b)) due to the interaction between the charged amine group and the RGO. Similarly, single-stranded DNA when tethered on graphene hybridises with its complementary DNA strand, which reversibly increases the hole density by 5.61×10^{12} cm^2. Also the bending-insensitive RGO FETs were able to detect the presence and dynamic cellular secretion of biomolecules. The specificity of the demonstrated detection is realised in the defined biological context. The RGO FETs can also specifically detect biomolecules with high sensitivity using specific antibodies [138]. The fabrication and characterisation of a highly sensitive and selective FET biosensor using AuNP antibody conjugates decorated with GO sheets have been reported by Mao et al. [139]. The study demonstrates a GO-based immuno-biosensor for detecting a rotavirus as a pathogen model. The sensor showed high sensitivity and selectivity by using GO. CdTe/RGO composite also exhibited the chemical–biological sensing where graphene worked as an amplified

electrogenerated chemiluminescence (ECL) of QDs platform [140]. The study opens avenues for glutathione drug detection with graphene-based electronics glutathione drug detector or sensor.

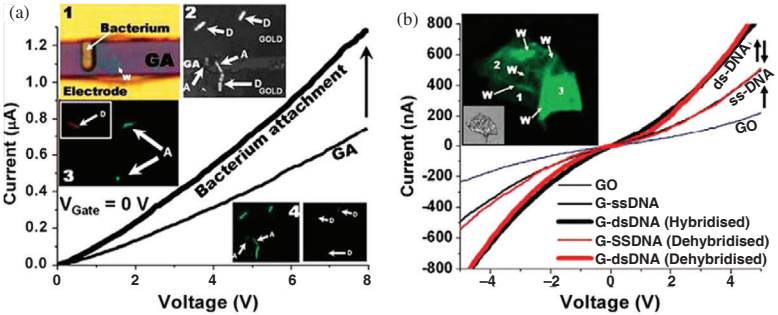

Figure 4.4 (a) The conductivity of the p-type graphene-amine (GA) device increases upon attachment of a single bacterial cell on the surface of GA (inset 1). LIVE/DEAD confocal microscopy test on the bacteria deposited on GA confirmed that most of the bacteria were alive after the electrostatic deposition (inset 3). (A) Alive and (D) dead. The LIVE/DEAD test conducted immediately after the electrical measurements on the GA-gold-bacteria device (inset 2 and inset 4) showed that the bacterial cells on GA atop silica remain alive, while the bacteria deposited on the GA atop gold electrodes die after electrical measurements (inset 4 (right)). (b) DNA transistor: ssDNA tethering on GO increases the conductivity of the device. Successive hybridisation and dehybridisation of DNA on the G-DNA device results in completely reversible increase and restoration of conductivity. Inset shows a G-DNA(ds) sheet with wrinkles and folds clearly visible. Reprinted with permission from Ref. [137], Copyright 2008, American Chemical Society.

4.1.1.1 Electronic sensors

As compared to the other methods available for biosensing applications, NM-based electronic biosensing offers significant advantages, such as high achievable sensitivities, high spatial resolution for localised detection, easy miniaturisation, facile integration with standard semiconductor processing and label-free, real-time detection, which can be achieved in a nondestructive manner [141]. In particular, these electronic sensors primarily utilise the principle of FETs to convert the biological recognition event to a measurable electronic signal. In a standard FET device, current flows along a semiconductor path (the channel), which connects two electrodes

(the source and the drain). The conductance of the channel between the source and the drain is then switched on and off by a third electrode (the gate), which is capacitively coupled to the device through a thin dielectric layer [142, 143]. Specifically, in FET-based biosensors, the channel is in direct contact with the sensing sample, which enhances the achievable sensitivity as any single biological event occurring at the channel surface could result in a variation in the surface potential thereby modulating the channel conductance [144]. Currently, FET sensors composed of Si nanowires or CNTs are the most heavily investigated [144, 145]. FET sensors utilising either of these materials exhibit exceptional performance with their achievable LOD falling in the range of picomolar (pM) to femtomolar (fM); however, the achievable sensitivity of devices which use these materials is limited by the rarity of binding events occurring between the probe and its target molecule due to the scarcity of available binding sites on the surface of the materials [142]. Moreover, the use of Si nanowires is expensive. On the other hand, while CNT sensors represent a significantly cheaper option, the reproducibility of CNT-based devices in terms of their fabrication and electrical properties is considered a significant limiting factor [146]. As such, graphene-based materials have a major advantage in FET sensing applications in that graphene has an extremely high surface-to-volume ratio, which increases the likelihood of binding events. In particular, graphene-based FET biosensors are able to compete with CNT and Si nanowire–based FET sensors with an ultrasensitive LOD down to a similar (pM to fM) and potentially lower range [147]. More specifically, because of this high surface-to-volume ratio, any analytes which adsorb onto the graphene surface could potentially alter its electronic properties (e.g. the conductivity can be altered when an analyte is adsorbed due to doping or a change in the carrier mobility of graphene). In addition, by utilising graphene–NP hybrid materials, it is possible to further push this limit to the attomolar (aM) range for biomolecule detection by utilising the synergism which occurs in these unique structures, wherein the combination of two materials results in additional surface area for analyte binding as well as signal amplification and enhanced electrical conductivity. For instance, Zhang et al. [148] determined that the covalent linkage of AuNPs to GO could enhance the electronic conductivity when compared to GO alone [148]. Similarly, Dinh et al. reported that the formation of

RGO–AgNPs decreased the sheet resistance from 10.93 kΩ/sq (for RGO) to 270 Ω/sq [149].

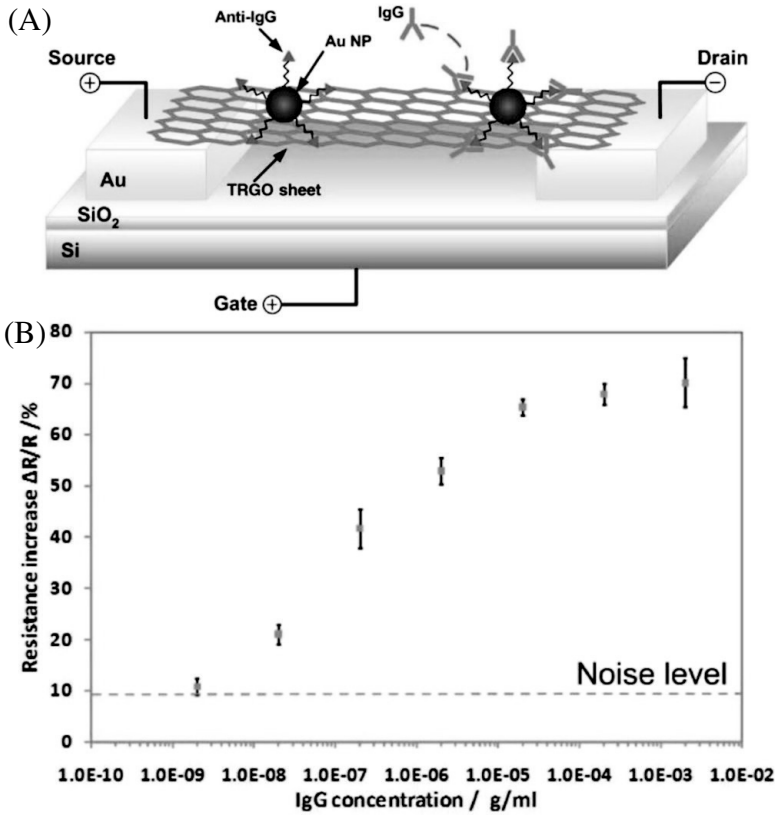

Figure 4.5 Protein detection using thermally reduced GO (TRGO) sheets decorated with gold NP–antibody conjugates. (A) Schematic of a TRGO FET. Anti-IgG is anchored to the TRGO sheet surface through AuNPs and functions as a specific recognition group for IgG binding. The electrical detection of protein binding is accomplished by FET and direct current measurements. (B) Sensor sensitivity versus IgG concentration. Dashed line represents the noise level from the buffer solution. Reprinted by permission from Ref. [150], Copyright 2010, John Wiley and Sons.

Demonstrations utilising graphene–NP hybrid-based FET biosensors have focused on exploiting variations of a single mechanism. Specifically, studies have shown that by conjugating the detection probe (e.g. antibody) to the NP and then using these

NP–probe conjugates to form graphene–NP composites, one can preserve the superb electrical properties of graphene.

In these cases, the formation of the graphene–NP hybrid generally occurs via electrostatic interaction and van der Waals binding. As such, as long as detection probe conjugation does not significantly affect the charge of the NPs, graphene–NP composites can be formed without any steric hindrance. One popular FET-based biosensing application which has utilised this concept is for the detection of proteins. Protein detection is particularly important as proteins play an essential role in all biological functions. As such, they are at the centre of almost all pathological conditions, and the majority of disease markers are composed of proteins. Chen et al. [150] reported the first graphene–AuNP hybrid sensor for the detection of proteins [150]. In this case, thermally reduced GO sheets (TRGO) (e.g. a few layers with a thickness of 3–6 nm) were decorated with 20 nm AuNPs, which were covalently conjugated to anti-immunoglobulin G (IgG) antibodies (Fig. 4.5A). Upon introduction of the target protein (e.g. IgG), FET and direct current was measured resulting in an LOD of approximately 13 pM (Fig. 4.5B), which is among the best LODs when compared to carbon NM-based protein sensors, including CNTs [151], graphene and GO [152]. This sensor also showed excellent selectivity when exposed to samples containing mismatched protein such as immunoglobulin M (IgM) or horse radish peroxidase (HRP). In particular, when 0.8 mg/mL IgM and 0.2 mg/mL HRP were introduced to the sensor using the exact procedure as that used for IgG, the sensor response was 15.3% and 12.4%, respectively, which was significantly lower than that from the complementary IgG (68%). Last, it was observed that binding of the IgGs to their anti-IgGs resulted in local geometric deformations and an increase in the number of scattering centres across the sheet, thereby reducing the mobility of holes and, subsequently, the conductivity of the TRGO sheets. Besides preserving the excellent electrical properties of graphene, graphene–NP composites also exhibit additional advantages such as increasing available surface area for the binding of target analyte, enhanced stability and also amplified transduction signals [153]. For example, Kwon et al. [153] reported a novel liquid-ion gated FET using large-scale graphene micropattern

nanohybrids decorated with closely packed conducting polymer NPs for the detection of HIV [153]. Specifically, this closely packed NP array was composed of 20 nm carboxylated polypyrrole NPs, which were covalently modified with HIV-2 gp antigen and provided an enlarged surface area and stable sensing geometry. Therefore, they could detect the HIV biomarker at concentrations as low as 1 pM, which is better than any biosensor which has been reported for this particular purpose. Moreover, this biosensor exhibited excellent mechanical flexibility and durability. On the other hand, Kim et al. [154] demonstrated that, in addition to preserving the superb electrical properties of graphene and increasing available surface area, graphene–NP hybrids could also be designed to amplify the transduction signal, thereby further increasing the achievable LOD by a full order of magnitude [154].

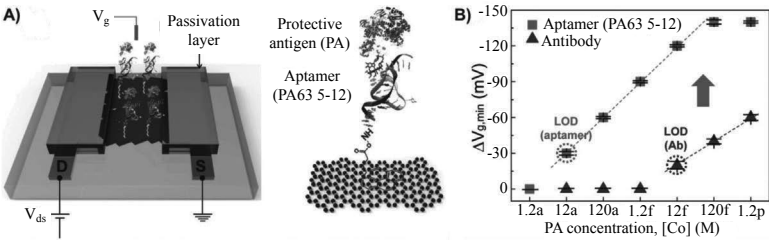

Figure 4.6 Electronic graphene–NP composite sensor utilising aptamers to detect anthrax toxin. (A) Schematic illustration of the aptamer-immobilised graphene FET for the detection of protective antigen (PA). (B) $V_{g,min}$ shift ($\Delta V_{g,min}$) versus PA concentration in PBS solutions with different probe molecules. The $\Delta V_{g,min}$ value was obtained by calculating the difference in the charge neutrality point, $V_{g,min}$, as a reference for the device with no binding of PA. Reprinted by permission from Ref. [154], Copyright 2013, John Wiley and Sons.

In this work, Kim et al. [154] fabricated a FET biosensor which had networked channels of chemically reduced GO nanosheets, which were modified with aptamers specific for the detection of anthrax toxin (e.g. protective antigen) (Fig. 4.6A). Briefly, in their design, the source/drain electrodes were formed on a networked film composed of RGO nanosheets using a shadow mask to prevent the deposition of polymeric residues during photolithography. Next, passivation of the electrodes was achieved with a 200 nm thick Al_2O_3

layer and direct pasting with PDMS, which minimised the local work function modulation and isolated the leakage current between the electrode and electrolytes. In this way, Kim et al. [154] achieved an ultralow LOD of 12 aM in 10 μM PBS. Furthermore, by utilising secondary aptamer-conjugated AuNPs, they were able to achieve an even lower LOD of 1.2 aM (Fig. 4.6B). This was attributed to the ability of the secondary aptamer-conjugated AuNPs to further amplify the transduction signal. As for the achievable selectivity, the authors exposed their sensor to a PBS solution containing carcinoembryonic antigen (CEA). The results showed no shift in voltage and no change in current, indicating that no CEA binding occurred. As a variation of the above-mentioned mechanism, encapsulating NPs with graphene can also enhance the surface-to-volume ratio, which is available for the capture of target analyte in FET sensors while enhancing stability. Myung et al. [155] developed an RGO-encapsulated NP-based FET sensor for the sensitive and selective detection of proteins (Fig. 4.7) [155]. In particular, they sought to detect human epidermal growth factor receptor 2 (HER2) and epidermal growth factor receptor (EGFR), which are both known to be overexpressed in breast cancers [156]. To this end, individual silicon oxide NPs (100 nm diameter) functionalised with APTES were coated with a thin layer of RGO (5 nm thick) due to the electrostatic interaction which could occur between the negatively charged GO sheets and the positively charged silicon oxide NPs. Arrays of RGO NPs (RGO-NP) were then patterned to form channels between gold electrodes, which occurred through a self-assembly process upon centrifugation of the device with a solution containing RGO–NPs (Fig. 4.7A). Finally, the RGO–NPs were functionalised with monoclonal antibodies against HER2 or EGFR (Fig. 4.7B).

Specifically, this was accomplished using a well-established process where the RGO surface was functionalised with 4-(pyren-1-yl)butanal via π–π stacking. Next, the aldehyde groups were coupled to the amine groups of the HER2 or EGFR antibodies through reductive amination and unreacted aldehyde groups were blocked using ethanolamine. In this way, the electrical properties of the RGO were preserved by not conjugating the antibodies directly to the

RGO surface while increasing the available surface area available for detection over RGO alone. Using this device, an LOD was achieved as low as 1 pM for HER2 and 100 pM for EGFR (Fig. 4.7D–F). In addition, the highly selective nature of biosensor was demonstrated in the presence of other proteins such as BSA (50 μg/mL), which did not induce a change in conductance. Finally, besides proteins, the detection of specific nucleic acids (e.g. DNA or RNA) has garnered significant attention as it can be utilised for various bioapplications, including, but not limited to, pathogen identification, recognition of genetic mutations and forensic analysis [157]. For instance, Yin et al. [158] reported a PtNP-decorated RGO FET where a thiolated DNA probe was attached to the PtNPs via Pt–S bonding [158]. Specifically, a large, continuous, few-layer thick film of GO was fabricated via the Langmuir–Blodgett method and subsequently reduced with high-temperature annealing in an Ar/H_2 atmosphere at 1000°C. To form graphene–NP composites, the PtNPs were directly synthesised on the RGO film by immersion of the RGO in an ethanolic solution of $PtCl_4$ followed by light irradiation. It was found that this graphene–NP composite-based FET, when modified with probe DNA, was able to detect the real-time hybridisation of target DNA in PBS with a calculated detection limit of 2.4 nM. Moreover, the sensor exhibited good selectivity. For instance, when 1 μM of noncomplementary DNA was added to the sensing chamber, there was no obvious change in the conductance. Overall, the performance of hybrid electronic sensors depends strongly on graphene morphology (e.g. wrinkles, folds, number of layers), the number of graphene sheets, the level of graphene reduction and the interface which exists between the NPs and graphene, which can all influence the electrical properties of the device. In particular, the morphology (e.g. wrinkles, folds, number of layers) of graphene should be free of defects and, as such, hinges on the synthesis method used. On the other hand, the NP–graphene interface is highly susceptible to modulations by adsorbed species, and the Schottky barrier of the interface has been shown to significantly change device conductance [150]. In particular, smaller sized NPs can be distributed more uniformly on graphene materials and provide more contact area than bigger sized NPs, resulting in an improvement in electrical properties [149].

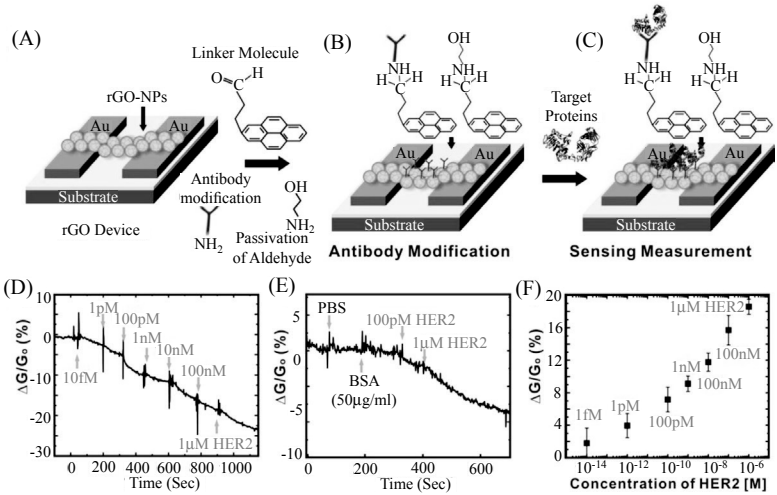

Figure 4.7 Real-time detection of cancer marker, HER2, using a graphene-encapsulated NP-based FET biosensor. (A) The preparation of the RGO–NP device. (B) Surface functionalisation of RGO for immobilising the antibody. (C) Measuring conductance of the devices when the target protein is introduced. (D) The sensitivity of the biosensor (relative conductance change, %) in response to the concentration of HER2 with V_{DS} (voltage drain to source) = 1 V and V_g (gate voltage) = 0 V. (E) The selectivity of the biosensor in response to PBS buffer, BSA with 50 μg/mL, and HER2 (100 pM and 1 μM). (F) Sensor sensitivity (relative conductance change, %) as a function of the HER2 concentration with V_{DS} = 1 V and V_g = 0 V. All experiments were performed multiple times (sample number, *n* = 30) to collect statistical data (with error bars) and confirm the reproducibility and robustness of the biosensing system. Reprinted by permission from Ref. [155], Copyright 2011, John Wiley and Sons.

4.1.1.2 Electrochemical sensors

Electrochemical sensors are, by far, the largest group of sensors and provide an especially attractive means with which to analyse the content of a biological sample due to the direct conversion of a biological recognition event to an electrical signal. A typical electrochemical sensor consists of a sensing (or working) electrode, which has a biological recognition element, and a counter-electrode, which are separated by a layer of electrolytes. Electrochemical biosensors can be divided into two main categories based on the nature of their biological recognition process: (i) affinity-based

sensors and (ii) catalytic sensors. Affinity sensors rely on the selective binding interaction which occurs between a biological component such as an antibody, enzyme, nucleic acid or a receptor (e.g. immunosensor or DNA hybridisation biosensor) and its target analyte, which results in the production of a measurable electrical signal. On the other hand, catalytic sensors generally incorporate NPs or enzymes which recognise the analyte of interest and produce electroactive species. The amount of analyte either reduced or oxidised at the sensing electrode would then correlate with the concentration of the target analyte present. In particular, various forms of voltammetry (e.g. linear sweep, differential pulse, square wave, stripping) and amperometry are commonly used for the electrochemical detection of biomolecules [159].

Graphene is an ideal material for electrochemical biosensors as it is an excellent conductor of electrical charge [160]. Moreover, because of its high surface area, graphene can facilitate a large number of defects and thus electroactive sites [161]. The electrochemical behaviour of graphene is also excellent and comparable to other carbon-based materials, including CNTs and graphite where recent reports have even demonstrated that graphene-based electrochemical sensors have superior performance when compared to CNTs due to the presence of more sp^2-like planes and edge defects on the surface of graphene [162]. While graphene exhibits great promise, graphene–NP hybrid structures have gained increasing attention for their applicability to electrochemical sensing. In particular, various types of NPs, including metal NPs such as Au and Pt, metal oxide NPs and semiconductor NPs, are already widely used for electrochemical sensing applications [163, 164]. These NPs can have different roles in electrochemical sensing platforms; for example, they can function to (i) immobilise biomolecules, (ii) catalyse electrochemical reactions, or (iii) act as a reactant. As such, by incorporating graphene–NP hybrid structures, one can impart unique and advantageous properties to electrochemical biosensors resulting in the exhibition of the advantages provided by the individual NP and graphene components as well as synergy from the hybrid. For example, graphene sheets decorated with NPs can help overcome the poor utilisation coefficient of aggregated NPs [165]. In certain cases, by decorating graphene with NPs, one can also efficiently improve the electron transfer which occurs between the

analyte and the electrode [166]. Finally, similar to the strategy used in some hybrid FET sensors, instead of immobilising the sensing biomolecules directly to graphene, which is often difficult and can negatively affect electrical properties, graphene–NP hybrids can be formed wherein the sensing biomolecules are first immobilised on the NPs prior to decoration onto graphene. As a result, this can enhance the achievable sensitivity of graphene–NP hybrid electrochemical sensors. RGO is highly promising for electrochemical and biological sensors due to their different functionalities on the edge [167–169], which are very sensitive to change in chemical and biological environment. The responses have been analysed by changes in conductivities, capacitances and doping effects on FETs made with RGO.

4.1.1.3 Optical sensors

The deoxidation of GO to RGO results in the formation of a material which is not only electrically conductive but also optically transparent with a transparency of ~97.7% and a transmittance which linearly decreases with the number of layers [170]. As such, besides their excellent electronic and electrochemical properties, graphene–NP hybrid materials which utilise graphene or RGO possess a number of advantageous optoelectronic properties as well, which can be utilised for optical sensing applications. In particular, optical sensors which incorporate graphene NMs fall into two categories: (i) fluorescence-based and (ii) SERS-based biosensors. In fluorescence-based biosensors, GO and RGO have the unique property that not only are they fluorescent over a broad range of wavelengths (e.g. visible to NIR range with their maximum intensity being located between 500 and 800 nm) [171], but they also have the ability to quench fluorescent molecules such as dyes and fluorescent NMs (QDs and upconversion NPs [UCNPs]) [172]. As such, graphene–NP composites composed of fluorescent NMs are immensely useful for the development of fluorescence resonance energy transfer (FRET)-based and nanometal surface energy transfer (NSET)-based biosensors, which can enable the quantitative analysis of molecular dynamics in living cells on the single cell level. On the other hand, graphene exhibits remarkable Raman scattering properties, which are related to its unique electron and phonon structure [173]. This Raman scattering can be greatly enhanced by the inclusion of

metal NPs (e.g. AuNPs and AgNPs) as graphene–metal NP hybrids, resulting in exceptional SERS effects, which can be used to detect the presence of individual biomolecules [174]. In the following subsections, the use of graphene–NP hybrid materials is described for optical sensing, in particular, fluorescence-based and SERS-based biosensors.

4.1.1.3.1 *Fluorescence-based sensors*

FRET is a type of fluorescence phenomenon which can occur when two fluorescent molecules are sufficiently close to one another (typically 1–10 nm). In this phenomenon, the energy from one fluorophore flows to the other via a nonradiative transfer [175]. Specifically, the first fluorophore, which is typically denoted as the "donor", is initially excited by an external optical source. Instead of emitting a photon, the excited donor transfers energy to the neighbouring fluorophore, which is termed the "acceptor". This leads to (i) the emission of fluorescence at the acceptor's characteristic wavelength and also (ii) quenching of the donor fluorophore. Because of the fact that the intensity of FRET depends strongly on the distance between the two fluorophores and their relative orientation as a donor or acceptor, FRET can be used to study, detect and quantify interactions which occur between two molecules. The donor and acceptor fluorophores can be brought together in many different configurations. For instance, one fluorophore can be attached to a substrate, while the other is attached to its binding site, and once the analyte of interest binds, FRET would be initiated. Alternatively, two fluorophores can be attached to a single protein and FRET can be initiated if and when the protein alters its conformation. Finally, the fluorophores can be linked to induce FRET, and once the linkage is cleaved (e.g. by an enzyme), FRET will cease to occur. As such, FRET is an excellent biosensing technique which can be superior to other optical detection methods in terms of its selectivity and sensitivity [176]. Moreover, FRET sensing is a nondestructive method, which can be used to detect molecular interactions within single living cells. Graphene and GO sheets were found to exhibit super quenching capabilities as energy acceptors for fluorescent dyes, whose efficiency is estimated to reach up to 30 nm, thereby providing greater flexibility for the construction of fluorescence sensors based on FRET. Similar to the quenching effect

seen with AuNPs, the mechanism underlying the superquenching effect of graphene and GO follows the NSET mechanism. Therefore, due to the superior quenching ability of graphene (e.g. the rate of this long-range resonance energy transfer depends on d^{-4}, where d is the distance, whereas traditional FRET depends on d^{-6}) [177], it can be coupled with other fluorophores such as fluorescent NPs (e.g. QDs and UCNPs) for use as FRET-based biosensors with enhanced capabilities.

In recent years, the use of anti-Stokes fluorophores such as UCNPs, which can be excited in the NIR, has successfully circumvented issues with autofluorescence and the scattering of light, which typically arise when utilising FRET in biological tissue. In particular, rare earth-containing UCNPs are able to emit high-energy photons under NIR excitation, which results from a nonlinear optical upconversion process, where the sequential absorption of two or more photons results in the emission of a single photon at a shorter wavelength [178]. As such, the use of UCNPs has made it possible to utilise FRET-based sensors directly on biological samples, wherein the use of graphene–UCNP hybrids has even greater advantages due to the superquenching properties of graphene, which greatly enhance the range of achievable FRET. As an example, Zhang et al. [173] utilised graphene–UCNP hybrids for glucose sensing [173]. In their system, they synthesised 50 nm water-soluble $NaYF_4$:Yb,Er UCNPs modified with poly(acrylic acid), which were then conjugated with concanavalin A (conA) via EDC coupling. On the other hand, the GO sheets were functionalised with chitosan, which also occurred via EDC coupling. In terms of the underlying mechanism, conA and chitosan were able to form tight bonds, which brought the UCNPs and GO into appropriate proximity to induce FRET (81% degree of quenching). However, in the presence of glucose, the FRET process was inhibited because of competition between glucose and chitosan for conA. By utilising this system, Zhang et al. were able to achieve an LOD of 0.025 μM even in the presence of serum. Specifically, the FRET process in the presence of serum was found to be nearly the same (with minor differences in the slope), suggesting the selectivity of the sensor. Similarly, Wu et al. [179] utilised $BaYF_5$:Yb,Er and $BaYF_5$:Yb,Tm UCNPs functionalised with aptamers against ochratoxin A (OTA) and fumonisin B_1 (FB_1), respectively [179].

In particular, OTA and FB_1 are mycotoxins, which are a group of chemical substances produced by some fungal species and can cause illness or even death. As such, strong π–π stacking between the aptamers and the sp^2 atoms of GO could be used to initiate FRET, and in the presence of OTA and FB_1, strong binding of the aptamers to the analytes resulted in the release of the UCNPs, thereby decreasing FRET (Fig. 4.8).

By utilising this mechanism, the authors achieved a linear range from 0.05 to 100 ng/mL for OTA and 0.1 to 500 ng/mL for FB_1 and a detection limit of 0.02 and 0.1 ng/mL for OTA and FB_1, respectively. In terms of selectivity, aflatoxins B_1, B_2, G_1 and G_2, fumonisin B_2, and zearalenone, which are all homologues of other mycotoxins found in foods, were evaluated. It was determined that only FB_1 and OTA could induce a dramatic fluorescence enhancement at their corresponding peaks, whereas the other analogues could not. QDs also exhibit a number of advantageous properties which make it an attractive NM for the formation of graphene–NP hybrids for FRET-based biosensors. In particular, QDs are inorganic and, as such, exhibit good resistance to photobleaching. Moreover, they exhibit a narrow emission band, broad absorption spectra, and have a size-tunable emission [180]. Dong et al. [181] gave the first report of efficient FRET between QDs and GO for biosensing applications [181]. Specifically, CdTe QDs which were conjugated with either a molecular beacon (MB), which is a single-stranded oligonucleotide hybridisation probe with a stem-and-loop structure in which the loop contains a probe sequence complementary to a target sequence and the annealing of self-complementary 5′ and 3′ ends forms a stem or aptamer, were used to detect DNA concentration and sequence (e.g. via MB) as well as proteins such as thrombin (e.g. via aptamer) (Fig. 4.9). By utilising this structure, a linear range was obtained from 50 to 1500 nM and an LOD of 0.5 and 50 nM was achieved for thrombin and ssDNA, respectively, which is highly sensitive and selective when compared to the other fluorescence or FRET-based methods (Fig. 4.9) [181]. Specifically, the MB-QD probe was able to differentiate between the perfectly complementary target, single-base mismatched strand (signal was 40% of the perfectly complementary target) and three-base mismatched strand (signal

was 15% of that perfectly complementary target). Moreover, the quenching efficiency was much higher for MB-QDs than the typical efficiency seen in MB-based detection, which helped improve the achievable sensitivity and dynamic range.

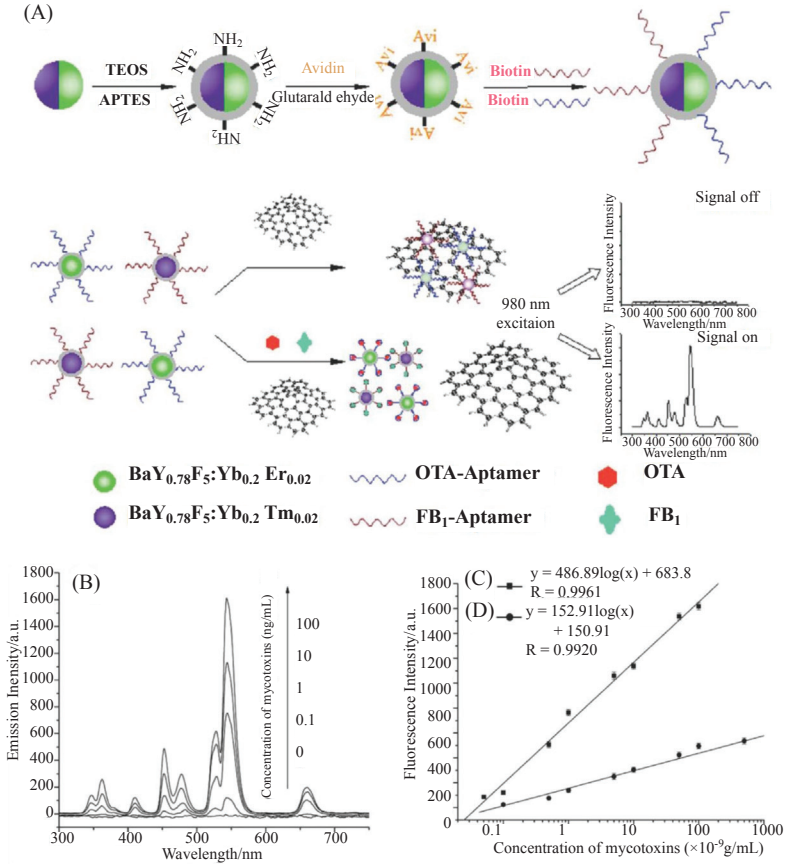

Figure 4.8 Multiplexed fluorescence resonance energy transfer aptasensor. (A) Schematic illustration of the multiplexed upconversion fluorescence resonance energy transfer between aptamers-UCNPs and GO for FB1 and OTA detection. (B) Upconversion fluorescence spectra of the multiplexed UCNPs-GO FRET aptasensor in the simultaneous presence of 0–100 ng/mL FB_1 and OTA. (C) A standard curve of the fluorescence intensity versus OTA concentration and (D) FB_1 concentrations measured by this developed method. Reprinted with permission from Ref. [179], Copyright 2012, American Chemical Society.

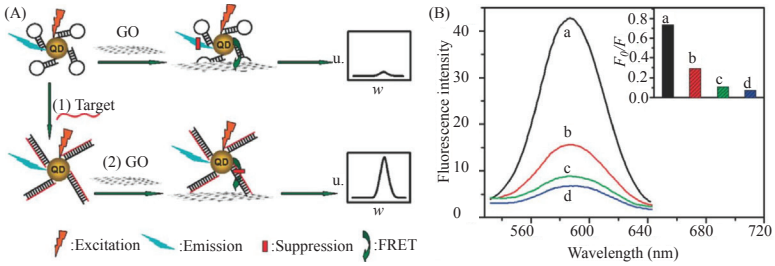

Figure 4.9 FRET between QDs and GO to sense biomolecules. (A) Schematic representation of GO-induced fluorescence quenching of MB-QDs and biosensing mechanism. (B) Fluorescence emission spectra of MB-QDs (50 nM) after incubation with (a) target (800 nM), (b) single-base mismatch strand (800 nM), (c) three-base mismatch strand (800 nM) and (d) no target and then addition of GO (0.1 μg/mL) for 5 min. Inset: Fluorescence intensity ratio F_0/F for four cases. Reprinted with permission from Ref. [181], Copyright 2010, American Chemical Society.

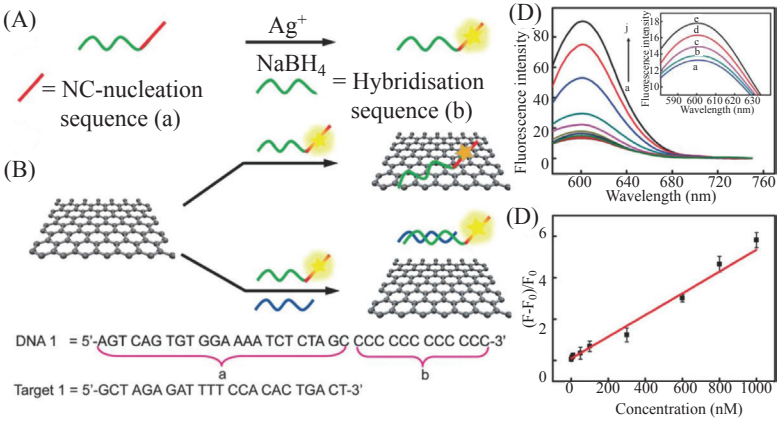

Figure 4.10 DNA-templated silver nanoclusters–GO hybrids for the detection of multiple nucleic acids. (A) Schematic representation of the preparation of silver nanoclusters on DNA scaffolds in aqueous solution. (B) Schematic illustration of the assay for label-free DNA detection using AgNCs–GO nanohybrid materials. (C) Fluorescence emission spectra of P1 (1 mM) upon addition of T1 with different concentrations: (a) control, (b) 1 nM, (c) 5 nM, (d) 10 nM, (e) 50 nM, (f) 100 nM, (g) 300 nM, (h) 600 nM, (i) 800 nM and (j) 1000 nM, which was then quenched with GO. Inset: A zoomed-in view of the data for low concentrations of target (a–e). (D) Linear relationship between $(F - F_0)/F_0$ (relative fluorescence intensity, where F_0 and F are the fluorescence intensities without and with the presence of target DNA, respectively) and the concentration of target DNA (1–1000 nM). Error bars were obtained from three parallel experiments. Reproduced from Ref. [184] with permission of The Royal Society of Chemistry.

Similarly, Li et al. [182] reported a novel "turn-on" fluorescent sensor which utilised a QD/aptamer-GO hybrid to detect lead(II) ions [182]. However, it should be noted that this concept could also be readily applied to the detection of biomolecules. Specifically, hybrids were formed between the aptamer-functionalised CdSe/ZnS QDs, which had a characteristic fluorescence emission at 569 nm, and GO via π–π stacking. In the presence of Pb^{2+}, these complexes were capable of changing their structural conformation from a 1D structure to a G-quadruplex/Pb^{2+} complex, leading to the detachment of the QD/aptamer complex from the surface of GO. This detachment then allowed for monitoring using fluorescence microscopy. In this way, a linear response range of 0.1–10 nM and an LOD of 90 pM (0.019 parts per billion) were achieved with this high sensitivity to the superquenching capabilities of GO, the significant difference in the affinity of the aptamer towards Pb^{2+} and GO, as well as the low-background signal due to the "turn-on" configuration. Moreover, when comparing the performance of this sensor to previous reports utilising fluorescence, colorimetric and electrochemical devices, this hybrid sensor exhibited an LOD which was 1–3 orders of magnitude better [183]. Finally, the sensor exhibited excellent selectivity towards Pb^{2+} wherein exposure to other metal ions such as Ag^{+}, Ca^{2+}, Cd^{3+}, CO^{2+}, Cu^{2+}, Fe^{2+}, Hg^{2+}, K^{2+} and Ni^{2+} did not induce any evident change in fluorescence. Last, researchers have combined GO with noble metal NPs to induce a double-quenching effect, which resulted in an increase in the achievable signal-to-noise ratio and thereby amplified the achievable sensitivity. For example, Qu et al. [184] reported a DNA-silver nanocluster–GO nanohybrid material for the detection of multiple nucleic acid targets (Fig. 4.10) [184].

In this biosensor, Ag nanoclusters were functionalised with an ssDNA reporter having a cytosine-rich DNA sequence (C_{12}) resulting in highly fluorescent Ag nanoclusters. These DNA–silver nanoclusters were then added to a solution of GO resulting in complex formation via π–π stacking and fluorescence quenching. Once the target sequence was introduced, the high binding affinity between the reporter DNA and the target sequence resulted in the release of the DNA–silver nanocluster and induced strong fluorescence which correlated with the concentration of target sequence DNA present. Using this mechanism, the multiple target nucleic acids could be detected with a high sensitivity (LOD: 1 nM), which was attributed to the high achievable signal-to-noise ratio resulting from the high

quenching efficiency of GO. In terms of selectivity, the sensor could discriminate between perfectly complementary target, one-base mismatched target (88.4% of the perfect target's signal), two-base mismatched target (67.4% of the perfect target's signal) and noncomplementary target (22% of the perfect target's signal). Chen et al. [185] also reported a similar detection platform which utilised AuNP-functionalised graphene for the detection of lead ions. This sensor was found to function in the concentration range of 50–1000 nM and had an LOD of 10 nm [185].

4.1.1.3.2 *SERS-based sensors*

SERS is a surface-sensitive technique for the enhancement of Raman scattering by molecules attached to or in close proximity of metal nanostructures and is one of the best techniques available for molecular analysis with sensitivities as low as the detection of single molecules [186]. In particular, SERS is a phenomenon which can amplify normally weak Raman signals by many orders of magnitude and occurs due to a combination of chemical enhancement, which is mainly related to the charge transfer between the metal nanostructure and the analyte molecules with electromagnetic enhancement (e.g. induced by the surface electron oscillation in the structure) [187]. As such, SERS-based sensors have been used in a variety of detection applications ranging from physics and engineering to biology and medicine [188]. To achieve high electric field intensities and to acquire significant enhancement in achievable sensitivities, it has become a common practice to pattern NPs/nanostructures composed of noble metals (e.g. Cu, Ag or Au) on substrates (e.g. silicon wafer). Enhancement is primarily caused by amplified, light-induced electric fields on the surface of the patterned metallic NPs. Specifically, when the incident light is in resonance with the oscillations of conducting electrons in a metallic NP, all of the electrons are collectively driven to oscillate in an optical phenomenon known as localised surface plasmon resonance (LSPR) [189]. This LSPR phenomenon is then responsible for the strong scattering and absorption of light, which is typically observed when utilising metallic NPs. This phenomenon is also responsible for the generation of enhanced E-fields on the surface of the NPs at sites known as "hotspots". Consequently, molecules within these hotspots experience enormous enhancement in their Raman cross section,

thereby potentially allowing for the detection of single molecules [190]. Interestingly, graphene and GO also have the ability to enhance Raman signals via a chemical enhancement mechanism, which is independent of the Raman enhancement caused by noble metal NPs [191]. In particular, it has been shown that mechanically exfoliated graphene sheets can induce Raman enhancement with a maximal enhancement of 17 fold, due to electron transfer between graphene and the molecules adsorbed on its surface [192]. Therefore, by using graphene or GO, which possesses numerous active oxygen sites which can enhance graphene–metal NP/molecule binding, it can be expected that the combination of graphene materials and metal NPs would act synergistically to further enhance SERS when compared to using either graphene or metal NPs alone (e.g. dual-enhancement of Raman signals by hybrid materials via chemical and electromagnetic enhancement). Using this strategy, graphene–NP hybrid materials have been developed to successfully detect a variety of biomolecules. For example, He et al. [193] developed an SERS-active substrate based on AuNP-decorated CVD graphene and used it for the multiplexed detection of DNA. Specifically, large films of graphene (120 μm × 120 μm) were generated and AuNPs (20 to 50 nm) were formed spontaneously on the film by immersion in $HAuCl_4$ wherein direct redox occurred between the metal ions and the graphene sheets. To detect DNA, the AuNPs were functionalised with thiolated DNA probes (up to two different DNA probes were used). Following the exposure of the device to the target DNA and the addition of a reporter DNA labelled with Cy3, which resulted in the formation of a sandwich composed of capture/target/reporter DNA, multiplex detection of DNA was achieved with an LOD of 10 pM (Fig. 4.11) [193].

Moreover, it was actually found that the SERS spectra of serum were quite similar to that in water with comparable intensities and the addition of a few peaks. He et al. [195] reported that the Raman signals of FA were much higher on GO–AgNP hybrid structures than on normal AgNPs due to the presence of strong electrostatic interactions. GO–AgNP hybrids have also been applied to monitor prohibited colorants in food [194, 195], wherein the GO–AgNP hybrids were used to detect mixtures of up to four prohibited red (e.g. allura red, ponceau, amaranth and erythrosine) or yellow (e.g. lemon yellow, sunset yellow, orange II and chrysoidin) colorants

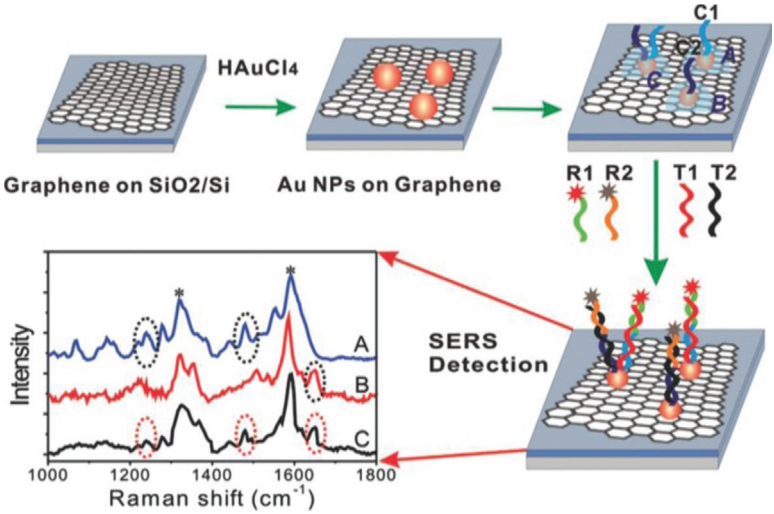

Figure 4.11 Graphene–AuNP-based SERS platform for multiplex DNA detection. The large-sized graphene films were grown by CVD on copper foils and then transferred onto SiO_2/Si substrate. Graphene film was then decorated with AuNPs by immersing it into $HAuCl_4$ solution. The detection of target and multiplex (two targets) DNA by Au-G–SiO_2/Si substrate-based SERS sensor. SERS spectra obtained in the absence of target DNA (black, C) and in the presence of 1 nM non-target DNA (red, B) and complementary target DNA (blue, A). Reprinted with permission from Ref. [193], Copyright 2012, American Chemical Society.

by their characteristic peaks with an LOD of 10^{-5} M. Similarly, GO–AgNP hybrids prepared via a one-pot method, where tannic acid, a water-soluble, phenolic hydroxyl-rich compound, was used as the reducing agent, were used to detect H_2O_2 and glucose without the need for glucose oxidase at an LOD of 7 and 100 μM, respectively [196]. Finally, Long et al. reported a disposable biosensor composed of a GO–AgNP composite on a screen-printed electrode which was capable of monitoring different polar antibiotics (e.g. MT, AT, 6-AA and PG) in situ with an LOD of 1 nM (Fig. 4.12) [197]. In this case, SERS was combined with electrophoretic preconcentration (EP), a process which draws charged analytes towards SERS substrates through electrostatic force, to increase the concentration of analyte in the enhancement regions of the graphene–NP hybrid device. By combining SERS with EP, the antibiotics could be selectively adsorbed on the GO–AgNP sensor by controlling the applied potential in the EP process, and the SERS spectra of a mixture of different analytes

could be obtained and distinguished within a 10 min timeframe without any preseparation. Last, GO nanocomposites have also been applied for live cell-based SERS applications. Liu et al. [198] recently reported a graphene–AuNP hybrid for SERS in which gold nanostructures were grown intracellularly [198]. Specifically, this process was assisted by polyvinylpyrrolidone (PVP)-functionalised GO, which acted as an activator for AuNP (IGAuNPs) biosynthesis. In terms of its mechanism of action, PVP is a nonionic, water-soluble and nontoxic polymer surfactant which can be employed as a stabilising and coordinating agent for the synthesis of metal NPs [199]. As such, by delivering trace amounts of PVP into the cell via functionalisation of GO, not only did PVP serve as a biocompatible stabiliser for GO, but it also provided a template to coordinate the reduction of gold ions via intracellular redox systems, thereby forming 100 nm graphene–AuNP hybrids termed PVP/GO/IGAuNPs (Figs. 4.13(A,B)) [198].

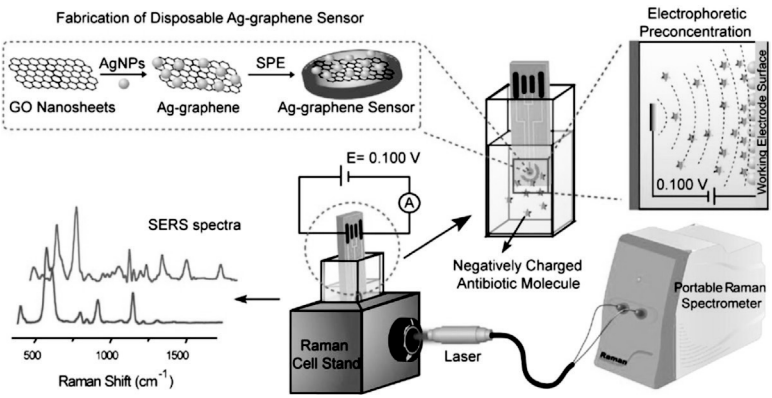

Figure 4.12 Graphene–AgNP sensor based on electrophoretic preconcentration and SERS. Schematic representation of a disposable Ag–graphene sensor for the detection of polar antibiotics in water. The magnification insets show the fabrication of Ag–graphene sensors and the electrophoretic preconcentration process of polar antibiotics. The distribution of antibiotics molecules is sketched for the case of a negatively charged analyte. At a given potential, most of the negatively charged antibiotics are concentrated onto the positively charged printed electrode, due to the generated electric field between the working electrode and the counter-electrode. In SERS experiments, the laser comes vertically from the side view of the spectro-electrochemical cell and is focused on the Ag–graphene sensor. SPE = screen-printed electrodes. Reprinted from Ref. [197], Copyright 2013, with permission from Elsevier.

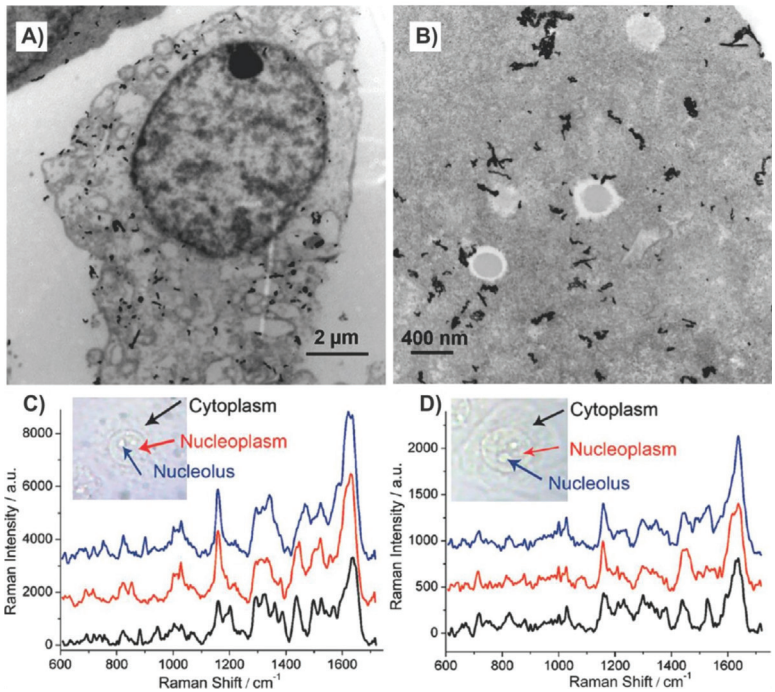

Figure 4.13 Intracellularly grown GO–AuNP hybrids for SERS. (A,B) TEM images of A549 cells containing GO/PVP/IGAuNs nanocomposites. (C, GO/PVP/IGAuNs; and D, IGAuNs) SERS spectra of A549 cells collected from the regions corresponding to the cytoplasm, nucleoplasm and nucleolus. Reprinted with permission from Ref. [198], Copyright 2012, American Chemical Society.

The distribution of PVP/GO/IGAuNs in the cells (A549, 4T1, HeLa cells) then allowed for the sensitive monitoring of intracellular chemical compositions, including proteins, nucleic acids, lipids and carbohydrates within 15 h. Moreover, the hybrids could be used to monitor the intracellular composition of the different cellular compartments, including the cytoplasm, nucleoplasm and even the nucleus using SERS (Figs. 4.13(C,D)). Specifically, a comparison between the SERS spectra of GO/PVP/IGAuNPs and IGAuNPs alone showed that the hybrid structure results in a five times larger Raman enhancement, possibly due to the formation of IGAuNP aggregates on GO; the device showed potential for cancer detection. Similarly, Liu et al. [201] also reported GO–AgNPs, which enabled very rapid cancer cell probing and imaging with a detection time of 0.06 s per

pixel [200]. In this case, the GO–AgNP composites were synthesised via an in situ reduction process which also used PVP as the reductant and stabiliser [201]. For their studies, Raman images of HeLa cells were taken after 8 h of incubation with 1 ug/mL GO or GO–AgNPs. The Raman signals of GO were almost undetectable in the cells incubated with GO alone. However, the hybrids showed remarkable enhancement (~48.4-fold enhancement). Finally, selective labelling of cancer cells could be achieved by covalently functionalising the GO–AgNPs with FA.

4.1.1.4 Plasmonic biosensors

SPR biosensors are currently the most widely used platform for label-free, real-time sensing and monitoring of biomolecules and molecular reaction events [202]. Typically there are two classes: The first class is prism-coupled SPR sensors, which utilise propagating SPP on a flat functionalised thin metal film [203]. SPPs are excited at specific angles and wavelengths resulting into a sharp dip in reflectance (see Fig. 4.14).

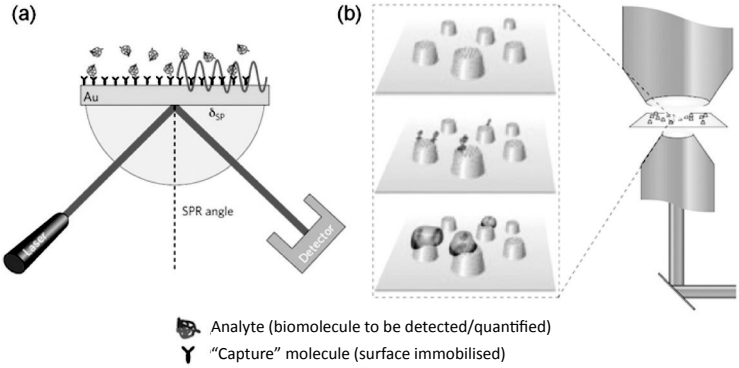

Figure 4.14 (a) Scheme of a prism-coupled SPR biosensor in the Kretschmann configuration (where a thin metallic layer is formed on the substrate and acts itself as the spacer). A high-index prism is used to match the incident wave's wavevector lateral component to the SPP wavevector. (b) Scheme of a nanoplasmonic biosensor. Functionalised NPs can be simultaneously interrogated within an optical imaging approach. Adapted by permission from Macmillan Publishers Ltd: *Nature Photonics*, Ref. [202], Copyright 2012.

Sensing occurs by monitoring the change in resonant angle or wavelength caused by adsorbed analytes on the metal surface.

This is the commercial standard providing the best sensitivity and proven functionality, at the expense, however, of necessitating bulky optical components and alignment systems, prohibiting compact, low-cost devices, and high-throughput bioanalytical measurements. Proposals to overcome this limitation [209, 210] include SPP excitation by nanoholes [202, 211], nanopits [212], nanoslits [213] or gratings [214], with the possibility of utilising SPP interference in a Mach–Zehnder interferometric configuration [215–217].

The second class of SPR biosensors is nanoplasmonic sensors [218–220], which utilise localised SPR (LSPR) in NP assemblies [221–223] and metamaterials [224, 225], typically excited by normally incident collimated beams. The plasmonic nanostructures exhibit sharp resonances due to LSPRs, and sensing occurs by monitoring the change in resonance wavelength caused by analytes adsorbed on the nanostructured metal surface (see Fig. 4.14). This configuration enables an imaging scheme for a low-cost, miniaturised, high-throughput on-chip biosensing platform. With careful tuning and optimisation of the metal nanostructures, nanoplasmonic sensors can surpass the performance levels of state-of-the-art commercial prism-coupled SPR sensors [226], offer single-molecule detection [215, 216] with label-free biosensing methods [227]. Graphene has several properties which could enhance biosensing: intrinsic plasmons in the infrared (IR) to terahertz (THz) range with high field concentration [228–230] and long lifetime [231–233], constant absorption in visible to IR [234], high biomolecule functionalisation capability due to π-stacking interactions [235–237], low small-molecule permeability offering passivation against corrosion [238–240]. In particular, graphene can provide new perspectives in plasmonic sensing in three main ways: (i) as a functional surface, which supports intrinsic surface plasmons at IR frequencies: SPPs in bulk and LSPRs in nanostructured graphene; (ii) as a functional gate tunable coating for existing plasmonic devices: functionalisation of Au and Ag surfaces (bulk or nanostructured), LSPR control and tuning via gating, protection against corrosion for Ag and Cu [241]; (iii) as a direct transducer eliminating the need for optical detection. The vision for graphene-based plasmonic sensing is the development of a low-cost, ultrasensitive, ultracompact, label-free, on-chip, high-throughput and real-time sensing platform.

4.1.2 Delivery of Drugs and Genes

The delivery of small-molecule drugs and biomacromolecules (e.g. proteins, peptides, genes) to specific tissues of interest has been a fundamental approach in medicine. As compared to the conventional method of oral administration or intravenous injection, significant effort has been dedicated to enhancing bioavailability, achieving targeted delivery, more effectively solubilising drugs/biomolecules of interest and protecting drugs/biomolecules from enzymatic degradation [242]. In this regard, NM-based delivery platforms have revolutionised drug delivery systems, providing benefits from both the effective delivery and imaging standpoints [243]. Since the discovery of graphene in 2004, there has been increasing interest in loading graphene-based NMs for the delivery of drugs/genes due to graphene's high specific surface area and unique modes of complex formation, including π–π stacking, electrostatic interactions and hydrophobic interactions [244]. The well-controlled modification of graphene materials with NPs to form graphene–NP hybrids has been applied to improve their utility for both in vitro cancer cell assays and in vivo chemotherapies. In particular, as with the other cellular applications mentioned so far, the formation of graphene–NP hybrids can prevent aggregation and provide additional functionalities over graphene or NPs alone. Additionally, graphene-NP hybrids can greatly improve the drug-loading capacity over graphene materials alone due to increases in overall surface area. To this end, early work focused on optimising synthetic procedures to achieve high drug loading of poorly soluble drugs while maintaining maximal potency. For example, Yang et al. [245] formed a GO–Fe_3O_4 hybrid to investigate the binding of the anticancer agent doxorubicin (DOX). The hybrids were prepared via chemical deposition, followed by conjugation of DOX via sonication and overnight stirring resulting in a drug-loading capacity as high as 1.08 mg/mg. AuNPs and GO further improved the DOX-loading capacity to 6.05 mg/mg with a hybrid containing IONPs, which is significantly higher than GO alone (2.35 mg/mg) [246]. While a range of drug-loading capacities have been demonstrated, the maximum achievable loading is heavily dependent on the synthetic conditions employed to prepare the hybrids, the chemical composition of individual components (e.g. GO, RGO, Fe_3O_4, Au, etc.) and the structure/composition of the

small-molecule drug. While attaining sufficient drug loading is a key criterion for achieving a therapeutic effect, the effective delivery of the hybrid nanocarrier into the desired cancer cell/tissue is equally important. In one study, gold nanocluster (GNC)–RGO nanocomposites were loaded with DOX to investigate the effect on hepatocarcinoma (HepG2) cells [247]. Specifically, GNCs ranging between 2 and 3 nm in diameter were noncovalently attached onto the RGO surface resulting in GNC–RGO nanocomposites which were less toxic than GNCs alone (IC50 values: 1.36 μg/mL for GNC–RGO versus 0.36 μg/mL for GNCs). Next, DOX was loaded onto the GNC–RGO nanocomposites at a 91% drug-loading efficiency, where the concentration of DOX was 0.22 mg/mL and that of GNC–RGO was 1 mg/mL. It was found that the DOX-loaded GNC–RGO inhibited HepG2 cell growth more strongly than DOX and GNC–RGO alone, which suggested that DOX was more effectively transported into the cell by the GNC–RGO nanocomposite than when used alone. Moreover, while DOX treatment alone led to DOX molecules resting on the cellular membrane, the DOX-loaded GNC–RGO allowed DOX to be well distributed inside the cells, thus suggesting the importance of such a composite vehicle to enhance membrane permeability. In a similar study, NGO sheets were wrapped onto the surface of individual AuNPs and then noncovalently bound with DOX for delivery into HeLa cells [248]. This methodology generated Au@NGO composites with a hydrodynamic size of 133.5 nm in culture media, a size range which allowed for facile cellular delivery. The intrinsic SERS signal from the Au@NGO further allowed for Raman imaging, which confirmed the efficient delivery and distribution of the nanocomposites in the cytoplasm. Interestingly, sustained release of the drug was observed in the DOX-loaded Au@NGO composite condition, wherein the red fluorescence (DOX) within the nucleus gradually increased over 48 h and became higher than that seen in the cytoplasm. In contrast, treatment with an equivalent amount of DOX showed fast nuclear accumulation within only 2 h, with no further enhancement in fluorescence over time. Moreover, DOX-loaded Au@NGO induced a significant decrease in HeLa cell viability when compared to free DOX (Fig. 4.15C). This work suggests that while treatment with free DOX led to a burst dosing profile, the Au@NGO composite allowed for sustained release within the cancer cells, showing promise for long-term therapeutic efficiency. Targeted

delivery of therapeutic agents is also highly desirable because it can allow for higher bioavailability of the agent at its site of action, while reducing side effects [250]. As compared to passive transfection into cancer cells, a number of studies have attempted to chemically or physically modify the drug-loaded hybrid nanocomposite to enhance cellular internalisation.

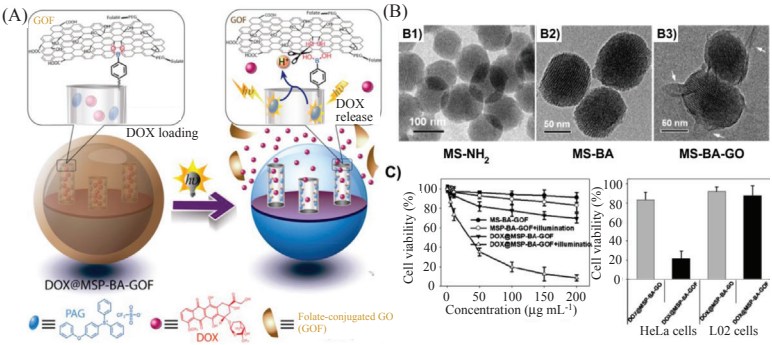

Figure 4.15 Remote-controlled drug release from GO-capped mesoporous silica to cancer cells by photoinduced pH-jump activation. (A) Schematic illustration of DOX@MS-BA-GOF as a drug delivery system for remote light control of drug release. (B) TEM images of amine-terminated mesoporous silica (b1), boronic acid-grafted MS (b2), and GO-capped MS-BA (b3). (C) Viability of HeLa cells after being incubated with different NPs (MS-BA-GOF, MSP-BA-GOF and DOX@MSP-BA-GOF). Cytotoxicity of DOX@MSP-BA-GOF and DOX@MSP-BA-GO incubated with HeLa cells and L02 cells for 24 h. Reprinted with permission from Ref. [249], Copyright 2014, American Chemical Society.

Fan et al. [251] prepared a graphene–CNT–MNP (Fe_3O_4) nanocomposite to investigate the delivery of the anticancer drug 5-fluorouracil (5-FU) into HepG2 cells. While the high specific surface area of graphene allowed for higher drug loading than graphene-based drug carriers alone and the IONPs imparted superparamagnetic behaviour to the nanocomposite, the incorporation of CNTs was found to enhance transportation of the graphene–CNT–Fe_3O_4 hybrid across the cell membrane. TEM images comparing magnetic CNT nanocomposites (CNT–Fe_3O_4) and magnetic graphene nanocomposites (graphene–Fe_3O_4) showed distribution of the CNT–Fe_3O_4 nanocomposites in the cell cytoplasm but graphene–Fe_3O_4 only outside of the cell. The study further showed dose-dependent in vitro cell toxicity studies using the graphene–CNT–Fe_3O_4 for fluorouracil (5-FU) drug

delivery, providing further evidence for improved cellular delivery. On the other hand, to achieve a more targeted drug delivery, Chen et al. [252] designed a QD-graphene-based hybrid composite which was conjugated with the transfer in (Trf) ligand. Specifically, Trf ligands are known to bind with high affinity to Trf receptors, which are expressed on the plasma membrane of various types of cancer cells [253]. DOX-graphene-QD-Trf (loading capacity 1.4 mg/mg) was incubated in a Trf positive cell line (HeLa) and a Trf negative cell line (HEK293). The DOX-graphene-QD-Trf exhibited increased toxicity to HeLa cells as compared to the HEK293 cells, while the DOX-graphene-QD and DOX-graphene-QD-Trf showed a similar effect on HEK293 cell viability. This effect was attributed to the specific Trf receptor recognition, which suggested that the ligand-specific conjugation of the nanocomposites could selectively increase drug cytotoxicity. Moreover, the QDs (CdTe–CdS nanocrystal clusters) allowed for fluorescence imaging, thus providing the capability to track and monitor drug delivery. In addition to targeted therapies, remotely triggerable drug delivery systems have become popular because they enable the user to adjust dosing regimens on demand based on a patient's physiological response [254]. In a recent study, He et al. describe a photocontrolled release system by incorporating a photoacid generator (PAG) into DOX-loaded, GO-capped MSNPs (Figs. 4.15(A,B)) [249]. In particular, PAG can generate strong acid via illumination with UV or near-UV light [255]. As such, by assembling GO as nanogates on the MSNPs with acid-labile boroester linkers, the PAG was used to generate a locally high concentration of H^+ upon illumination. This, in turn, induced the hydrolysis of the boroester linkers to open the pores (by releasing the GO cap) and release the loaded DOX. The nanocomposites were further conjugated with folate, which allowed for targeted delivery to cancer cells overexpressing FRs. Selective cell death from the DOX-loaded nanocomposites was indicated by the significant cell death of approximately 80% in HeLa cells (high expression of FRs), but a negligible change in cell viability of L02 cells (low expression of FRs) (Fig. 4.15C). While the majority of studies on graphene-based nanocomposites for drug delivery applications have employed inorganic NPs for complexation with GO, Wang et al. [256] were among the first to demonstrate the use of a soft NP in this regard, by adsorbing zwitterionic dioleoyl-*sn*-glycero-3-phosphocholine (DOPC) liposomes onto NGO. The ra-

tionale for using DOPC liposomes was to adsorb multiple molecules on the same surface with little intermolecular competition, thus allowing for highly effective drug loading and controlled release. The nanoscale heterogeneity of the GO surface proved to be ideal, wherein DOX was loaded using the well-established hydrophobic interactions with the basal aromatic surface. On the other hand, the DOPC liposomes were speculated to adsorb using hydrogen bonding and hydration forces with the peripheral carboxyl groups. As such, DOPC liposomes may be adsorbed on GO at different sites from DOX, thereby avoiding competition. Interestingly, the DOPC/NGO complex not only exhibited improved aqueous dispersion and colloidal stability, but also allowed for an increased loading capacity of DOX (~500%) as compared to loading on only GO (~300%), which indicated that the DOPC liposomes did not interfere with the drug loading. In addition, it was also found that while free DOPC liposomes were not internalised by HeLa cells, the DOPC/NGO complex had high colloidal stability and readily entered the cells. Finally, the DOPC liposomes were simultaneously loaded with a calcein dye and delivered to HeLa cells, which exhibited a decrease in cellular viability (due to DOX) and green fluorescence from calcein. As such, this new soft NP-based GO hybrid system exhibited the ability to codeliver molecules with opposite properties (e.g. DOX is cationic and hydrophobic, while calcein is negatively charged and hydrophilic) using a single platform. Last, while the delivery of small-molecule drugs has been extensively explored using graphene–NP composites, there have been limited studies demonstrating their use for gene delivery. PEG and polyethylenimine (PEI)-grafted graphene/Au composites (PPGA) have recently been used for the delivery of small interfering RNA (siRNA) into human promyelocytic leukaemia cells (HL-60) [258]. The polymer coatings served specific functions, wherein the cationic PEI was used to bind electrostatically with negatively charged siRNA, while the PEG promoted high water dispersibility and excellent blood compatibility. The PPGA composites showed biocompatibility for in vitro cultures when used at concentrations below 20 μg/mL, as well as knockdown of BCL-2 protein expression at a PPGA/siRNA mass ratio of 100:4. Moreover, because these composites also contained AuNPs, the photothermal effect of PPGA was demonstrated under NIR laser irradiation. Finally, Wang et al. [257] developed a strategy to combine chemotherapy and gene therapy using a single chitosan magnetic–graphene (CMG) nanocomposite platform.

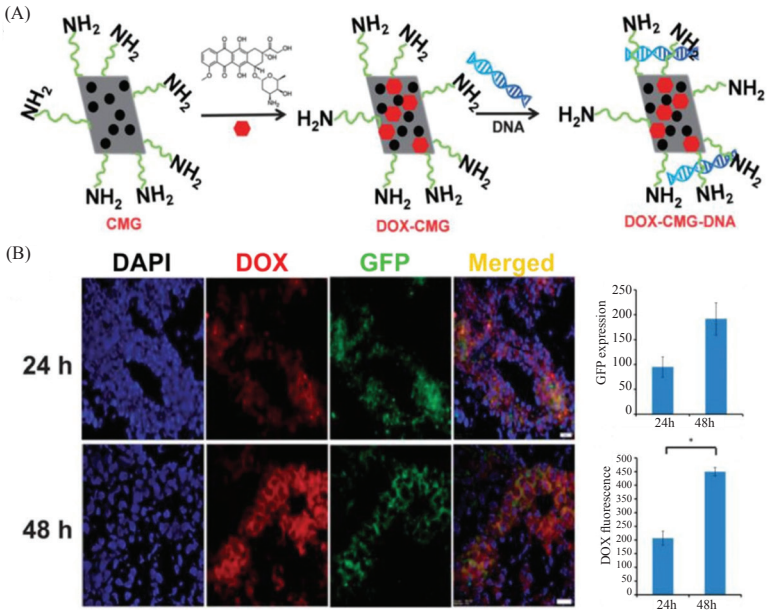

Figure 4.16 Multifunctional chitosan magnetic-graphene NPs for tumour-targeted codelivery of drugs, genes and MRI contrast agents. (A) Schematic showing the generation of DOX-loaded chitosan functionalised magnetic graphene complexed with DNA plasmids encoding GFP (DOX-CMG-GFP-DNA) complexes. (B) GFP expression and DOX fluorescence in frozen sections from mice injected with DOX-CMG-GFP-DNA (30 μg of DOX and 25 μg of GFP-DNA), examined using a fluorescent microscope at 400× magnification. Expression was quantified and normalised to control background. Reproduced from Ref. [257] with permission of The Royal Society of Chemistry.

The CMG nanocomposites were synthesised by the in situ growth of IONPs on the RGO surface, followed by the covalent binding of chitosan. Thereafter, DOX was physically adsorbed onto the CMG composites (via interaction with GO) and a green fluorescent protein (GFP) reporter DNA plasmid (via interaction with positively charged chitosan). These DOX-CMG-GFP complexes (30 μg of DOX and 25 μg of GFP-pDNA per mouse) were administered intravenously to LLC1 tumour-bearing mice, whereby the presence of DOX (red) and GFP (green) expression was observed in frozen mouse sections (Fig. 4.16) after 24 h and 48 h. Biodistribution studies further showed significant accumulation in the tumour site, with lower accumulation

in the liver and spleen. Moreover, the MNPs in the CMG composites allowed for MR imaging. Delivering medicines, as shown in Fig. 4.17, to a patient in a controlled manner is one of the main research areas in nanomedicine [81]. The nanodevices carrying the medicines should deliver a certain amount of a therapeutic agent for a controlled period of time to a targeted diseased area within the body. Graphene's water-soluble derivatives have potential application in drug delivery [259] and enzyme immobilisation [260]. PEG-GO was applied as a nanocarrier to load anticancer drugs via non-covalent physisorption [261].

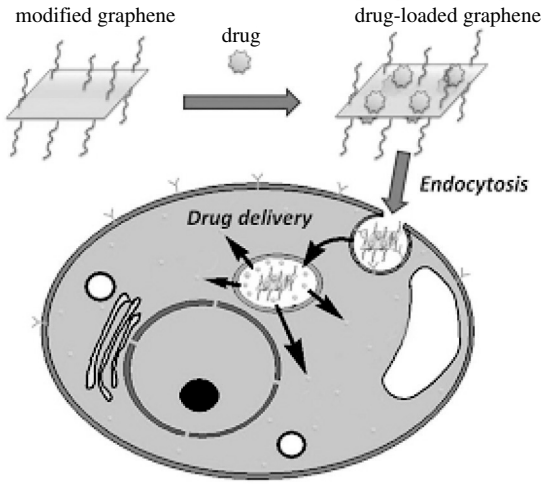

Figure 4.17 Scheme of drug delivery. Functionalised graphene loaded with the drug is internalised via endocytosis. The drug then escapes from the endosome and is released into the cytoplasm. Adapted from Ref. [262] under the Creative Commons Attribution License.

The loading and release of doxorubicin hydrochloride, e.g., was investigated as anticancer treatment [261]. The loading ratio (weight ratio of loaded drug with respect to carriers) of GO was up to 200% higher than with others nanocarriers, such as NPs, which usually have a loading ratio lower than 100% [102]. It was also reported that GO functionalised with sulphonic acid followed by covalent binding of folic acid allows to specifically target human breast cancer cells [263]. Controlled loading of two cancer drugs, such as doxorubicin [264] and camptothecin [265], via π–π stacking and hydrophobic

interactions was investigated [263]. These results paved the way to engineering graphene-based drug delivery.

4.1.3 Stem Cell and Tissue Engineering Approaches

Tissue engineering is a growing field of study which combines living cells and biocompatible materials to create constructs which can potentially repair or replace the function of living tissues and organs [266]. With regard to living cells, stem cells are an attractive cell source for tissue engineering applications because they exhibit the ability to self-renew and differentiate into specific cell lineages. However, guiding stem cell differentiation towards a desired cell type tends to require precise control over the biochemical and physical microenvironmental cues. In this regard, engineering cellular microenvironments to promote stem cell attachment, growth, viability and differentiation has been a major area of focus. As such, graphene has proven to be a promising candidate for stem cell engineering, exhibiting excellent biocompatibility and tunable functionalities for cultures of embryonic stem cells (ESCs), induced pluripotent stem cells (iPSCs), mesenchymal stem cells (MSCs) and neural stem cells (NSCs) [267, 268]. Moreover, further work has explored ways to arrange graphene-based NMs into 3D architectures, with the goal of designing tissue-like transplantable scaffolds [269]. With the increasing interest in adding greater functionality to cellular scaffolds, a handful of studies have investigated the potential of graphene–NP hybrids for stem cell and tissue engineering with great success. Graphene-coated surfaces have been found to be conducive to protein attachment, potentially due to the hydrophobic and hydrophilic patches found on the surface of proteins [270]. As mentioned previously, an early study conducted by Deng et al. [112] demonstrated the incorporation of proteins on the GO surface to efficiently assemble NPs of different size, shape composition and surface properties. Using BSA as a model protein, BSA-coated GO were used to assemble presynthesised metallic NPs (Au, Pt, Pd, Ag) and/or nonmetallic NPs (latex). The work concluded that multiple interactions mediated via specific chemical groups led to the adsorption of protein (e.g. cysteine, lysine, histidine residues) and that the GO surface could serve as a “universal adhesive” to facilitate the attachment of NMs and, potentially, cells.

The nanoscale topography of hybrid surfaces can also present a unique extracellular microenvironment to control stem cell behaviour (e.g. cell shape, adhesion, proliferation and differentiation) [271]. For this purpose, nanotopographical substrates composed of RGO and positively charged polysaccharide chitosan have been fabricated with the hypothesis that the unique, biocompatible nanotopography could provide an effective environment for the differentiation of human MSCs [269]. The mixture of RGO and chitosan at varying ratios (0–5% w/w) produced NP-like composites, which upon spin-coating onto bare glass substrates introduced surface roughness which ranged from 0.9 to 7.7 nm. While it was observed that the presence of higher concentrations of graphene on the substrates decreased the proliferation rate of human MSCs, concentrations of less than 0.1 mg/mL had minimal cytotoxicity. On the other hand, cellular adhesion was found to be greatest on the 5% RGO–chitosan substrates and provided a suitable environment for proliferation. These nanocomposite substrates were further observed to enhance bone differentiation, both with and without osteogenic induction media, as well as neurogenesis under neurogenic conditions. In this way, the unique nanoscale topographical cues of the graphene–chitosan nanocomposites are likely to play a crucial role for human MSC differentiation, although the exact mechanism is not yet understood. Along these lines, Solanki et al. [272] generated arrays of graphene–NP hybrid structures to guide the differentiation and alignment of human NSCs. Positively charged SiNPs (300 nm) were assembled on glass substrates using a centrifugation process, after which negatively charged GO was deposited (Fig. 4.18). These hybrid films were further coated with the extracellular matrix protein laminin to facilitate adhesion and growth of human NSCs. After 2 weeks of culture, the graphene–NP hybrid nanostructures were observed to promote a higher efficiency of differentiation into the neuronal cell lineage. Interestingly, cellular extensions were seen to spread in a unidirectional manner after 5 days of culture. This axonal alignment was observed to be maximal on the hybrid films, in which the SiNP–GO substrates showed the smallest variation in the angle of orientation of axons as compared to control substrates (Fig. 4.18B).

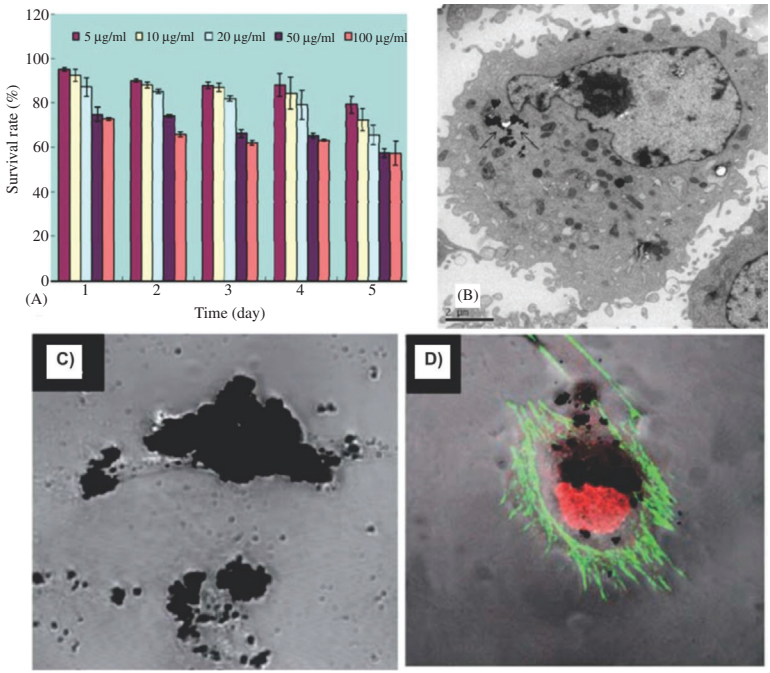

Figure 4.18 Biocompatibility of graphene materials. Effects of GO on human fibroblast cells. (A) The survival rate at different concentrations of GO and at different periods of exposure. (B) TEM picture showing the location of GO inside human fibroblast cells as indicated by the black arrows. Reprinted from Ref. [273] under the Creative Commons Attribution License. (C) Differential interference contrast image showing the accumulation of pristine graphene on the plasma membrane of Vero cells. (D) Fluorescence confocal microscopy of cytoskeletal F-actin arrangement of cells treated with pristine graphene. Reproduced from Ref. [274] with permission of The Royal Society of Chemistry.

This behaviour was further observed on hybrid films generated on flexible and biocompatible polymeric substrates, underscoring the potential of using the graphene–NP hybrids for guided neural tissue engineering. However, a further study is required to fully understand the underlying mechanisms governing the observed neuronal differentiation and axonal alignment. Finally, an essential step in conducting stem cell studies is the ability to monitor the differentiation process and identify the stage of differentiation, which can give insight into the development of effective stem-cell-based therapies. Many of the conventional techniques used to

distinguish undifferentiated versus differentiated stem cells, such as immunostaining, fluorescence-activated cell sorting (FACS) and Western blotting, tend to be laborious, time-consuming and destructive. A graphene–NP platform based on SERS detection was shown to be an effective and highly sensitive tool which could distinguish undifferentiated and differentiated stem cells while maintaining cell viability [275]. In particular, GO-encapsulated AuNP films were generated on indium tin oxide (ITO) surfaces, followed by use for the culture of mouse NSCs. On the basis of several reports, undifferentiated stem cells have been found to contain molecules bearing a high number of C–C bonds (high degree of saturation) as compared to differentiated cells [276]. Given that such bonds have strong affinity to GO, the GO–AuNP films were effectively used to measure the SERS signal and distinguish such chemical heterogeneity between C–C bonds (1656/cm) and C–H bonds (1470/cm). By measuring differences in the SERS signal, the differentiation state of the NSCs was detected and validated via immunostaining. These results were further verified by detecting the electrochemical signals with CV in a microgap configuration containing GO–AuNP films. As such, the use of GO–NP composites provided unique multifunctionalities wherein the GO–AuNP films could act as a biocompatible substrate for cell differentiation as well as SERS and electrochemical detection to provide a noninvasive and effective method for the in situ monitoring of stem cell differentiation.

4.1.4 Imaging and Diagnosis

Luminescent QDs are widely used for bio-labelling [277] and bioimaging [278]. However, their toxicity [279] and potential environmental hazard [280] have limited their widespread use and in vivo applications. Fluorescent biocompatible carbon-based NMs might be a more suitable alternative. Fluorescent species in the IR and NIR are useful for biological applications, because cells and tissues show little auto-fluorescence in this region [281]. The optical properties could be exploited in biological and medical research, such as imaging and, consequently, diagnosis. Luminescent graphene-based materials can now be routinely produced covering IR, visible and blue [89, 282–284].

4.2 Energy Applications

Following are the major energy-related applications of graphene-based nanostructures [51–62, 68–71]. Storage and conversion are essential for energy production and saving. Energy can be stored in a variety of ways depending on the intended use with each method having its advantages and disadvantages. Batteries, capacitors and fuel cells have been used and studied for over a century to store energy. The need to develop sustainable and renewable energy sources is leading society to develop energy from sources which are not continuously available such as Sun and wind. In addition, there is a significant need to have portable energy not only for portable devices but also for transportation, to decrease the reliance on fossil fuels. Batteries and electrochemical capacitor storage devices are the most common means of storing energy, and fuel cells are also coming into their own. However, a number of challenges need to be addressed to improve their performance and viability. Therefore, high-energy electrodes are increasingly important.

4.2.1 Lithium-Ion Batteries

Increasing energy demands have motivated researchers to look for alternative energy resources. Among various alternatives, a considerable attention has been given to the LIBs due to its rechargeable characteristics, higher specific energy and longer life cycle. Graphene sheets have unique properties, including superior electrical conductivity, high surface-to-volume ratio, ultra-thin flexible nature and chemical stability, which make them an ideal candidate to build composites with metal and metal oxide NPs for energy-storage applications. Various electrode materials based on transition metal oxides such as SnO_2, Co_3O_4, Fe_3O_4, TiO_2 and Mn_3O_4 are proposed for LIBs to achieve higher specific capacities than currently being used. These transition metal oxides have very high theoretical capacities but extremely low electrical conductivity, which restricts their direct application in LIBs. For instance, Mn_3O_4 has electrical conductivity about 10^{-7}–10^{-8} S/cm, which limits its specific capacity lower than 400 mA·h/g. Higher reversible capacity (794–1054 mA·h/g) and cyclic stability were also demonstrated in disordered graphene nanosheets, as the presence of edge and

vacancy defects in graphene sheets provides additional reversible storage sites for Li ions. Researchers have made significant efforts towards the development of high cyclic performance of the LIBs using nano metal oxide and graphene composite, summarised in Table 4.1.

Table 4.1 Graphene-based LIB materials and properties

Graphene-based hybrid nanocomposites	Energy density (mA·h/g)	Energy density (mA/g)	Cycles
Graphene-encapsulated Co_3O_4	1000–1100	74	130
Graphene-anchored Co_3O_4	935	50	30
Graphene–Mn_3O_4	730–780	400	50
SnO_2–graphene	625	10	10
Graphene-wrapped Fe_3O_4	1026	35	30
Anatase TiO_2-FGS	160	—	100
Rutile TiO_2-FSG	170	—	—
Graphene–Si	2200	—	50
(GNS) GNS + C60	600	50	20
GNS + CNT	480	50	20
Graphene–SnO_2 (nanoporous electrode)	810	50	30

Source: Reprinted from Ref. [4], Copyright 2011, with permission from Elsevier.

These metal oxide NPs are grown on GO using solution chemistry followed by hydrothermal, thermal or chemical reduction to intimate contact between RGO and NPs. The use of anionic surfactant (i.e. sodium dodecyle sulphate) helps in dispersing individual graphene sheets and in situ crystallisation of metal oxide particles. TiO_2/RGO composites were prepared for LIB electrodes using surfactant-assisted growth of NPs of TiO_2 and showed more-than-double specific capacity than control rutile TiO_2 at a high discharge rate. An advantage of graphene–CNT composites lies in the fact that the basal spacing between the graphene layers can be enlarged with CNT spacers, which benefits the storage capacity of LIB applications. [4, 51–62]. The unique properties of graphene make it an ideal candidate to build composites with metal and metal oxide NPs for

energy-storage applications. In such composites, graphene provides support for NPs and prevents the volume expansion–contraction of NPs during charge and discharge processes. Studies show that the addition of graphene-based materials to transition metal oxide enhances the specific capacity of the electrodes at high discharge rate and improves the electrochemical stability for longer cycles. The improvement was attributed to the excellent electronic conductivity, high surface area, thermal and chemical stability and mechanical flexibility of monolayer graphene sheets.

The flexible graphene sheets accommodate a large volume expansion of metal oxide during the charge–discharge process and prevent the pulverisation of electrodes leading to higher electrical conductivity of the electrodes. Moreover, high surface area of graphene facilitates Li ions intercalation. Researchers have made a significant effort towards the development of high cyclic performance of the LIBs using nano metal oxide and graphene composite (Fig. 4.19). These metal oxide NPs are grown on GO using solution chemistry followed by hydrothermal, thermal or chemical reduction to intimate contact between RGO and NPs [285].

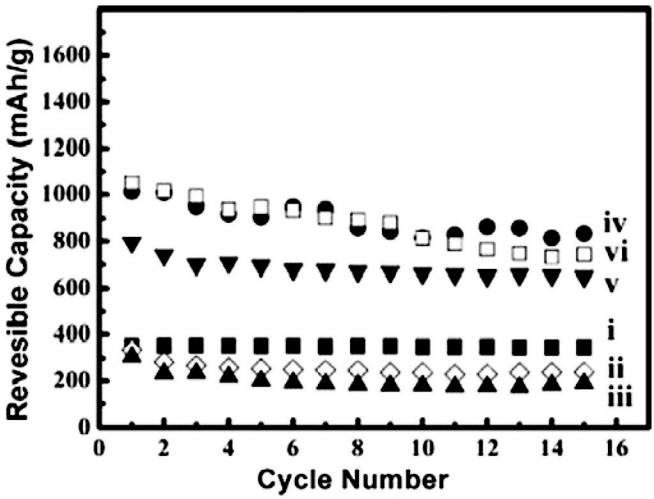

Figure 4.19 Reversible (charge) capacity versus cycle numbers at a current density of 0.05 A/g, for natural graphite (i), pristine GO (ii), hydrazine-reduced GO (iii), 300°C pyrolytic GO (iv), 600°C pyrolytic GO (v) and electron-beam-reduced GO (vi). Reprinted with permission from Ref. [285], Copyright 2009, American Chemical Society.

Many forms of storage exist, including large-scale storage such as hydroelectric power and compressed air, as well as fly wheels and electrochemical energy storage (Li-ion batteries, redox flow batteries and SCs). At present, Li-ion batteries, using the chemistry of an $LiCoO_2$ cathode and a graphite anode [286–289], are considered by the batteries community the leading candidates for hybrid, plugin hybrid and all electrical vehicles and for utility applications. The energy density and performance of Li-ion batteries largely depend on the physical and chemical properties of the cathode and anode materials. Conventional Li-ion batteries utilise graphite as the anode [290]. The low theoretical specific capacity (i.e. the total ampere-hours (Ah) available when a battery is discharged at a defined value of discharge current, per unit weight) of graphite (372 mA·h/g [290]) makes it important to find alternative negative electrodes. Si (4200 mA·h/g) [291] or Sn (994 mA·h/g) [292] has higher capacity. However, their application as anodes in Li-ion batteries has been limited by their poor cycling (i.e. the number of charge–discharge cycles before the battery fails to meet performance criteria, e.g. specific capacity below 60% of nominal value) caused by large volume changes during the uptake and release of Li [293]. The search for suitable cathode and anode materials has proven challenging. The possibilities for the improvement of cathode materials are quite limited due to stringent requirements such as high-voltage potential, structural stability and inclusion of Li in the structure [294, 295]. Many potential electrode materials (e.g. metal oxide) in Li-ion batteries are limited by slow Li-ion diffusion and poor electron transport at high charge–discharge rates [288, 289]. To improve the charge–discharge rate performance of Li-ion batteries, extensive work has focused on Li-ion and/or electron transport in electrodes [296]. Nanostructures (e.g. nanoscale size [297] or nanoporous [298] materials) have been widely investigated to improve Li-ion transport in electrodes by shortening the Li-ion insertion/extraction pathway [296, 299]. Varieties of approaches were developed to increase electron transport in the electrode materials, such as the use of conductive coatings (e.g. carbon black, CNTs [300–302]). In Li-ion batteries, higher energy requires electrodes with high conductivity and improved resistance to reaction with electrolytes. Graphene may be an ideal conductive additive for hybrid nanostructured electrodes [303, 304]. Other advantages include high surface

area (theoretical ~2630 m^2/g) for improved interfacial contact and potential for low manufacturing cost [305]. High–surface area RGO sheets were studied for Li-ion storage [306]. In addition, RGO was used to form composites with SnO_2 in order to improve specific capacity and cyclic stability of anodes [307]. GRMs were also used as a conductive additive in self-assembled hybrid nanostructures to enhance performance (i.e. charge–discharge capacity and current and energy density) of electrochemical active materials [308, 309]. However, the majority of electrodes were fabricated exploiting CMG, and only the full potential of graphene produced by LPE was exploited in electrodes for Li-ion batteries [310]. It was reported [310] that electrodes based on Cu-supported graphene nanoflakes ink can reach specific capacities of ~1500 mA·h/g at a current rate of ~100 mA/g and specific capacities of ~650 mA·h/g at a current rate of ~700 mA/g over 150 cycles, when tested in half-cell configuration (i.e. with a structure containing a conductive electrode and a surrounding conductive electrolyte separated by a Helmholtz double layer). By balancing the cell composition and suppressing the initial irreversible specific capacity of the anode (~7500 mA·h/g), principally due to the decomposition of the electrolyte at the surface of the electrode with the formation of a solid electrolyte interphase (SEI), it was reported [310] that an optimal battery performance in terms of specific capacity, i.e. 165 mA·h/g , estimated energy density of ~190 W·h/kg, operation over 80 charge–discharge cycles. Graphene as a hybrid system with VO5 could be used as cathode to fabricate flexible, thin-film Li-ion rechargeable batteries. Here, graphene could act as the flexible current collector, replacing the traditionally used Al, offering additional volumetric capacity, electrochemical stability and mechanical flexibility. In addition, free-standing or substrate-bound, electrochemically lithiated graphene can be used as anode. For batteries, future activities should focus on graphene-coated lamellar Li^+ hosting oxide electrodes, graphene nanocomposites with Li^+ intercalated between graphene sheets for improved morphology preservation at the nanoscale during battery charge–discharge and graphene–Si composite electrodes with additives for more stable surface electrode interphase. The long-term aim would be to develop novel Li–O_2 battery concepts (Li–O_2 is a metal–air battery which uses the oxidation of lithium at the anode and reduction of oxygen at the cathode to induce a current flow [311]), able to supply high en-

ergy density (~3500 Wh/kg) due to the high specific energy density of lithium with respect to air (3840 mA·h/g) [311, 312], an order of magnitude more than a conventional Li battery [312]. Graphene may also be used in other energy-storage systems as current collector. In this case, free-standing or substrate-bound films with high accessible surface-area-to-volume ratio could replace traditional activated carbon materials (i.e. processed to have small, low-volume pores which increase the surface area available for adsorption or chemical reactions) in the cathode and as current collectors in transparent devices. Adsorption of Li, as well as Na, K and Ca, on MXene compound (e.g. Ti_3C_2) was studied by first-principles DFT calculations [313], and it was calculated that these alkali atoms exhibit different adsorption energies depending on the coverage. The adsorption energies of Na, K and Ca decrease as coverage increases, while Li shows little sensitivity to variance in coverage [313]. It was also associated with the observed relationship between adsorption energies and coverage of alkali ions on Ti_3C_2 to their effective ionic radii. A larger effective ionic radius increases interaction between alkali atoms, thus obtaining a lower coverage [313]. The calculated capacities for Li, Na, K and Ca on Ti_3C_2 are 447.8, 351.8, 191.8 and 319.8 mA·h/g, respectively [313]. Another MXene material, i.e. Ti_2AlC, has shown experimentally, by cyclic voltammetry, lithiation/delithiation peaks at 1.6 V and 2 V versus Li^+ /Li [314]. At 1C rate, the specific capacity was 110 mA·h/g after 80 cycles. Compared to materials currently used in Li- and Na-ion battery anodes, MXene shows promise in increasing overall battery performance [313].

4.2.2 SCs

The SCs or ultra-capacitors are passive and static electrical energy-storage devices for short load cycle applications. SCs with very high power density, fast charge–discharge ability without degradation and burst release characteristics make them ideal candidates for applications in mobile electronic gadgets and hybrid electric automobiles.

Energy stored in SCs is through the ion adsorption at the electrode interface, which makes electrical double layer (EDL capacitors, EDLC), or due to the electron transfer between the

electrolyte and the electrode through fast Faradic redox reactions (pseudocapacitors).

Table 4.2 Graphene-based SC materials and properties

Graphene nanocomposites	Specific capacitance (F/g)	Energy density/ power density	Electrolyte
Graphene–hydrous RuO_2	570	20.1 W·h/kg at 100 mA/g	1 M H_2SO_4
Graphene–PANi	1046	—	6 M KOH
Graphene–MnO_2	216	—	1 M Na_2SO_4
Polymer-modified graphene sheet + MWCNT	120	—	—
MnO_2 nanowire–graphene	31	30.4 W·h/kg	Neutral aq. Na_2SO_4

Source: Reprinted from Ref. [4], Copyright 2011, with permission from Elsevier.

Various graphene-based SC materials are summarised in Table 4.2. A new class of material, e.g. graphene and RGO, has also been predicted as a potential candidate for SC electrodes due to very high specific surface area (2675 m^2/g), chemical stability, excellent electrical, thermal conductivity and capacitance and low cost. In the case of RuO_2/graphene nanocomposite, graphene sheets were well separated by RuO_2 NPs, which were attached through the oxygen-containing functional groups on graphene surfaces. The composite exhibited a high specific capacitance of 570 F/g for 38.3% Ru loading with excellent electrochemical stability (97.9% retention after 1000 cycles) and high energy density (20.1 W·h/kg) at high power density (10 kW/kg). Similarly, MnO_2/GO composite electrode had a capacitance of 216 F/g, which is much higher than that of individual GO (10.9 F/g) and bulk MnO_2 (6.8 F/g) [4].

The mesoporous structures of the curved graphene sheet are responsible to prevent face to face restacking and maintain large pore size (2–25 nm) and capacitance (Fig. 4.20a). Graphene–PANi composite paper was also prepared by in situ anodic electro-polymerisation of PANi film on graphene paper (Fig. 4.20b).

The flexible as-prepared composite paper combined the high conductivity and flexibility properties of graphene sheet with large capacitance polymer and showed the gravimetric capacitance of 233 F/g [4, 8, 9].

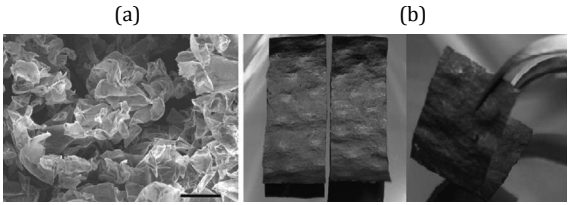

Figure 4.20 (a) SEM image of curved graphene sheets (scale bar 10 μm). Reprinted with permission from Ref. [9], Copyright 2009, American Chemical Society. (b) Digital camera images of (left) two free-standing G-papers (30 mm, 10 mm) and (right) a flexible G-paper. Reprinted by permission from Ref. [10], Copyright 2011, John Wiley and Sons.

Several SC materials have been studied to enhance specific capacitance and power density. Among them, carbon-based materials such as activated carbons, carbon fibres and CNTs have been extensively investigated as an electrode material for EDL SCs owing to their good electrical conductivity, chemical and mechanical stability, long life cycle and highly modifiable nanostructures [315a–318a]. Whereas materials such as RuO_2 and MnO_2 and polymers are promising for pseudocapacitors. SCs store charge electrostatically by the adsorption of ions onto electrodes which have high accessible specific surface area. Therefore, a high specific capacitance active electrode plays a vital role in efficient energy storage. Various forms of porous carbon, for instance CNT [319a–322a], mesoporous carbon [323a] and carbide-derived carbon [324a], have been studied for electrodes in this respect. Graphene sheets and RGO, a new class of material, have also been predicted as a potential candidate for SC electrodes due to very high specific surface area (2675 m^2/g), chemical stability, excellent electrical, thermal conductivity and capacitance and low cost [325a–328a]. Interestingly, graphene has demonstrated an intrinsic capacitance near 21 lF/cm^2, which set a new upper limit for capacitance [329a]. Ruoff et al. [326a] pioneered the application of chemically reduced graphene in SCs. They have shown

CRG's potential as an electrode for SC, even though the used surface area was 707 m^2/g and graphene sheets were not fully accessible by the electrolyte. The SCs had specific capacitances of 135 F/g and 99 F/g in aqueous KOH and organic electrolytes, respectively. Improved capacitance (191 F/g, in KOH) was obtained after using microwave power to expand GO layers and reduce the GO to RGO (surface area 463 m^2/g) [442]. Wang et al. [327a] have achieved a specific capacitance value of 205 F/g for hydrazine-reduced GO of effective surface area 320 m^2/g. It is worth noting that the surface area of graphene sheets plays a significant role, which directly affects the performance of the SCs.

A main drawback of using graphene and RGO is the agglomeration and restacking due to van der Waals attraction between the neighbouring sheets. The aggregation reduces the effective surface area, resulting in loss of capacitance. Therefore, a few researchers have made effort to keep graphene sheets separated by the addition of metal oxide NPs [330a]. The approach utilising NPs to improve the electrochemical performance is an indication of a positive synergistic effect of graphene sheets and NPs. For example, in RuO_2/graphene composite, graphene sheets were well separated by RuO_2 NPs attached through the oxygen-containing functional groups on graphene surfaces. The composite exhibited a high specific capacitance of 570 F/g for 38.3% Ru loading with excellent electrochemical stability (97.9% retention after 1000 cycles) and high energy density (20.1 W·h/kg) at high power density (10 kW/kg). Similarly, MnO_2/GO composite electrode had a capacitance of 216 F/g, which is much higher than that of individual GO (10.9 F/g) and bulk MnO_2 (6.8 F/g) [331]. Wu et al. [332a] demonstrated an MnO_2/graphene high-voltage asymmetric capacitor based on graphene as a negative electrode and MnO_2/graphene composite as a positive electrode, which exhibited a superior energy density of 30 kW/kg and power density (5 kW/kg at 7 W·h/kg). The metal oxide–graphene nanocomposites have shown a great prominence for the SCs and high energy density capacitor. A study by Jang et al. [333a] reveals the graphene-based SC which exhibits specific energy density of 85.6 W·h/kg at room temperature and 136 W·h/kg at 80°C at very high current

density of 1 A/g. These values are comparable to Ni metal hydride (40–100 W·h/kg). They have reported that the mesoporous structure of the curved graphene sheet is responsible. The curved nature of graphene sheets prevents face-to-face restacking and maintains large pore size (2–25 nm) and capacitance. Further, quick charge–discharge ability in seconds and minimal loss of capacity or energy density make it a prominent candidate better than existing batteries. Graphene–polymer composites have also received much attention owing to their flexibility and superior capacitance than the existing carbon–polymer-based capacitor. Among various conductive polymers, PANi has been considered a most promising conductive electrode material and studied considerably with CNT and carbon system [334a–339a]. A graphene nanosheet–PANi composite was synthesised by in situ polymerisation [334a]. The specific capacitance of 1046 F/g was obtained at a scan rate of 1 mV/s. Conductive graphene nanosheets provide more active sites for nucleation of PANi and are homogeneously coated by PANi NPs on both sides, resulting in an energy density of 39 kW·h/g at a power density of 70 kW/kg. Graphene–PANi composite paper was also prepared by in situ anodic electropolymerisation of polyaniline film on graphene paper [340a]. The flexible as-prepared composite paper combined the high conductivity and flexibility properties of graphene sheet with large capacitance polymer and showed the gravimetric capacitance of 233 F/g.

GRMs can significantly change electrode and electrolyte properties and, consequently, their performance for energy storage and conversion. There are several potential advantages associated with the development of SCs based on these NMs. First, the use of thin layers of conductive TMDs, TMOs and graphene will reduce the electrode thickness and increase the surface area of the active units. Exfoliated TMOs (or hybrid graphene-TMOs) are ultra-thin (capacitance and thickness of electrodes are inversely proportional), conductive and with high dielectric constants. Results have shown the possibility to develop graphene-based SCs with high performance, superior to existing SCs based on activated carbon. The EDLC energy density is determined by the square of the operating voltage and

the specific capacitance (capacitance per unit mass F/g or volume F/cm^3) of the electrode/electrolyte system [315b]. The specific capacitance, in turn, is related to the electrode's SSA accessible by the electrolyte, its interfacial capacitance (F/cm^2) and, in the case of specific capacitance, the electrode material density [316b, 317b]. Graphene-based SCs have been developed with energy density comparable with that of Ni metal hydride batteries [318b].

In particular, exploiting microwave-expanded graphite oxide (MEGrO) activated by KOH, i.e. activated MEGrO (a-MEGrO) [319b], an interfacial capacitance of 22 $\mu F/cm^2$ was achieved [320b]. Aerosol spray drying of GO with a hierarchical pore 3D structure yielded a specific capacitance of ~103 F/cm^3 in a IL electrolyte [321b]. Higher specific capacitance values were obtained exploiting a-MEGrO made by vacuum filtering (177 F/cm^3 in IL electrolyte) [322b]. Capillary compression of RGO gave ~206 F/cm^3 in IL [323b]. Intercalation of cations (e.g. Na^+, K^+, NH^{4+}, Mg^{2+} and Al^{3+}) from aqueous salt solutions between Ti_3C_2 MXene was reported [324b]. A capacitance in excess of 300 F/cm^3, a value much higher than that achieved by porous carbons, was demonstrated [324b]. For SCs, future investigations should also include activated GO, its surface being covered (or decorated) with chemicals, e.g. potassium hydroxide, with controlled GO sheet curvature, controlled mesoporous electrodes combining GO sheets with CNTs, graphene-like structures with controlled and highly uniform pore sizes (TiC chlorination-derived process). Upstream support activities need to focus on systematic exploration on how layer spacing affects capacitance. NMR characterisation will also help identifying charging mechanisms and the role of different functional groups. These development should lead to more robust SCs able to operate in more demanding conditions (−30 to 100°C). The development and implementation of a new generation of SCs based on GRMs should target (i) power electronics systems to improve operation efficiency, in particular electrical power delivery and propulsion systems (minimisation of energy losses, power quality improvement, DC power transmission, etc.); (ii) power electronics systems for efficient renewable energy sources and integration in power grid; (iii) power grid equipment to provide

efficient operation in power production system and "smart grid"; (iv) electric vehicles, in particular electric buses and commercial electric vehicles employing energy-efficient electric and hybrid vehicle propulsion systems; (v) remote, GSM-based systems to monitor and control power electronics controlled drives, etc.; remote control and monitoring systems of distributed industrial objects based on wide area networks (Internet/Extranet) and wireless communication (GSM).

4.2.3 Fuel Cells and Hydrogen Storage

A fuel cell is a device which converts the chemical energy from a fuel into electricity through a reaction with oxygen or another oxidising agent [325b]. Fuel cells are different from batteries and SCs in that they require a constant source of fuel and oxygen to run, but they can produce electricity for as long as these inputs are supplied. There are many types of fuel cells, such as proton exchange membrane (PEMFCs) [326b, 327b], solid oxide fuel cells [328b], molten carbonate [329b], phosphoric acid [330b], etc., but they all consist of an anode (negative side), a cathode (positive side) and an electrolyte which allows charges to move between the two sides of the fuel cell. Electrons are drawn from the anode to the cathode though an external circuit, resulting in a current. The target is to develop novel inexpensive fuel cell catalyst exploiting GRMs [331b, 332b].

It is also reported [331b] that graphene performs better than a commercial Pt catalyst in terms of ORR. GRMs are also promising materials as electro-catalyst, e.g. in PEMFCs, for the electro-oxidation of fuel [333b] at the anode. It is [334b] demonstrated that graphene-supported Pt and Pt–Ru NPs have enhanced efficiency for both methanol and ethanol electro-oxidations with respect to Vulcan XC-72R carbon black, which is the widely used catalyst [335b]. It is demonstrated [336b] that RGO modifies the properties of Pt cluster electro-catalysts supported on it. Pt/graphene hybrid electro-catalysts were reported with a higher activity for methanol oxidation compared to Pt/carbon black [336b]. The edges of LMs, such as MoS2 and WS2, were shown to be active catalytic sites

[337b], thus promising for the hydrogen evolution reaction (HER) in hydrogen fuelled fuel cells [338b].

Fuel cells are considered one of the most promising power sources for mobile and stationary applications due to their high energy conversion efficiency, low operating temperature and ease of handling. Pt and Pt-based materials are widely used for fuel cells, which render them ineffective and prevent fuel oxidation. Recently, graphene/Pt-based hybrid materials have been explored for fuel cell applications, e.g. methanol oxidation, RGO/Pt-based fuel cell showed a maximum power of 161 mW/cm^2 compared to 96 mW/cm^2 for an unsupported Pt-based fuel cell [4]. Hydrogen is currently considered one of the most promising fuels for cells, since its specific energy exceeds that of petroleum by a factor of three [339b] and the product of its combustion is water vapour. However, hydrogen is not an energy source but a secondary energy carrier. It means that hydrogen must be produced, and the amount of energy needed in the production process is subsequently released during its use in fuel cells. Consequently, the advantage of hydrogen for energy must be carefully considered with respect to other carriers, such as electricity. In light of this, the issue of finding ways and materials for efficient hydrogen storage assumes a primary importance. During the past decades, several means for hydrogen storage were considered [340b, 341]. The efficiency of storage is usually evaluated by the gravimetric density (GD), i.e. the weight percentage of hydrogen stored relative to the total weight of the system (hydrogen + container), and the volumetric density (VD), i.e. the stored hydrogen mass per unit volume of the system [342–344]. The US Department of Energy (DoE) targets locate "good" storage systems at a level of 5.5% GD and 0.04 kg/m^3 VD, which would correspond to an usable energy per mass of 1.8 kW·h/kg [345]. Sodium alanate ($NaAlH_4$) is also extensively studied as one of the most promising solid state hydrogen-storage materials [346, 347]. Other classes of compounds are hydrocarbons and Nb hydrides [348–350]. These satisfy the GD and VD requirements and require chemical reactions to control hydrogen charge–discharge. Graphene offers several potential advantages when considered as a medium for hydrogen storage. It is stable

and robust, and therefore can be transported for long distances. At the same time, it is mechanically flexible, enabling new charging–discharging strategies at RT which exploit the dependence of hydrogen–carbon binding on local curvature [351]. It was theoretically suggested that CNTs behave similar to curved graphene [351]: curvature favours physisorption (a process in which the electronic structure of atoms or molecules is barely perturbed upon adsorption) (into concavities) [352] and chemisorption (a process where the electronic structure of bonding atoms or molecules is changed and covalent or ionic bonds are formed) (on convexities) [353, 354]. In particular, it was shown that for small-diameter (0.5–0.6 nm) CNTs, the chemisorption barrier can become negligible [353, 354], favouring the spontaneous molecular hydrogen chemisorption. This should also happen on small-diameter fullerenes. There is also some theoretical work on the physisorption in the interstitial volumes of nanotubes bundles [355], where hydrogen, in metal-intercalated nanotube bundles, is substantially enhanced compared with adsorption onto pure CNTs [355]. What, however, is new and unique to graphene is the possibility of manipulating the local curvature, consequently controlling the hydrogen uptake. This is not possible with CNTs or fullerenes. In perspective, assuming that methods for the production of bulk graphene samples will improve with time, graphene's flexibility and unique electronic properties could enable new approaches for hydrogen storage, such as the integration of hydrogen-storage modules into flexible and light, all-graphene-based devices. It is also possible that integration of graphene into the aforementioned hydrogen-storage materials might offer additional routes for the realisation of optimised hybrid tanks. Hydrogen can be adsorbed on graphene in two different ways: either by physisorption, i.e. interacting by van der Waal forces, or by chemisorption, i.e. by forming a chemical bond with the C atoms. Physisorption usually happens with hydrogen in molecular form [356]. It was shown that in the most favourable conditions (high pressure and low temperature), H_2 can form a uniform compact monolayer on the graphene sheet, corresponding to GD = 3.3% [357] (doubled if two sides are considered). The VD depends on the possibility of compacting

graphene sheets in multilayer, 3D assemblies or nanostructures of graphene. In multilayers, calculations based on hybrid post-Hartree–Fock/empirical potentials and including quantum treatment for hydrogen [356] indicate that both GD and VD depend on the interlayer separation, with highest values for an interlayer separation of 6–8 Å [356]. Monte Carlo simulation of an artificial 3D structure composed of graphene layers placed at an interlayer distance of 12 Å and stabilised by CNTs inserted perpendicularly to the graphene planes [358] showed GD up to 8% at low temperature and high pressure, decreasing by an order of magnitude at room conditions, but raising up to 6% at room temperature and ambient pressure after doping the pillared structure with Li cations [358]. Experimentally, it was shown that such a layered structure can be realised by using GO and the interaction between hydroxyl groups and boronic acids [359] (i.e. an aryl- or alkyl-substituted boric acid containing a carbon–boron bond) with a predicted GD of ~6% at 77 K at a pressure of 1 bar. The enhancement of van der Waals interaction [360] can be similarly postulated in any hollow graphene nanostructure. For example, an empirical estimate of the maximal VD versus GD relation of hydrogen physisorbed in CNTs can be obtained assuming a level of compression similar to that of liquid H_2 and a full occupation of the cavity. Experimentally, however, the best reproducible results yield GD of ~1% at a pressure of 120 bar at room temperature [361]. Molecular hydrogen adsorption in graphene-like flakes obtained by chemically reducing exfoliated GO has been studied [362], leading to a molecular hydrogen adsorption of 1.2% at 77 K and a pressure of 10 bar and 0.68% and ambient pressure [362]. A GD of ~2.7% at 25 bar and room temperature was reported in GO after ultrasonic exfoliation in liquid [363]. Chemisorption processes may reach a GD of 8.3%, i.e. even larger than the "ultimate" goal of DOE. This corresponds to the formation of a completely saturated graphene sheet, with 1:1 C versus H stoichiometry, i.e. "graphane", whose stability was first hypothesised in a DFT-based theoretical study [364] and subsequently studied in experiments [365]. It has been shown one-side hydrogenation and its reversibility by thermal annealing [365]. The chemisorption of atomic hydrogen is a favourable process: ac-

cepted values for H binding energy and chemisorption barriers are ~0.7 and ~0.3 eV [366–371].

STM experiments have focused on atomic-scale imaging of adsorption and clustering of hydrogen atoms on graphite [372–375]. Atomic hydrogen absorption on graphene grown on SiC was also investigated by STM [376, 377], showing formation of dimer structures, preferential adsorption of protruding graphene areas and clustering at large hydrogen coverage [376, 377]. As in the case of physisorption, VD depends on the possibility of building compact structures with graphene (or graphane) sheets. Considering interlayer spacing from two to four times that of graphite, it is possible to obtain VD values from 0.03 to 0.08 kg H_2/L, which fit and exceed the DOE goals. However, chemisorption of molecular hydrogen on graphene presents rather high barriers of ~1.5 eV [378], requiring the dissociation of H_2 (dissociative adsorption). Analogously, the desorption of hydrogen (associative desorption) has a barrier of similar height. This makes H_2 storage on graphene stable but poses problems in the release phase. These problems are common with other storage media based on hydrocarbons or, in general, on chemical adsorption. Based on these results, one could envisage that if the curvature of the sheet is inverted and convexities are transformed in concavities, hydrogen might spontaneously release even at room temperature [351]. The large variation of H binding energy makes chemisorption a favourable process on convex sites, and hydrogen release a favourable process on graphene concave sites, offering a new route towards hydrogen storage/release.

GRMs might also be exploited for the production of clean fuels, such as H_2, in a cost-effective renewable process. Photocatalytic splitting of water into H_2 and O_2 using semiconductor-based heterogeneous systems could be a viable method for H_2 production [379, 380]. A major limitation is the lack of stable semiconductor photocatalysts which can carry out the water splitting in the visible region of the solar spectrum. Stable, efficient and visible-light-driven photocatalysts might be achieved by using chemically derived graphene as a support for chalcogenide nanocatalysts. Graphene will serve several purposes. Its layered structure might

not only suppress the semiconductor particle growth but also act as an electron collector and transporter to lengthen the lifetime of the photogenerated charge carriers (see Fig. 4.21).

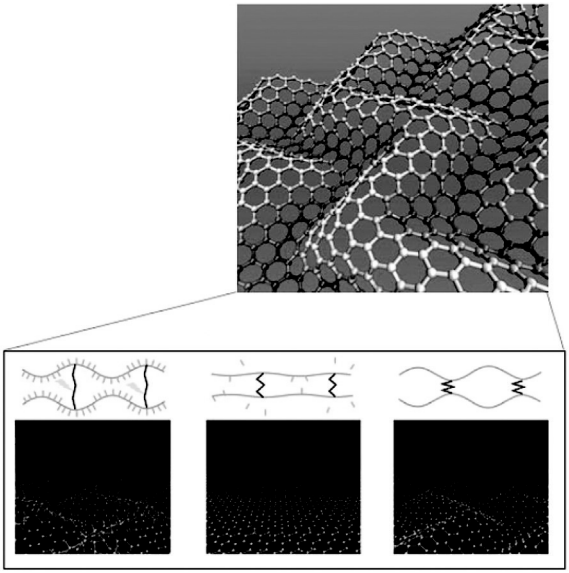

Figure 4.21 Corrugated graphene sheet by lateral compression and illustration of controlled hydrogen adsorption and release by curvature inversion. Reprinted with permission from Ref. [351], Copyright 2011, American Chemical Society.

4.2.4 Solar Cells

RGO transparent electrodes can be used for solar cell electrode. Several studies suggest that GO/RGO can also be used as hole-transport layer (HTL) as well as part of active material. In vertical bulk heterojunction (BHJ) devices, both the donor and acceptor phases are in the direct electrical contact with the cathode and anode electrodes. Most vertical organic solar cells are composed of ITO/P3HT:PCBM/Al configuration. The polymeric donor and acceptor materials often result in the recombination of carriers and current leakage. To minimise such detrimental effects, electron blocking and HTLs are deposited on top of the transparent and conducting ITO anode (Fig. 4.22) [162a, 162b].

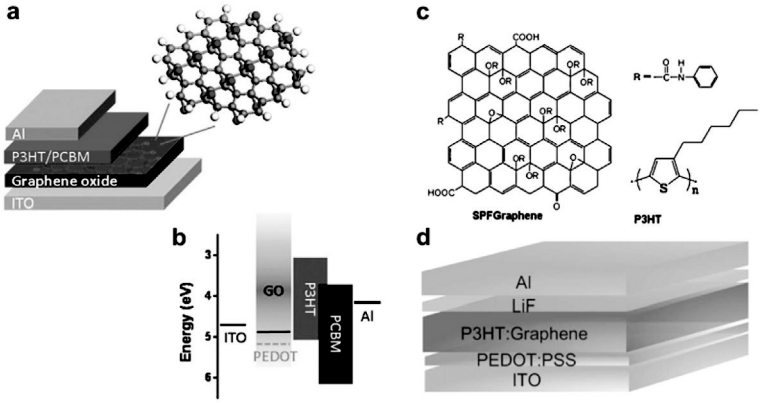

Figure 4.22 (a) Schematic of the photovoltaic device structure consisting of the following: ITO/GO/P3HT:PCBM/Al. (b) Energy-level diagrams of the bottom electrode ITO, interlayer materials (PEDOT:PSS, GO), P3HT (donor), and PCBM (acceptor), and the top electrode Al. Reproduced from Ref. [162b] under the Creative Commons Attribution License. (c) The schematic chemical structure of SPF graphene and P3HT. (d) Schematic structure of the devices with the P3HT/SPF graphene thin film as the active layer; ITO/PEDOT:PSS (40 nm)/P3HT:SPF Graphene (100 nm)/LiF (1 nm)/Al (70 nm). Reprinted by permission from Ref. [163b], Copyright 2009, John Wiley and Sons.

The most common HTL in polymer solar cells is PEDOT:PSS. However, the PEDOT:PSS combination has been made from highly acidic aqueous suspensions which corrodes the ITO at high temperatures and contributes water/moisture into the active layer, which leads to poor device performance [162a, 162b]. To overcome this issue, ITO/GO/P3HT:PCBM/Al configuration was introduced for more efficient collection of holes and the band energies of the configuration are 4.4–4.5/4.9/4.9:4.2/4.2 eV, respectively. Interestingly, the power efficiency values are dependent on GO film thinness. GO thickness of 2 nm has shown best efficiency performance compared to higher thickness (>4 nm) due to the increase in serial resistance and the slightly lower transmittance of the films with thickness. Other studies have shown the use of RGO as acceptor materials in the BHJ photovoltaic devices. For instance, Liu et al. [163a, 163b] reported the organic solution-processable RGO as an acceptor material in organic photovoltaic devices with P3HT as an electron-donor material. Figure 4.22b shows a schematic diagram of a solar cell using RGO as an active material. The RGO was

well dispersed in P3HT with 10 wt% doping. The properties of the materials induce quenching of the photoluminescence of the P3HT and lead to strong electron/energy transfer from the P3HT to the RGO. A power-conversion efficiency of 1.1% was achieved by using RGO as an active material.

The direct exploitation of solar radiation to generate electricity in PV devices is at the centre of an ongoing research effort. Si is by far the most widely used absorber [381] and currently dominates the PV market [381], with energy conversion efficiency (η) up to ~25% [382]. Efficiency η is defined as $\eta = P_{max}/P_{inc}$, where P_{inc} is the incident power and P_{max} = VOC × ISC × FF, where VOC is the maximum open-circuit voltage, ISC is the maximum short-circuit current and FF is the fill factor, defined as FF = $(V_{max} \times I_{max})/(\text{VOC} \times \text{ISC})$, with I_{max} and V_{max} the maximum current and voltage [383]. Despite significant development [384], the cost [382, 384] of crystalline Si-based solar cells, often referred to as first-generation solar cells [381], is still a bottleneck for the implementation of solar electricity on a large scale. The development of new materials and concepts for the PV devices is thus fundamental to increase efficiency, especially for mobile applications with limited surface area. Thin-film solar cells such as a-Si [385], cadmium telluride (CdTe) [386], copper indium gallium diselenide (CIGS) [387] and thin-film crystalline Si are known as second-generation PVs, because they are based on thin-film technology. The development of thin-film solar cells is driven by the potential costs reduction [388]. An even cheaper and versatile approach relies on the exploitation of emerging organic PV cells [389] and DSSCs [390]. They can also be manufactured by a R2R process [391], even though they have lower η. An organic photovoltaic cell relies on polymers for light absorption and charge transport [389]. It consists of a TC, a photoactive layer and the electrode [389]. DSSCs use an electrolyte (liquid or solid) as a charge-transport medium [390].

This solar cell consists of a high-porosity nanocrystalline photoanode, comprising TiO_2 and dye molecules, both deposited on a TC [390]. When illuminated, the dye captures the incident photon, generating e–h pairs. The electrons are injected into the TiO_2 conduction band and then transported to the CE [390].

Dye molecules are regenerated by capturing electrons from the electrolyte. Another class of solar cells, called meso-super-structured solar cells (MSSCs), was proposed by Kjima et al. [392]. These are based on organic halide perovskite LMs (e.g. $CH_3NH_3PbX_3$ where X is Cl, Br, I or their combination) as photosensitiser [392–395] and an organic hole-transport material [393]. An efficiency of 20.1% was recently reported [396], which is a very promising value considering that the device structure can still be further optimised. However, these LMs may not satisfy sustainability requirements because of their lead content. Graphene, thanks to its mechanical, electronic and optical properties, can fulfil multiple functions in PV devices: as TC window, antireflective layer, photoactive material, channel for charge transport and catalyst [293].

GTCFs can be used as window electrodes in inorganic [397], organic [398, 399] and DSSCs [400]. The best performance has been achieved to date in graphene/n-Si Schottky junction solar cells with η = 8.6% [401]. The GTCFs were doped with bis(trifluoromethanesulfonyl)-amide[((CF3SO2)2NH)] polymer [401]. Higher η~10.34% [402] was achieved in an organic/Si cell exploiting GTCF doped with HNO_3, with potential for having work function tuning capability, important to control the contact resistance [403]. Charge transport and collection have also a fundamental role in organic PV (OPVs). In a poly-3-hexyl thiophene (P3HT)/phenyl-C61-butyric acid methyl ester (PCBM) solar cell, both donor (P3HT) and acceptor (PCBM) materials are in direct electrical contact with the cathode (back electrode) and anode (ITO) electrodes, leading to carriers recombination [404]. This negative effect can be reduced using electron blocking and HTLs, usually deposited on top of ITO [404, 405]. GO dispersions were also used in bulk heterojunction PV, as electron-acceptors [406, 407] with η ~3.5% [404]. Higher η with respect to GO was achieved with the use of RGO as HTL [408], demonstrated η = 3.98%, superior to PEDOT:PSS (η = 3.85%). Hybrid structures (e.g. GO/SWNTs) were also investigated as HTL [409]. The addition of a small amount of SWNTs in the GO layer significantly improved the devices' FF [409]. Indeed OPVs fabricated with GO/SWCNTs as HTL have shown higher performance (η = 4.10%) compared to devices using PEDOT:PSS (η = 3.28%). GQDs

can also be efficient HTLs for OPVs, with η = 6.82% [410], showing longer lifetime and more reproducible PV performances with respect to PEDOT:PSS-based cells [410]. It is reported that the short-circuit current of P3HT:PCBM solar cells is enhanced by ~10% by the addition of graphene produced by LPE, with a 15% increase in the photon to electric conversion efficiency [411]. The addition of graphene flakes to the P3HT:PCBM blend also improves the balance between electron and hole mobilities with respect to a standard P3HT:PCBM solar cell [411]. GRMs have also been proposed as photosensitisers [412] to absorb the incident light and convert it into an electrical current [381]. For OPVs, the key requirements of a photosensitiser are: (i) ability to absorb light over a wide energy range [412]; (ii) high carriers mobility [412]; (iii) thermal and photochemical stability [389]; (iv) efficient charge separation between donor/acceptor materials [389]. Simulations based on equivalent electrical circuits for OPVs indicate that η~12% should be possible with graphene as photosensitiser [413]. RMs might be implemented in different types of solar cells. This may facilitate their use in a variety of applications, ranging from mobile devices, printed electronics, building technologies, etc. Apart from the improvement in energy-storage devices, with reduced size and weight and with longer and more stable performance, the development of more efficient energy-harvesting methods could lead to energetically autonomous devices. Graphene maintains its properties even under extreme bending and stretching. This is ideal for its integration in polymeric, rigid and flexible substrates, for integration in smart windows and other building components. This increases fabrication flexibility in addition to having economic advantages. The efficient electric field concentration of MNPs can increase the light-harvesting capacity of graphene by more than an order of magnitude [414].

A multilayer structure solar cell (see Fig. 4.23) can be envisaged with graphene and QDs to achieve total light absorption, thus higher efficiency. Another option is a multilayer structure heterojunction based on QDs (MoS_2, WS_2, CdS, PbS, ZnS, etc.) alternating with graphene conductive layers, or coupling a standard DSSC with a graphene/MoS_2 (or WS_2) tandem solar cell. The aim is to overcome the η of state-of-the-art solar cells extending it beyond the Shockley–

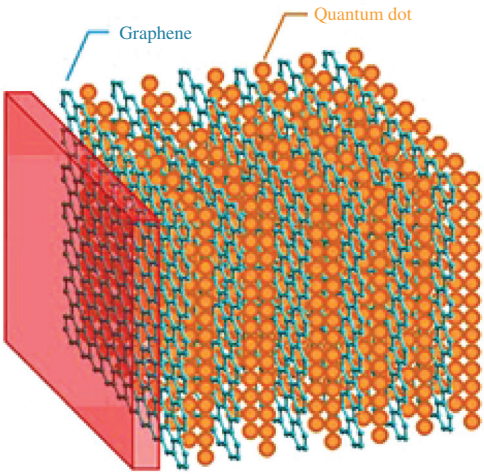

Figure 4.23 Multilayer solar cell composed of alternating stacked SLG and quantum dots. Reproduced from Ref. [21] under Creative Commons Attribution License.

Queisser limit (i.e. the maximum theoretical efficiency of a p–n junction solar cell) by using multiple sub-cells in a tandem device. Ideally, the sub-cells would be connected optically and electrically and stacked in band gap decreasing order. This configuration shifts the absorption onset of the complete device towards longer wavelengths. In addition, high-energy photons are converted more efficiently since thermalisation losses of the generated e–h pairs are reduced with the graded band gap structure. For example, in a series-connected double-junction device, the ideal optical band gaps are ~1.6–1.7 eV for the top cell and ~1.0–1.1 eV for the bottom cell, which extends the efficiency limit to ~45% [21, 415]. Another possibility is to assemble hybrid graphene/nanodiamonds [416, 417] motivated by the properties of both materials, and possible interactions between sp^2 and sp^3 carbon [418]. The <111> diamond surface could form an ideal interface for heteroepitaxial graphene, with ~2% mismatch. The armchair diamond rings on the <111> surface can be interfaced to the six-membered C rings of graphene. There are several impacting interests in these interfaces. Undoped nanodiamond could serve as gate insulator. A controllable functionalisation of nanodiamond may be used to tune graphene's

μ and work function other than the optical properties. This might be achieved by coupling graphene to nanodiamond using organic chemistry routes via linkers with functional properties. In these solar cells, conductive B-doped nanodiamond would serve as anode, while graphene would be the cathode. If donor–acceptor organic dyes are used for such interfacing, the proposed full carbon structure would have effective charge transfer from the highest occupied molecular orbital (HOMO) of the organic dye to the diamond valence band, and in a reversed process on the graphene/lowest unoccupied molecular orbital (LUMO) side. Another approach relies on the use of chemically synthesised GNRs and/or GQD sensitisers in solar cells. GQDs have been synthesised with molar extinction coefficients ($\sim 1 \times 10^5$ $M^{-1}cm^{-1}$ [419], one order of magnitude larger than inorganic dyes (e.g. ruthenium complexes), 956 commonly used in DSSCs) and absorption edge beyond 900 nm [419].

4.2.5 Transparent Conductive Electrodes

It has been demonstrated that a thin film (<30 nm) of RGO is semi-transparent in visible and NIR region, while thick films are opaque. The transmittance and conductivity of the GO/RGO film can be tuned by tuning the thickness of the film and the degree of reduction [420].

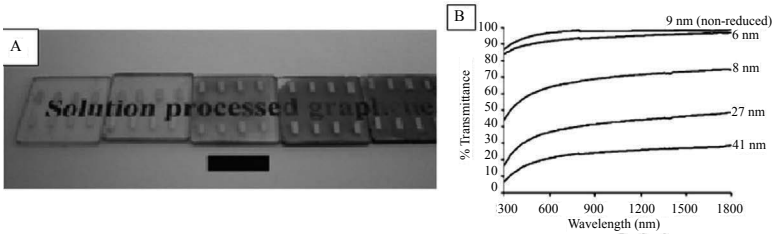

Figure 4.24 Optical and electrical characterisation of spin-coated GO films on quartz. (A) Photograph of an unreduced (leftmost) and a series of high-temperature-reduced GO films of increasing thickness. Black scale bar is 1 cm. (B) Optical transmittance spectra of the films in (A) with the film thickness indicated. Reprinted with permission from Ref. [420], Copyright 2008, American Chemical Society.

Figure 4.24b shows how the transparency of RGO varies with film thickness. The upper-most film is 9 nm thick GO, while the rest of the films are RGO (annealed in 1100°C for 3 h) with thickness 6, 8,

27 and 41 nm (from left to right). It can be seen that as the film gets thicker, the transmittance gets reduced. While the conductivity of the RGO thin film increases with the degree of reduction and transmittance decrease. Therefore, the optimisation of film thickness and reduction parameters is the key in achieving high-performance transparent and conducting RGO thin film. Optical and mechanical properties of RGO thin film were also studied on flexible substrates. For example, Yin et al. [421] studied the bending effect on the properties of RGO for film thickness of 4–21 nm. After applying tensile stress (tensile strain of 2.9%) on the device, the performance was monitored by resistance change with the number of bending cycles. The device showed an excellence stability of resistance, even when bending cycles reached about 1000 times. Due to their transparency, conducting and flexible nature, RGO thin film is considered to be a promising electrode material for organic electronic and optoelectronic applications. Presently, indium-doped tin oxide is widely used as transparent and conducting electrodes in optoelectronic application. However, the ITO-based materials are expensive [422] and their limitation of mechanical flexibilities [423] makes them unattractive for flexible display and solar cell applications. In this respect, RGO electrodes provide several advantages: (i) possibilities of one-phase reaction without additional surfactant due to water-soluble properties; (ii) the homogeneity and composition of the films are simply determined by the composition of the parent suspension and surface modification of the substrate; (iii) relatively inexpensive starting materials and (iv) low-temperature and high-throughput processing. In addition, the work function of RGO (4.2–4.6 eV) matches with the HOMO level of most of the organic materials, and p–p interaction exists between RGO and organic material [421, 424].

Several research groups successfully used RGO electrode for the fabrication of organic light-emitting diodes (OLED) and solar cells. Efficient RGO-based OLEDs have been first demonstrated by Wu et al. [277]. The RGO-based OLED performance nearly matches with that of ITO-based devices, despite higher resistance (800X/square) and different work function of the RGO anodes. Wang et al. [425] reported that RGO films can be employed for fabrication of dye-sensitised solar cells. In this application, Spiro-OMeTAD was used as a hole-transport material, and porous TiO_2 was used for electron

transport materials. The solar cell was fabricated using RGO as an anode and Au as cathode (Fig. 4.25A).

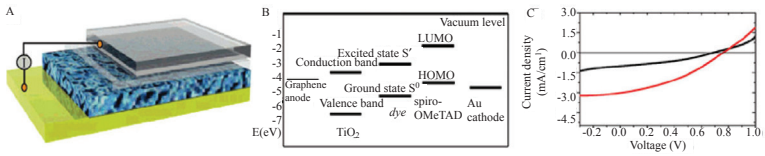

Figure 4.25 (A) Illustration of dye-sensitised solar cell using graphene film as electrode. The four layers from bottom to top are Au, dye-sensitised heterojunction, compact TiO_2 and graphene film. (B) The energy-level diagram of graphene/TiO_2/dye/spiroOMeTAD/Au device. (C) I–V curve of graphene-based cell (black) and the FTO-based cell (red), illuminated under AM solar light (1 sun). Reprinted with permission from Ref. [425], Copyright 2008, American Chemical Society.

Figure 4.25 shows the energy-level diagram of an RGO (4.42 eV)/TiO_2/dye/spiro-OMeTAD/Au (5.0 eV) device. The electrons are first injected from the excited state of the dye into the LUMO level of TiO_2 and then reached the RGO electrode via a percolation mechanism inside the porous TiO_2 structure. Meanwhile, the photo-oxidised dyes are regenerated by the spiro-OMeTAD hole conducting molecules (HOMO) and then hole injected into Au cathode. Figure 4.25C shows the I–V curve of the solar cell using RGO (black curve) as anode and the comparison with fluorine tin oxide (FTO) (red curve) electrode. Lower short-circuit current in RGO electrode leads to low power-conversion efficiency (0.26%) compared to FTO (0.84%). This may be due to the series of resistance of the device, lower transmittance of the materials (70.7%) and space charge limited conduction on contact between active materials and RGO electrodes. To overcome the contact problem, Yin et al. [424] suggested the use of hole-transport interlayer (ZnO nanorod) between RGO electrodes and active polymeric materials by electrochemical deposition. The structures of the device were RGO/ZnO/P3HT/PEDOT:PSS/Au. The observed higher power-conversion efficiency of 0.31% was demonstrated, compared to ZnO-free interlayer. As can be seen, the solar cell fabricated with RGO electrode suffers from low efficiency and more work is needed to make RGO an efficient electrode material.

4.2.6 Clean Energy Devices

Graphene is a promising electrode material due to its high theoretical surface area and electron transferability along its 2D surface. Graphene-based electrodes are used as rechargeable lithium-ion batteries and electrochemical double-layer capacitors. Graphene nanocomposites can form conducting 3D network due to uniform dispersion of silicon particles and reconstitution of graphene platelets, which are important aspects for the high storage capacities. Chemically modified graphene sheets have potential to act as an electrode material for ultra-capacitors. Lithium-doped graphane was used for hydrogen adsorption and its storage applications [426–428].

4.2.7 Memory and Photovoltaic Devices

Graphene-related NMs have also been used in memory devices, transparent electrodes, electron acceptor and light adsorber due to their good electronic properties, transparency and large specific surface area [429]. Lots of studies on graphene-based photovoltaic applications have been reported, in which graphene-based materials are used as the transparent electrodes, electron acceptor and light absorber. ZnO film is electrochemically deposited on the RGO electrode and subsequently incorporated to a hybrid solar cell based on a ZnO–P3HT system. The graphene–TiO_2 composite, a type of effective electron acceptor, has been used as the photo anode in dye-sensitised solar cell. A novel graphene/CdS-QD bilayer structure can work as the electron transfer system in photovoltaic devices [10].

4.3 Electronics

Graphene has already demonstrated high potential in most ICT areas, ranging from top-end, high-performance applications in ultrafast (>1 THz) information processing, to consumer applications using transparent or flexible electronic structures. The great promise of graphene is testified by the increasing number of chip-makers now

active in graphene research. Most importantly, graphene is considered to be among the candidate materials for post-Si electronics by ITRS [430]. To extend the application of graphene-based electronics to the field of optoelectronics, it has been proposed to incorporate with excited states of semiconducting NPs so that the optoelectronic properties of the composite materials can be tuned over a wider range of the spectrum. The photocurrent generation in graphene/semiconducting NP quantum dot composite shows potential for large-area optoelectronic devices. Several semiconducting NPs such as CdS, CdSe, ZnO, TiO_2, TSCuPc and Co_3O_4 have been anchored on graphene for hybrid solar cell and optoelectronic device applications. For example, RGO/CdSe NPs composite showed a dramatically enhanced photo response with fast time response under visible light. Another study detected a picoseconds ultrafast electron transfer from the excited CdS to graphene by time-resolved fluorescence spectroscopy, suggesting that CdS/graphene can also be a potential candidate for harvesting optoelectronic applications [4, 18, 63–80].

4.3.1 Field-Effect Transistors

Graphene is a suitable material for metallic transistor applications. The graphene carriers are bipolar with electrons and holes, which can be tuned by a gate electrical field due to unique band structure. A graphene-QDs-based single-electron transistor was made by electron beam lithography technique. GNRs prepared from "unzipped" CNTs by plasma etching and chemical oxidisation methods are potential production techniques for future graphene FET devices. Graphene derivatives are better material, which can be used as SCs than silicon-based ones because graphene derivatives possess band gap and semiconductor properties [426, 427, 429, 431–435].

Myung et al. [436] reported the assembly of AuNPs fabricated on top of a reduced GO junction. At the crossing point, the forward bias from –10 to 10 V (or reverse bias from 10 to –10 V) sweep curves showed a positive (or negative) slope indicating an n-type (or p-type) FET behaviour (Fig. 4.26a).

It indicates that in the forward sweep, charges move along in n-type channels (right of Fig. 4.26b). While in reverse sweep,

charge transfer shows p-type characteristics left of Fig. 4.26a. These properties suggested that the metal NPs–based graphene device can be operated as a conventional conductive switching memory by adjusting the charge density on the metal NPs. GNR FET devices with both top and back gates were fabricated. The fabrication started by back-gated GNR FETs. Then using 1 nm e-beam evaporated Al as a seed layer, 30 nm ALD-Al_2O_3 was deposited. The channel length of the fabricated devices is 2 μm, and the length of the top-gate electrode is about 1 μm, covering half of the channel. The SEM image on Fig. 4.27 shows a typical FET.

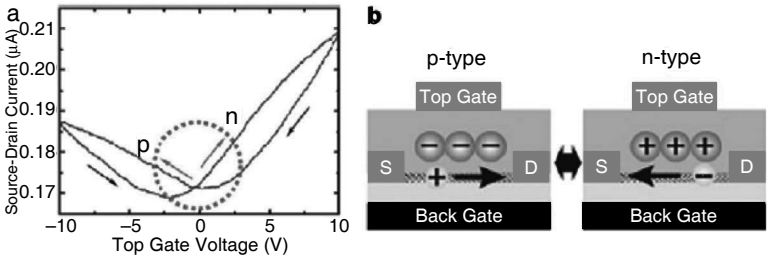

Figure 4.26 ''Type-switching'' memory devices and reconfigurable logic circuits. (a) Typical hysteresis curve of a type-switching memory device based on GO and NPs. It exhibited both n-type and p-type characteristics near zero gate bias voltage. (b) Operation principle of type-switching memory device. Reprinted by permission from Ref. [436], Copyright 2010, John Wiley and Sons.

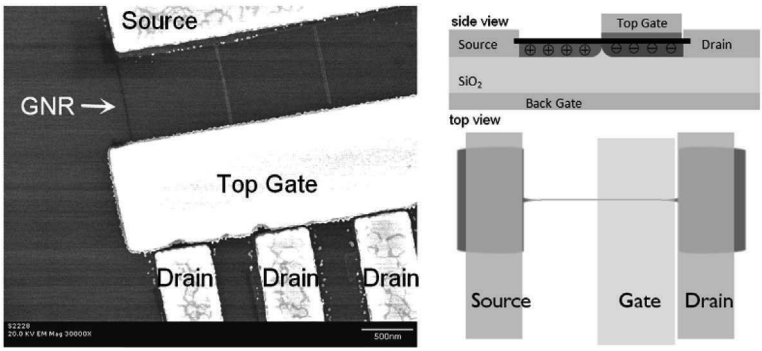

Figure 4.27 (a) SEM image and (b) schematics of the GNR FET. Half of the channel is top-gated, while the whole device is back-gated. Device parameters: L = 2 μm, LG = 1 μm, W = 30 nm. Reproduced from Ref. [437] under Creative Commons Attribution License.

The G-FETs used in this study were fabricated on a 285-nm-thick thermally grown SiO_2 layer on a heavily p-doped silicon substrate ($\rho<0.01\ \Omega\cdot cm$). Single-layer graphene flakes were obained by micromechanical exfoliation using natural graphite and clear adhesive tape. The graphene flakes were searched by an optical microscope after slowly peeling off the tape from the substrate. As a result of this procedure, various types of graphene layers (or thick graphite) were identified on the surface SiO_2/Si substrate. Single-layer graphene flakes were identified by analysing the shift in green intensity under optical microscope observation and by Raman spectroscopy. Ti (5 nm)/Au (30 nm) source and drain electrodes were formed by electron beam lithography and lift-off method. The degenerately doped silicon substrate was also used for the back gate. The device was surrounded by a silicone rubber pool attached to the substrate. Then the Ag/AgCl reference electrode was immersed into the solution contained within a silicone rubber barrier. The Ag/AgCl reference electrode was used as the top-gate electrode to minimise environmental effects. The electrical characteristics of the G-FETs were measured by a semiconductor parameter analyser using two-terminal measurement. On the contrary, the stability of G-FETs is superior to the CNT-FETs. Single-layer graphene was obtained by a micromechanical cleavage method. Changes in the solution pH were electrically detected with a lowest detection limit (signal/noise = 3) of the 0.025. Their ID showed protein-concentration dependence, and their ID changes with BSA concentration were fitted well by the Langmuir adsorption isotherm. In addition, the G-FETs clearly detected the different charge types of a biomolecule owing to its isoelectric point. G-FETs are promising devices for highly sensitive chemical and biological sensors [437].

The progress in digital logic relies in downscaling of CMOS devices through the demand for low voltage, low power and high performance. This size scaling has permitted the IC complexity to double every 18 months [438, 439]. The decrease in gate lengths corresponds to an increase in the number of transistors per processor. Nowadays, processors containing 2 billion MOSFETs,

many with gate lengths of 30 nm, are in mass production (Fig. 4.28) [440].

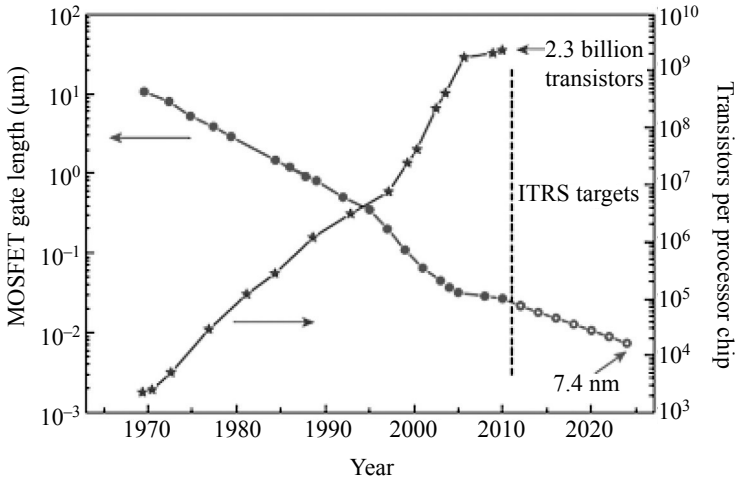

Figure 4.28 Evolution of MOSFET gate length integrated circuits (filled circles). The ITRS targets a gate length of 7.4 nm in 2025 (open circles). With the decrease in gate lengths, the number of transistors per processor increased (stars). New materials, such as graphene, are needed to maintain these trends. Reprinted by permission from Macmillan Publishers Ltd: *Nature Nanotechnology*, Ref. [440], Copyright 2010.

However, CMOS scaling is approaching fundamental limits due to various factors, such as increased power density, leakage currents and production costs, with diminishing performance returns [438, 439]. For example, static (leakage) power dissipation in state-of-the-art Si microprocessors has already exceeded the dynamic (switching) power [441] and is expected to increase further with the continuation of the aggressive scaling of CMOS technology. The outstanding thermal properties [442] of graphene provide an extra motivation for its integration with CMOS technology, as well as beyond CMOS with the possibility to overcome state-of-the-art Si and III–V semiconductor-based high-frequency FETs at the ultimate scaling limits [443]. G-FETs with controlled threshold voltage and both n-channel and p-channel need to be demonstrated for CMOS

logic. New graphene device concepts, such as tunnel FETs (TFETs) and bilayer pseudospin FETs (BiSFET) [444], and different design options are under evaluation stage. The BiSFET is based on the electrical properties of two layers of graphene in close proximity [444]. Electrons in one layer can pair with holes (both Fermions) in the opposite layer, resulting in e–h pairs/excitons (Bosons), which can then condense [444]. The condensation alters the quantum wavefunctions in the bilayer structure, converting states which were isolated in one of the two layers into states which are a coherent linear combination of top- and bottom-layer components [445]. This qualitative change effectively shorts the two layers, reducing the tunnel resistance from a large value to a value limited by contacts only [444]. The reduction in tunnel resistance applies only for small interlayer bias, however, because high current destroys the condensate [445]. The BiSFET exploits the I–V nonlinearities associated with this maximum tunnel current, allowing, in principle, lower voltage, lower power operation than possible with CMOS FETs [444]. Moreover, the integration with exiting CMOS technology is a critical step in establishing a pathway for graphene electronics.

4.3.2 Graphene-Based Antennas

Along with the progressive shrinking in size of devices, engineers have developed efficient communication means tailored to the peculiarities of each type of device. The resulting networks have expanded the applications of the individual nodes by providing them a mechanism to cooperate. A good example of such applications is the Internet. The main challenge to enable communications among nanomachines and at the nanoscale is that reducing the size of a classical metallic antenna down to a few hundred nm would impose the use of extremely high resonant frequencies [446]. Graphene-based nano-antennas (width: few nanometres; length: tens of micrometres) could be a key technology to overcome this issue, since this material supports the propagation of tightly confined SPPs [447, 448]. Due to their high effective mode index [449], the SPP propagation speed can be up to two orders of magnitude below the electromagnetic wave

propagation speed in vacuum. The main consequence is to reduce the resonant frequency of the antenna [450]. Research works [451, 452] point to THz bands at short ranges, thereby enabling graphene-enabled wireless communications (GWC) [453]. The particularities of wireless communications at the nanoscale, their applications and those aspects specifically inherent to GWC, such as the THz band, require that well-established communication protocols and network architectures undergo a profound revision in order to be applied to this scenario. One must develop a radically new medium access control (MAC), which provides channel access control mechanisms which make it possible for network nodes to communicate within a multiple access network, routing and addressing protocols along with network paradigms for GWC. GWC might enable a variety of ICT applications. First, embedding nano-antennas into multi-core processors, allowing them to scale up to thousands of cores and overcoming the challenge of global wiring and the associated delay. This multi-core architecture is known as wireless network-on-chip (WNC) [454]. Second, GWC may allow networks of small sensors which can measure nanoscale magnitudes with unprecedented accuracy. Nanosensors might measure physical characteristics of structures a few nm in size, chemical compounds in concentrations as low as one part per billion or the presence of biological agents. Such networks of sensors, known as wireless nanosensor network (WNSN) [455], are, per se, a new networking paradigm. WNSN requires the integration of several nanoelectronic components and could be commercially feasible in 20 years from now. Third, GWC may enable communications in any device, regardless of its size. In this context, long-awaited applications such as true ubiquitous computing or programmable matter [456], a material which inherently has the ability to perform information processing, may be possible with GWC. These applications may change the way in which society understands and interacts with technology, and push the boundaries of what technology can achieve. Moreover, the flexibility of graphene, coupled with the high σ [457] and transparency [234], makes it a good candidate for printed antennas on top of touchscreens on smartphones. Traditionally, these types of antennas

are based on ITO [458]. Furthermore, the variable resistivity can also lead to graphene's use in antenna design applications, as a smart material where its conductivity can be adapted according to external stimuli. Reconfigurable antennas may be designed controlling the radiation pattern and efficiency, depending on the application [459]. For example, by stacking several layers of graphene, the conductivity and band gap could also be tuned. Therefore, graphene's properties could be tuned either by an external electric field or through an interaction-induced symmetry breaking between several layers, thus leading to atomically thin insulators or conductors.

4.3.3 Graphene-Nanocrystal Hybrid–Based LED

Shape-controlled semiconductor core/shell colloidal inorganic nanocrystals (CINs) show advantageous luminescent properties [460], including high quantum yield [461] and the possibility to precisely tailor their emission wavelength by tuning the core size [461]. The organisation of such CINs into ordered arrays, e.g. microscale ensembles of laterally and vertically aligned nanorods, has been achieved, with promising optoelectronic properties [462]. Graphene can open up new horizons in terms of designing hybrid architectures consisting of light-emitting semiconductor CINs [463, 464] and plasmonic MNPs [465]. Apart from being the scaffold for complex assembly structures, graphene can contribute to the functionality due to its electrical properties, which can be used for charge transport, but also for modulation of electrical interaction between metal and semiconductor NPs. The aims are (i) fabrication of homogenous and preferably ordered CIN layers on graphene, (ii) using graphene as a template for more complex NC assemblies, (iii) implementing graphene as an interface between metal NPs for plasmonics and semiconductor CINs for enhanced light emission, (iv) optimising the graphene-NC interface for achieving efficient charge injection into semiconductor CINs while maintaining their bright emission, (v) design of novel device architectures exploiting the flexibility of graphene. The first aim is the controlled fabrication of NC layers on graphene surfaces in bilayer and multilayer

configurations for light-emitting applications, and the efficient charge injection from graphene into the CIN layer. The future target is the bottom-up approach to graphene–CIN-based electrically pumped LEDs and lasers, in which the optical gain material also constitutes the resonant cavity.

4.3.4 Transparent Conductive Films

Graphene materials are promising candidates for TCFs because of their high carrier mobility, electrical conductivity and optical transmittance in the visible range of the spectrum. Optical transmittance (transparency) of chemically modified graphene is reported to be 83% at wavelength of 1000 nm. Disordered films of randomly stacked few-layer graphene platelets have shown ~75% transmittance at wavelength of 550 nm. GO-based TCF shows ~87% transmittance at a wavelength of 550 nm.

Graphene-based TCFs have been used as electrodes for dye-sensitised solar cells, liquid crystal devices and OLEDs [433]. The current performances of GTCFs are very promising in view of commercial applications, already matching requirements for many of them [466]. Graphene can be used as a window in inorganic (Fig. 4.29a), organic (Fig. 4.29b) and DSSCs (Fig. 4.29c). A uniform graphene layer can be transferred to the required substrate, and large-area graphene has been transferred to 30 × 30 cm^2 substrates with low-temperature lamination techniques [468].

4.3.4.1 Solar cells

The TC layer is a necessary component of all thin-film solar cells, and it has a major impact on efficiency, resulting in a 10–25% power loss even for the best TCs [469]. For the development or adoption of any new TC material, it is useful to know the impact on efficiency and the requirements to improve overall efficiency. Graphene can reduce losses, since it can have $T_r > 90\%$, with $R_s < 100\ \Omega/cm$.

A figure of merit is the ratio of DC conductivity and absorptivity (absorption coefficient). This does not depend on device architecture or film thickness and can be determined from R_s and absorption.

4.3.4.2 Organic LEDs

OLEDs can also take advantage of graphene [470]. They consist of an electroluminescent layer between two charge-injecting electrodes, at least one of which is transparent [467]. In these diodes, holes are injected into the HOMO of the polymer from the anode, and electrons into the LUMO from the cathode. For efficient injection, the anode and cathode work functions should match the HOMO and LUMO of the light-emitting polymer [467]. Traditionally, ITO is used as TCF. However, besides cost issues, ITO is brittle and limited as a flexible substrate. In addition, it tends to diffuse into the active OLED layers, which reduces device performance over time. Graphene has a work function of 4.5 eV [467], similar to that of ITO. This, combined with its promise as a flexible and cheap TC, makes it an ideal candidate for OLED anodes (Fig. 4.29d), while eliminating the issues related to In diffusion. Electroluminescence was also reported in graphene [471]. Although the power-conversion efficiency is lower than CNTs [467], this could lead to light-emitting devices based on graphene. Key to this is the inability of monolithic vibrations to provide localised tactile feedback associated with visual images, and this is related to the difficulty in implementing tactile feedback directly from a display surface [472, 473]. To address the problem, a flexible and optically transparent graphene-based programmable electrostatic tactile (ET) system was developed capable of delivering localised tactile information to the user's skin, directly from the display's surface and in accordance with the displayed visual information [474].

It has been reported [475] about the development of a transparent and stretchable graphene-based actuator, composed of transparent and compliant graphene electrodes and a dielectric elastomer substrate, for tactile displays. The graphene electrode is coated onto the designed region of the substrate layer by layer. Thus, only the area of the dielectric elastomer substrate with electrodes bumps up in response to the input voltage, which consequently produces actuation [475]. Apart from being simple in fabrication, cost-effective and extendible to multiple arrays, the actuator preserves its electrical and mechanical properties even under 25% stretching [475].

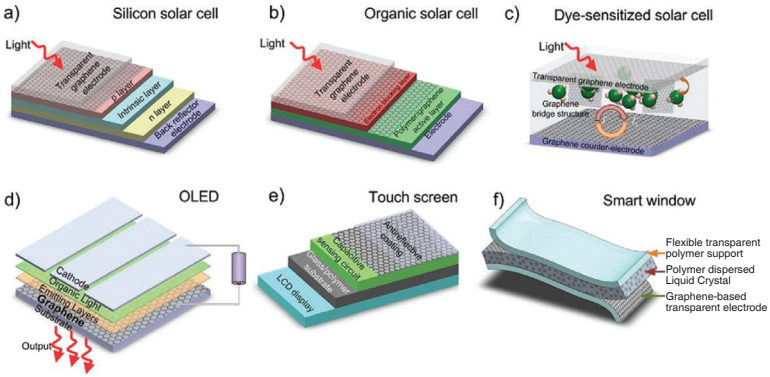

Figure 4.29 Graphene-based optoelectronics: (a) inorganic, (b) organic, (c) DSSCs, (d) OLED, (e) capacitive touchscreen, (f) smart windows. Reprinted by permission from Macmillan Publishers Ltd: *Nature Photonics*, Ref. [467], Copyright 2010.

4.4 Sensors and Metal Detectors

The rapidly increasing use of sensors throughout society and the demand for cheaper and better devices with less power consumption depend critically on the emergence of new sensor materials and concepts. GRMs have great potential for sensor development [476, 477] within a very wide range of applications, including industrial monitoring, surveillance, security, interactive electronics, communications, lab-on-chip, point of care, environmental monitoring, transportation and automation. This could result in a wave of cheap and compact sensor devices with functionalities not seen in existing sensor technology. A sensor is a very general concept, covering essentially any device which converts physical quantities into a signal an observer can interpret. The target is to demonstrate proof-of-principle sensing schemes for a variety of applications: pressure sensors and microphones, mass (including gas) and force sensing, as well as electrical sensors for microwaves and biosensors. An essential part of the sensor is the read-out scheme. Mechanical, optical, electrical transduction schemes for GRM sensors must be explored [477]. Efficient transduction

schemes which operate in a variety of environments (air, vacuum, liquid), as well as high pressures, high/low temperature and harsh conditions are needed for applications. In the short term, the development of GRM-based sensors will take advantage of the progress in high-frequency electronics, in particular concerning THz detection, as there is a lack of sensitive detectors for this frequency range. Optoelectronics is an interesting direction as it can provide new means for sensitive read-out and transduction schemes, and graphene-based plasmonic sensors [476–478], e.g. chemical sensors with single-molecule sensitivity. Furthermore, discoveries within the fundamental and spintronics research areas may lead to new detection schemes. The performance of sensor-based devices may profit from further development of better GRM fabrication methods, as well as from emerging flexible electronics technology, e.g. to realise cheap, scalable, flexible sensors [480, 481]. In a longer time frame, when the working principle of novel GRMs sensor types will become established, the inputs and requirements, e.g. derived from themes in Section 4.3, might lead to the design and fabrication of highly specific, commercially competitive sensors. The challenge is to exploit the unique properties of GRMs [482], optimise their chemical, optoelectronic and mechanical response for efficient on-chip individual and array sensors, and integrate them with fast, accurate and cheap read-out. GRM sensors can be divided into two categories: contact sensors, where substances make physical contact to the surface and induce a response, or non-contact sensors, which do not necessarily have to be in contact with the environment. Contact sensors include chemical and electrochemical sensors [483, 484] (gas and biosensors), as well as mass [485, 486], mechanical force and stress [487] sensors, while optical/optoelectronic sensors [488, 489], magnetic [477, 490], radiation [491, 492], electric field (single-electron devices) [493] and strain sensors are, in most cases, non-contact [494].

4.4.1 Gas Sensors

Graphene-based hybrid nanostructures have been found in NO_2, CO_2, as pH sensor and biosensor. Epitaxially grown single-layer and

multilayer graphene on SiC devices was fabricated and compared for response towards NO_2. Due to an electron donation from SiC, single-layer graphene is n-type with a very low carrier concentration. The choice of substrate is demonstrated to enable tailoring of the electronic properties of graphene with an SiC substrate realising simple resistive devices tuned for extremely sensitive NO_2 detection [44–50].

A monolayer graphene sheet has the ability to sense a variety of gases and biomolecules. Its sensing ability is based on large specific surface area and change in conductance as a function of surface adsorption. As molecules adsorb to the graphene's surface, adsorption experiences a charge transfer with graphene sheet as a donor or acceptor. This changes fermi level, electrical resistance and carrier density of graphene due to which chemical sensing occurs. Many studies suggest that monolayer graphene and functionalised graphene are promising candidates for detecting a variety of gas molecules of LPG, ammonia and CO, organic vapours, protein molecules and DNA. The large elastic region of graphyne and graphdyne has the ability to strain and relax to its original shape by releasing strain without permanent deformation. These enable the resilient electromechanical coupling, which is required in high-temperature sensing. Graphane is also used in the application of biosensing due to its electrochemical oxidation [426–429, 433].

4.4.2 Nanoelectromechanical Sensors

Suspended graphene is the ultimate membrane, and the steadily improving control over N6, GB [495], defects [496], large-area growth and transfer [497] implies that the quality and availability of such structures will make graphene membranes increasingly relevant, not just in terms of improving existing state-of-the-art sensor technology with better performance or cheaper price, but in making radically new sensor concepts possible. Nanoelectromechanical (NEM) mass sensing is a viable route for high-performance devices [498]. Mass sensing involves monitoring the shift of the mechanical resonance frequency of a resonating mechanical structure, as the mass is increased by adsorption of the particles onto the resonator [499].

The surface-area-to-mass ratio of a graphene is very high (~2630 m^2/g) [500]; hence even a molecular level of deposited material on a micro- or nanosized graphene membrane can constitute a measurable fraction of the total mass. Mass sensors based on graphene membranes were predicted to approach a mass resolution of 10^{-6} femtograms [501]. Although strong and flexible, graphene is, nevertheless, difficult to handle due to its extreme thinness [502]. Suspended graphene can be fabricated either by transferring CVD graphene onto a structure containing gaps, cavities or trenches [503, 504] by partial sacrificial etching in hydrofluoric acid of the SiO_2 layer on which graphene is supported [505, 506], or by mechanical exfoliation of graphene directly on trenches [502].

4.4.3 Chemical Sensors

The development of CNT chemical sensors is inhibited by the intrinsic heterogeneity of SWNTs ensembles [507]. Although numerous approaches address the separation of s-from mSWNTs [508–514], further improvement is needed to solve this in a way that is practical in a commercial scenario [515]. The blends of m- and s-SWNTs can be statistically consistent and have a potential for sensing, the attention turned to GRMs. A hall bar graphene device was used with the charge density in the graphene tuned to its lowest possible level to minimise electrical noise. This allowed detection of elementary charge adsorption events [516] corresponding to individual gas molecules. It was estimated [516] that a detection limit in the ppb range, comparable to existing sensor technologies, and detection of gas molecules concentration in the sub-ppt range has since been observed [517]. Graphene could become an important chemical sensor technology not just in terms of sensitivity but also price. Compact devices may be fabricated in large areas, on rigid as well as flexible [518, 519] substrates, which greatly enhances the practical applicability compared to conventional solid state sensors.

Substantial efforts were done to relate the adsorption processes to the observed change in conductivity [520]. As the conductivity is proportional to both carrier concentration and μ, $\sigma = ne\mu$, it can be

difficult to determine which, if not both, of these are affected by a specific adsorption process, i.e. whether the dominating process is a doping or a scattering effect. Schedin et al. [516] reported about sign reversal of the conductivity change depending on the adsorbent being a donor or an acceptor (Fig. 4.30), however with minimal change in μ, as confirmed by Lohmann et al. [521]. Numerous reports found μ improvement upon cleaning graphene from adsorbents [522–524]. A better understanding of the adsorption processes and their effect on the electrical properties of graphene is necessary. Contamination poses a serious challenge for graphene sensors, both in terms of cleaning during fabrication and for maintaining integrity during operation. While most graphene applications directly benefit from a reduction in defects, contamination and corrugations, this is not necessarily the case for graphene chemical sensors.

Similarly to CNTs, graphene has no dangling bonds on its surface. The gaseous molecules of interest may not easily adsorb onto pristine graphene surfaces [525]. The sensitivity may thus be limited by the chemical inertness, both by inhibiting chemical binding of analytes and functionalisation layers [526]. A possible solution is the deliberate introduction of defects, which has been shown to enhance the chemical sensitivity of graphene conductivity sensors as compared to pristine graphene [526, 527], as adsorbents predominantly bind to defects. Upon adsorption, edge and line defects have a far larger effect on conductivity than point defects, where current pathways around the defect exist [527]. While this situation may occur in other materials, graphene is superior due to its high σ (even when few carriers are present) and low noise, making even small changes in resistance detectable [516]. Functionalisation with molecules can improve the sensor performance in terms of sensitivity and selectivity. DNA deposited on a graphene chemical sensor improved response and recovery time, with the response being specific to a certain DNA sequence [528, 529] (see Figs. 4.30c,d). Large-area nanopatterning of graphene using colloid lithography was shown to be a viable route towards even higher sensitivities [528] (see Fig. 4.30b).

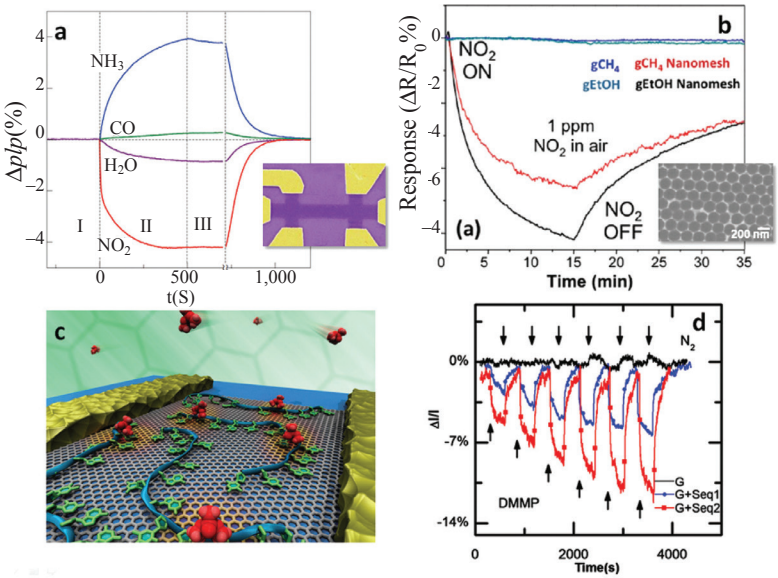

Figure 4.30 (a) Ref. [516] demonstrated chemoresistive sensing using graphene field-effect devices (inset), with the response depending on the type of analyte. (b) Nanopatterning can enhance the sensitivity of graphene chemical sensors. Large-area nanopatterning (inset) using colloidal lithography, could lead to a strongly increased response to various gas molecules. The gCH4 and gEtOH labels refer to graphene grown with methane and ethanol, respectively. The higher response of gEtOH samples was related to a higher defect density. (c) Decoration with DNA molecules of a graphene field-effect device can affect the chemoresistive response according to the specific DNA sequence. (d) Normalised changes in current versus time for ssDNA graphene vapour responses. Lower arrows indicate introduction of analyte at progressively larger concentrations, while upper arrows indicate flushing with pure carrier gas. Graphene devices (black data) show very weak vapour responses which are barely above the noise floor. Devices functionalised with sequence 1 (red data with squares) or sequence 2 (blue data with circles) show significant responses which are sequence dependent. Measurement of dimethyl methylphosphonate (DMMP) at concentrations of 20, 40, 60, 80, 100 and 120 ppm. Reprinted by permission from Macmillan Publishers Ltd: *Nature Materials*, Ref. [516], Copyright 2007.

4.4.4 Strain Sensors

Depending on their chirality, SWNTs show large relative resistance change ($\Delta R/R$) per strain – ξ- ($\Delta L/L_0$, with ΔL change in length and

L_0, original length) [507], the so-called gauge factor, typically ~103, mainly due to strain-induced changes in the band gap. Graphene is capable of withstanding very large strains without permanent mechanical damage (26%) [530] and without major changes in σ (6%) [530]. For graphene, a gauge factor of 6 was reported [531] far from what can be achieved with CNTs. CVD-grown graphene transferred on PDMS has shown a much higher gauge factor (~151) [532]. However, due to possible presence of defects, GBs and possible damage to graphene in the transfer process, it is difficult to determine the reason for the high measured gauge factor [532]. Nevertheless, the reason why graphene is suggested as a strain sensor [479, 533] is not the sensitivity, but the high mechanical flexibility combined with optical transparency, which paves the way for new applications in human–interface technology [479]. In comparison with most solid state strain sensors, graphene-based sensors are better suited for polymer-based flexible electronics, displays and surfaces. It has been demonstrated [479] that graphene-based strain sensors integrated into epoxy gloves are able to read out the bending of the fingers. It was shown theoretically [534, 535] and experimentally [536, 537] that a large uniaxial strain can change the electronic properties in a way which closely resembles the effect of a large magnetic field. This pseudomagnetic field led to an experimental observation of QHE at zero field in highly strained graphene bubbles formed on Pt(111) [537]. This effect could be envisioned for ultra-high level pressure sensors, with the pressure range being tunable by adjusting the size of suspended graphene membranes [536].

4.4.5 Magnetic Sensors

The detection of small (micro to nano Tesla) magnetic fields is a challenging issue for the development of scanning probe magnetometry [538], biosensing [539] or magnetic storage [540]. Current technologies based on giant magnetoresistance and tunnelling magnetoresistance are limited by thermal magnetic noise and spin-torque instabilities [490]. Integrated Hall sensors have numerous applications, including automobiles, computers, industrial controls and consumer devices [541] with a ~870 B Euro market size [542], and 90% of the market for magnetic sensors

[542]. Graphene-based Hall sensors can be fabricated in a cross-shaped geometry [541], in which the Hall effect is used to determine the magnetic field. Such sensors might be used to measure small magnetic particles, or be made into a scanning probe to map magnetic fields with a high spatial resolution.

4.4.6 Metal Recovery

The removal of toxic metal ions is important for the provision of safe drinking water, but its removal in the presence of natural organic matter is challenging. Nafion-graphene nanocomposites solution with in situ plated mercury film electrode was used to determine Zn, Cd, Pb and Cu ions [66].

4.4.7 Photodetection

It is clear from different characterisation and transport studies that RGO contains a lot of defects, and they do not have the same extraordinary electrical properties as pristine graphene. However, extraordinary electrical characteristics are not required, including sensors, transparent electrodes, solar cells, field emitters, etc. In addition, their graphitic domain nature may also be of great use for optoelectronic applications. Photoconductivity of bulk RGO thin film has been studied using various intensities of light, external field and photon energies [543]. The study showed higher photocurrent under same photon energy with the increase in incident light intensity and external electric field. This indicates that the charge carrier generation is influenced by the number of photons and the external field intensity in RGO sheets. Higher photoconductivity has also been observed with higher photon energy under same intensity and electric field. The time-dependent photocurrent decay results show extra time required to recombine charge carriers upon increase in external field and light intensity. It can be concluded that the RGO film generates more charge carriers per unit volume upon irradiation of higher photon energy. In comparison with SWCNT, the RGO film shows high photocurrent generation efficiency [543a]. Position-dependent RGO thin-film photo-detector has been reported by using NIR (wavelength of 800 nm) light [544a].

Figure 4.31a shows a schematic diagram of the device and electron transport measurements set-up. L corresponds to illumination on the left electrode/film interface; R corresponds to illumination on the right electrode/film interface, and M corresponds to the middle position of the film. Figure 4.31b shows the photocurrent with different laser spot positions. The photocurrent increases, decreases or remains almost zero depending on the position of the laser spot with respect to the electrodes. In detail, the I–V curves for position M and in dark lie on top of one another and pass directly through the origin. Whereas when light is illuminated at positions L and R, the I–V curve is shifted above or below the origin, respectively. A large enhancement of photocurrent as well as a finite photo-voltage at the interface indicates that there is an existence of locally generated electric field at the metal–RGO film interface. This mechanism of the local electric field generation was explained using Schottky barrier model. In the schematic diagram (Fig. 4.31c), the black filled and open circles inside the dotted oval region represent the photogenerated excitons (bound electron–hole pair) due to the absorption of NIR source (curved red arrow). Solid line is the potential variation within the graphene channel, and dashed lines are the Fermi levels (EF) of the two electrodes. When NIR is illuminated on the left electrode/RGO film interface, excitons are generated and dissociated into free charge carriers at the interface. Since RGO thin film has a lot of defects, it will also help in the dissociation of excitons into free carriers. Some of the free carriers (holes) might have sufficient energy to overcome the SB and enter into the metal electrode leaving the electron in the film. This causes a hole–electron separation at the interface creating a positive photo-voltage. In addition, the time constant of the dynamic photo response was 2.5 s, which is much larger compared to the single sheets of pristine graphene, possibly due to the disorder from the chemical synthesis and interconnection of sheets. RGO FET phototransistor also has been studied based on their energy band gap values [545a]. In this case, RGO FET, in which few-layer RGO sheets serves as the semiconducting channel and is designed to conduct positive and negative charge carriers (holes and electrons, respectively). The band gap, which ranges from 2.2 eV to 0.5 eV, can be made tunable by reduction treatments. These results also indicate that the photosensitivity is strongly related to the num-

ber of oxidised functional group. The rough estimation of the photosensitivity of RGO FET was calculated to be around 0.85 A/W, three orders lower than that of pristine graphene [546a].

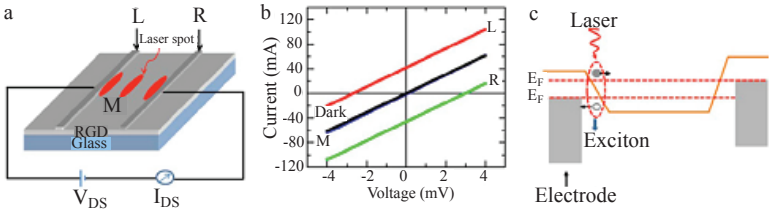

Figure 4.31 (a) Schematic diagram of the device and electron transport measurement set-up. L, M and R are three different positions of NIR illumination. (b) Current–voltage characteristics of the device at three different illumination positions (L, R and M) and under dark condition. (c) An illustration for photovoltage generation at the metallic electrode/RGO interface. Reprinted from Ref. [544b], with the permission of AIP Publishing.

Graphene-based hybrid systems are interestingly found in the field of photocatalysis because the high electronic conduction of graphene sheets can promote a very efficient charge separation in many hybrid nanostructured systems constituted by semiconductors (e.g. TiO_2, CdS) supported on graphene [2]. Metal–graphene–metal (MGM) PDs were the first class of graphene-based devices to be investigated [543b–545b]. In early reports [543b–545b], photocurrent was generated by local illumination of one of the MG interfaces of a back-gated G-FET. The resulting current was attributed to the PV effect [543b–545b]. It was shown that the field arises from charge transfer from the respective contact metal to graphene [547, 548] and can thus be adjusted by proper choice of the metal [543, 549]. It can be further enhanced by graphene doping via electrostatic gating [543–545]. Metal is replaced by $FeCl_3$-intercalated graphene multilayers to realise an all-graphene-based PD [550]. In addition to the PV effect, the PTE effect may also contribute [551]. Both mechanisms were disentangled in specifically designed experiments. Ultrasensitive PDs and image sensor arrays for visible and IR imaging have been developed [552] based on sensitised graphene: A film of semiconducting particles or QDs is deposited on the graphene sheet [552] (see Fig. 4.32).

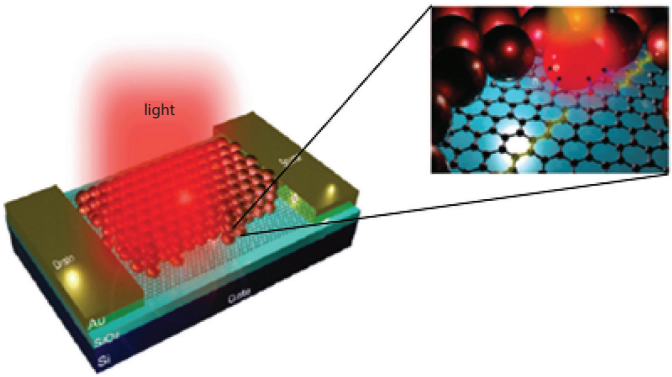

Figure 4.32 Schematic of GQD hybrid phototransistor, in which a graphene flake is deposited onto Si/SiO_2 coated with PbS QDs. Incident photons create e–h pairs in the PbS QDs. Reprinted by permission from Macmillan Publishers Ltd: *Nature Nanotechnology*, Ref. [552], Copyright 2012.

Colloidal QDs offer high absorption and band gap tunability from UV to SWIR [553] and could be employed as a vehicle to demonstrate the potential of this technology. Through sensitisation, strong absorption of ~50–100% can be achieved [552]. Graphene has advantages but also disadvantages with respect to other materials for PD applications.

4.4.7.1 High-speed applications

High-speed photodetection superior to existing technologies is desirable for optical communication applications. The current bandwidth of graphene-based PDs was measured to be 262 GHz [554]. Due to the broadband absorption of graphene, photoresponsivity for visible, NIR and SWIR light was shown to be fairly constant (up to ~3 μm [555]), with R_{ph} up to ~0.13 A/W, exploiting integration with waveguides [556, 557] or enhancements by plasmonics [558]. In terms of bandwidth, graphene is, thus, capable of outperforming other technologies being investigated for optical communications, such as monolithically integrated Ge [559, 560]. High-speed PDs were also realised with III–V semiconductors (>300 GHz) [561], but these are difficult to integrate with Si optical and electronic technologies. An outstanding challenge for graphene-based PDs remains the increase in responsivity and effective detection area. Heterostructure stacks of 2D materials for vertical

photocurrent extraction have large detection areas [562] and may, therefore, address the latter issue. An additional distinct advantage compared to existing technologies is that graphene is a platform for high-speed light modulation and detection on the same chip. While the individual elements have been realised, the integration of an all-optical link and the implementation of large-scale circuitry remain an outstanding challenge.

4.4.7.2 Highly sensitive detection

High-sensitivity photodetection has become a major functionality for a plethora of applications, such as remote sensing, biomedical imaging, optical communications and gas sensing. For the vast majority of applications, such as digital imaging and metrology, Si photodiodes exhibit excellent performance and are cost-effective due to their ease of integration with CMOS electronics. For applications where transparency and flexibility are important, GRM-based photodiodes represent a promising alternative. For applications where detection of SWIR to MIR is required, Si is not a suitable absorber, and III–V semiconductors offer an alternative, but they are costly and difficult to integrate with Si read-out electronics. In this case, GRM-based photodiodes, photoconductors and hybrid phototransistors are particularly promising because they exhibit high photoconductive gain due to the high mobility of GRMs, do not require high voltages and can be monolithically integrated with existing Si-based multi-pixel focal-plane arrays [552, 563–565]. By sensitising the GRM with QDs, the sensitivity range can cover UV visible [566, 567] as well as SWIR [568] and MIR [569]. The outstanding challenge of this type of photoconductive detectors is the dark current, which can be addressed by the read-out circuitry (similar to bolometric systems). The reported projected NEP (~10–17 W) and specific detectivity D*(7×10^{13} Jones) [552] are on par with existing technologies, such as InGaAs. Outstanding challenges include improvement in speed (currently up to 100 Hz), large-scale production and integration of multi-pixel arrays. Alternatively, p–n photodiode-based TMDs exhibit high sensitivity (see Refs. [570, 571]) and low dark current. Outstanding challenges include the improvement of the sensitive area and large-scale production. The detection of mid-infrared (MIR) light is important for biosensing, security, thermal imaging, etc. For this frequency

range, graphene can offer an appealing advantage compared to other materials, by employing plasmons, which resonantly enhance absorption for a wavelength which is tunable by a gate, offering in situ tunable spectral selectivity. The major outstanding challenge for this wavelength range is the carrier extraction, e.g. by utilising p–n junctions in lateral or vertical structures or by employing bolometric detection. Graphene bolometers have shown excellent performance [572] at low temperature, with NEP ~33 fW per √Hz, comparable to existing technologies. The main challenge remains the matching of the high graphene impedance (tens of kΩ) to that of free space (377 Ω) for efficient photon coupling.

4.4.7.3 Terahertz detection

Photodetection of FIR radiation is significant for a variety of applications, ranging from medical diagnostics to process control, homeland security and cultural heritage. Commercially available THz detectors are based on thermal sensing elements which are either very slow (10–400 Hz modulation and NEP~10^{-10} W per√Hz) or require deep cryogenic cooling (4 K for superconducting hot-electron bolometers), while those exploiting fast nonlinear electronics (Schottky diodes) or high-mobility transistors are usually limited to sub-THz frequencies [573]. Graphene can exceed these limits by exploiting THz plasma waves which are weakly damped in high-quality samples, allowing for resonant detection regimes in an FET. This could potentially beat all other technologies at RT, but a major challenge is the demonstration of the resonant DS detection mechanism [574, 575] by integrating high-mobility graphene with appropriate THz antennas. However, graphene THz detectors have already been demonstrated for the range 0.29–0.38 THz with an NEP~10^{-9} W per√Hz [576], and for the range 2 THz with an NEP~10^{-8} W per √Hz [577]. The combination of scalability at higher frequencies, prospects for integration with Si-platforms as well as potential for implementing flexible devices makes graphene highly competitive for a future generation of THz detection systems. Although photodetection platforms based on GRMs have been developed for a wide variety of applications at a remarkable pace, outstanding challenges remain to demonstrate the true potential and to exploit the distinct advantages of 2D crystals. The prospects for commercialisation will not just depend on the detector

performance, but likely also on some of the distinct advantages and capabilities, in addition to the ability to realise production of large-scale high-quality 2D materials at a low cost and to establish large-scale integration with existing photonic and electronic platforms, such as CMOS technologies.

4.5 Conclusion and Perspectives

Experimental studies on the independent electromagnetic properties and the industrial applications of functionalised graphene in electronics, spintronics, energy harvesting and other applications still need to be compared. The synthetic issues must be resolved so that the graphene derivatives can accomplish their promising technical potentials. Graphene-related NMs have an exciting future for utilisation, but their stability and physical and chemical properties need to be investigated.

The 3D manipulation of 2D graphene materials is challenging but the manipulation of graphene into higher-order nanostructures has already shown its potential for different applications. Graphene-related systems can be used as model systems for potential applications, e.g. CMG systems for electro-catalysts. Applications of GRMs include transparent flexible electrodes, sensors, graphene/polymer composites for mechanical parts, energy storage and organic electronics. The opportunities and challenges rest on these targets and have attracted efforts of many scientists and engineers.

Graphene-related 2D crystals and hybrids are now rapidly evolving and growing from pure science to technology. Different applications require GRMs with diverse properties, from structurally perfect for high-tech electronics, to defective materials for energy applications, e.g. batteries and SCs. A current and near future market for GRM applications can be driven by the production strategies for these materials. As the production route will mature, widespread practical implementation of these strategies would be possible. The cheapest GRMs and with the least stringent requirements can be the first to be available on the market, e.g. in conductive inks–based flexible electronic devices such as flexible solar cells, batteries and SCs, while devices with the highest, electronic quality grades, such as spin valves, non-volatile memories, will take more time to

progress. The main target is to develop novel applications to use the unique properties of GRMs. GRMs can replace the existing standard materials only if properties of the new components are competitive enough to justify the cost of the changing current industrial processes.

References

1. Sarkar J., Ghosh P., Adil A. (2015). *Renew. Sust. Ener. Rev.*, **43**, 164–177.
2. Agnoli S., Granozzi G. (2013). *Surf. Sci.*, **609**, 1–5.
3. Gilje S., Han S., Wang M., Wang K.L., Kaner R.B. (2007). *Nano Lett.*, **7(11)**, 3394–3398.
4. Singh V., Joung D., Zhai L., Das S., Khondaker S.I., Seal S. (2011). *Prog. Mater. Sci.*, **56**, 1178–1271.
5. Wang H., Robinson J.T., Diankov G., Dai H. (2010). *J. Am. Chem. Soc.*, **132**, 3270.
6. Wang D., Kou R., Choi D., Yang Z., Nie Z., Li J. (2010). *ACS Nano*, **4**, 1587.
7. Yang S., Feng X., Ivanovici S., Müllen K. (2010). *Angew. Chem. Int. Ed.*, **49**, 8408.
8. Liu C., Yu Z., Neff D., Zhamu A., Jang B.Z. (2010). *Nano Lett.*, **10**, 4863.
9. Wang D.W., Li F., Zhao J.P., Ren W.C., Chen Z.G., Tan J. (2009). *ACS Nano*, **3**, 1745.
10. Huang X., Yin Z., Wu S., Qi X., He Q., Zhang Q., Yan Q., Boey F., Zhang H. (2011). *Small*, **7(14)**, 1876–1902.
11. Yang S., Feng X., Ivanovici S., Müllen K. (2010). *Angew. Chem. Int. Ed.*, **49**, 8408.
12. Zhou H.Q., Qiu C.Y., Liu Z., Yang H.C., Hu L.J., Liu J., Yang H.F., Gu C.Z., Sun L.F. (2010). *J. Am. Chem. Soc.*, **132**, 944.
13. Chaudhuri R.G., Paria S. (2012). *Chem. Rev.*, **112**, 2373–2433.
14. Zhu B.Y., Murali S., Cai W., Li X., Suk J.W., Potts J.R., Ruoff R.S. (2010). *Adv. Mater.*, **22**, 3906–3924.
15. Rangappa D., Jang J.H., Honma I. (2011). 45–58. Available on: http://dx.doi.org/10.5772/21783
16. Rao C.N.R., Subrahmanyam K.S., Ramakrishna Matte H.S.S., Govindaraj A. Available at: http://www.worldscibooks.com/physics/7989.html
17. Tang Q., Zhou Z., Chen Z. (2013). *Nanoscale*, **5**, 4541.

18. Georgakilas V., Otyepka M., Bourlinos A.B., Chandra V., Kim N., Christian Kemp K., Hobza P., Zboril R., Kim K.S. (2012). *Chem. Rev.*, **112(11)**, 6156–6214.
19. Terrones M., Méndez A.R.B., Delgado J.C., Urías, F.L. Cantú Y.I.V., Macías F.J.R., Elías A.L., Sandoval E.M., Márquez A.G.C., Charlier, Terrones J.C. (2010). *Nano Today*, **5(4)**, 351–372.
20. Novoselov K.S., Falko V.I., Colombo L., Gellert P.R., Schwab M.G., Kim K. (2012). *Nature*, **490**, 192–200.
21. Ferrari A.C., Bonaccorso F., Fal'ko V., Novoselov K.S., Roche S., Bøggild P., Borini S., Koppens F.H.L., Palermo V., Pugno N., Garrido J.A., Sordan R., Bianco A., Ballerini L., Prato M., Lidorikis E., Kivioja J., Marinelli C., Ryhänen T., MorpuRGO A., Coleman J.N., Nicolosi V., Colombo L., Fert A., Hernandez M.G., Bachtold A., Schneider G.F., Guinea F., Dekker C., Barbone M., Z. Sun, Galiotis C., Grigorenko A.N., Konstantatos G., Kis A., Katsnelson M., Vandersypen L., Loiseau A., Morandi V., Neumaier D., Treossi E., Pellegrini V., Polini M., Tredicucci A., Williams G.M., Hong B.H., Ahn J.H., Kim J.M., Zirath H., Wees van B.J., Zant van der H., Occhipinti L., Di Matteo A., Kinloch I.A., Seyller T., Quesnel E., Feng X., Teo K., Rupesinghe N., Hakonen P., Neil S.R.T., Tannock Q., Löfwander T., Kinare J. (2015). *Nanoscale*, **7**, 4598.
22. Cong H.P., Chen J.F., Yu, S.H. (2014). *Chem. Soc. Rev.*, **43**, 7295–7325.
23. Kim H., Abdala A.A., Macosko C.W. (2010). *Macromolecules*, **43**, 6515–6530.
24. Kuilla T., Bhadra S., Yaoa D., Kim N.H., Bose S., Leea J.H. (2010). *Prog. Polym. Sci.*, **35**, 1350–1375.
25. Information available at http://www.nanowerk.com/news2/newsid=32603.php
26. Galpaya D., Wang M., Liu M., Motta N., Waclawik E., Yan C. (2012). *Graphene*, **1**, 30–49.
27. Das S., Wajid A.S., Shelburne J.L., Liao Y.C., Green M.J. (2011). *ACS Appl. Mater. Interf.*, **3(6)**, 1844–1851.
28. Paul D.R., Robeson L.M. (2008). *Polymer*, **49**, 3187–3204.
29. Chao Z., Xi L.T. (2012). *Chin. Sci. Bull.*, **57(23)**, 3010–3021.
30. Das T.K., Prusty S. (2013). *Polym. Plast. Technol. Eng.*, **52**, 319–331.
31. Potts J.R., Dreyer D.R., Bielawski C.W., Ruoff R.S. (2011). *Polymer*, **52**, 5–25.
32. Feng L., Guan G., Li C., Zhang D., Xiao Y., Zheng L., Zhu W. (2013). *J. Macromol. Sci. A*, **50**, 720–727.

33. Ha H.W., Choudhury A., Kamal T., Kim D.H., Park S.Y. (2012). *ACS App. Mater. Interf.*, **4**, 4623–4630.
34. Yoonessi M., Shi Y., Scheiman D.A., Colon M.L., Tigelaar D.M., Weiss R.A., Meador M.A. (2012). *ACS Nano*, **6(9)**, 7644–7655.
35. Vickery J.L., Patil A.J., Mann S. (2009). *Adv. Mater.*, **21**, 2180–2184.
36. Bernard C., Nguyen T., Pellegrin B., Holbrook R.D., Zhao M., Chin J. (2011). *J. Phys. Conference Series*, **304**, 012063.
37. Denga C., Wua J., Cheng R., Menga F., Klok H.A., Zhong Z. (2014). *Prog. Polym. Sci.*, **39**, 330–364.
38. Shen H., Zhang L., Liu M., Zhang Z. (2012). *Theranostics*, **2(3)**, 283–294.
39. Dato A., Radmilovic V., Frenklach M. (2012). http://dx.doi.org/10.1002/9783527610419.ntls0230
40. Lee Z., Jeon K.J., Dato A., Erni R., Richardson T.J., Frenklach M., Radmilovic V. (2009). *Nano Lett.*, **9**, 3365–3369.
41. Chatterjee K., Sarkar S., Rao K.J., Paria S. (2014). *Adv. Coll. Interf. Sci.*, **209**, 8–39.
42. Mandal B., Bhattacharjee H., Mittal N., Sah H., Balabathula P., Thoma L.A., Wood G.C. (2013). *Nanomedicine: NBM*, **9(4)**, 1–18,
43. Zhong J., Huang H.L., Li J., Qian F.C., Li L.Q., Niu P.P., Dai L.C. (2015). *Hepatobiliary Pancreat. Dis. Int.*, **14(1)**, 82–89.
44. Mannoor M.S., Tao H., Clayton J.D., Sengupta A., Kaplan D.L., Naik R.R., Verma N., Omenetto F.G., Mcalpine M.C. (2012). *Nature Comm.*, **3**, 1–8.
45. Zhang Y.H., Chen Y.B., Zhou K.G., Liu C.H., Zeng J., Zhang H.L., Peng Y. (2009). *Nanotechnology*, **20(18)**, 1–8.
46. Horsell D. (2014). *Graphene-Based-Sensors*, Avalibale at http://ubic.org.uk/wp-content/uploads/2014/05/David-Horsell-Graphene-Based-Sensors.pdf
47. Pearce R., Iakimov T., Andersson M., Hultman L., Spetz A.L., Yakimova R. (2011). *Sens. Actuators B*, **155(2)**, 451–455.
48. Zhao Y., Zhao L., Yao K.X., Yang Y., Zhang, Q., Han, Y. (2012). *J. Mater. Chem.*, **22**, 19726.
49. Lei N., Li P., Xue W., Xu J., Available at http://arxiv.org/ftp/arxiv/papers/1207/1207.0851.pdf
50. Shao Y., Wang J., Wu H., Liu J., Aksay I.A., Lina Y. (2010). *Electroanalysis*, **2(10)**, 1027–1036.
51. Sun Y., Shi G. (2013). *J. Polym. Sci. B*, **51**, 231–253.
52. Liu J., Xue Y., Zhang M., Dai L. (2012). *MRS Bull.*, **37**, 1265–1272.

53. Fan Z., Yan J., Zhi L., Zhang Q., Wei T., Feng J., Zhang M., Qian W., Wei F. (2010). *Adv. Mater.*, **22**, 3723–3728.

54. Yusoff bin Mohd A.R., Dai L., Cheng H.M., Liu J. (2015). *Nanoscale*, **7**, 6881–6882.

55. Ding Z., Yi C., Hang H.B. (2012). *Chi. Sci. Bull.*, **57(23)**, 2983–2994.

56. Song M., Jin J., Wang X., Lin Y., Rafiq R. *Graphene hybrid materials for energy storage and high performance polymer-graphene nanocomposites*. Available at http://www.phantomsnet.net/imaginenano/Abstracts2013/Graphene2013_Song_Mo_m.song@lboro.ac.uk_Graphene-2013-MS.pdf

57. Kosidlo U., Available at http://cordis.europa.eu/project/rcn/99100_en.pdf

58. Leng K., Zhang F., Zhang L., Zhang T., Wu Y., Lu Y., Huang Y., Chen Y. (2013). *Nano Res.*, **6(8)**, 581–592.

59. Wrightn M., Uddin A. (2012). *Solar Cell.*, **107**, 87–111.

60. Yan W., Yang Z., Bian W., Yang R. (2015). *Carbon*, **92**, 74–83.

61. Gao T., Huang K., Qi X., Li H., Yang L., Zhong J. (2014). *Ceram. Int.*, **40**, 6891–6897.

62. Song Z., Xu T., Gordin M.L., Jiang Y.B., Bae I.T., Xiao Q., Zhan H., Liu J., Wang D. (2012). *Nano Lett.*, **12**, 2205–2211.

63. Park J.U., Nam S.W., Lee M.S., Lieber C.M. (2012). *Nature Mater.*, **11**, 120–125.

64. Hasan T., Scardaci V., Tan P.H., Bonaccorso F., Rozhin A.G., Sun Z., Ferrari A.C., Available at http://dx.doi.org/10.1007/978-1-4419-9443-1_9

65. Logothetidis S., Available at http://dx.doi.org/10.1016/b978-1-78242-035-4.01001-0

66. Park H.S., Koduru J.R., Choo K.H., Lee B. (2015). *J. Hazard. Mater.*, **286**, 315–324.

67. Woo H.G., Li H. (ed.) (2011). *Advanced Functional Materials*, Springer-Verlag Berlin Heidelberg, available at http://www.springer.com/gb/book/9783642190773

68. Shearer C.J., Cherevan A., Eder D. (2014). In *Carbon Nanotubes and Graphene*, 2nd edition, Elsevier, pp. 387–433. http://dx.doi.org/10.1016/b978-0-08-098232-8.00016-4

69. Srivastava S., Kotov N.A. (2011). *Comprehensive Nanoscience and Technology, Acadenic Press*., **5**, 51–67.

70. Malshe A., Rajurkar K., Samant A., Hansen H.N., Bapat S., Jiang W. (2013). *CIRP Annals Manuf. Technol.*, **62(2)**, 607–628.

71. Sanchez C., Rozes L., Ribot F., Laberty-Robert C., Grosso D., Sassoye C., Boissiere C., Nicole L. (2010). *Chimie Douce C.R. Chimie*, **13**, 3–39.
72. Morales C.S., Zhang L., Langer R., Farokhzad O.C. (2009). *Biomaterials*, **30**, 2231–2240.
73. Paul W., Sharma C.P., Chitra S. (2010). Chapter 8: Inorganic nanoparticles for targeted drug delivery, In *Biointegration of Medical Implant Materials*, A volume in Woodhead Publishing Series in Biomaterials, pp. 204–235.
74. Espí R.M., Weiss C.K., Landfester K. (2012). *Curr. Opinion. Coll. Interf. Sci.*, **17**, 212–224.
75. Zhong H., Mirkovic T., Scholes G.D. (2011). *Nanocry. Synt.*, **5**, 153–201.
76. Shervedani R.K., Amini A. (2014). *Electroch. Acta*, **121**, 376–385.
77. Chen T., Cao Z., Guo X., Nie J., Xu J., Fan Z., Du B. (2011). *Polymer*, **52**, 172–179.
78. Qi D., Cao Z., Ziener U. (2014). *Adv. Coll. Interf. Sci.*, **211**, 47–62.
79. Athar T. (2015). In *Emerging Nanotechnologies for Manufacturing*, 2nd edition, William Andrew, pp. 444–538. http://dx.doi.org/10.1016/B978-0-323-28990-0.00017-8
80. Salas G., Costo R., Morales del Puerto M. (2012). *Front. Nanosci.*, **4**, 35–79. http://dx.doi.org/10.1016/B978-0-12-415769-9.00002-9
81. Freitas R.A. (1999). *Nanomedicine*, *Volume I: Basic Capabilities*, Landes Bioscience Georgetown, TX, USA.
82. Xie J., Lee S., Chen X. (2010). *Adv. Drug Deliv. Rev.*, **62**, 1064–1079.
83. Torchilin V.P. (2006). *Nanoparticulates as Drug Carriers*, Imperial College Press, London, UK.
84. Bitounis D., Ali-Boucetta H., Hong B.H., Min D.-H., Kostarelos K. (2013). *Adv. Mater.*, **25**, 2258–2268.
85. Stankovich S., Dikin D.A., Dommett G.H.B., Kohlhaas K.M., Zimney E.J., Stach E.A., Piner R.D., Nguyen S.T., Ruoff R.S. (2006). *Nature*, **442**, 282–286.
86. Eda G., Lin, Y.Y. Mattevi C., Yamaguchi H., Chen H.A., Chen I., Chen C.W., Chhowalla M. (2009). *Adv. Mater.*, **22**, 505–509.
87. Loh K.P., Bao Q., Eda G., Chhowalla M. (2010). *Nat. Chem.*, **2**, 1015–1024.
88. Schniepp H.C., Li J.L., McAllister M.J., Sai H., Herrera-Alonso M., Adamson D.H., Prud'homme R.K., Car R., Saville D.A., Aksay I.A. (2006). *J. Phys. Chem. B*, **110**, 8535–8539

89. Eda G., Lin Y.Y., Mattevi C., Yamaguchi H., Chen H.A., Chen C.W., Chhowalla M. (2009). *Adv. Mater.*, **22**, 505–509.
90. Dankerl M., Hauf M.V., Lippert A., Hess L.H., Birner, S. Sharp I.D., Mahmood A., Mallet P., Veuillen J.Y., Stutzmann M., Garrido J.A. (2010). *Adv. Funct. Mater.*, **20**, 3117–3124.
91. Ang P.K., Chen W., Wee A.T.S., Loh K.P. (2008). *J. Am. Chem. Soc.*, **130**, 14392–14393.
92. Sun X., Liu Z., Welsher K., Robinson J.T., Goodwin A., Zaric S., Dai H. (2008). *Nano Res.*, **1**, 203–212.
93. Klingeler R., Sim R.B. (2011). *CNTs for Biomedical Applications*, Carbon Nanostructures Series, Springer.
94. Liu Z., Robinson J.T., Tabakman S.M., Yang K., Dai H. (2011). *Mater. Today*, **14**, 316–323.
95. Friedrich J.F., Wettmarshausen S., Hanelt S., Mach R., Mix R., Zeynalov E.B., Meyer-Plath A. (2010). *Carbon*, **48**, 3884–3894.
96. Liong M., Lu J., Kovochich M., Xia T., Ruehm S.G., Nel A.E., Tamanoi F., Zink J.I. (2008). *ACS Nano*, **2**, 889–896.
97. Gratton S.E.A., Ropp P.A., Pohlhaus P.D., Luft J.C., Madden V.J., Napier M.E., DeSimone J.M. (2008). *Proc. Natl. Acad. USA*, **105**, 11613–11618.
98. Choi H.S., Liu W., Liu F., Nasr K., Misra P., Bawendi M.G., Frangioni J.V. (2010). *Nat. Nanotechnol.*, **5**, 42–47.
99. Maragó O.M., Bonaccorso F., Saija R., Privitera G., Gucciardi P.G., Iatí M.A., Calogero G., Jones P.H., Borghese F., Denti P., Nicolosi V., Ferrari A.C. (2010). *ACS Nano*, **4**, 7515–7523
100. Hernandez Y., Nicolosi V., Lotya M., Blighe F.M., Sun Z., De S., McGovern I.T., Holland B., Byrne M., Gun'ko Y.K., Boland J.J., Niraj P., Duesberg G., Krishnamurthy S., Goodhue R., Hutchison J., Scardaci V., Ferrari A.C., Coleman J.N. (2008). *Nat. Nanotechnol.*, **3**, 563–568.
101. Green A.A., Hersam M.C. (2009). *Nano Lett.*, **9**, 4031–4036.
102. Yang X., Zhang X., Liu Z., Ma Y., Huang Y., Chen Y. (2008). *J. Phys. Chem. C*, **112**, 17554–17558.
103. Hess L.H., Seifert M., Garrido J.A. (2013). *Proc. IEEE*, **101**, 1780–1792.
104. Wang X.M., Zhang W.H. (2013). *New Carbon Mater.*, **28**, 321.
105. Pumera M. (2011). *Mater. Today*, **14**, 308.
106. Sun X.M., Liu Z., Welsher K., Robinson J.T., Goodwin A., Zaric S., Dai H.J. (2008). *Nano Res.*, **1**, 203.

107. (a) Shah B., Yin P.T., Ghoshal S., Lee K.B. (2013). *Angew. Chem.*, *Int. Ed.*, **52**, 6190. (b) Bai S., Shen X. (2012). *RSC Adv.*, **2**, 64. (c) Wu Z.S., Zhou G.M., Yin L.C., Ren W., Li F., Cheng H.M. (2012). *Nano Energy*, **1**, 107.

108. Myung S., Yin P.T., Kim C., Park J., Solanki A., Reyes P.I., Lu Y.C., Kim K.S., Lee K.B. (2012). *Adv. Mater.*, **24**, 6081.

109. Shi X., Gong H., Li Y., Wang C., Cheng L., Liu Z. (2013). *Biomaterials*, **34**, 4786.

110. Solanki A., Chueng S.T.D., Yin P.T., Kappera R., Chhowalla M., Lee K.B. (2013). *Adv. Mater.*, **25**, 5477.

111. Tjoa V., Jun W., Dravid V., Mhaisalkar S., Mathews N.J. (2011). *Mater. Chem.*, **21**, 15593.

112. Liu J.B., Fu S.H., Yuan B., Li Y.L., Deng Z.X. (2010). *J. Am. Chem. Soc.*, **132**, 7279.

113. Luo J.Y., Zhao X., Wu J.S., Jang H.D., Kung H.H., Huang J.X. (2012). *J. Phys. Chem. Lett.*, **3**, 1824.

114. (a) Yang S.B., Feng X.L., Ivanovici S., Müllen K. (2010). *Angew. Chem.*, *Int. Ed.*, **49**, 8408. (b) Artiles M.S., Rout C.S., Fisher T.S. (2011). *Adv. Drug Deliv. Rev.*, **63**, 1352. (c) Du Y., Guo S.J., Dong S.J., Wang E.K. (2011). *Biomaterials*, **32**, 8584.

115. Yang K., Feng L.Z., Shi X.Z., Liu Z. (2013). *Chem. Soc. Rev.*, **42**, 530.

116. Zrenner E. (2002). *Science*, **295**, 1022–1025.

117. Moore D.R., Shannon R.V. (2009). *Nat. Neurosci.*, **12**, 686–691.

118. Hess L.H., Jansen M., Maybeck V., Hauf M.V., Seifert M., Stutzmann M., Sharp I.D., Offenhäusser A., Garrido J.A. (2011). *Adv. Mater.*, **23**, 5045–5049.

119. Cohen-Karni T., Qing Q., Li Q., Fang Y., Lieber C.M. (2010). *Nano Lett.*, **10**, 1098–1102.

120. Hess L.H., Hauf M.V., Seifert M., Speck F., Seyller T., Stutzmann M., Sharp I. D., Garrido J.A. (2011). *Appl. Phys. Lett.*, **99**, 033503.

121. Cheng Z., Li Q., Li Z., Zhou Q., Fang Y. (2010). *Nano Lett.*, **10**, 1864–1868.

122. Backes C., Smith R.J., McEvoy N., Berner N.C., McCloskey D., Nerl H.C., O'Neill A., King P.J., Higgins T., Hanlon, D. (2014). *Nat. Commun.*, **5**, 4576.

123. Krasnozhon D., Lembke, D.C. Nyffeler Y., Kis A.L. (2014). *Nano Lett.*, **14**, 5905–5911.

124. Kravets V.G., Jalil R., Kim Y.J., Ansell D., Aznakayeva D.E., Thackray B., Britnell L., Belle B.D., Withers F., Radko I.P. (2014). *Sci. Rep.*, **4**, 5517.

125. Cabruja E., Merlos A., Cané C., Lozano M., Bausells J., Esteve J. (1991). *Surf. Sci.*, **251–252**, 364–368.

126. Cogan S.F. (2008). *Annu. Rev. Biomed. Eng.*, **10**, 275–309.

127. Jewett S.A., Makowski M.S., Andrews B., Manfra M.J., Ivanisevic A. (2012). *Acta Biomater.*, **8**, 728–733.

128. Santavirta S., Takagi M., Nordsletten L., Anttila A., Lappalainen R., Konttinen Y.T. (1998). *Arch. Orthop., Trauma Surg.*, **118**, 89–91.

129. Tang L., Tsai C., Gerberich W., Kruckeberg L., Kania D. (1995). *Biomaterials*, **16**, 483–488.

130. Härtl A., Schmich E., Garrido J.A., Hernando J., Catharino S.C.R., Walter S., Feulner P., Kromka A., Steinmüller D., Stutzmann M. (2004). *Nat. Mater.*, **3**, 736–742.

131. Dankerl M., Hofmann B., Eick S., Hauf V.M, Ingebrandt S., Offenhäuser A., Stutzmann M., Garrido J.A. (2009). *Adv. Funct. Mater.*, **19**, 2915–2923.

132. Li C., Han J., Ahn C.H. (2007). *Biosens. Bioelectron.*, **22**, 1988–1993.

133. Ronkainen N.J., Halsall H.B., Heineman W.R. (2010). *Chem. Soc. Rev.*, **39**, 1747.

134. Wang W., Guo S.R., Penchev M., Zhong J.B., Lin J., Bao D.D., Vullev V., Ozkan M., Ozkan C.S. (2012). *J. Nanosci. Nanotechnol.*, **12**, 6913.

135. Kuila T., Bose S., Khanra P., Mishra A.K., Kim N.H., Lee J.H. (2011). *Biosens. Bioelectron.*, **26**, 4637.

136. (a) Pingarron J.M., Yanez-Sedeno P., Gonzalez-Cortes A. (2008). *Electrochim. Acta*, **53**, 5848. (b) Haun J.B., Yoon T.J., Lee H., Weissleder R. (2010). *WIREs Nanomed. Nanobiotechnol.*, **2**, 291.

137. Mohanty N., Berry V. (2008). *Nano Lett.*, **8**, 4469.

138. He Q.Y., Sudibya H.G., Yin Z.Y., Wu S.X., Li H., Boey F. (2010). *ACS Nano*, **4**, 3201.

139. Mao S., Lu G., Yu K., Bo Z., Chen J. (2010). *Adv. Mater.*, **22**, 3521.

140. Wang Y., Lu J., Tang L., Chang H., Li J. (2009). *Anal. Chem.*, **81**, 9710.

141. Liu, S. Guo X.F. (2012). *NPG Asia Mater.*, **4**, 1.

142. Arya S.K., Chaubey A., Malhotra B.D., (2006). *Proc. Indian Natn. Sci. Acad.*, **72(4)**, 249–266.

143. Lee C.S., Kim S.K., Kim M. (2009). *Sensors*, **9**, 7111.

144. Allen B.L., Kichambare P.D., Star A. (2007). *Adv. Mater.*, **19**, 1439.

145. Chen K.I., Li B.R., Chen Y.T. (2011). *Nano Today*, **6**, 131.

146. (a) Lee K., Nair P.R., Scott A., Alam M.A., Janes D.B. (2009). *J. Appl. Phys.*, **105**, 102046. (b) Makowski, M.S., Ivanisevic A. (2011). *Small*, **7**, 1863.

147. (a) Yang W.R., Ratinac K.R., Ringer S.P., Thordarson P., Gooding J.J., Braet F. (2010). *Angew. Chem.*, *Int. Ed.*, **49**, 2114. (b) Ohno Y., Maehashi K., Yamashiro Y., Matsumoto K. (2009). *Nano Lett.*, **9**, 3318. (c) Kim D.J., Sohn I.Y., Jung J.H., Yoon O.J., Lee N.E., Park J.S. (2013). *Biosens. Bioelectron.*, **41**, 621.

148. Zhang Y.J., Geng M.K., Zhang H., He Y., Peng C., Huang Q., Fan C.H. (2012). *Chin. Sci. Bull.*, **57**, 3086.

149. Dinh D.A., Hui K.S., Hui K.N., Cho Y.R., Zhou W., Hong X.T., Chun H.H. (2014). *Appl. Surf. Sci.*, **298**, 62.

150. Mao S., Lu G.H., Yu K.H., Bo Z., Chen J.H. (2010). *Adv. Mater.*, **22**, 3521.

151. Abe M., Murata K., Ataka T., Fuku Y., Matsumoto K. (2009). *J. Nanosci. Nanotechnol.*, **9**, 1947.

152. Mao S., Yu K.H., Lu G.H., Chen J.H. (2011). *Nano Res.*, **4**, 921.

153. Kwon O.S., Lee S.H., Park S.J., An J.H., Song H.S., Kim T., Oh J.H., Bae J., Yoon H., Park T.H., Jang J. (2013). *Adv. Mater.*, **25**, 4177.

154. Kim D.J., Park H.C., Sohn I.Y., Jung J.H., Yoon O.J., Park J.S., Yoon M.Y., Lee N.E. (2013). *Small*, **9**, 3352.

155. Myung S., Solanki A., Kim C., Park J., Kim K.S., Lee K.B. (2011). *Adv. Mater.*, **23**, 2221.

156. Melisko M.E., Glantz M., Rugo H.S. (2009). *Nat. Clin. Pract. Oncol.*, **6**, 25.

157. Wang J. (2000). *Nucleic Acids Res.*, **28**, 3011.

158. Yin Z.Y., He Q.Y., Huang X., Zhang J., Wu S.X., Chen P., Lu G., Chen P., Zhang Q.C., Yan Q.Y., Zhang H. (2012). *Nanoscale*, **4**, 293.

159. Chikkaveeraiah B.V., Bhirde A.A., Morgan N.Y., Eden H.S., Chen X. (2012). *ACS Nano*, **6**, 6546.

160. Shao Y.Y., Wang J., Wu H., Liu J., Aksay I.A., Lin Y.H. (2010). *Electroanalysis*, **22**, 1027.

161. Ambrosi A., Pumera M. (2010). *Chem. Eur. J.*, **16**, 10946.

162. (a) Alwarappan S., Erdem A., Liu C., Li C.Z. (2009). *J. Phys. Chem. C*, **113**, 8853. (b) Kim T., Yang S.J., Park C.R. (2011). *Carbon Letters*, **12(4)**, 194–206.

163. (a) Luo X.L., Morrin A., Killard A.J., Smyth M.R. (2006). *Electroanalysis*, **18**, 319. (b) Liu Q., Liu Z., Zhang X., Yang L., Zhang N., Pan G., Yin S., Chen Y., Wei J. (2009). *Adv Funct Mater*, **19(6)**, 894–904.

164. Qu W.D., Zhang L.Y., Chen G. (2013). *Biosens. Bioelectron.*, **42**, 430.

165. Sun C.L., Lee H.H., Yang J.M., Wu C.C. (2011). *Biosens. Bioelectron.*, **26**, 3450.

166. Xiao Y., Patolsky F., Katz E., Hainfeld J.F., Willner I. (2003). *Science*, **299**, 1877.

167. Jung I., Dikin D., Park S., Cai W., Mielke S.L., Ruoff R.S. (2008). *J. Phys. Chem. C*, **112**, 20264.

168. Fowler J.D., Allen M.J., Tung V.C., Yang Y., Kaner R.B., Weiller B.H. (2009). *ACS Nano*, **3**, 301.

169. Lu G., Ocola Chen L.E. (2009). *J. Appl. Phys. Lett.*, **94**, 083111.

170. (a) Nair R.R., Blake P., Grigorenko A.N., Novoselov K.S., Booth T.J., Stauber T., Peres N.M.R., Geim A.K. (2008). *Science*, **320**, 1308. (b) Johari P., Shenoy V.B. (2011). *ACS Nano*, **5**, 7640.

171. (a) Shang J.Z., Ma L., Li J.W., Ai W., Yu T., Gurzadyan G.G. (2012). *Sci. Rep.*, **2**, 792. (b) Thomas H.R., Valles C., Young R.J., Kinloch I.A., Wilson N.R., Rourke J.P. (2013). *J. Mater. Chem. C*, **1**, 338.

172. Matte H.S.S.R., Subrahmanyam K.S., Rao K.V., George S.J., Rao C.N.R. (2011). *Chem. Phys. Lett.*, **506**, 260.

173. Malard L.M., Pimenta M.A., Dresselhaus G., Dresselhaus M.S. (2009). *Phys. Rep.*, **473**, 51.

174. Goncalves G., Marques P.A.A.P., Granadeiro C.M., Nogueira H.I.S., Singh M.K., Gracio J. (2009). *Chem. Mater.*, **21**, 4796.

175. Roy R., Hohng S., Ha T. (2008). *Nat. Methods*, **5**, 507.

176. (a) Jares-Erijman E.A., Jovin T.M. (2003). *Nat. Biotechnol.*, **21**, 1387. (b) Nagai T., Yamada S., Tominaga T., Ichikawa M., Miyawaki A. (2004). *Proc. Natl. Acad. Sci. USA*, **101**, 10554.

177. Swathi R.S., Sebastian K.L. (2009). *J. Chem. Phys.*, **130**, 086101.

178. Cheng L., Wang C., Liu Z. (2013). *Nanoscale*, **5**, 23.

179. Wu S.J., Duan N., Ma X.Y., Xia Y., Wang H.G., Wang Z.P., Zhang Q. (2012). *Anal. Chem.*, **84**, 6263.

180. Medintz I.L., Uyeda H.T., Goldman E.R., Mattoussi H. (2005). *Nat. Mater.*, **4**, 435.

181. Dong H.F., Gao W.C., Yan F., Ji H.X., Ju H.X. (2010). *Anal. Chem.*, **82**, 5511.

182. Li M., Zhou X.J., Guo S.W., Wu N.Q. (2013). *Biosens. Bioelectron.*, **43**, 69.

183. (a) Wang Z.H., Qin Y.X., Wang C., Sun L.J., Lu X.L., Lu X.Q. (2012). *Appl. Surf. Sci.*, **258**, 2017. (b) Zhang M., Yin B.C., Tan W.H., Ye B.C. (2011). *Biosens. Bioelectron.*, **26**, 3260. (c) Li T., Wang E., Dong S. (2010). *Anal. Chem.*, **82**, 1515.

184. Tao Y., Lin Y.H., Huang Z.Z., Ren J.S., Qu X.G. (2012). *Analyst*, **137**, 2588.

185. Fu X.L., Lou T.T., Chen Z.P., Lin M., Feng W.W., Chen L.X. (2012). *ACS Appl. Mater. Interf.*, **4**, 1080.

186. Ahijado-Guzman R., Gomez-Puertas P., Alvarez-Puebla R.A., Rivas G., Liz-Marzan L.M. (2012). *ACS Nano*, **6**, 7514.

187. (a) Graham D., Thompson D.G., Smith W.E., Faulds K. (2008). *Nat. Nanotechnol.*, **3**, 548. (b) Le Ru E.C., Blackie E., Meyer M., Etchegoin P.G. (2007). *J. Phys. Chem. C*, **111**, 13794.

188. Das G., Chirumamilla M., Toma A., Gopalakrishnan A., Zaccaria R.P., Alabastri A., Leoncini M., Di Fabrizio E. (2013). *Sci. Rep.*, **3**, 1792.

189. Hutter E., Fendler J.H. (2004). *Adv. Mater.*, **16**, 1685.

190. Rycenga M., Camargo P.H.C., Li W.Y., Moran C.H., Xia Y.N. (2010). *J. Phys. Chem. Lett.*, **1**, 696.

191. Xu W.G., Mao N. N., Zhang J. (2013). *Small*, **9**, 1206.

192. Otto A.J. (2005). *Raman Spectrosc.*, **36**, 497.

193. He S.J., Liu K.K., Su S., Yan J., Mao X.H., Wang D.F., He Y., Li L. J., Song S.P., Fan C.H. (2012). *Anal. Chem.*, **84**, 4622.

194. Ren W., Fang Y.X., Wang E.K. (2011). *ACS Nano*, **5**, 6425.

195. Xie Y.F., Li Y., Niu L., Wang H.Y., Qian H., Yao W.R. (2012). *Talanta*, **100**, 32.

196. Zhang Y.W., Liu S., Wang L., Qin X.Y., Tian J.Q., Lu W.B., Chang G.H., Sun X.P. (2012). *RSC Adv.*, **2**, 538.

197. Li Y.T., Qu L.L., Li D.W., Song Q.X., Fathi F., Long Y.T. (2013). *Biosens. Bioelectron.*, **43**, 94.

198. Liu Z.M., Hu C.F., Li S.X., Zhang W., Guo Z.Y. (2012). *Anal. Chem.*, **84**, 10338.

199. Sun Y.G., Xia Y.N. (2002). Science, **298**, 2176.

200. Liu Z.M., Guo Z.Y., Zhong H.Q., Qin X.C., Wan M.M., Yang B.W. (2013). *Phys. Chem. Chem. Phys.*, **15**, 2961.

201. Zhang Z., Xu F., Yang W., Guo M., Wang X., Zhang B., Tang J. (2011). *Chem. Commun.*, **47**, 6440.

202. Brolo A.G. (2012). *Nat. Photonics*, **6**, 709–713.

203. Homola J. (2008). *Chem. Rev.*, **108**, 462–493.

204. Kretschmann E. (1971). *Z. Physik*, **241**, 313–324.

205. Kretschmann E., Raether H.Z. (1968). *Naturforsch. A*, **23**, 2135–2136.

206. Raether H. (1988). *Surface Plasmons on Smooth and Rough Surfaces and on Gratings*, *Springer Tracts in Modern Physics*, Vol. 111, Springer Berlin Heidelberg.

207. Chen S., Svedendahl M., Van Duyne R.P., Kall M. (2011). *Nano Lett.*, **11**, 1826–1830.

208. Fan M., Andrade G.F.S., and Brolo A.G. (2011). *Anal. Chim. Acta*, **693**, 7–25.

209. Hoa X.D., Kirk A.G., Tabrizian M. (2007). *Biosens. Bioelectron.*, **23**, 151–160.

210. Abbas A., Linman M.J., Cheng Q. (2011). *Biosens. Bioelectron.*, **26**, 1815–1824.

211. Yanik A.A., Cetina A.E., Huanga M., Artara A., Mousavic S.H., Khanikaevc A., Connord J.H., Shvetsc G., Altug H. (2011). *Proc. Natl. Acad. Sci. USA*, **108**, 11784–11789.

212. Gao H., Yang J.C., Lin J.Y., Stuparu A.D., Lee M.H., Mrksich M., Odom T.W. (2010). *Nano Lett.*, **10**, 2549–2554.

213. Lee M.H., Gao H., Odom T.W. (2009). *Nano Lett.*, **9**, 2584–2588.

214. Kvasnička P., Chadt K., Vala M., Bocková M., Homola J. (2012). *Opt. Lett.*, **37**, 163–165.

215. Wu X., Zhang J., Chen J., Zhao C., Gong Q. (2009). *Opt.Lett.*, **34**, 392–394.

216. Gao Y., Gan Q., Xin Z., Cheng X., Bartoli F.J. (2011). *ACS Nano*, **5**, 9836–9844.

217. Feng J., Siu V.S., Roelke A., Mehta V., Rhieu S.Y., Palmore G.T.R., Pacifici D. (2012). *Nano Lett.*, **12**, 602–609.

218. Stewart M.E., Anderton C.R., Thompson L.B., Maria J., Gray S.K., Rogers J.A., Nuzzo R.G. (2008). *Chem. Rev.*, **108**, 494–521.

219. Mayer K.M., Hafner J.H. (2011). *Chem. Rev.*, **111**, 3828–3857.

220. Anker J.N., Hall W.P., Lyandres O., Shah N.C., Zhao J., Van Duyne R.P. (2008). *Nat. Mater.*, **7**, 442–453.

221. Aćimović S.S., Kreuzer M.P., González M.U., Quidant R. (2009). *ACS Nano*, **3**, 1231–1237.

222. Ament I., Prasad J., Henkel A., Schmachtel S., Sonnichsen C. (2012). *Nano Lett.*, **12**, 1092–1095.

223. Zijlstra P., Paulo P.M.R., Orrit M. (2012). *Nat. Nanotechnol.*, **7**, 379–382.

224. Cubukcu E., Zhang S., Park Y.S., Bartal G., Zhang X. (2009). *Appl. Phys. Lett.*, **95**, 043113.

225. Kabashin A.V., Evans P., Pastkovsky S., Hendren W., Wurtz G.A., Atkinson R., Pollard R., Podolskiy V.A., Zayats A.V. (2009). *Nat. Mater.*, **8**, 867–871.

226. Otte M.A., Sepúlveda B., Ni W., Juste J.P., LizMarzán L.M., Lechuga L.M. (2010). *ACS Nano*, **4**, 349– 357.

227. Kravets V.G., Schedin F., Jalil R., Britnell L., Gorbachev R.V., Ansell D., Thackray B., Novoselov K.S., Geim A.K., Kabashin A.V., Grigorenko A.N. (2013). *Nat. Mater*., **12**, 304–309.

228. Fei Z., Rodin S., Andreev G.O., Bao W., McLeod A.S., Wagner M., Zhang L.M, Zhao Z., Thiemens M., Dominguez G. (2012). *Nature*, **487**, 82–85.

229. Jablan M., Buljan H., Soljačić M. (2009). *Phys. Rev. B*, **80**, 245435.

230. Chen J., Badioli M., Alonso-Gonzalez P., Thongrattanasiri S., Huth F., Osmond J., Spasenovic M., Centeno A., Pesquera A., Godignon P., Zurutuza Elorza A., Camara N., Abajo de F.J.G., Hillenbrand R., Koppens F.H.L. (2012). *Nature*, 487, 77–81

231. Jablan M., Buljan H., Soljačić M. (2009). *Phys. Rev. B*, **80**, 245435.

232. Yan H., Li X., Chandra B., Tulevski G., Wu Y., Freitag M., Zhu W., Avouris P., Xia F. (2012). *Nat. Nanotechnol.*, **7**, 330–334.

233. Yan H., Low T., Zhu W., Wu Y., Freitag M., Li X., Guinea F., Avouris Ph., Xia F. (2013). *Nat. Photonics*, **7**, 394–399.

234. Nair R.R., Blake P., Grigorenko A.N., Novoselov K.S., Booth T.J., Stauber T., Peres N.M.R., Geim A.K. (2008). *Science*, **320**, 1308–1308

235. Song B., Li D., Qi W., Elstner M., Fan C., Fang H. (2010). *Chem. Phys. Chem.*, **11**, 585–589.

236. Wang L., Zhu C., Han L., Jin L., Zhou M., Dong S. (2011). *Chem. Commun.*, **47**, 7794–7796.

237. Salihoglu O., Balci S., Kocabas C. (2012). *Appl. Phys. Lett.*, **100**, 213110.

238. Schriver M., Regan W., Gannett W.J., Zaniewski A.M., Crommie M.F., Zettl A. (2013). *ACS Nano*, **7**, 5763–5768.

239. Zhou F., Li Z., Shenoy G.J., Li L., Liu H. (2013). *ACS Nano*, **7**, 6939–6947.

240. Prasai D., Tuberquia J.C., Harl R.R., Jennings G.K., Bolotin K.I. (2012). *ACS Nano*, **6**, 1102–1108.

241. Kravets V.G. (2014). *Sci. Rep.*, **4**, 5517.

242. (a) Panyam J., Labhasetwar V. (2003). *Adv. Drug Deliv. Rev.*, **55**, 329. (b) Shah S., Solanki A., Sasmal P.K., Lee K.B. (2013). *J. Am. Chem. Soc.*, **135**, 15682.

243. Farokhzad O.C., Langer R. (2009). *ACS Nano*, **3**, 16.

244. Goenka S., Sant V., Sant S. (2014). *J. Controlled Release*, **173**, 75.

245. Yang X., Zhang X., Ma Y., Huang Y., Wang Y., Chen Y. (2009). *J. Mater. Chem.*, **19**, 2710.

246. Balcioglu M., Rana M., Yigit M.V. (2013). *J. Mater. Chem. B*, **1**, 6187.

247. Wang C., Li J., Amatore C., Chen Y., Jiang H., Wang X.M. (2011). *Angew. Chem.*, *Int. Ed.*, **50**, 11644.

248. Ma X., Qu Q.Y., Zhao Y., Luo Z., Zhao Y., Ng K.W., Zhao Y.L. (2013). *J. Mater. Chem. B*, **1**, 6495.

249. He D., He X., Wang K., Zou Z., Yang X., Li X. (2014). *Langmuir*, **30**, 7182.

250. Fahmy T.M., Fong P.M., Goyal A., Saltzman W.M. (2005). *Mater. Today*, **8**, 18.

251. (a) Fan X., Jiao G., Gao L., Jin P., Li X.J. (2013). *Mater. Chem. B*, **1**, 2658. (b) Zhang L., Xia J., Zhao Q., Liu L., Zhang Z. (2009). *Small*, **6**, 537–544.

252. Chen M.-L., He Y.J., Chen X.W., Wang J.H. (2013). *Bioconjugate Chem.*, **24**, 387.

253. Hogemann-Savellano D., Bos E., Blondet C., Sato F., Abe T., Josephson L., Weissleder R., Gaudet J., Sgroi D., Peters P.J., Basilion J.P. (2003). *Neoplasia*, **5**, 495.

254. Shah S., Sasmal P.K., Lee K.B. (2014). *J. Mater. Chem. B*, **2**, 7685.

255. Shirai M., Tsunooka M. (1996). *Prog. Polym. Sci.*, **21**, 1.

256. Wang F., Liu B., Ip A. C., Liu J. (2013). *Adv. Mater.*, **25**, 4087.

257. Wang C., Ravi S., Garapati U.S., Das M., Howell M., Mallela J., Alwarapan S., Mohapatra S.S., Mohapatra S. (2013). *J. Mater. Chem. B*, **1**, 4396.

258. Cheng F.F., Chen W., Hu L.H., Chen G., Miao H.T., Li C., Zhu J.J. (2013). *J. Mater. Chem. B*, **1**, 4956.

259. Zhang L., Xia J., Zhao Q., Liu L., Zhang Z. (2009). *Small*, **6**, 537–544.

260. Zhang F., Zheng B., Zhang J., Huang X., Liu H., Guo S., Zhang J. (2010). *J. Phys. Chem. C*, **114**, 8469–8473.

261. Xu X., Chen X., Ma P., Wang X., Jing X. (2008). *Eur. J. Pharm. Biophys.*, **70**, 165–170.

262. Huang P., Xu C., Lin J., Wang, C. Wang X., Zhang C., Zhou X., Guo S., Cui D. (2011). *Theranostics*, **1**, 240–250. Available from http://www.thno.org/v01p0240.htm

263. Zang L., Xia J., Zhao Q., Liu L., Zhang Z. (2010). *Small*, **6**, 537–544.

264. Zhang L., Xia J., Zhao Q., Liu L., Zhang Z. (2009). *Small*, **6**, 537–544.

265. Bao H., Pan Y., Ping Y., Sahoo N.G., Wu T., Li L., Li J., Gan L.H. (2011). *Small*, **7**, 1569–1578.

266. Berthiaume F., Maguire T.J., Yarmush M.L. (2011). *Annu. Rev. Chem. Biomol. Eng.*, **2**, 403.

267. Lee W.C., Lim C.H.Y.X., Shi H., Tang L.A.L., Wang Y., Lim C. T., Loh K.P. (2011). *ACS Nano*, **5**, 7334.

268. (a) Chen G.Y., Pang D.W.P., Hwang S.M., Tuan H.Y., Hu Y.C. (2012). *Biomaterials*, **33**, 418. (b) Nayak T.R., Andersen H., Makam V.S., Khaw C., Bae S., Xu X., Ee P.L.R., Ahn J.H., Hong B.H., Pastorin G., Ö zyilmaz B. (2011). *ACS Nano*, **5**, 4670. (c) Park S.Y., Park J., Sim S.H., Sung M.G., Kim K.S., Hong B.H., Hong S. (2011). *Adv. Mater.*, **23**, 263. (d) Sebaa M., Nguyen T.Y., Paul R.K., Mulchandani A., Liu H. (2013). *Mater. Lett.*, **92**, 122.

269. (a) Shah S., Yin P.T., Uehara T.M., Chueng S.T.D., Yang L., Lee K.B. (2014). *Adv. Mater.*, **26**, 3673. (b) Kim J., Kim Y.R., Kim Y., Lim K.T., Seonwoo H., Park S., Cho S.P., Hong B.H., Choung P.H., Chung T.D., Choung Y.-H., Chung J.H. (2013). *J. Mater. Chem. B*, **1**, 933.

270. Hu W., Peng C., Lv M., Li X., Zhang Y., Chen N., Fan C., Huang Q. (2011). *ACS Nano*, **5**, 3693.

271. (a) Watt F.M., Huck W.T.S. (2013). *Nat. Rev. Mol. Cell Biol.*, **14**, 467. (b) Solanki A., Shah S., Memoli K.A., Park S.Y., Hong S., Lee K.B. (2010). *Small*, **6**, 2509.

272. Solanki A., Chueng S.-T.D., Yin P.T., Kappera R., Chhowalla M., Lee K.B. (2013). *Adv. Mater.*, **25**, 5477.

273. Wang K., Ruan J., Song H., Zhang J.L., Wo Y., Guo S.W., Cui D.X. (2011). *Nanoscale Res. Lett.*, **6**, 8.

274. Sasidharan A., Panchakarla L.S., Chandran P., Menon D., Nair S., Rao C.N. R., Koyakutty M. (2011). *Nanoscale*, **3**, 2461.

275. Kim T.H., Lee K.B., Choi J.W. (2013). *Biomaterials*, **34**, 8660.

276. (a) Ramm Sander P., Hau P., Koch S., Schutze K., Bogdahn U., Kalbitzer H.R., Aigner L. (2013). *Trends Biotechnol.*, **31**, 204. (b) Yanes O., Clark J., Wong D.M., Patti G.J., Sanchez-Ruiz A., Benton H.P., Trauger S.A., Desponts C., Ding S., Siuzdak G. (2010). *Nat. Chem. Biol.*, **6**, 411.

277. Michalet X., Pinaud F.F., Bentolila L.A., Tsay J.M., Doose S., Li J.J., Sundaresan G., Wu A.M., Gambhir S.S., Weiss S. (2005). Science, **307**, 538–544.

278. Smith A.M., Duan H., Mohs A.M., Nie S. (2008). *Adv. Drug Deliv. Rev.*, **60**, 1226–1240.

279. Dobrovolskaia M.A., McNeil S.E. (2007). *Nat. Nanotechnol.*, **2**, 469–478.

280. Colvin V. (2003). *Nat. Biotechnol.*, **21**, 1166–1170.

281. Frangioni J.V. (2003). *Curr. Opin. Chem. Biol.*, **7**, 626–634.

282. Luo Z., Vora P.M., Mele E.J., Johnson A., Kikkawa J.M. (2009). *Appl. Phys. Lett.*, **94**, 111909.

283. Lu J., Yang J.X., Wang J., Lim A., Wang S., Loh K.P. (2009). *ACS Nano*, **3**, 2367–2375.

284. Gokus T., Nair R., Bonetti A., Bohmler M., Lombardo A., Novoselov K., Geim A., Ferrari A., Hartschuh A. (2009). *ACS Nano*, **3**, 3963–3968.

285. Pan D., Wang S., Zhao B., Wu M., Zhang H., Wang Y. (2009). *Chem. Mater.*, **21**, 3136.

286. Winter M., Brodd R.J. (2004). *Chem. Rev.*, **104**, 4245–4269.

287. Bruce P.G., Scrosati B., Tarascon J.M. (2008). *Angew. Chem.*, *Int. Ed.*, **47**, 2930–2946.

288. Maier J. (2005). *Nat. Mater.*, **4**, 805–815.

289. Tarascon J.M., Armand M. (2001). *Nature*, **414**, 359–367.

290. Bruce P.G., Freunberger S.A., Hardwick L.J., Tarascon J.M. (2012). *Nat. Mater.*, **11**, 19.

291. Wilson A., Way B., Dahn J., Van Buuren T. (1995). *J. Appl. Phys.*, **77**, 2363–2369.

292. Yu Y., Gu L., Dhanabalan A., Chen C.H., Wang C. (2009). *Electrochim. Acta*, **54**, 7227–7230.

293. Bonaccorso F., Colombo L., Yu G., Stoller M., Tozzini V., Ferrari A.C., Ruoffand R.S., Pellegrini V. (2015). *Science*, **347**, 1246501.

294. Wakihara M. (2001). *Mater. Sci. Eng. R*, **33**, 109–134.

295. Whittingham M.S. (2004). *Chem. Rev.*, **104**, 4271–4302.

296. Arico A.S., Bruce P., Scrosati B., Tarascon J.M., Van Schalkwijk W. (2005). *Nat. Mater.*, **4**, 366–377.

297. Barborini E., Piseri P., Li Bassi A., Ferrari A.C., Bottani C.E., Milani P. (1999). *Chem. Phys. Lett.*, **300**, 633–638.

298. Milani P., Ferretti M., Piseri P., Bottani C.E., Ferrari A.C., Li Bassi A., Guizzetti G., Patrini M. (1997). *J. Appl. Phys.*, **82**, 5793.

299. Sakamoto J.S., Dunn B. (2002). *J. Mater. Chem.*, **12**, 2859–2861.

300. Chen Z., Dahn J. (2002). *J. Electrochem. Soc.*, **149**, A1184–A1189.

301. Prosini P.P., Zane D., Pasquali M. (2001). *Electrochim. Acta*, **46**, 3517–3523.

302. Dominko R., Bele M., Gaberscek M., Remskar M., Hanzel D., Pejovnik S., Jamnik J. (2005). *Electrochem. Soc. J.*, **152**, A607–A610.

303. Hu L.H., Wu F.Y., Lin C.T., Khlobystov A.N., Li L.J. (2013). *Nat. Commun.*, **4**, 1687.

304. Yang S.B., Feng X., Ivanovici S., Müllen K. (2010). *Angew. Chem. Int. Ed.*, **49**, 8408–8411.

305. Stoller M.D., Park S., Zhu Y., An J., Ruoff R.S. (2008). *Nano Lett.*, **8**, 3498–3502.

306. Yoo E.J., Kim J., Hosono E., Zhou H., Kudo T., HonmaI. (2008). *Nano Lett.*, **8**, 2277–2282.

307. Paek S.M., Yoo E.J., Honma I. (2008). *Nano Lett.*, **9**, 72–75.

308. Wang D., Kou R., Choi D., Yang Z., Nie Z., Li J., Saraf L.V., Hu D., Zhang J., Graff G.L., Liu J., Pope M.A., Aksay I.A. (2010). *ACS Nano*, **4**, 1587–1595.

309. Wang J.Z., lu L., Choucair M., Stride J.A., Xu X., Liu H.K. (2011). *J. Power Sources*, **196**, 7030–7034.

310. Hassoun J., Bonaccorso F., Agostini M., Angelucci M., Betti M.G., Cingolani R., Gemmi M., Mariani C., Panero S., Pellegrini V., Scrosati B. (2014). *Nano Lett.*, **14**, 4901–4906

311. Kumar B., Kumar J. (2010). *J. Electrochem. Soc.*, **157**, A611.

312. Girishkumar G., McCloskey B., Luntz A.C., Swanson S., Wilcke W. (2010). *J. Phys. Chem. Lett.*, **1**, 2193–2203.

313. Er D., Li J., Naguib M., Gogotsi Y., Shenoy V.B. (2014). *ACS Appl. Mater. Interf.*, **6**, 11173–11179.

314. Naguib M., Come J., Dyatkin B., Presser V., Taberna P.L., Simon P., Barsoum M.W., Gogotsia Y. (2012). *Electrochem. Commun.*, **16**, 61–64

315. (a) Vivekchand S., Rout C., Subrahmanyam K., Govindaraj A., Rao C. (2008). *J. Chem. Sci.*, **120**, 9. (b) Conway B.E. (1999). *Electrochemical SCs: Scientific Fundamentals and Technological Applications*, Plenum Publishers, New York.

316. (a) Pandolfo A.G., Hollenkamp A.F. (2006). *J. Power Sour.*, **157**, 11. (b) Stoller M.D., Ruoff R.S. (2010). *Energy Environ. Sci.*, **3**, 1294–1301.

317. (a) Barbieri O., Hahn M., Herzog A., Kötz R. (2005). *Carbon*, **43**, 1303. (b) Gogotsi Y., Simon G.P. (2011). *Science*, **334**, 917–918.

318. (a) Frackowiak E. (2007). *Phys. Chem. Chem. Phys.*, **9**, 1774. (b) Liu C., Yu Z., Neff D., Zhamu A., Jang B.Z. (2010). *Nano Lett.*, **10**, 4863–4868.

319. (a) Frackowiak E., Metenier K., Bertagna V., Beguin F. (2000). *Appl. Phys. Lett.*, **77**, 2421. (b) Zhu Y., Murali S., Stoller M.D., Ganesh K.J., Cai W., Ferreira P.J., Pirkle A., Wallace R.M., Cychosz K.A., Thommes M., Su D., Stach E.A., Ruoff R.S. (2011). Science, **332**, 1537–1541.

320. (a) Niu C., Sichel E.K., Hoch R., Moy D., Tennent H. (1997). *Appl. Phys. Lett.*, **70**, 1480. (b) Zhang L.L., Zhao X., Ji H., Stoller M.D., Lai L., Murali S., Mcdonnell S., Cleveger B., Wallace R.M., Ruoff R.S. (2012). *Energy Environ. Sci.*, **5**, 9618–9625.

321. (a) An K.H., Kim W.S., Park Y.S., Choi Y.C., Lee S.M., Chung D.C. (2001). *Adv. Mater.*, **13**, 497. (b) Kim T., Jung G., Yoo S., Suh D.S., Ruoff R.S. (2013). *ACS Nano*, **7**, 6899–6905.

322. (a) Du C., Yeh Y., Pan N. (2005). *Nanotechnology*, **16**, 350. (b) Ghaffari M., Zhou Y., Xu H., In M.L, Kim T.Y., Ruoffand R.S., Zhang Q.M. (2013). *Adv. Mater.*, **25**, 4879–4885.

323. (a) Yoon S., Lee J., Hyeon T., Oh S.M. (2000). *J. Electrochem. Soc.*, **147**, 2507. (b) Yang X., Cheng C., Wang Y., Qiu L., Li D. (2013). Science, **341**, 534–537. (b) Lukatskaya M.R., Mashtalir O., Ren C.E., Dall'Agnese Y., Rozier P., Taberna P.L., Naguib M., Simon P., Barsoum M.W., Gogotsi Y. (2013). *Science*, **341**, 1502–1505.

324. (a) Chmiola J., Largeot C., Taberna P.L., Simon P., Gogotsi Y. (2010). *Science*, **328**, 480. (b) Lukatskaya M.R., Mashtalir O., Ren C.E., Dall'Agnese Y., Rozier P., Taberna P.L., Naguib M., Simon P., Barsoum M.W., Gogotsi Y. (2013). *Science*, **341**, 1502–1505.

325. (a) Wang H.L., Hao Q.L., Yang X.J., Lu L.D., Wang X. (2009). *Electrochem. Commun.*, **11**, 1158. (b) Grove W.R. (1839). *Philos. Mag. Ser.*, **3**, 127.

326. (a) Stoller M.D., Park S., Zhu Y., An J., Ruoff R.S. (2008). *Nano Lett.*, **8**, 3498. (b) Liebhafsky H.A., Cairns E.J. (1969). *Fuel Cells and Fuel Batteries: A Guide to Their Research and Development*, John Wiley & Sons, New York.

327. (a) Wang Y., Shi Z., Huang Y., Ma Y., Wang C., Chen M. (2009). *J. Phys. Chem. C*, **113**, 13103. (b) Mehta V., Cooper J.S. (2003). *J. Power Sources*, **114**, 32–53.

328. (a) Lv W., Tang D.M, He Y.B., You C.H., Shi Z.Q., Chen X.C. (2009). *ACS Nano*, **3**, 3730. (b) Ormerod R.M. (2003). *Chem. Soc. Rev.*, **32**, 17–28.

329. (a) Xia J., Chen F., Li J., Tao N. (2009). *Nat. Nanotechnol.*, **4**, 505. (b) Plomp L., Veldhuis J.B.J., Sitters E.F., Molen van der S.B. (1992). *J. Power Sources*, **39**, 369–373.

330. (a) Wu Z.S., Wang D.W., Ren W., Zhao J., Zhou G., Li F. (2010). *Adv. Funct. Mater.*, **20**, 3595. (b) Watanabe M., Tsurumi K., Mizukami T., Nakamura T., Stonehart P. (1994). *J. Electrochem. Soc.*, **141**, 2659.

331. (a) Chen S., Zhu J.W., Wu X.D., Han Q.F., Wang X. (2010). *ACS Nano*, **4**, 2822. (b) Jeon I.Y., Choi H.J., Choi M., Seo J.M., Jung S.M., Kim M.J., Zhang S., Zhang L., Xia Z., Dai L., Park N., Baek J.B. (2013). *Sci. Rep.*, **3**, 1810.

332. (a) Wu Z.S., Ren W.C., Wang D.W., Li F., Liu B.L., Cheng H.M. (2010). *ACS Nano*, **4**, 5835. (b) Choi H.J., Jung S.M., Seo J.M., Chang D.W., Dai L., Baek J.B. (2012). *Nano Energy*, **1**, 534–551.

333. (a) Liu C., Yu Z., Neff D., Zhamu A., Jang B.Z. (2010). *Nano Lett.*, **10**, 4863. (b) Gyenge E.L., Zhang J. (ed.) (2008). Electrocatalytic oxidation of methanol, ethanol and formic acid. In *PEM Fuel Cell Electrocatalysts and Catalyst Layers*, pp. 165–270, Springer, New York.

334. (a) Yan J., Wei T., Shao B., Fan Z., Qian W., Zhang M. (2010). *Carbon*, **48**, 487. (b) Dong L., Gari R.R.S., Li Z., Craig M.M., Hou S. (2010). *Carbon*, **48**, 781–787.

335. (a) Gupta V., Miura N. (2006). *Electrochim. Acta*, **52**, 1721. (b) Bonaccorso F., Colombo L., Yu G., Stoller M., Tozzini V., Ferrari A.C., Ruoffand R.S., Pellegrini V. (2015). *Science*, **347**, 1246501.

336. (a) Gupta V., Miura N. (2006). *J. Power Sour.*, **157**, 616. (b) Yoo E.J., Okata T., Akita T., Kohyama M., Nakamura J., Honma I. (2009). *Nano Lett.* **9**, 2255–2259.

337. (a) Peng C., Zhang S., Jewell D., Chen G.Z. (2008). *Prog. Nat. Sci.*, **18**, 777. (b) Yang A.J., Shin H.S. (2014). *J. Mater. Chem. A*, **2**, 5979–5985.

338. (a) Wang Y.G., Li H.Q., Xia Y.Y. (2006). *Adv. Mater.*, **18**, 2619. (b) Jacobson M.Z., Colella W.G., Golden D.M. (2005). *Science*, **308**, 1901–1905.

339. (a) Fan L.Z., Hu Y.S., Maier J., Adelhelm P., Smarsly B., Antonietti M. (2007). *Adv. Funct. Mater.*, **17**, 3083. (b) Available at: http://en.wikipedia.org/wiki/Energy_density.

340. (a) Wang D.W., Li F., Zhao J.P., Ren W.C., Chen Z.G., Tan J. (2009). *ACS Nano*, **3**, 1745. (b) Fellay C., Dyson P.J., Laurenczy G. (2008). *Angew. Chem., Int. Ed.*, **47**, 3966–3968.

341. Stracke M.P., Ebeling G., Cataluña R., Dupont J. (2007). *Energy Fuels*, **21**, 1695.

342. Joó F. (2008). *Chem. Sus. Chem.*, **1**, 805–808.

343. Teichmann D., Arlt W., Wasserscheid P., Freymann R. (2011). *Energy Environ. Sci.*, **4**, 2767–2773.

344. Hynek S., Fuller W., Bentley J. (1997). *Int. J. Hydrogen Energy*, **22**, 601–610.

345. http://www1.eere.energy.gov/hydrogenandfuelcells/storage/current_technology.html.

346. Schlapbach L., Züttel A. (2001). *Nature*, **414**, 353.

347. Bogdanovic B., Felderhoff M., Pommerin A., Schuth T., Spielkamp N. (2006). *Adv. Mater.*, **18**, 1198.

348. Bluhm M.E., Bradley M.G., Butterick R., Kusari U., Sneddon L.G. (2006). *J. Am. Chem. Soc.*, **128**, 7748.

349. Müller K., Stark K., Müller B., Arlt W. (2012). *Energy Fuels*, **26**, 3691.

350. Li H.W., Yan Y., Orimo S.I., Züttel A., Jensen C.M. (2011). *Energies*, **4**, 185.

351. Tozzini V., Pellegrini V. (2011). *J. Phys. Chem. C*, **115**, 25523.

352. Mpourmpakis G., Froudakis G.E., Lithoxoos G.P., Samios J. (2007). *J. Chem. Phys.*, **126**, 144704.

353. Lee S.M., Lee Y.H. (2000). *Appl. Phys. Lett.*, **76**, 2877.

354. Chan S.P., Chen G., Gong X.G., Liu Z.F. (2001). *Phys. Rev. Lett.*, **87**, 205502.

355. Simonyan V.V., Johnson J.K. (2002). *J. Alloys Compd.*, **330–332**, 659–665.

356. Patchkovskii S., Tse J.S., Yurchenko S.N., Zhechkov L., Heine T., Seifer G. (2005). *Proc. Natl. Acad. Sci. USA*, **102**, 10439.

357. Züttel A., Sudan P., Mauron Ph., Kiyobayashi T., Emmenegger Ch., Schlapbach L. (2002). *Int. J. Hydrogen Energy*, **27**, 203–2012.

358. Dimitrakakis G.K., Tylianakis L., Froudakis G.E. (2008). *Nano Lett.*, **8**, 3166.

359. Burress J.W., Gadipelli S., Ford J., Simmons J.M., Zhou W., Yildirim T. (2010). *Angew. Chem. Int. Ed.*, **49**, 8902.

360. Cho M., Silbey R.J. (1996). *J. Chem. Phys.*, **104**, 8730–8741.

361. Panella B., Hirscher M., Roth S. (2005). *Carbon*, **43**, 2209.

362. Srinvas G., Zhu Y., Piner R., Skipper N., Ellerby M., Ruoff R. (2010). *Carbon*, **48**, 630.

363. Yuan W., Li B., Li L. (2011). *Appl. Surf. Sci.*, **257**, 10183.

364. Sofo J.O., Chaudhari A.S., Barber G.D. (2007). *Phys. Rev. B*, **75**, 153401.

365. Elias D.C., Nair R.R., Mohiuddin T.M.G., Morozov S.V., Blake P., Halsall M.P., Ferrari A.C., Boukhvalov D.W., Katsnelson M.I., Geim A.K., Novoselov K.S. (2009). *Science*, **323**, 610–613.

366. Zecho T., Güttler A., Sha X., Jackson B., Küppers J. (2002). *J. Chem. Phys.*, **117**, 8486.

367. Jeloaica L., Sidis V. (1999). *Chem. Phys. Lett.*, **300**, 157.

368. Sha X., Jackson B. (2002). *Surf. Sci.*, **496**, 318.

369. Ferro Y., Marinelli F., Allouche A. (2002). *J. Chem. Phys.*, **116**, 8124.

370. Rougeau N., Teillet-Billy D., Sidis V. (2006). *Chem. Phys. Lett.*, **431**, 135–138.

371. Šljivančanin Ž., Rauls E., Hornekaer L., Xu W., Besenbacher F., Hammer B. (2009). *J. Chem. Phys.*, **131**, 084706.

372. Hornekaer L., Šljivančanin Ž., Xu W., Otero R., Rauls E., Stensgaard I., Lægsgaard E., Hammer B., Besenbacher F. (2006). *Phys. Rev. Lett.*, **96**, 156104.

373. Hornekaer L., Rauls E., Xu W., Šljivančanin S., Otero R., Stensgaard I., Lægsgaard E., Hammer B., Besenbacher F. (2006). *Phys. Rev. Lett.*, **97**, 186102.

374. Andree A., Lay Le M., Zecho T., Küpper J. (2006). *Chem. Phys. Lett.*, **425**, 99.

375. Hornekaer L., Xu W., Otero R., Lægsgaard E., Besenbacherm F. (2007). *Chem. Phys. Lett.*, **446**, 237.

376. Balog R., Jørgensen B., Wells J., Lægsgaard E., Hofmann P., Besenbacher F., Hornekær L. (2009). *J. Am. Chem. Soc.*, **131**, 8744.

377. Guisinger N.P., Rutter G.M., Crain J.N., First P.N., Stroscio J.A. (2009). *Nano Lett.*, **9**, 1462.

378. Miura Y., Dino W., Nakanishi H. (2003). *J. Appl. Phys.*, **93**, 3395.

379. Ni M., Leung M.K.H., Leung D.Y.C., Sumathy K. (2007). *Renewable Sustainable Energy Rev.*, **11**, 401–425.

380. Zou Z., Ye J., Sayama K., Arakawa H. (2001). *Nature*, **414**, 625–627.

381. Chapin D., Fuller C., Pearson G. (1954). *J. Appl. Phys.*, **25**, 676–677.

382. Green M.A., Emery K., Bücher K., King D.L., Igari S. (1999). *Prog. Photovoltics Res. Appl.*, **7**, 321–326.

383. Green M.A. (1982). *Solar Cells: Operating Principles*, *Technology*, *and System Applications*, Prentice-Hall Inc., Englewood Cliffs, NJ, pp. 288.

384. Peter L.M. (2011). *Philos. Trans. R. Soc. London*, *Ser. A*, **369**, 1840–1856.

385. Carlson D., Wronski C. (1976). *Appl. Phys. Lett.*, **28**, 671–673.

386. Lebrun J. (1970). In *Proceedings of the International Conference on the Physics and Chemistry of Semiconductor Heterojunctions and Layer Structures*, Budapest, Hungary, pp. 163.

387. Kazmerski L., White F., Morgan G. (1976). *Appl. Phys. Lett.*, **29**, 268–270.

388. Goetzberger A., Hebling C. (2000). *Sol. Energy Mater. Sol. Cells*, **62**, 1–19.

389. Hoppe H., Sariciftci N.S. (2004). *J. Mater. Res.*, **19**, 1925.

390. O'Regan B., Grätzel M. (1991). *Nature*, **353**, 737–740.

391. Krebs F.C. (2009). *Org. Electron.*, **10**, 761–768.

392. Kojima A., Teshima K., Shirai Y., Miyasaka T. (2009). *J. Am. Chem. Soc.*, **131**, 6050–6051.

393. Liu M., Johnston M.B., Snaith H.J. (2013). *Nature*, **501**, 395–398.

394. Lee M.M., Teuscher J., Miyasaka T., Murakami T.N., Snaith H.J. (2012). *Science*, **338**, 643–647.

395. Stranks S.D., Eperon G.E., Grancini G., Menelaou C., Alcocer M.J.P., Leijtens T., Herz L.M., Petrozza A., Snaith H.J. (2013). *Science*, **342**, 341–344.

396. www.nrel.gov/ncpv/images/efficiency_chart.jpg.

397. Li X., Zhu H., Wang K., Cao A., Wei J., Li C., Jia Y., Li Z., Li X., Wu D. (2010). *Adv. Mater.*, **22**, 2743–2748.

398. Wang X., Zhi L., Tsao N., Tomović Z., Li J., Müllen K. (2008). *Angew. Chem. Int. Ed.*, **47**, 2990–2992.

399. Kymakis E., Savva K., Stylianakis M.M., Fotakis C., Stratakis E. (2013). *Adv. Funct. Mater.*, **23**, 2742–2749.

400. Granqvist C.G. (2007). *Sol. Energy Mater. Sol. Cells*, **91**, 1529–1598.

401. Miao X., Tongay S., Petterson M.K., Berke K., Rinzler A.G., Appleton B.R., Hebard A.F. (2012). *Nano Lett.*, **12**, 2745–2750.

402. Wu Y., Zhang X., Jie J., Xie C., Zhang X., Sun B., Wang Y., Gao P. (2013). *J. Phys. Chem. C*, **117**, 11968–11976.

403. Ishii H., Sugiyama K., Ito E., Seki K. (1999). *Adv. Mater.*, **11**, 605–625.

404. Li S.S., Tu K.H., Lin C.C., Chen C.W., Chhowalla M. (2010). *ACS Nano*, **4**, 3169–3174.

405. Stratakis E., Stylianakis M.M., Koudoumas E., Kymakis E. (2013). *Nanoscale*, **5**, 4144–4150.

406. Stylianakis M.M., Spyropoulos G.D., Stratakis E., Kymakis E. (2012). *Carbon*, **50**, 5554–5561.

407. Liu Z., Liu Q., Huang Y., Ma Y., Yin S., Zhang X., Sun W., Chen Y. (2008). *Adv. Mater.*, **20**, 3924–3930.

408. Jeon Y.J., Yun J.M., Kim D.Y., Na S.I., Kim S.S. (2012). *Sol. Energy Mater. Sol. Cells*, **105**, 96–102.

409. Kim J., Tung V.C., Huang J. (2011). *Adv. Energy Mater.*, **1**, 1052–1057.

410. Li M., Ni W., Kan B., Wan X., Zhang L., Zhang Q., Long G., Zuo Y., Chen Y. (2013). *Phys. Chem. Chem. Phys.*, **15**, 18973–18978.

411. Robaeys P., Bonaccorso F., Bourgeois E., D'Haen J., Dierckx W., Dexters W., Spoltore D., Drijkoningen J., Liesenborgs J., Lombardo A. (2014). *Appl. Phys. Lett.*, **105**, 083306.

412. Green M.A. (1982). *Solar Cells: Operating Principles, Technology, and System Applications*, Prentice-Hall Inc., Englewood Cliffs, NJ, pp. 288.

413. Yong V., Tour J.M. (2009). *Small*, **6**, 313–318.

414. Echtermeyer T.J., Britnell L., Jasnos P.K., Lombardo A., Gorbachev R.V., Grigorenko A.N., Geim A.K., Ferrari A.C., Novoselov K.S. (2011). *Nat. Commun.*, **2**, 458.

415. Bremner S., Levy M., Honsberg C.B. (2008). *Prog. Photovoltics Res. Appl.*, **16**, 225–233.

416. Wang Y., Jaiswal M., Lin M., Saha S., Özyilmaz B., Loh K.P. (2012). *ACS Nano*, **6**, 1018–1025.

417. Manga K.K., Wang J., Lin M., Zhang J., Nesladek M., Nalla V., Ji W., Loh K.P. (2012). *Adv. Mater.*, **24**, 1697–1702.

418. Odkhuu D., Shin D., Ruoffand R.S., Park N. (2013). *Sci. Rep.*, **3**, 3276.

419. Yan X., Cui X., Li B., Li L. (2010). *Nano Lett.*, **10**, 1869–1873.

420. Becerril H.A., Man J., Liu Z., Stoltenberg R.M., Bao Z., Chen Y. (2008). *ACS Nano*, **2**, 463.

421. Yin Z.Y., Sun S.Y., Salim T., Wu S.X., Huang X.A., He Q.Y. (2010). *ACS Nano*, **4**, 5263.

422. Forrest S.R. (2004). *Nature*, **428**, 911.

423. Chen Z., Cotterell B., Wang W., Guenther E., Chua S.J. (2001). *Thin Solid Films*, **394**, 201.

424. Yin Z.Y., Wu S.X., Zhou X.Z., Huang X., Zhang Q.C., Boey F. (2010). *Small*, **6**, 307.

425. Wang X., Zhi L.J., Müllen K. (2008). *Nano Lett.*, **8**, 323.

426. Zhu Y., Murali S., Cai W., Li X., Suk J.W., Potts J.R., Ruoff R.S. (2010). *Adv. Mat.*, **22(35)**, 3906–3924.

427. Peng Q., Dearden A.K., Crean J., Han L., Liu S., Wen X., De S. (2014). *Nanotechnol. Sci. Appl.*, **2014(7)**, 1–29.

428. Zhou C., Chen S., Lou J., Wang J., Yang Q., Liu C., Huang D., Zhu T. (2014). *Nanoscale Res. Lett.*, **9(1)**, 26–34.

429. Huang X., Yin Z., Wu S., Qi X., He Q., Zhang Q., Yan Q., Boey F., Zhang H. (2011). *Small*, **7(14)**, 1876–1902.

430. http://www.itrs.net

431. Novoselov K.S., Geim A.K., Morozov S.V., Jiang D., Zhang Y., Duobonos S.V., Grigorieva I.V., Firsov A.A. (2004). *Science*, **306(5696)**, 666–669.

432. Fuhrer M.S., Lau C.N., MacDonald A.H. (2010). *MRS Bull.*, **35(4)**, 289–295.

433. Li N., Wang Z., Shi Z. (2011). Chapter 2: Synthesis of graphenes with arc-discharge method, In *Physics and Applications of Graphene*, Mikhailov S., (ed.), Rijeka, Croatia: Intech Open Publishing, pp. 23–36.

434. Balandin A.A. (2011). *Nat. Mater.*, **10(8)**, 569–581.

435. Schwierz F. (2010). *Nat. Nanotechnol.*, **5(7)**, 487–496.

436. Myung S., Park J., Lee H., Kim K.S., Hong S. (2010). *Adv. Mater.*, **22**, 2045.

437. Mikhailov S. (2011). *Physics and Applications of Graphene*, Available at www.intechopen.com

438. Moore G.E. (2003). IEEE International Solid-State Circuits Conference, ISSCC 2003, In *Tech. Dig.*, **1**, 20–23. (doi.org/10.1109/ISSCC.2003.1234194)

439. Schwierz F., Wong H., Liou J.J. (2010). *Nanomaterials,* CMOS, Pan Stanford Publishing, Singapore.

440. Schwierz F. (2010). *Nat. Nanotechnol.*, **5**, 487–496.

441. Houssa M., Pourtois G., Afanas'ev V.V., Stesmans A. (2010). *Appl. Phys. Lett.*, **97**, 112106.

442. Balandin A.A. (2011). *Nat. Mater.*, **10**, 569–581.

443. Meindl J.D., Chen Q., Davis J.A. (2001). *Science*, **293**, 2044–2049.

444. Banerjee S.K., Register L.F., Tutuc E., Reddy D., MacDonald A.H. (2009). *IEEE Electron Device Lett.*, **30**, 158–160.

445. Su J., MacDonald A.H. (2008). *Nat. Phys.*, **4**, 799–780.

446. Jornet J.M., Akyildiz I.F. (2011). *IEEE Trans. Wireless Commun.*, **10**, 3211–3221.

447. Cunningham S.L., Maradudin A.A., Wallis R.F. (1974). *Phys. Rev. B*, **10**, 3342–3355.

448. Bozhevolnyi S.I., Volkov V.S., Devaux E., Laluet J.Y., Ebbesen T.W. (2006). *Nature*, **440**, 508–511.

449. Holmgaard T., Bozhevolnyi S.I. (2007). *Phys. Rev. B*, **75**, 245405.

450. Best S.R., Morrow J.D. (2002). *IEEE Antennas Wireless Propag. Lett.*, **1**, 112–115.

451. Ryzhii V., Ryzhii M., Satou A., Otsuji T., Dubinov A., Aleshkin V.Y. (2009). *J. Appl. Phys.*, **106**, 084507.

452. Ryzhii V. (2006). *Jpn. J. Appl. Phys.*, **45**, L923.

453. Yang X., Liu G., Balandin A.A., Mohanram K. (2010). *ACS Nano*, **4**, 5532–5538.

454. Benini L., Micheli G.D. (2002). *Computer*, **35**, 70–78.

455. Akyildiz I.F., Jornet J.M. (2010). *Nano Commun. Networks*, **1**, 3–19.

456. Toffoli T., MaRGOlus N. (1991). *J. Phys. D Appl. Phys.*, **47**, 263–272.

457. Geim A.K., Novoselov K.S. (2007). *Nat. Mater.*, **6**, 183–191.

458. Serra C.C., Medeiros C.R., Costa J.R., Fernandes C.A. (2011). *IEEE Antennas Wireless Propag. Lett.*, **10**, 776–779.

459. Tamagnone M., Fallahi A., Mosig J.R., Perruisseau-Carrier J. (2014). *Nat. Photonics*, **8**, 556–563.

460. Coe S., Woo W.K., Bawendi M., Bulovic V. (2002). *Nature*, **420**, 800–803.

461. Lee J., Sundar V., Heine J., Bawendi M.G., Jemsen K.F. (2000). *Adv. Mater.*, **12**, 1102.

462. Carbone L., Nobile C., De Giorgi M., Sala F.D., Morello G., Pompa P., Hytch M., Snoeck E., Fiore A., Franchini I.R., Nadasan M., Silvestre A.F., Chiodo L., Kudera S., Cingolani R., Krahne R., Manna L. (2007). *Nano Lett.*, **7**, 2942–2950.

463. Dabbousi B., Rodriguez-Viejo J., Mikulec F.V., Heine J., Mattoussi H., Ober R., Jensen K., Bawendi M. (1997). *J. Phys. Chem. B*, **101**, 9463–9475.

464. Talapin D.V., Rogach A.L., Kornowski A., Haase M., Weller H. (2001). *Nano Lett.*, **1**, 207–211.

465. Maier S.A., Atwater H.A. (2005). *J. Appl. Phys.*, **98**, 011101.

466. Thiele C., Das R., Available at http://www.IDTechEx.com

467. Bonaccorso F., Sun Z., Hasan T., Ferrari A.C. (2010). *Nat. Photonics*, **4**, 611.

468. Yoon T., Shin W.C., Kim T.Y., Mun J.H., Kim T.S., Cho B.J. (2012). *Nano Lett.*, **12**, 1448–1452.

469. Rowell M.W., McGehee M.D. (2011). *Energy Environ. Sci.*, **4**, 131–134.

470. Wu J., Agrawal M., Becerril H.A., Bao Z., Liu Z., Chen Y., Peumans P. (2009). *ACS Nano*, **4**, 43–48.

471. Essig S., Marquardt C.W., Vijayaraghavan A., Ganzhorn M., Dehm S., Hennrich F., Ou F., Green A.A., Sciascia C., Bonaccorso F., Bohnen K.P., Löhneysen H.V., Kappes M.M., Ajayan P.M., Hersam M.C., Ferrari A.C., Krupke R. (2010). *Nano Lett.*, **10**, 1589.

472. Mallinckrodt E., Hughes A.L., Sleator W. (1953). *Science*, **118**, 277.

473. Strong R.M., Troxel D. (1970). *IEEE Trans. Hum. Mach. Syst.*, **11**, 72–79.

474. Nathan A., Ahnood A., Cole M.T., Sungsik L., Suzuki Y., Hiralal P., Bonaccorso F., Hasan T., Garcia-Gancedo L., Dyadyusha A., Haque S., Andrew P., Hofmann S., Moultrie J., Daping C., Flewitt A.J., Ferrari A.C.,

Kelly M.J., Robertson J., Amaratunga G.A.J., Milne W.I. (2012). *Proc. IEEE*, **100**, 1486–1517.

475. Kim U., Kang J., Lee C., Kwon H.Y., Hwang S., Moon H., Koo J.C., Nam J.D., Hong B.H., Choi J.B., Choi H.R. (2013). *Nanotechnology*, **24**, 145501.
476. Chen J., Badioli M., Alonso-Gonzalez P., Thongrattanasiri S., Huth F., Osmond J., Spasenovic M., Centeno A., Pesquera A., Godignon P., Zurutuza Elorza A., Camara N., de Abajo F.J.G., Hillenbrand R., Koppens F.H.L. (2012). *Nature*, **487**, 77–81.
477. Hill E.W., Vijayaragahvan A., Novoselov K. (2011). *IEEE Sens. J.*, **11**, 3161–3170.
478. Rangel N.L., Seminario J.M. (2010). *J. Chem. Phys.*, **132**, 125102.
479. Bae S.H., Lee Y., Sharma B.K., Lee H.J., Kim J.H., Ahn J.H. (2013). *Carbon*, **51**, 236–242.
480. Lee C., Ahn J., Lee K.B., Kim D., Kim J. (2012). *Thin Solid Films*, **520**, 5459–5462.
481. Kinaret J., Falko V., Ferrari A., Kivioja J., Löfwander T., Neumaier D., Novoselov K., Palermo V., Roche S. (2012). Graphene Flagship, WP3 Defining the Research Agenda, Deliverable 3.2 "Research agenda for the GRAPHENE flagship", pp. 1–29.
482. Poot M., Zant van der H.S.J. (2008). *Appl. Phys. Lett.*, **92**, 063111.
483. Liu Y., Dong X., Chen P. (2012). *Chem. Soc. Rev.*, **41**, 2283.
484. He Q.Y., Wu S.X., Yin Z.Y., Zhang H. (2012). *Chem. Sci.*, **3**, 1764–1772.
485. Avdoshenko S.M., Rocha da C.G., Cuniberti G. (2012). *Nanoscale*, **4**, 3168–3174.
486. Wong C.L., Annamalai M., Wang Z.Q., Palaniapan M. (2010). *J. Micromech. Microeng.*, **20(20)**, 115029.
487. Frank O., Tsoukleri G., Riaz I., Papagelis K., Parthenios J., Ferrari A.C., Geim A.K., Novoselov K.S., Galiotis C. (2011). *Nat. Commun.*, **2**, 255.
488. Hwang G., Acosta J.C., Vela E., Haliyo S., Regnier S. (2009). *International Symposium on Optomechatronic Technologies*, pp. 169–174.
489. Lai K.W.C., Xi N., Chen H.Z., Fung C.K.M., Chen L.L. (2011). *IEEE Sens.*, 398–401.
490. Pisana S., Braganca P.M., Marinero E.E., Gurney B.A. (2009). *Nano Lett.*, **10**, 341–346.
491. Foxe M., Lopez G., Childres I., Jalilian R., Roecker C., Boguski J., Jovanovic I., Chen Y.P. (2009). *IEEE Nuclear Science Symposium Conference Record*, **1–5**, pp. 90–95.

492. Patil A., Koybasi O., Lopez G., Foxe M., Childres I., Roecker C., Boguski J., Gu J., Bolen M.L., Capano M.A., Ye P., Jovanovic I., Chen Y.P. (2011). *IEEE Nuclear Science Symposium and Medical Imaging Conference*, pp. 455–459

493. Hassoun J., Bonaccorso F., Agostini M., Angelucci M., Betti M.G., Cingolani R., Gemmi M., Mariani C., Panero S., Pellegrini V., Scrosati B. (2014). *Nano Lett.*, **14**, 4901–4906.

494. Wang Y., Yang R., Shi Z.W., Zhang L.C., Shi D.X., Wang E., Zhang G.Y. (2011). *ACS Nano*, **5**, 3645–3650.

495. Murdock A.T., Koos A., Britton T.B., Houben L., Batten T., Zhang T., Wilkinson A.J., Dunin Borkowski R.E., Lekka C.E., Grobert N. (2013). *ACS Nano*, **7**, 1351–1359

496. Li X., Magnuson C.W., Venugopal A., Tromp R.M., Hannon J.B., Vogel E.M., Colombo L., Ruoff R.S. (2011). *J. Am. Chem. Soc.*, **133**, 2816–2819.

497. Tao L., Lee J., Holt M., Chou H., McDonnell S.J., Ferrer D.A., Babenco M.G., Wallace R.M., Banerjee S.K., Ruoffand R.S., Akinwande D. (2012). *J. Phys. Chem. C*, **116**, 24068–24074.

498. Chen G., Paronyan T.M., Harutyunyan R. (2012). *Appl. Phys. Lett.*, **101**, 053119.

499. Ekinci K.L., Huang X.M.H., Roukes M.L. (2004). *Appl. Phys. Lett.*, **84**, 4469–4471.

500. Stoller M.D., Park S., Zhu Y., An J., Ruoff R.S. (2008). *Nano Lett.*, **8**, 3498–3502.

501. Sakhaee-Pour A., Ahmadian M.T., Vafai A. (2008). *Solid State Commun.*, **145**, 168–172.

502. Lau C.N., Bao W.Z., Velasco J. (2012). *Mater. Today*, **15**, 238–245.

503. Zande van der A.M., Barton R.A., Alden J.S., Ruiz-Vargas C.S., Whitney W.S., Pham P.H.Q., Park J., Parpia J.M., Craighead H.G., McEuen P.L. (2010). *Nano Lett.*, **10**, 4869–4873.

504. Bunch J.S., Zande Van Der A.M., Verbridge S.S., Frank I.W., Tanenbaum D.M., Parpia J.M., Craighead H.G., McEuen P.L. (2007). *Science*, **315**, 490–493.

505. Bolotin K.I., Sikes K., Jiang Z., Klima M., Fudenberg G., Hone J., Kim P., Stormer H. (2008). *Solid State Commun.*, **146**, 351–355.

506. Du X., Skachko I., Barker A., Andrei E.Y. (2008). *Nat. Nanotechnol.*, **3**, 491–495.

507. Tombler T.W., Zhou C.W., Alexseyev L., Kong J., Dai H.J., Lei L., Jayanthi C.S., Tang M.J., Wu S.Y. (2000). *Nature*, **405**, 769–772.

508. Crochet J.J., Clemens M., Hertel T. (2007). *J. Am. Chem. Soc.*, **129**, 8058–8059.

509. Arnold M.S., Green A.A., Hulvat J.F., Stupp S.I., Hersam M.C. (2006). *Nat. Nanotechnol.*, **1**, 60–65.

510. Bonaccorso F., Hasan T., Tan P.H., Sciascia C., Privitera G., Di Marco G., Gucciardi P.G., Ferrari A.C. (2010). *J. Phys. Chem. C*, **114**, 17267–17285.

511. Krupke R., Hennrich F., Löhneysen H.V., Kappes M.M. (2003). *Science*, **301**, 344–347.

512. Zheng M., Jagota A., Strano M.S., Santos A.P., Barone P., Chou S.G., Diner B.A., Dresselhaus M.S., McLean R.S., Onoa G.B., Samsonidze G.G., Semke E.D., Usrey M., Walls D.J. (2003). *Science*, **302**, 1545–1548.

513. Tu X.M., Manohar S., Jagota A., Zheng M. (2009). *Nature*, **460**, 250–253.

514. Ghosh S., Bachilo S.M., Weisman R.B. (2010). *Nat. Nanotechnol.*, **5**, 443–450.

515. Yang W.R., Ratinac K.R., Ringer S.P., Thordarson P., Gooding J.J., Braet F. (2010). *Angew. Chem., Int. Ed.*, **49**, 2114–2138.

516. Schedin F., Geim A.K., Morozov S.V., Hill E.W., Blake P., Katsnelson M.I., Novoselov K.S. (2007). *Nat. Mater.*, **6**, 652–655.

517. Chen G., Paronyan T.M., Harutyunyan R. (2012). *Appl. Phys. Lett.*, **101**, 053119.

518. Jeong H.Y., Lee D.S., Choi, H.K., Lee D.H., Kim J.E., Lee J.Y., Lee W.J., Kim S.O., Choi S.Y. (2010). *Appl. Phys. Lett.*, **96**, 213105.

519. Chung M.G., Kim D.H., Seo D.K., Kim T., Im H.U., Lee H.M., Yoo J.B., Hong S.H., Kang T.J., Kim Y.H. (2012). *Sens. Actuators B*, **169**, 387–392.

520. Subbiah A., Shreekumar P., Shree R.S., Ashok K. (2011). In *Graphene: Synthesis and Applications*, CRC Press, pp. 233–262, DOI: 10.1201/b11259-910.1201/b11259-9.

521. Lohmann T., Klitzing von K., Smet J.H. (2009). *Nano Lett.*, **9**, 1973–1979.

522. Pirkle A., Chan J., Venugopal A., Hinojos D., Magnuson C.W., McDonnell S., Colombo L., Vogel E.M., Ruoffand R.S., Wallace R.M. (2011). *Appl. Phys. Lett.*, **99**, 122108.

523. Wang Y.J., Huang B.C., Zhang M., Woo J.C.S. (2012). *Microelectron. Reliab.*, **52**, 1602–1605.

524. Chen J.H., Jang C., Adam S., Fuhrer M.S., Williams E.D., Ishigami M. (2008). *Nat. Phys.*, **4**, 377–381.

525. Dan Y.P., Lu Y., Kybert N.J., Luo Z.T., Johnson A.T.C. (2009). *Nano Lett.*, **9**, 1472–1475.

526. Cagliani A., Mackenzie D.M.A., Tschammer L.K., Pizzocchero F., Almdal K., Bøggild P. (2014). *Nano Res.*, **7**, 743–754.

527. Salehi-Khojin A., Estrada D., Lin K.Y., Bae M.H., Xiong F., Pop E., Masel R.I. (2011). *Adv. Mater.*, **24**, 53.

528. Paul R.K., Badhulika S., Saucedo N.M., Mulchandani A. (2012). *Anal. Chem.*, **84**, 8171–8178.

529. Lu Y., Goldsmith B.R., Kybert N.J., Johnson A.T.C. (2010). *Appl. Phys. Lett.*, **97**, 083107.

530. Wang Y., Yang R., Shi Z.W., Zhang L.C., Shi D.X., Wang E., Zhang G.Y. (2011). *ACS Nano*, **5**, 3645–3650.

531. Lee Y., Bae S., Jang H., Jang S., Zhu S.E., Sim S.H., Song Y.I., Hong B.H., Ahn J.H. (2010). *Nano Lett.*, **10**, 490.

532. Fu X.W., Liao Z.M., Zhou J.X., Zhou Y.B., Wu, H.C. Zhang R., Jing G.Y., Xu J., Wu X.S., Guo W.L., Yu D.P. (2011). *Appl. Phys. Lett.*, **99**, 213107.

533. Cocco G., Cadelano E., Colombo L. (2010). *Phys. Rev. B*, **81**, 241412 (R).

534. Fogler M.M., Guinea F., Katsnelson M.I. (2008). *Phys. Rev. Lett.*, **101**, 226804.

535. Guinea F., Katsnelson M.I., Geim A.K. (2009). *Nat. Phys.*, **6**, 30–33.

536. Klimov N.N., Jung S., Zhu S., Li T., Wright C.A., Solares, S.D., Newell D.B., Zhitenev N.B., Stroscio J.A. (2012). *Science*, **336**, 1557–1561.

537. Levy N., Burke S.A., Meaker K.L., Panlasigui M., Zettl A., Guinea F., Neto A.H.C., Crommie M.F. (2010). *Science*, **329**, 544–547.

538. Rondin L., Tetienne J.P., Spinicelli P., Savio Dal C., Karrai K., Dantelle G., Thiaville A., Rohart S., Roch J.F., Jacques V. (2012). *Appl. Phys. Lett.*, **100**, 153118.

539. Chemla Y.R., Grossman H.L., Poon Y., McDermott R., Stevens R., Alper M.D., Clarke J. (2000). *Proc. Natl. Acad. Sci. USA*, **97**, 14268–14272.

540. Busham B. (1990). *Tribology and Mechanics of Magnetic Storage Devices*, Springer.

541. Ramsden E. (2006). *Hall-Effect Sensors*, Elsevier.

542. Source: IHS iSuppli Market Research.

543. (a) Lee E.J.H., Balasubramanian K., Weitz R.T., Burghard M., Kern K. (2008). *Nat. Nanotechnol.*, **3**, 486–490. (b) Lv X., Huang Y., Liu Z., Tian J., Wang Y., Ma Y. (2009). *Small*, **5**, 1682. (c) Chandra V., Kim K.S. (2011). *Chem. Commun.*, **47**, 3942.

544. (a) Park J., Ahn Y., Ruiz-Vargas C. (2009). *Nano Lett.*, **9**, 1742–1746. (b) Ghosh S., Sarker B.K., Chunder A., Zhai L., Khondaker S.I. (2010). *Appl. Phys. Lett.*, **96**, 163109.

545. (a) Xia F., Mueller T., Golizadeh-Mojarad R., Freitag M., Lin Y., Tsang J., Perebeinos V., Avouris P. (2009). *Nano Lett.*, **9**, 1039–1044. (b) Chang H., Sun Z., Yuan Q., Ding F., Tao X., Yan F. (2010). *Adv. Mater.*, **22**, 4872.

546. Giovannetti G., Khomyakov P., Brocks G., Karpan V., Brink Van den J., Kelly P. (2008). *Phys. Rev. Lett.*, **101**, 26803.

547. Xia F., Mueller T., Lin Y.M., Valdes-Garcia A., Avouris P. (2009). *Nat. Nanotechnol.*, **4**, 839.

548. Huard B., Stander N., Sulpizio J., Goldhaber Gordon D. (2008). *Phys. Rev. B*, **78**, 121402.

549. Urich A. (2012). *Appl. Phys. Lett.*, **101**, 153113.

550. Withers F., Bointon T.H., Craciun M.F., Russo S. (2013). *ACS Nano*, **7**, 5052–5057.

551. Xu X., Gabor N.M., Alden J.S., Zande van der A.M., McEuen P.L. (2009). *Nano Lett.*, **10**, 562–566.

552. Konstantatos G., Badioli M., Gaudreau L., Osmond J., Bernechea M., De Arquer F.P.G., Gatti F., Koppens F.H.L. (2012). *Nat. Nanotechnol.*, **7**, 363–368.

553. Konstantatos G., Sargent E.H. (2010). *Nat. Nanotechnol.*, **5**, 391–400.

554. Urich A., Unterrainer K., Mueller T. (2011). *Nano Lett.*, **11**, 2804–2808.

555. Zhang B.Y., Liu T., Meng B., Li X., Liang G., Hu X., Wang Q.J. (2013). *Nat. Commun.*, **4**, 1811.

556. Wang X., Cheng Z., Xu K., Tsang H.K., Xu J.B. (2013). *Nat. Photonics*, **7**, 888–891.

557. Pospischil A., Humer M., Furchi M.M., Bachmann D., Guider R., Fromherz T., Mueller T. (2013). *Nat. Photonics*, **7**, 892–896.

558. Echtermeyer T.J., Britnell L., Jasnos P.K., Lombardo A., Gorbachev R.V., Grigorenko A.N., Geim A.K., Ferrari A.C., Novoselov K.S. (2011). *Nat. Commun.*, **2**, 458.

559. Chen L., Lipson M. (2009). *Opt. Express*, **17**, 7901–7906.

560. Novack A., Gould M., Yang Y., Xuan Z., Streshinsky M., Liu Y., Capellini G., Lim A.E.J., Lo G.Q., Baehr-Jones T. (2013). *Opt. Express*, **21**, 28387.

561. Ito H., Furuta T., Kodama S., Watanabe S., Ishibashi T. (1999). *Electron. Lett.*, **35**, 1556–1557.

562. Britnell L., Ribeiro R.M., Eckmann A., Jalil R., Belle B.D., Mishchenko A., Kim Y.J., Gorbachev R.V., Georgiou T., Morozov S.V., Grigorenko A.N., Geim A.K., Casiraghi C., Castro Neto A.H., Novoselov K.S. (2013). *Science*, **340**, 1311–1314.

563. Guo W., Xu S., Wu Z., Wang N., Loy M.M.T., Du S. (2013). *Small*, **9**, 3031–3036.

564. Sun Z., Liu Z., Li J., Tai G.A., Lau S.P., Yan F. (2012). *Adv. Mater.*, **24**, 5878–5883.

565. Roy K., Padmanabhan M., Goswami S., Sai T.P., Ramalingam G., Raghavan S., Ghosh A. (2013). *Nat. Nanotechnol.*, **8**, 826–830.

566. Sukhovatkin V., Hinds S., Brzozowski L., Sargent E.H. (2009). *Science*, **324**, 1542–1544.

567. Konstantatos G., Clifford J., Levina L., Sargent E.H. (2007). *Nat. Photonics*, **1**, 531–534.

568. Konstantatos G., Howard I., Fischer A., Hoogland S., Clifford J., Klem E., Levina L., Sargent E.H. (2006). *Nature*, **442**, 180–183.

569. Keuleyan S., Lhuillier E., Brajuskovic V., GuyotSionnest P. (2011). *Nat. Photonics*, **5**, 489–493.

570. Pospischil A., Furchi M.M., Mueller T. (2014). *Nat. Nanotechnol.*, **9**, 257–261.

571. Baugher B.W.H., Churchill H.O.H., Yang Y., Jarillo-Herrero P. (2014). *Nat. Nanotechnol.*, **9**, 257–261.

572. Yan J., Kim M.H., Elle J.A., Sushkov A.B., Jenkins G.S., Milchberg H.M., Fuhrer M.S., Drew H.D. (2012). *Nat. Nanotechol.*, **7**, 472–478.

573. Tonouchi M. (2007). *Nat. Photonics*, **1**, 97–105.

574. Dyakonov M., Shur M. (1993). *Phys. Rev. Lett.*, **71**, 2465–2468.

575. Dyakonov M., Shur M. (1996). *IEEE Trans. Electron Devices*, **43**, 380–387.

576. Vicarelli L., Vitiello M., Coquillat D., Lombardo A., Ferrari A., Knap W., Polini M., Pellegrini V., Tredicucci A. (2012). *Nat. Mater.*, **11**, 865.

577. Cai X., Sushkov A.B., Suess R.J., Jadidi M.M., Jenkins G.S., Nyakiti L.O., Myers-Ward R.L., Yan J., Gaskill D.K., Murphy T.E. (2014). *Nat. Nanotechnol.*, **9**, 814–819.

Chapter 5

Summary

Graphene-based NMs have been studied and successfully investigated intensively during the past two decades, which shows that there has been a demand to increase efforts to search graphene-related new functional NMs. However, this book endeavours to summarise the current status of graphene research and the state-of-the-art techniques for graphene-related NMs and their derivatives that have predominated as functionalised graphene-based NMs. Graphene has already shown its potential as a nanocarbon material because of its ability for electronic conduction , functionalisation and a versatile nanoscale design.

During the past decade, scientists have devoted their ever increasing efforts to develop new graphene-related functional and hybrid NMs. This book also summarises the current scenario of different graphene derivatives including functionalised graphene, doped graphene, oxidised graphene, hydrogenated and fluorinated graphene, edge-functionalised GNRs, graphdiyne, graphyne and porous graphene. These functional 2D carbon–based NMs have boosted the fundamental interest in technical and scientific points of view, which opens new avenues for the applications due to their distinct properties. Compared to the perfect graphene having absence of a band gap, graphene derivatives possess electronic properties varying from semiconductors, half-metals to metals that demonstrate encouraging technological potentials in the fields of

Graphene Nanomaterials: Fabrication, Properties and Applications
Satyendra Mishra and Dharmesh Hansora

ISBN 978-981-4745-41-3 (Hardcover), 978-1-315-36455-1 (eBook)
www.panstanford.com

electronics, memory, optical devices, energetic applications of fuel cell electrodes, SCs and batteries, catalysis, sensors, biotechnology, gas/ion separation, etc. As a new family of 2D carbon NMs, graphene derivatives offer prospective platforms to investigate new structures with characteristic properties, chemistry, engineering and technological applications. A clear understanding of these carbon NMs is crucial for the birth of graphene-based nanoscience and technology.

Some challenges requiring great efforts still exist in achieving these novel NMs. Versatile properties of NMs are essentially much more needed to be explored and the focus must be on the (i) control of the doping behaviours of graphene to achieve the magnetic and electronic properties; (ii) modification and fabrication of GNRs with smooth edges and nanoscale widths with as-expected edges; (iii) interpretation of atomic structures of GO; (iv) removal of the oxygen groups during the reduction process, which can enhance the electrical conductivity; (v) preparation of fully and partially hydrogenated and fluorinated graphene with controllable hydrogenation/fluorination ratios. Graphyne and graphdiyne have been predicted to have great potentials, but the optimisations in synthesis methods are needed for large-scale production. The ordered and tunable surface porosity of porous graphene might be difficult to achieve during the synthesis. It has been researched and demonstrated that the exceptional properties (mechanical, thermal, electrical, optical and long electron mean free paths) of graphene make it compatible for various engineering applications. Efforts have been made to explore the fundamental physics and chemistry of graphene, their derivatives and related NMs. Novel properties of 2D graphene nanostructures, such as highest charge transport, room temperature quantum Hall effect and thermal conductivity, have not been reported from 3D NMs. Research work done in the past 5 years indicates the importance of graphene-related NMs and it has surpassed silicon research for the development of microelectronics because silicon-based research is at a mature stage to overcome the technological barrier. The semimetal characteristic of GNRs and bilayer graphene has been modified to realise their applications in FET. However, graphene has some challenges in the development of the final device fabrication. Exceptional properties of defect-free graphene have been reported. The epitaxially grown single, bilayer and few-

layer graphene have been prepared by alternative methods such as CVD. The scalability of wafer scale using CVD method on different substrates and transfer of graphene layers for device fabrication has been demonstrated. Graphene-related researches are tremendous breakthroughs that offer novel opportunities for semiconductor applications. The graphite flakes exfoliation into GO sheets followed by thermal and chemical reduction has offered a cost-effective large-scale production route for RGO. However, the lowered electrical and mechanical properties result in a lack in control of functionalisation by other groups. But these can be controlled by oxidation/reduction and functionalisation by tuning the mechanical properties, band gap and electrical conductivity. Therefore, modified graphite, GO and RGO become crucial for the development of graphene-related NMs. The large surface of GO and RGO may be difficult to handle during mass production and may also lead to health risks due to inhaling and handling toxic chemicals. The health risk issues of graphene, their derivatives and related NMs need to be investigated by considering their toxicity and biocompatibility.

Graphene/polymer composites have shown improved thermal, mechanical and gas barrier properties. The potential applications of graphene, its derivatives, related NMs and graphene/polymer nanocomposites include the development of sensors, transparent flexible electrodes, energy storage, and organic electronics and mechanical parts. The higher charge mobility of RGO, compared to semiconducting conjugated polymers and amorphous silicon, enlightens the path for its electronic applications. The main hurdles in any device fabrication in which defects at atomic level and folding, wrinkling and overlapping at macro-scale of RGO are used require continuous research. A single-layer graphene sheet on suitable substrate can be viewed under an optical microscope, depending upon the substrate thickness and incident light wavelength. A pristine graphene should be researched by a simple detection method that is independent of support material. A high-resolution TEM micrograph can interpret the doping level and also reveal the defect structures in graphene quantum dots at atomic resolutions.

The advanced deposition technique of single- and bilayer graphene sheets makes it possible to use them in fabrication of large-area devices. Several factors such as GNRs dimension quantum confinement, tuning the substrates properties, bilayer graphene and

chemical functionalisation have been proposed for nanoelectronics. GNR with nanoscale dimension (i.e. 10 nm) can provide the right band gap for the development of efficient FET devices. Cutting graphene into GNR has shown their applications in FET logic applications but is associated with the electron scattering at the rough edges and disorder from the back substrate. The new options such as tunnel and bilayer pseudospin FETs have been researched to tackle the challenge observed during development of graphene-based FET devices. Recent investigations provided evidence of the reduction process and varying the oxidation level for tuning the band gap. Therefore, opening the band gap of graphene, GNR and GO has encouraged the development of future practical nanoelectronic devices which is comparable to metal oxide–based semiconductor circuits.

In summary, nanoengineering and technology can play a vital role in the development of devices made of graphene-related NMs, hybrid nanostructures and graphene/polymer nanocomposites with improved properties. By controlling the distribution, density, kind of chemical bonding as well as 3D arrangement of the components, the performances of graphene-based NMs and nanocomposites can be enhanced.

Index